UNIVERSITY OF SOUTHAMPTON

Modelling of the Thermal Chemical Damage Caused to Carbon Fibre Composites

by

Richard D Chippendale

A thesis submitted for the
degree of Doctor of Philosophy

in the
Faculty of Physical Sciences and Engineering
Department of Electronics and Computer Science

July 2013

UNIVERSITY OF SOUTHAMPTON

ABSTRACT

FACULTY OF PHYSICAL SCIENCES AND ENGINEERING
DEPARTMENT OF ELECTRONICS AND COMPUTER SCIENCE

Doctor of Philosophy

by Richard D Chippendale

Previous investigations relating to lightning strike damage of Carbon Fibre Composites (CFC), have assumed that the energy input from a lightning strike is caused by the resistive (Joule) heating due to the current injection and the thermal heat flux from the plasma channel. Inherent within this statement, is the assumption that CFCs can be regarded as a perfect resistor. The validity of such an assumption has been experimentally investigated within this thesis. This experimental study has concluded that a typical quasi-isotropic CFC panel can be treated as a perfect resistor up to a frequency of at least $10\,kHz$. By considering the frequency components within a lightning strike current impulse, it is evident that the current impulse leads predominately to Joule heating.

This thesis has experimentally investigated the damage caused to samples of CFC, due to the different current impulse components, which make up a lightning strike. The results from this experiment have shown that the observed damage on the surface is different for each of the different types of current impulse. Furthermore, the damage caused to each sample indicates that, despite masking only the area of interest, the wandering arc on the surface stills plays an important role in distributing the energy input into the CFC and hence the observed damage. Regardless of the different surface damage caused by the different current impulses, the resultant damage from each component current impulse shows polymer degradation with fracturing and lifting up of the carbon fibres.

This thesis has then attempted to numerically investigate the physical processes which lead to this lightning strike damage. Within the current state of the art knowledge there is no proposed method to numerically represent the lightning strike arc attachment and the subsequent arc wandering. Therefore, as arc wandering plays an important role in causing the observed damage, it is not possible to numerically model the lightning strike damage. An analogous damage mechanism is therefore needed so the lighting strike damage processes can be numerically investigated. This thesis has demonstrated that damage caused by laser ablation, represents a similar set of physical processes, to those which cause the lightning strike current impulse damage, albeit without any additional electrical processes.

Within the numerical model, the CFC is numerically represented through a homogenisation approach and so the relevance and accuracy of a series of analytical methods for predicting the bulk thermal and electrical conductivity for use with CFCs have been investigated. This study has shown that the electrical conductivity is dominated by the percolation effects due to the fibre to fibre contacts. Due to the more comparable thermal conductivity between the polymer and the fibres, the bulk thermal conductivity is accurately predicted by an extension of the Eshelby Method. This extension allows the bulk conductivity of a composite system with more than two composite components to be calculated. Having developed a bespoke thermo-chemical degradation model, a series of validation studies have been conducted. First, the homogenisation approach is validated by numerically investigating the electrical conduction through a two layer panel of CFC. These numerical predictions showed initially unexpected current flow patterns. These predictions have been validated through an experimental study, which in turn validates the application of the homogenisation approach.

The novelty within the proposed model is the inclusion of the transport of produced gasses through the decomposing material. The thermo-chemical degradation model predicts that the internal gas pressure inside the decomposing material can reach 3 orders of magnitude greater than that of atmospheric pressure. This explains the de-laminations and fibre cracking observed within the laser ablated damage samples. The numerical predictions show that the inclusion of thermal gas transport has minimal impact on the predicted thermal chemical damage. The numerical predictions have further been validated against the previously obtained laser ablation results. The predicted polymer degradation shows reasonable agreement with the experimentally observed ablation damage. This along with the previous discussions has validated the physical processes implemented within the thermo-chemical degradation model to investigate the thermal chemical lightning strike damage.

Contents

Nomenclature

1	Local Axis direction 1 - Along fibres
2	Local Axis direction 2 - Perpendicular to fibres in ply plane
3	Local Axis direction 3 - Perpendicular to fibres through ply plane
A	Pre exponential Factor (s)
AC	Alternating Current (V)
A_{cell}	Area of control volume sides
A_{G}	Area under Gaussian Curve
A_{xs}	Cross sectional Area $[m^2]$
C	Capacitor (F)
C_c	Contact Capacitance [F]
C_p	Specific heat Capacity at Constant Pressure $[Jkg^{-1}K^{-1}]$
C_v	Specific heat Capacity at Constant Volume $[Jkg^{-1}K^{-1}]$
D	Electrode Spacing
DC	Direct Current
$\mathbf{E}$	Electric Field $[Vm^{-1}]$
E_a	Activation energy $[J\mathrm{mol}^{-1}]$
H	Height
I	Current [A]
$\widehat{I}$	Identity matrix
I_o	Peak Current [A]
$\mathbf{J}$	Current density $[Am^{-2}]$
K	Generic Conductivity
L	length of sample in direction perpendicular to cross sectional area [m]
L_{CFC}	Latent heat of CFC
L_x	Length along x direction
L_y	Length along y direction
L_z	Length along z direction
M	Molar Mass $[kg\mathrm{mol}^{-1}]$
$\mathbf{N}$	Main negative charge region
$\mathbf{P}$	Main positive charge region
P	Pressure (Pa)
Q_{CFC}	Change in enthalpy of CFC

Q_d	Change in enthalpy of pyrolysis [J]
Q_j	Joule loss [W]
R	Resistance (Ω)
Re	Reynolds Number
R_c	Contact Resistance [Ω]
R_n	Low inductance known Resistor [ω]
S	Eshebly Shape Tensor
T	Temperature [K]
T_m	Temperature at Peak reaction rate
V	Volume [m^3]
V_{cell}	Volume of cell [m^3]
V_a	Anode fall Voltage [V]
W	Width
X	Electrical Reactance [ω]
Z	Electrical Impedance [ω]
$\|Z\|$	Impedance Magnitude
e	Electron charge
h	Convective Heat Transfer Coefficient [W/m^2K]
i	Grid element
j	Complex term
m	Mass (kg)
$m^\dagger$	Effective Mass (kg)
n	Reaction Order
n_R	Number of chemical reaction sub time steps
n_T	Number of thermal sub time steps
n_m	Number of mass transport sub time steps
p'	Small positive charge region
r_f	Radius of Carbon fibre
t	Time [s]
t_R	Size of chemical reaction sub time step
t_T	Size of thermal sub time step
t_m	Size of mass transport sub time step
u	Dummy dependent variable
v_g	Velocity of Gas (ms^{-1})
x	Spatial coordinate in x direction (m)
x_0	Centre of Gaussian curve along x
y	Spatial coordinate in y direction (m)
z	Spatial coordinate in z direction (m)
z_0	Centre of Gaussian curve along z
Γ	Remaining fraction of mass
$\dot{\Gamma}$	Reaction Rate

$\triangle t$	Global time step size
$\Delta X(1)$	Element Growth rate x direction [m]
$\Delta Y(1)$	Element Growth rate y direction [m]
$\Delta Z(1)$	Element Growth rate z direction [m]
Λ_x	Gaussian 1/eth peak value in x direction
Λ_z	Gaussian 1/eth peak value in z direction
Π	Difference in the mass of degraded polymer
Φ	Volume Fraction
Φ_{perc}	Percolation Volume Fraction Threshold
Ψ_v	Vapour Flux
$\Re$	Molar Gas Constant $[J\text{mol}^{-1}\,K^{-1}]$
α	Lightning strike current rise time $[s^{-1}]$
β	Lightning strike current fall time $[s^{-1}]$
γ	Permeability $[m^2]$
δ	Skin Depths [m]
ϵ_{cfc}	Emissivity
ϵ	Maximum Temperature difference
ζ_{ch}	Fractional mass of char produced via pyrolysis
ζ_g	Fractional mass of gas produced via pyrolysis
θ	Phase Shift
κ	Thermal Conductivity $[W/mK]$
μ	Viscosity $[kgs^{-1}m^{-1}]$
μ_m	Magnetic Permeability $[NA^{-2}]$
ρ	Density $[kg/m^3]$
σ	Electrical Conductivity $[Sm^{-1}]$
σ_{sb}	Stefan-Boltzmann Constant $[kgs^{-3}K^{-4}]$
τ	Tourosity
ϕ	Potential difference [V]
ψ_s	Work function [eV]
ω	Angular Frequency (Hz)

Subscripts

1	Local Axis direction 1 - Along fibres
2	Local Axis direction 2 - Perpendicular to fibres in ply plane
3	Local Axis direction 3 - Perpendicular to fibres through ply plane
ch	Char
f	Carbon fibre
g	Gas
p	Polymer

Acknowledgements

I would like to express my deep gratitude to my supervisors, Igor Golosnoy and Paul Lewin for their support and patience during my studies. I am also grateful to the Tony Davies High Voltage Laboratory for both the technical support with my experiments and also for making it possible for me to attend international conferences during my studies.

This study would not have been possible without the financial support given by EADS Innovation Works and furthermore, I would especially like to thank Stephanie Hellsten and Matthew Cole for all their input.

I would also especially like to extent my gratitude to Stephen Haigh and Dean Kemp from Cobham Lightning Testing Services, not only for allowing me to conduct lightning strike current impulse tests, but also for granting me access to their vast library of past ICOLSE and ICLP conference proceedings. During the few days I spent there, my knowledge of this research area increased beyond measure. I would also like to acknowledge the Cobham Lightning Club, for the part they played in allowing me to conduct the lightning strike current impulse tests.

I am also very grateful to my family for their support, not only during my PhD studies, but also throughout my entire academic career. Finally, but not least, I want to extend my gratitude to Carla Gomez Blanco for putting up with the long working hours and also giving endless encouragement whilst completing my PhD studies.

Chapter 1

Introduction

Aircraft have dramatically changed our perception of the size of the world over the last 100 years. Despite the passing of time, there is still an ever constant drive for further innovation within the aircraft industry. One of the main areas of research today is in developing new, stronger, lighter materials which can be used to build aircraft. However as this study will explain, it is not just as simple as finding a stronger lighter material. This is because aircraft suffer from a variety of different types of damage, and it is important these new materials can withstand these varying types of damage and/or fatigue.

1.1 Aircraft Construction materials

Aircraft have been constructed from a wide variety of different materials. The earliest powered aeroplane, built by the Wright brothers, was constructed from wood and muslin [1]. However, since these early days, aircraft have generally been constructed from aluminium alloys, although more recently composite materials such as fibre glass and carbon fibre composites [2, 3] have been used. The reason for this move towards composite materials, is that they are generally lighter than the traditional aluminium alloys [4, 5].

The very first aeroplanes to use composite materials in their construction used fibre glass composites on non-key structural components, such as spoilers and rudders. The first aircraft to enter commercial service having major components constructed from composite materials was the Airbus A310-300 [2]. Since then, there has been an ever increasing trend to use more and more composite materials. This is evident by considering the Boeing 777 and the Airbus A340, which were designed in the early 1990's and constructed from between 10-12% of composites materials by weight. Today, the new Boeing 787 Dreamliner and the proposed Airbus A350 XWB will be constructed from

of 50% and 53% by weight composite materials, respectively [3, 6]. This growing trend in using composite materials is shown in Figure 1.1

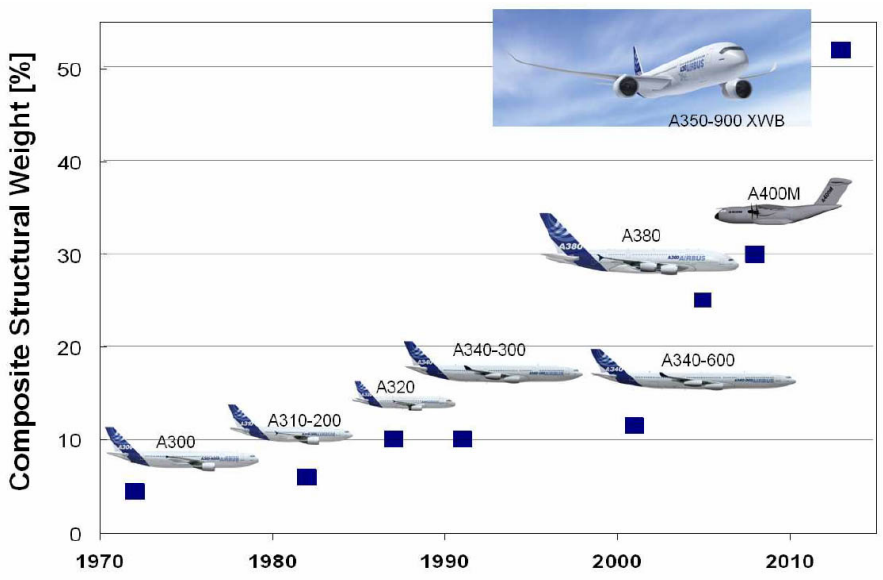

FIGURE 1.1: Use of composites materials in Airbus aircraft throughout the years [3]

With composites already in use within aircraft for non-structural components, the drive today is to use Carbon Fibre Composite (CFC) materials within key structural components. This is evident by considering the proportion of each different materials used in the construction of the Boeing 787, as shown in Figure 1.2

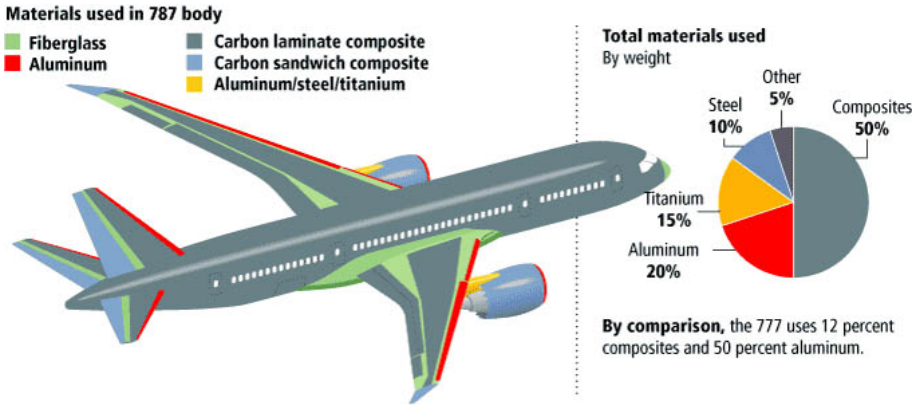

FIGURE 1.2: Shows the use of the different construction materials within a Boeing 787 [6]

The reason for using CFCs in the construction of aircraft, is that they offer similar mechanical properties to those of the more traditionally used materials such as aluminium alloys, whilst being up to 40 % lighter [7, 4]. This means an aircraft can be designed to carry similar payloads, whilst having a reduced net weight. This reduction in aircraft weight permits the use of smaller less powerful engines and so reduces the fuel consumption and the aircraft's environmental impact.

The main focus around the development of CFCs, is centred on their mechanical prop-

erties and weight reduction. As a result, whilst CFCs can be designed to have similar mechanical performance to aluminium alloys, their thermal and electrical properties are very different. It is these differences in thermal and electrical properties, which need careful consideration when considering some of the possible hazards which an aircraft might encounter during a flight.

1.2 Aircraft Hazards

During an aircraft's flight there are a wide variety of different hazards, to which it could fall foul of. Some of the more commonly considered hazards are bird strikes, engine failures or turbulence, but one less commonly discussed hazard is that of a lightning strike. It is recognised that a typical commercial aircraft is struck by lightning at least once a year or once for every 3000 flight hours [8].

Studies by V. Rakov [8] and J. Plumer [9] investigated at what point, during an aircraft's flight, it is more likely to be struck by lightning. This was achieved by examining hundreds of flight records. They concluded that lightning strikes to aircraft, typically occur when an aircraft passes through the bottom region of a cloud, typical between an altitude of between $1 - 6\,km$ i.e. either during take-off or landing. The recorded data from these test flights is shown in Figure 1.3.

There are typically fewer strike interactions with aircraft above $6\,km$, as at these altitudes an aircraft can be easily diverted around possible thunderclouds [9]. A detailed discussion outlining how an aircraft is struck by lightning is given in Chapter 2.

Whilst the majority of these aircraft hazards are managed through the mechanical performance of a material, the damage from lightning strikes is managed through the thermal and electrical properties of the material.

1.3 Lightning Strike Damage

In 1964, the Federal Aviation Administration (FAA) recognised that numerous aircraft had been lost as a result of lightning strikes [10], and required that in future, all commercial aircraft must have adequate protection. The type of damage caused to an aircraft due to a lightning strike is divided into two categories, direct and indirect. Direct effects are any physical effects caused to an aircraft due to the attachment of the lightning strike and/or conduction of the subsequent high current i.e. puncture of the airframe [11]. Indirect effects are those which are caused by electrical transients inducing electrical currents within the aircraft due to a lightning strike. This can result in damaging/interfering with electric circuits used for navigation or fly-by-wire systems [11]. This investigation is focused on the direct effects.

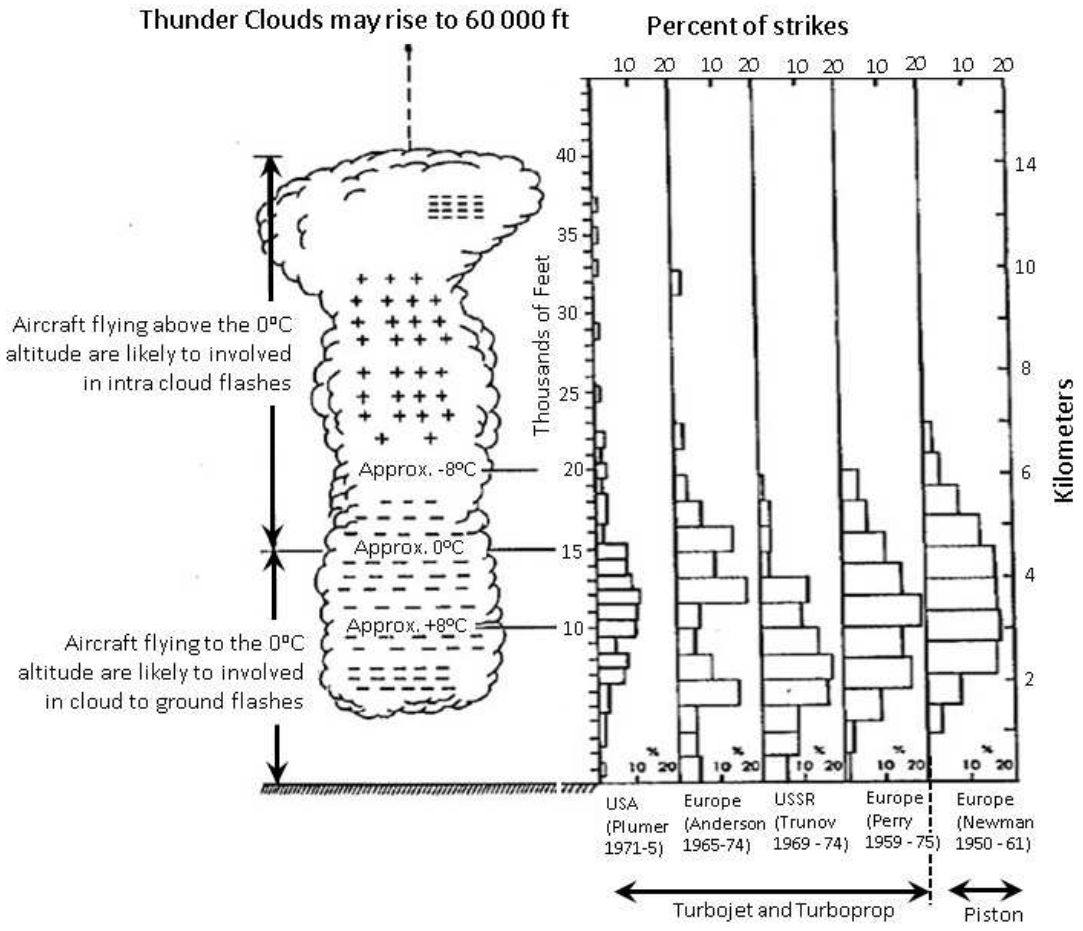

FIGURE 1.3: Number of lightning strikes at different altitudes. [9]

The typical lightning damage caused to metallic aircraft is pitting and even melt through. Surface pitting is more common, with only the longest lightning strike attachments resulting in a melt through. This damage is understood to be caused by the heating of the metals surface due to the heat flux from the plasma arc [9]. A visual example of the damage caused to a piece of aluminium following a lightning strike is shown below in Figure 1.4a).

It has been observed that the damage caused to a composite material due to a lighting strike is very different to that caused to a piece of aluminium, as evident by Figure 1.4, as the damage caused to a piece of CFC (shown in Figure 1.4b) due to a lightning strike, shows the lifting and breaking of the carbon fibres in the top few plies as opposed to the melting of aluminium. It is believed this differing damage, is caused by the comparatively poor electrical and thermal conductivity of the CFC when compared to aluminium.

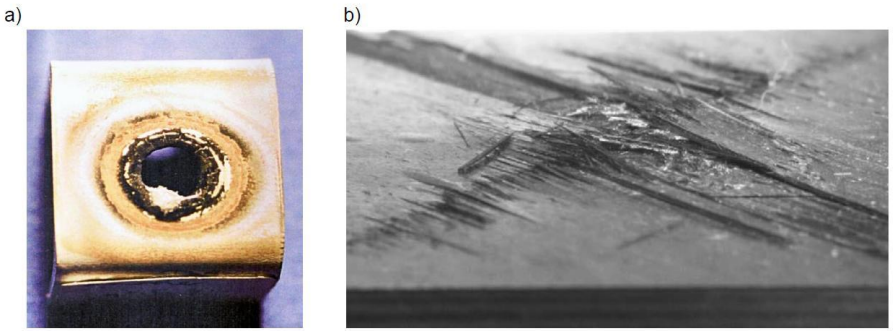

FIGURE 1.4: The images above shows the typical damage which results from a lightning strike to (a) aluminium [12] and (b) CFC. The aluminium damage (a) has been caused by a continuous current of 927 A, for a duration of 118 ms [12]. The CFC damage (b) has been caused by current impulse with a peak current of 50 kA, for a duration of 160 ms [13].

1.4 Research Motivation

Due to the different type of damage caused to CFCs (compared to metals), there have been many investigations aimed at reducing the damage caused to CFCs due to a lightning strike. All these investigations begin by damaging panels of CFC with laboratory produced lightning strikes. The investigations are then repeated with different fibre layups and/or composite components. From this collection of results, it is possible to consider what parameters reduce the recorded damage. This approach is very expensive and time consuming.

One way to reduce the number of experiments, is to use an appropriate simulation tool. This simulation tool could also be used to investigate the physical damage processes caused by a lightning strike on a piece of CFC. By understanding the physical processes, it is possible to guide the variation in the material parameters to more effectively reduce the damage. However, there is currently no appropriate simulation tool to predict the damage caused by a lightning strike to CFC.

The aim of this study is develop a simulation tool to investigate and predict the damage caused to a piece of CFC due to lightning strike damage. However, lightning strike damage is driven by a complex phenomenon, and so the following objectives have been identified:

- Investigate the physical processes which cause the damage to a panel of CFC due to a lightning strike.
- Obtain material properties for the required physical process and if required conduct experimental studies to determine the required material properties.
- Develop a modelling framework, which can accurately numerically represent a piece of CFC and its material properties.

- Develop and implement an appropriate numerical method by which the physical processes can be solved to obtain a numerical solution.
- Validate the numerical model by comparing results against an experimental study.
- Investigate the numerical predictions to determine what role each physical processes has on the predicted damage caused.

1.5 Contribution of this Thesis

This thesis makes significant contributions to the current knowledge on lightning strike damage to composite materials through the following aspects:

- When developing the numerical framework required to represent a CFC, the author has developed a series of modifications to the existing Eshelby method, which permits its application to predict the bulk thermal conductivity of composites with more than two components.
- A bespoke numerical model designed to investigate the thermo-chemical degradation has been developed. Due to the highly coupled nature of the physical processes, the modelling strategy required to obtain a converged solution is not straightforward. The author of this study has developed a fractional step method and verified the choice of sections into which the physical equations have been divided up into.
- The implementation of the numerical method has been validated by decoupling the thermal effects from the electrical effects and comparing against experimental studies. The validation of the electrical conduction model showed an initially unexpected current flow pattern, which has been subsequently validated experimentally.
- By investigating the thermo-chemical degradation predictions, the author has shown that the gas thermal transport has minimal impact on the predictions from the thermo-chemical degradation model, but the predicted peak pressure could explain the de-lamination and lifting up of fibres.

1.6 Thesis Outline

Chapter 2 is focused on conducting a comprehensive review of previous work that has been conducted in this area. The literature review is broken down as follows. The first aspect considers, what a CFC material is and what the properties of such a material are. The review then considers the fundamentals of lightning strikes and how they interact

with metals and CFCs. Next, having understood what makes up CFCs, methods to numerically represent a panel of CFC are reviewed. To do this, a review of the current literature is considered. The final part of the literature review considers how previous studies have developed models to predict the thermo-chemical degradation of different materials in different situations.

In Chapter 3, a review of the different experimental techniques which are required for this study are given. These include, outlining a series of experimental techniques required to investigate the material properties of a piece of CFC. This chapter concludes by outlining two experiments which have been conducted to damage samples of CFC.

The first part of Chapter 4 considers a series of experiments to determine the electrical properties of CFC. This investigation first addresses the question of whether there are any frequency dependent effects within the electrical properties of CFC. From the answer of this question, measurements are taken to determine the electrical properties of the bulk material. In the second half of Chapter 4, a series of experiments are conducted to investigate the thermo-chemical degradation processes of a piece of CFC. The results from both of these studies are required for directing the future numerical models.

In Chapter 5, a laser ablation experiment and a lightning strike current impulse experiment are conducted. The damaged caused to samples of CFC from these energy inputs are then compared and investigated.

Having experimentally observed the damage from a lightning strike in Chapter 5, the study then considers developing a bespoke numerical degradation model, designed to investigate the physical damage processes. To this end, Chapter 6 considers the framework required to represent a piece of CFC numerically for the bespoke degradation model. This framework is developed through the use of a homogenisation approach. With the framework in place, Chapter 7 outlines the physical equations required and their implementation within the bespoke degradation model. The last part of this chapter then considers validating the implementation of the bespoke (thermo-chemical) degradation model. This is done by considering each modelling section in turn against a known benchmark.

Chapter 8 begins by validating the homogeneous anisotropic approach used to represent a CFC numerically, by considering the current flow within a piece of CFC. The current flow pattern is not as obvious as one might initially believe, and this leads to an interesting result. This validation is conducted by comparing the numerical predictions against experimental results. The experimental laser ablation results from Chapter 5 are compared against the predictions from the bespoke degradation model. This comparison includes investigating the gas filtration and resultant internal pressure build up within the CFC. The study then concludes by conducting a parametric study to investigate the importance of a series of material properties.

In the final chapter, conclusions from the entire study are drawn together and presented.

Chapter 2

Literature Review

In order to obtain a view of how a lightning strike affects a carbon fibre composite structure, a comprehensive survey of related technical literature has been undertaken. The first part of this chapter provides an introduction to Carbon Fibre Composite (CFC) materials and their properties, followed by a discussion on what comprises a lightning strike and how it can damage different materials. The second half of this chapter introduces a series of numerical models, and the relevant modelling techniques which have been previously used to investigate the thermo-chemical degradation processes of composite materials. The findings from these discussions have been used to plan the direction of this study.

2.1 Carbon Fibre Composite Materials

Carbon Fibre Composites (CFC) are comprised of two constituents, fibres made of carbon, which are then encapsulated in a polymer matrix. The majority of the CFC strength comes from the fibres [14]. There are two forms of CFC: Short fibres composites, where short carbon fibres are randomly scattered within a matrix. A second, much stronger approach is to use long uni-directional strands of carbon fibres encapsulated in a matrix. Using these long fibre strands, thin sheets of CFCs, called plies, which are typically $0.25\,mm$ thick can be formed. The typical fibre volume fraction within these plies is between $60 - 70\%$. The CFC plies can then be stacked together, one on top of each other, with the fibres orientated at different angles in each ply, as shown in Figure 2.1. The net result is a material which has quasi-isotropic material properties and a very high tensile strength. A general quasi-isotropic ply lay-up is given in Appendix A.

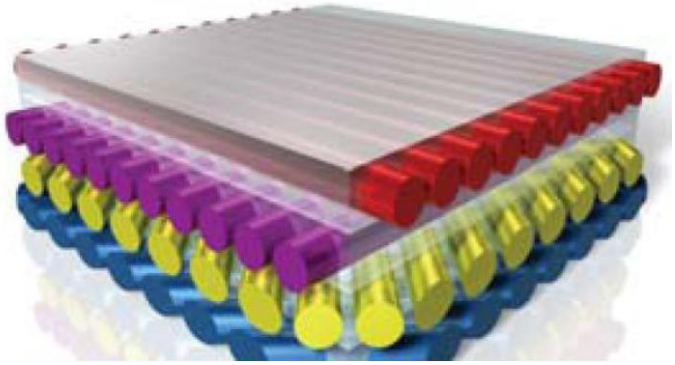

FIGURE 2.1: An illustration of a series of CFC plies highlighting the different orientations of fibres [15]

2.1.1 Carbon Fibres

There are two main types of carbon fibres, PAN (polyacrylonitrile) or PITCH derived fibres [7, 16, 5]. For a detailed discussion on the different manufacturing process for PAN and PITCH carbon fibres refer to [7, 17]. This discussion is kept to PAN fibres as they are the most commonly used within the hi-tech construction industry [18, 19]. PAN fibres typically have a diameter of $8 - 10\,\mu m$ and comprise 92 % by weight carbon atoms [14, 7]. The remaining weight is typically sodium and potassium, plus other trace elements [20]. It is important to consider the atomic structure of PAN fibres to gain an understanding of the conduction physics within these fibres.

PAN carbon fibres are made up of graphite layers. Graphite, itself, is composed of layers of sp^2 hybridized carbon atoms arranged in a planar hexagonal structure (x-y plane), as shown in Figure 2.2. The carbon atoms, within each graphite layer (x-y plane), are bonded together in plane by σ bonds and perpendicular to the plane by π bonding [17, 21]. As a result of the σ bonding, the graphite planes are very strong in plane. The π bonding produces de-localized electrons which makes graphite a good electrical and thermal conductor in plane [7]. These layers of graphite planes are then held together by the Van Der Waals force. This is considerably weaker than the in plane σ bonding. The graphite layers fit together to form a turbostratic arrangement. Given that there are no de-localized electrons due to the Van Der Waals force, graphite is said to have poor electrical and thermal properties perpendicular to the plane. Due to the different bondings within each layer, graphite is highly anisotropic [7].

A diagram of the internal graphite structure for a PAN fibre is shown in Figure 2.3. It is evident that the long range internal structure of the graphite layers within the PAN carbon fibres portray a very wavy pattern. Further it is evident from Figure 2.3 that there are two distinct regions of graphite structure within PAN fibres: a) thin skin region and b) the main core region [7, 17]. The skin region consists of a few layers where the graphite planes are aligned roughly parallel to the fibre surface. Below the skin region, in the main core, the graphite planes appear to be more randomly distributed. It has

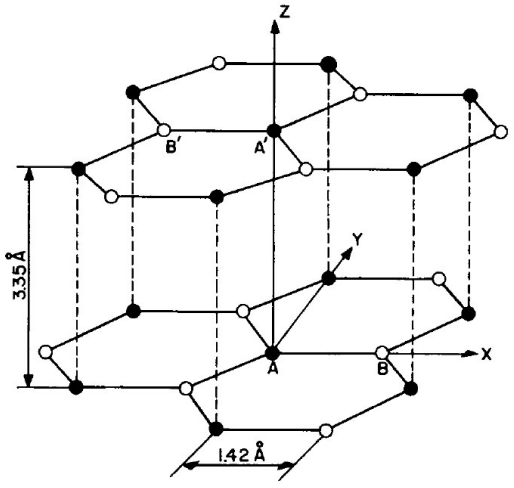

FIGURE 2.2: Diagram of the atomic structure of the graphite [7]

been noted that the size of the skin region is dependent on the manufacturing process [7, 17].

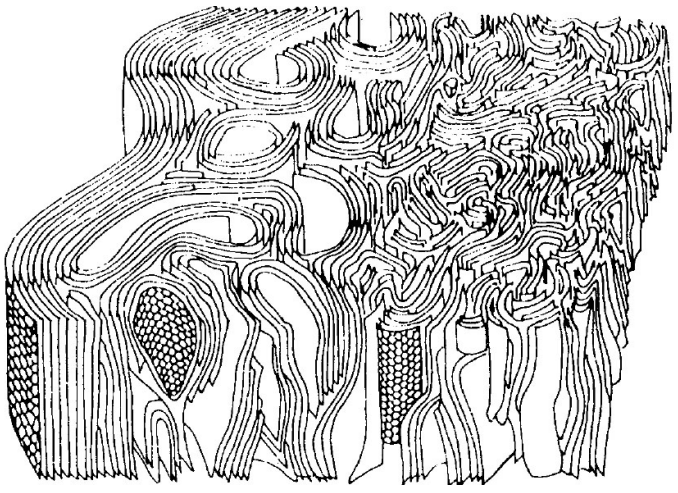

FIGURE 2.3: Diagram of the long range structure of carbon fibre [7]

It is evident that due to the long range internal structure of a PAN fibre, the high degree of anisotropy of graphite is reduced to an almost isotropic material.

2.1.2 Matrix

Typically, polymers are used as a matrix material. However, in some cases, ceramic, metals [22] and concrete [23] are used. Polymer matrices are commonly used primarily due to the easier fabrication processes. The most prevalent reason for this is that polymer matrices are processed at comparatively low temperatures, 100 - 200 $^{\circ}C$, whereas metal or ceramics require much higher temperatures [7].

Depending on the material properties ultimately required, there is a vast range of dif-

ferent types of polymers which can be used [5, 17]. The main types of polymers considered are divided into two sub categories; thermosets (e.g. epoxy or phenolic based polymers) or thermoplastics (e.g. polyimide and polyethermide). The fundamental difference between these two types is that when thermosets are subjected to a sufficiently high temperature and pressure (i.e. in the curing process), they undergo an irreversible reaction which means they can only be moulded once. Thermoplastics, however, can be remoulded repeatedly when reheated. Other differences between these two types of polymers, which are also considered, are their rate of water absorption, the strength and the stiffness [7, 5]. In the aerospace industry, thermosetting epoxies are the main type of polymer used [24, 5]. Epoxies generally are considered to be poor thermal and electrical conductors.

2.1.3 CFC Properties

CFCs are highly anisotropic, this is due to the long stands of highly conductive carbon fibres in a poorly conductive polymer matrix. Due to this anisotropy, it is important to define a local axis within each ply. A local axis is defined for each ply so that:

- Direction 1: parallel to the fibre direction.
- Direction 2: in-plane perpendicular to the fibre direction.
- Direction 3: through plane and perpendicular to the fibre direction.

This local axis group is shown in Figure 2.4. This local axis is important when considering a quasi-isotropic CFC material, where the fibre orientation is different in each ply.

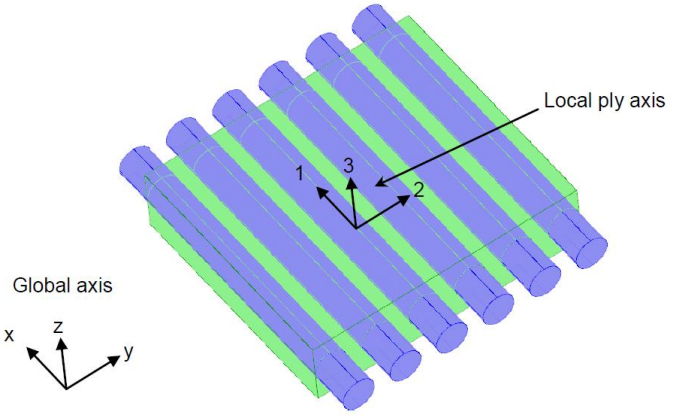

FIGURE 2.4: Local axis for a single ply of CFC. Direction 1 is parallel to the fibre direction, direction 2 is perpendicular to the fibre direction in plane and direction 3 is perpendicular to the fibre direction through the plane

It is evident from the discussion above, that the bulk thermal and electrical conductivity of a piece of CFC in direction 1 (i.e. along fibre), is far greater than in the directions

2 and 3 (i.e. perpendicular to the fibres). This is because in directions 2 and 3 the poorly conductive polymer has a substantial impact on the bulk conductivity, whereas in direction 1, the conductive fibres dominate. The electrical and thermal properties for a piece of CFC are now considered in detail.

2.1.3.1 Thermal Properties

It has been reported by E. Savage [21] that the thermal conduction is dominated by the lattice vibrations within the CFC. It has also been experimentally shown by C. Pradere et al. [25] that the thermal conductivity of PAN carbon fibres increases with increased temperature. Similar behaviour has also been reported for the bulk CFC properties in the experimental work presented by F. Uhlig [12]. The thermal conductivity presented by F. Uhlig is shown in Figure 2.5.

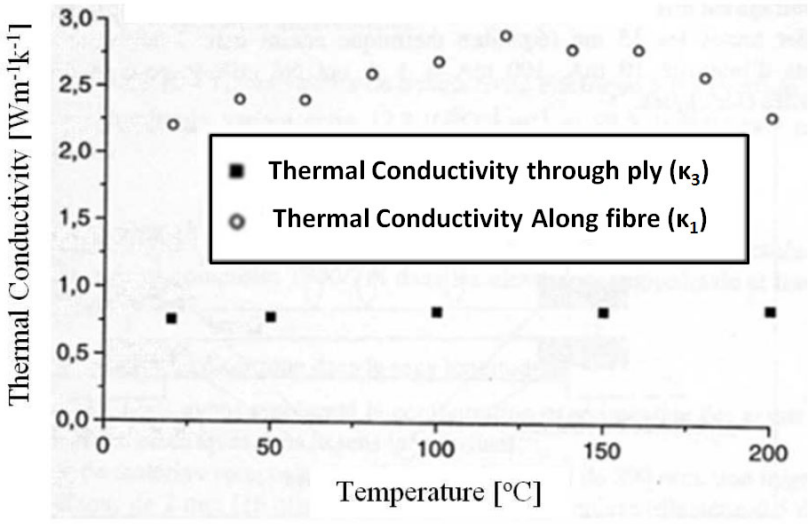

FIGURE 2.5: Experimentally measured thermal conductivity for a piece of CFC [12].

Figure 2.5 shows that the thermal conductivity along the fibre (direction 1) is greater than through the ply (direction 3). This is as expected based on the theory presented above. The results also show that there is a slight increase in conductivity as the fibre temperature increases. Above 120 $^{\circ}C$, there a slight decrease of the conductivity in direction 1.

2.1.3.2 Electrical Properties of CFC

The electrical properties for a piece of CFC are not as straightforward as the thermal properties. This is because, the carbon fibres and epoxy have very different electrical properties. By initially considering the electrical DC case, it is believed the conduction is dominated by the carbon fibres and their fibre to fibre contacts [26]. It has been

reported that the electrical conductivity [7, 27] of carbon fibres increases with an increased temperature. This is shown experimentally by the results presented by F. Uhlig [12] in Figures 2.6 and 2.7. This increase occurs despite the metallic like free de-localised electrons being present, as when the temperature increases, there is an increase in the charge carrier density, as more electrons are excited into the conduction band [7]. This indicates that carbon fibres exhibit signs of a semiconducting nature.

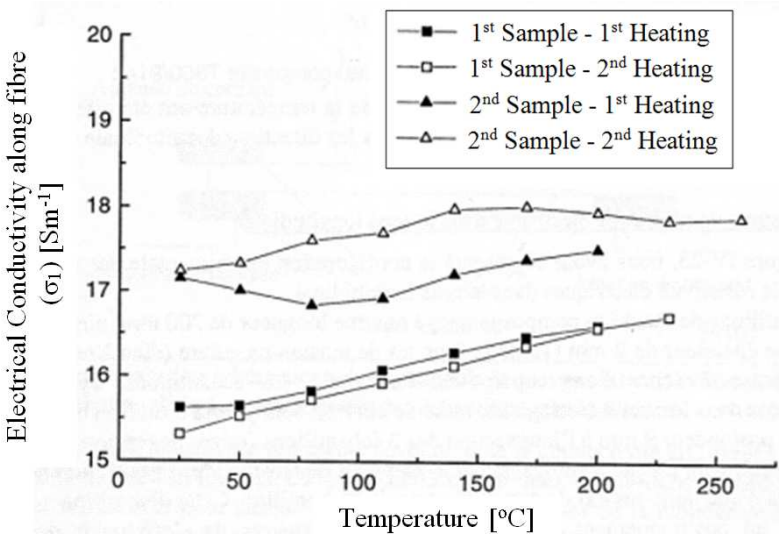

FIGURE 2.6: Electrical conductivity for CFC along the fibre direction [12]

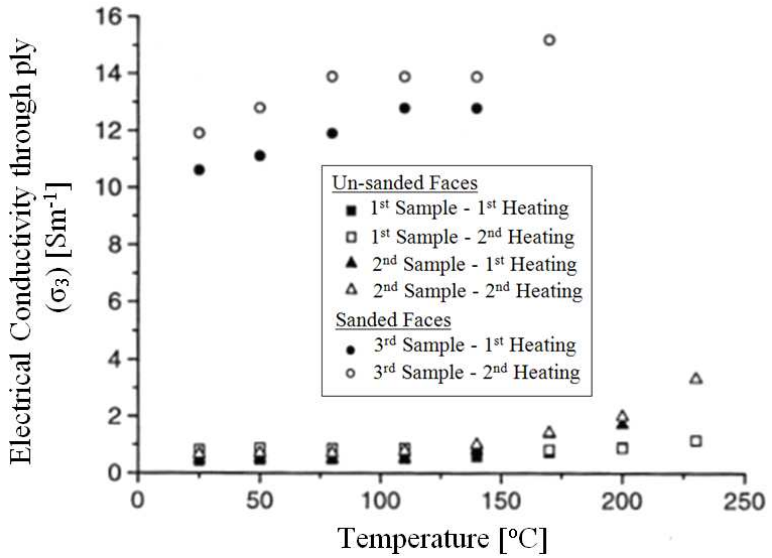

FIGURE 2.7: Electrical conductivity perpendicular to the fibre direction [12]

The experimental results shown in Figure 2.7 include the electrical conductivity when the CFC samples have been sanded and un-sanded. The sanded samples have had the top and bottom surfaces sanded down to remove the thin polymer film present on these faces. These results show that the thin polymer film greatly reduces the measured bulk conductivity. Given this thin polymer film is only on the top and bottom surfaces, it is

therefore not part of the general internal bulk conductivity of the material and should be removed before considering the true bulk properties. From the above figures, it is further obvious that the conductivity in direction 1 (Figure 2.6) is far greater than direction 2 (Figure 2.7). It is also evident that for a given temperature change, the increase in electrical conductivity is greater than the increase in thermal conductivity. However, for the temperature range presented in Figure 2.6 and Figure 2.7, the variation in electrical conductivity is not very significant.

Whilst the fibres act as standard conductors, there are regions of polymer between these fibres, which can act as a dielectric. Due to these dielectric regions, and given that a lightning strike is an impulse (discussed in the next section), the real and imaginary parts of the CFCs impedance needs to be considered. Previous studies have investigated the electrical behaviour of CFCs under alternating current (AC) conditions. However, the majority of these studies concentrated on short fibre composites [28, 29], with only one study considering long fibre composites [30]. The study by L. Scruggs and W. Gajda and Kim [30] considered the electrical properties for unidirectional samples of CFC (akin to a single ply of CFC). Their investigation demonstrated that at frequencies below 1 Mhz, the impedance is independent of frequency, and there is no phase angle [30]. This implies that a unidirectional ply of CFC can be treated as a pure resistor. This study only considered unidirectional plies and did not consider quassi-isotropic CFCs with fibres arranged in a variety of directions. The study by Z. Rimska et al. [28] investigated the impedance of short fibre CFC. Their results showed if the material had fibre volume fraction of above 2.5%, there were minimal capacitive effects below 500 kHz. During this study, they discussed a possible simple equivalent circuit which could be used to describe these electrical properties. The same equivalent circuit has also been applied to a composite comprising of rubber and conductive filler [31]. The equivalent circuit is shown in Figure 2.8 and is comprised of three parts:

- The resistance of the carbon fibre (R_f).
- The resistance of the contact region between fibres (R_C). This is the inter-facial boundary resistance between the fibre and polymer.
- The polymer gap between the fibres can also act as a capacitor; this is termed the contact capacitor (C_c).

From this equivalent circuit, it is evident that at low frequencies the current flows mainly through the contact resistor (R_c) since at low frequencies the reactance of the contact capacitor (C_c) is very high. This leads to the total resistance being equal to the series combination of the fibre resistance (R_f) and the contact resistance (R_c). At high frequencies, the impedance of the contact capacitor is now much lower than the contact resistor and so the contact capacitor effectively short circuits the resistor. This leads to the net resistance of the CFC at high frequencies being dominated by the fibre resistance.

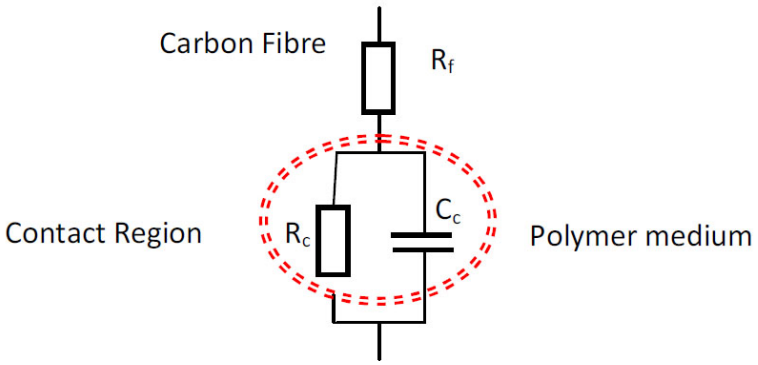

FIGURE 2.8: Suggested equivalent electrical circuit for within a short fibre CFC

In the following chapters, the equivalent circuit will be investigated to see whether the same equivalent circuit can be applied to a multi-layer non-unidirectional composite. The next section of this discussion considers what comprises a lightning strike.

2.2 An Introduction to Lightning Strikes

A lightning strike is an electrical discharge in air that originates from charged regions within cumulonimbus clouds [32]. For the charged regions to form, a cloud must contain water in three phases: solid (ice), liquid, and gas (vapour). It is known that the interaction between these multiphase particles leads to the formation of the charged regions. The precise physics behind what causes the charged regions to form is unclear and currently under discussion. A range of current theories are discussed in [33]. Some of the possible theories for the creation of charged regions are due to the freezing and melting of raindrops and/or the movements and collisions of particles. For this study, the mechanism(s)are not important, what is important is that they do occur.

Independent of which process/processes causes the charging of the cumulonimbus cloud, a tripolar electrostatic structure is created within, as shown in Figure 2.9 [33] [32]. There is a main dipole created between the top and the middle of the cloud, with the top being positively charged (**P**) and the middle being negatively charged (**N**). Below this, there is another, 'inverted' dipole, due to a small positively charged region (p') at the base of the cloud. The charge magnitude of the bottom positive region is smaller than both the magnitude of the main positive and negative regions.

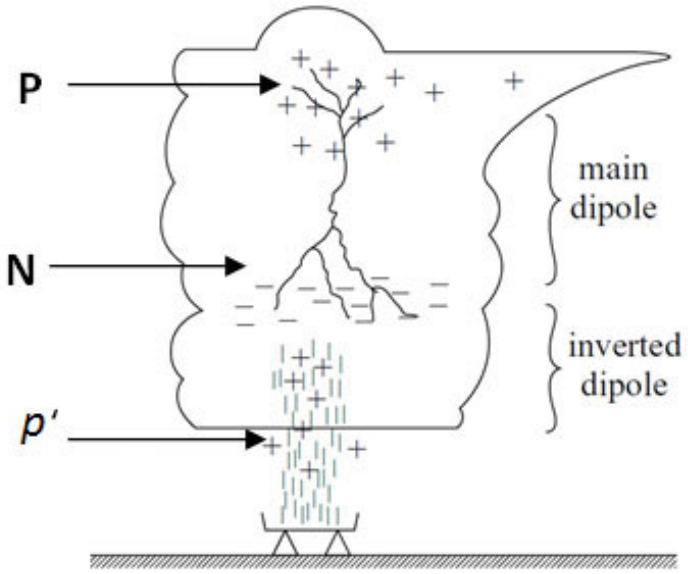

FIGURE 2.9: Tripolar structure of a typical cumulonimbus cloud which leads to a lightning strike. [33]

It is from these charged regions that a lighting strike occurs.

2.2.1 Lightning Strike Fundamentals

There are a variety of different discharge mechanisms available to the charge cloud:

- Intra Cloud Strikes: discharges between the N and P regions within a cloud.
- Inter Cloud Strikes: discharges between neighbouring charged clouds.
- Cloud to Ground Strikes: discharges between a cloud and the ground.
- Air Discharge: discharge between **N** and p', where there is no contact with the ground.

Of these, the two most common types are intra cloud strikes and cloud to ground strikes [8, 33]. A diagram summarising these two discharge mechanisms is shown in Figure 2.10.

2.2.1.1 Intra Cloud Strikes

Intra cloud strikes occur between the main dipole regions of the cloud. Over 50% of all discharge flashes are intra cloud discharges [11, 32]. This type of event is instrumental in redistributing the charge within a cloud. A typical intra cloud return stroke has a peak current between $20 - 30kA$ [11]. This is considerably less than the peak current

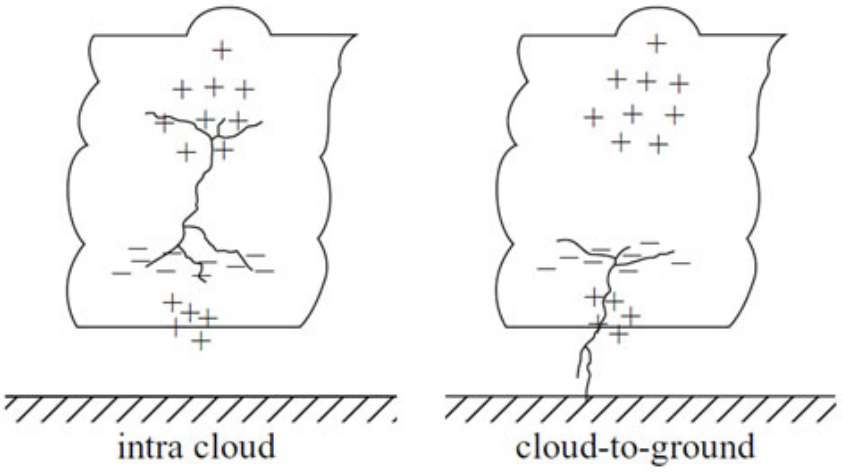

FIGURE 2.10: Illustration of the typical intra cloud discharge process (left) and the typical cloud to ground discharge processes (right) [33]

associated with a cloud to ground strike (discussed below), and as a result, this type of strike contains much less energy and so is far less damaging.

2.2.1.2 Cloud to Ground Strikes

Cloud to ground strikes are what is commonly referred to as a lightning strike. This type of lightning strike is initiated by an electrical breakdown between the **N** and p' regions in the cloud. Due to the larger magnitude of negative charges in the **N** region over the magnitude of positive charges in the p' region, a strong concentration of negative charge remains in the cloud base. This produces a strong electric field from which a negative charged column is propelled down towards the earth. This column, is called a step leader and it travels towards the earth in what appears as small 'zig-zag' like segments. Each segment is typical $50\,m$ long and has an average velocity of $1.5 \times 10^5\,ms^{-1}$ [32]. As the step leader approaches the ground, the electric field at ground level begins to increase. When the step leader is close enough to the ground such that the electric field becomes large enough, a series of upward moving streamers begin to form from the ground [33]. The ground level electric field is caused by the repulsion of the negative charges away from the region below the stepped leader. If one of these upward streamers connects with the downward step leader, a complete circuit is made. This creates a conductive path, which allows the remaining charge stored in the **N** region to discharge to ground [9]. This is called a return stroke. After the return stroke, there is a comparatively slow decay in current, this is called the intermediate current. It has been observed that following an initial return stroke and an intermediate current, there can be several further subsequent returns strokes [11, 8]. This somewhat disproves the old adage that, lightning never strikes twice.

Some lightning strikes also exhibit a continuous current component, typically occurring

towards the end of the lightning strike after several return strokes. They comprise of a low level current of between $200 - 800\ A$ persisting for several milliseconds [11]. A typical current profile for a cloud to ground strike is shown in Figure 2.11.

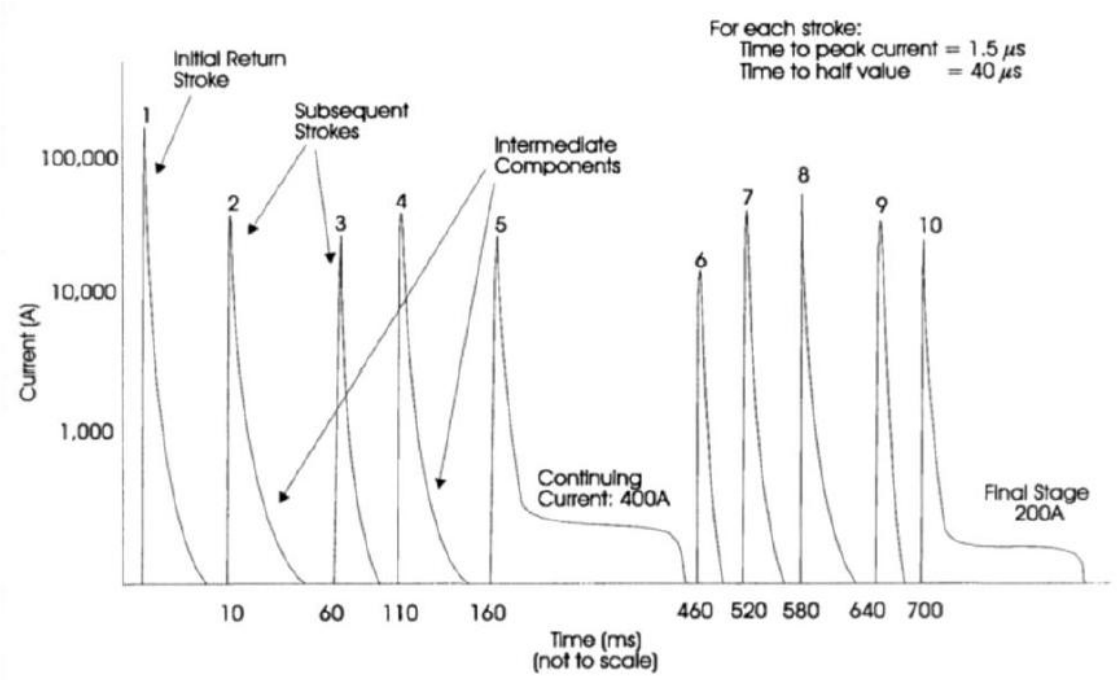

FIGURE 2.11: Typical negative cloud to ground lightning strike current impulse [11]

2.2.2 Positive Lightning Strikes

The discussion above has focused on negative polarity lightning strikes. There is, however, the possibility to form positive polarity lightning strikes. These differ from the strikes above, as whilst the negative cloud to ground flash lowers a negative charge to ground the positive strikes lower a positive charge to ground. These strikes are formed by an upward moving leader emanating from mountains or tall buildings and not from flat terrain [11]. These strikes normally only contain one return stroke followed by a continuous current [32] with no re-strikes. The peak current for positive strikes is normally higher than for a negative strike, with a peak current of $200 - 300\,kA$ [32]. This type of strike is far less common than the above strikes. As they are less common, this study will only consider the negative cloud to ground strikes.

2.2.3 Lightning Strike Standards

A lightning strike is a chaotic event, with no two strikes ever being the same. Therefore, an industrial standard has been developed which can be used by laboratories to generate replica lightning strike events. To certify that all aircraft are capable of withstanding

the most damaging lightning strikes, the standards are designed to replicate a severe cloud to ground strike as shown in Figure 2.11. For this study, the standards used to represent a lightning strike are taken from Eurocae ED-84 [11]. There is a further series of documents, Eurocae ED-91 and Eurocae ED-105, which define the experimental certification tests, which specific parts of the aircraft must withstand [34, 35]. As this study considers the lightning strike defined by ED-84 [11], it is therefore important to understand Eurocae ED-84. Eurcoae ED-84 covers several aspects of the standardised lightning strikes, including the current and voltage profiles. As will become apparent later in this chapter, only the current profile is required for this study.

2.2.3.1 Current Profile

The lightning strike current profile given by ED-84 is shown in Figure 2.12. The current profile is composed of a series of components which correspond to the different parts of a lightning strike as discussed in Section 2.2.1.2. Current component A represents the initial return stroke, Current component B represents the intermediate current flowing following an initial return stroke. Current component C represents the continuous current section. Current component D represents any subsequent re-strokes.

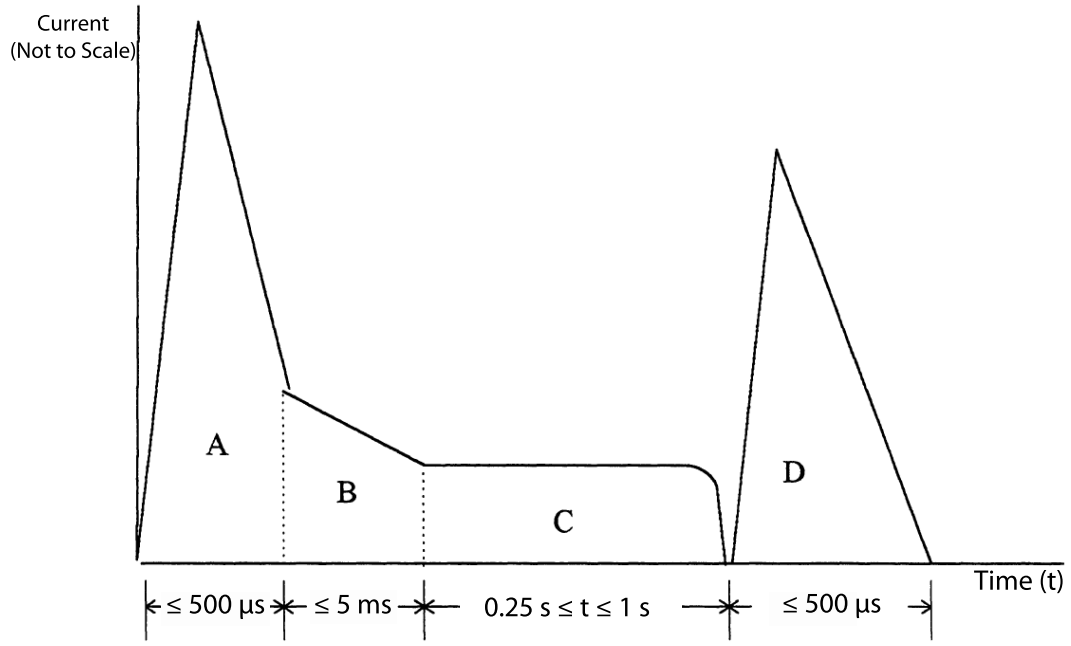

FIGURE 2.12: Lightning strike current profile as stated in [11]

Profiles A,B and D are defined mathematically by a double exponential expression [11]

$$I(t) = I_0(e^{-\alpha t} - e^{-\beta t}) \tag{2.1}$$

Where I(t) is the current at time (t) and I_0, α, β are constants defined in Table 2.1

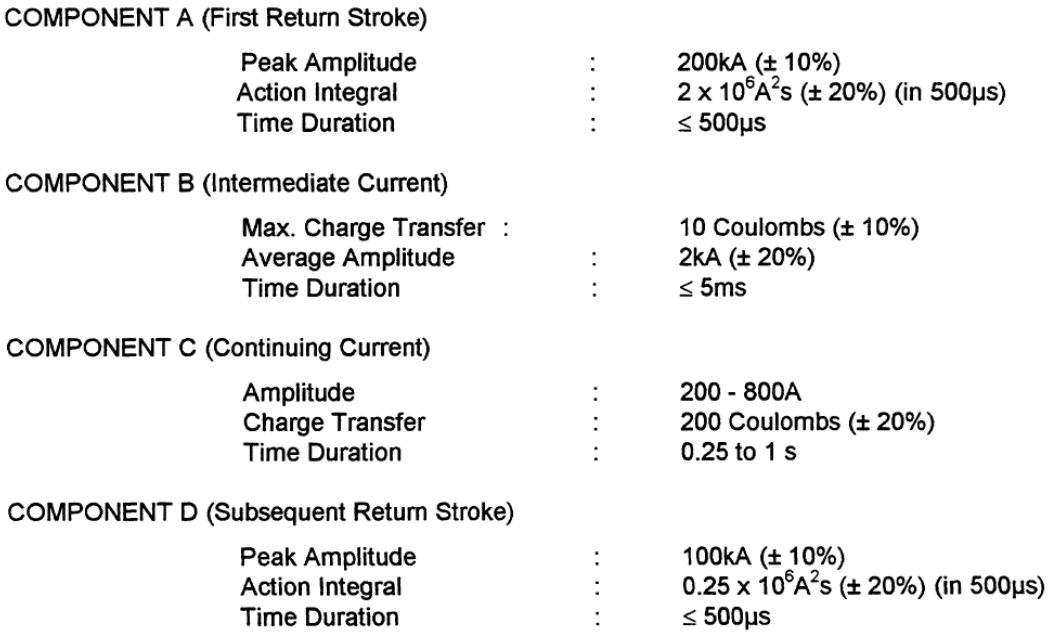

FIGURE 2.13: Lightning strike current profile parameters as stated in [11]

	I_0	$\alpha(s^{-1})$	$\beta(s^{-1})$
Current Profile A	218 810	11354	647265
Current Profile B	11300	700	2000
Current Profile D	109 405	22708	1294530

TABLE 2.1: Parameters required to mathematically model the different sections of current profiles shown in eqn. 2.1 [11]

Current profile C is defined mathematically by a square wave with the total charge transfer of $200\,C$ in a duration of between 0.25 and 1 s [11].

2.2.3.2 Frequency Components

As lightning strike current components are impulse events, they can be Fourier decomposed into a series of frequencies components. The decomposed current impulses for component A and D are shown in Figure 2.14 and Figure 2.15, respectively [11].

From figures 2.14 and 2.15 it can be seen that the frequency amplitudes for component A and D are roughly constant up to $1.8\,kHz$ for component A and $3.6\,kHz$ for component D. These frequencies are refereed to as the 'Initial Break Point'. Above this initial break point, the frequency amplitude begins to decrease. When the frequency amplitude reaches 1% of its initial amplitude, the frequency is called the 'final break point'. These figures show the dominant frequencies within a lightning strike are below approximately $200\,kHz$.

The frequency components from current component B are not presented here because α and β for component B (shown in Table 2.1) are much smaller than for component A

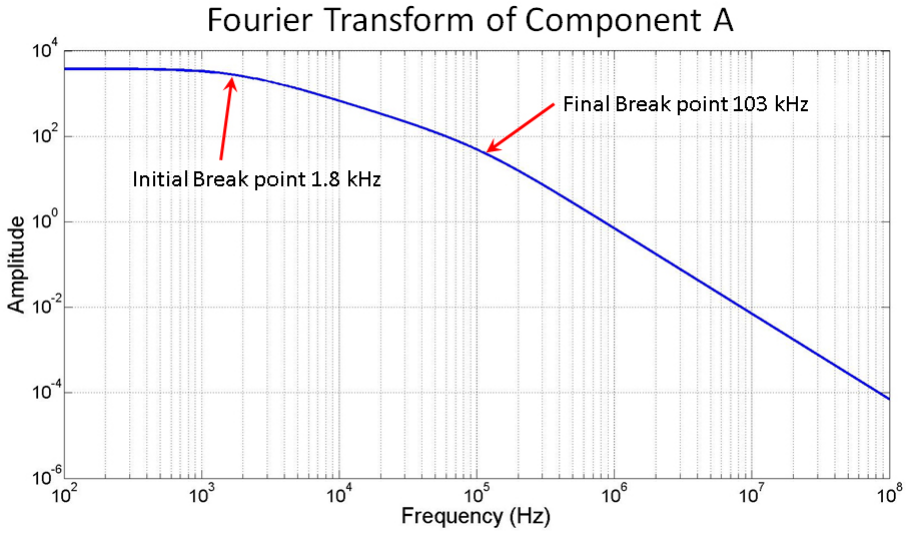

FIGURE 2.14: Frequency components for component A. Graph obtained using a fast Fourier transform of component A, which had a duration of 1 ms

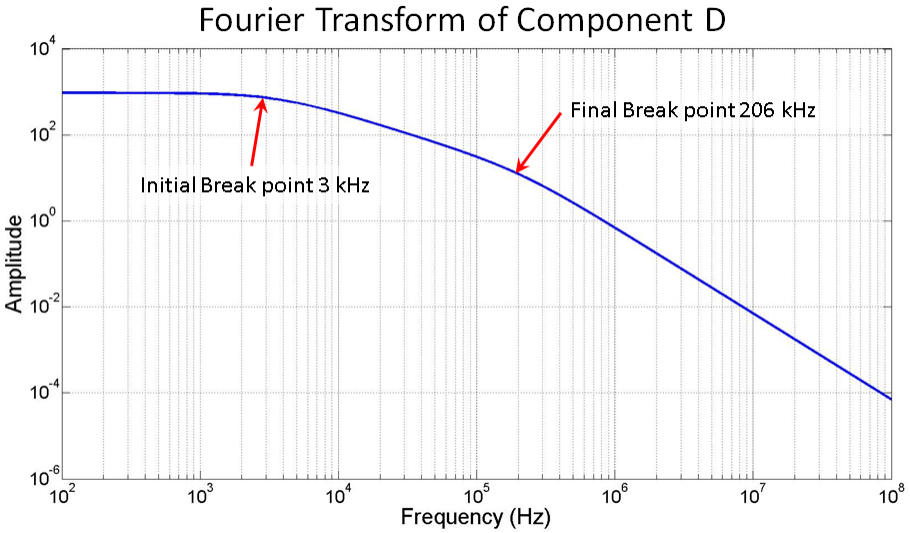

FIGURE 2.15: Frequency components for component D. Graph obtained using a fast Fourier transform of component D, which had a duration of 1 ms

and D. Therefore, component B has a considerably larger rise and fall time, and hence it has lower frequencies components.

2.2.4 Mechanisms for Energy Input

Next, a review of the different physical mechanisms by which energy is deposited into a material due to a lightning strike is considered. A lightning strike has two main energy inputs into any material, these are:

- Joule (Resistive) heating inside the material from the injected current.

- Heat flux onto the material's surface from the plasma channel.

2.2.4.1 Joule Heating

The injected current causes the material to heat up, due to Joule (resistive) heating. The volumetric Joule heat is given by

$$Q_J = \int (J \cdot E) dV \tag{2.2}$$

Where Q_J is the thermal input power due to the volumetric Joule heat for a given volume (dV) given the local current density (J) and the electric field (E).

An indication of the amount of energy which is deposited into the system due to the injected current can be obtained from the action integral stated in Figure 2.13. The action integral refers to the integral of the current squared during the duration of the current impulse. To calculate the total energy deposited into the system, the action integral needs to be multiplied by the resistance. Therefore, considering only the energy input from the current injection, it is possible to conclude that Component A, would deposit the most volumetric Joule heat energy into a material.

2.2.4.2 Plasma Heat Flux

The energy input from the plasma channel due to a negative polarity continuous current component i.e. component C, to a piece of metal (surface) has been extensively investigated in previous studies [36, 37, 38, 39]. Whilst the approach discussed in these studies was originally designed for metallic materials, it has since been shown to be equally applicable to CFCs [27]. The heat flux from the plasma arc is derived by considering the current and energy conservations. These studies assume that the region between the arc and the anode (material surface) can be considered to be ohmic. From this, the standard boundary equation used to incorporate the heat flux from the plasma channel is given by [27]

$$\left[-\kappa \left(\frac{\partial T}{\partial x}\right)\right]_{cfc} = \left[-\kappa \left(\frac{\partial T}{\partial x}\right)\right]_{plasma} + J\left(\frac{5k_B}{2e}(T_{cfc} - T_{plasma}) + V_a + \psi_s\right) - L_{cfc}\Psi_v \tag{2.3}$$

Where J, V_a and ψ_s are the current density, anode fall voltage and the material work function, respectively. The left hand side (LHS) and the first term on the right hand side (RHS) refer to the thermal conduction between the plasma and the material surface. The second half of the right hand side refers to the current conservation, and can be split into three components. The first term considers the electrons enthalpic flux due to their kinetic energy. The second part of the term refers to potential energy gained

by the electrons whilst crossing the anodic sheath. This is the thin region between the main plasma channel and the material surface (anode). For a lightning strike, the anode fall voltage is assumed to be constant at $3.5\,V$ [27]. The third part is the work function, which is related to the energy restored by the electron during its integration in the material. The work function defines the amount of energy that is required to remove an electron from an atom. Hence, this energy needs to be restored to the material when an electron is re-integrated into an atom. Therefore, it is evident that the work function is a property of the anode material, and for graphite, this value is typically taken to be $\sim 8\,V$ [40] whereas, for metals (aluminium), it is $4.7\,eV$. The final term on the RHS considers the latent heat of evaporation of the material (L_{cfc}) due to the phase changes and associated changes in enthalpy. The amount of phased changed material is defined by the vaporisation flux (Ψ_V). The importance of each of these terms is considered for metals and CFCs in the following section. However, as stated above, this method only considers the heat flux from the continuous current component of a lightning strike. There is no published record of this method or any other method being applied to determine the heat flux from component A or D.

2.2.4.3 Principle Input - CFC vs Metals

It has already been highlighted in Chapter 1, that different materials are damaged in different ways due to a lightning strike. This is due to the different material properties causing different heating mechanisms to dominate. It is, therefore, worth discussing the relative importance of the different energy inputs for metals and CFCs.

Previous studies have shown that for a metallic structure, the principal energy input from a lightning strike comes from the heat flux from the plasma channel [37]. This has been shown by comparing the experimentally obtained temperature profiles for the rear face of a sample of steel which has been subject to lightning strike component C with a set of numerical model predictions. Good agreement was achieved between the numerical model and the experimental results. The numerical model only included the heat flux from the plasma arc, as given by Equation (2.3) and did not include any volumetric Joule heat terms. The absence of the volumetric Joule heat indicates that the heat flux from the plasma flux dominates the heating for a metallic panel. The volumetric Joule heat has minimal affect because as the lightning strike current flows between its entry point and exit point on the aircraft's surface, the current is spread out due to the metal's high conductivity. This minimises the current density, and as a result, there is negligible Joule heating [9]. This is despite the skin effects which are known to occur within metals.

This minimal Joule heating in metals can further be seen by estimating the temperature increase (ΔT), due to the Joule heat which results from the interaction of lightning strike component A, with a $5\,mm$ cubed piece of aluminium. The temperature increase

due to a energy input, Q_{tot}, is expressed as

$$Q_{tot} = \rho_{Al}\, V_{Al}\, C_{Al}\, \Delta T \tag{2.4}$$

Where ρ_{Al} and C_{Al} are the density and specific heat capacity of the aluminium sample, which has a volume, V_{Al}. The total Joule energy input from component A, is given by the action integral multiplied by the resistance of the aluminium sample, which is expressed as

$$Q_{tot} = \int I^2(t) R\, dt \tag{2.5}$$

Where $I(t)$ is the current impulse and R is the resistance of the aluminum sample. By equating Equation (2.5), to Equation (2.4) and rearranging for the temperate increase, the following equation is obtained

$$\Delta T = \frac{\int I^2 R\, dt}{\rho_{Al}\, V_{Al}\, C_{Al}} \tag{2.6}$$

By substituting the material properties given in Appendix C and the action integral quoted in Figure 2.12, the calculated temperature increase for this piece of aluminium is 37 K. This temperature increase, is not significant enough to cause any damage to this piece of aluminium

However, the conclusions above are not valid for CFCs, as they are not as electrically conductive, and so the current density cannot be minimised quite so easily. The most notable attempt to determine the principle energy input for CFC comes from F. Lago et al. [27, 41, 42]. They published a series of papers in which, they numerically modelled a lightning strike, including the plasma channel and its energy inputs. As part of their study, they conducted a parametric study to investigate which physical process deposited the largest amount of energy into a piece of CFC. Firstly, they considered the energy input from the plasma arc as given by Equation (2.3). In [27], they showed that the fall voltage, work function and the thermal conduction from the plasma arc all significantly contributed to the thermal input into the CFC, whilst the enthalpic term and the latent heat had minimal effect on the heating. This study also considered the Joule heating. The model assumed that a CFC can be treated as a pure resistor i.e. no capacitive or inductive affects, and so all the current results in Joule heat. This study then concluded that whilst the plasma heat flux does contribute to the overall temperature increase, for CFCs, the Joule heat is by far the most dominant heating mechanism. This is due to the lower electrical conductivity within a CFC, when compared to metals [27].

The above discussion shows that any numerical model which investigates the thermal degradation of CFCs must consider the electrical current flow inside the CFC.

2.2.5 Lightning Strike Interaction with CFC

The standards mentioned previously (ED-84, ED-91, ED-105) were initially designed for metal structures. It is, therefore, important to consider if there are any distinctions between the lightning strike attachment to a piece of CFC compared to a piece of metal. An experimental study by Mc Brayer et al. [43] concluded that there were minimal differences in the attachment processes between metals and CFCs. This result was explained by considering that the conductivities of CFCs and metals not being sufficiently different to affect the streamer development significantly.

2.2.6 Lightning Strike Discussion

It has been documented that there are two energy inputs from a lightning strike. The dominate heating for CFC is considered to result from the Joule heating. However, by considering these studies, the following two pertinent questions have been raised. Firstly, can the same plasma heat flux equation as given in Equation (2.3) be used to model the heat flux from component A and D? Secondly, the above studies have all assumed that there were no capacitive or inductive effects present within the CFC. It is, therefore, imperative to investigate the properties of the CFC to confirm this assumption, since if there are capacitive or inductive effects the amount of Joule heat will be different.

2.3 Typical damage to CFC

From the literature, it appears that there are two main ways in which a panel of CFC can be damaged by a lightning strike. Firstly, via direct mechanical failure due to the rapid expansion of gas which surrounds the plasma channel [9, 44]. The rapid expansion of gas which surrounds the plasma arc leads to the thunder that is heard as part of thunder and lightning. The second damage mechanism is the thermo-chemical degradation (phase change and polymer pyrolysis) due to the heating [45, 46].

A series of experimental studies has previously been conducted to determine the damage caused to panels of CFCs due to lightning strikes [13, 47, 45, 46]. The earliest published record, which discusses the lightning strike damage to a piece of CFC is given by G. Reid [45, 46]. In these papers, G. Reid [45, 46] damaged CFC panels with both lightning strike component A and component C separately. The investigation considered how scaling the action integral for component A or increasing the total charge transfer for component C, affected the observed damage. Reid described the resultant damage due to both current components as, 'Splitting and fracturing of the fibres with burning of the resin'. The results presented showed a linear increase in damage depth and damage area as either the action integral or the total charge transfer was varied. The experimental

results further showed that component C caused a larger damage area than component A, although the rate at which the damage depth increases as function of increased action integral is greater than for an increase in total charge transfer for component C. Similar studies have been conducted by P. Feraboli and M. Miller [13], and an image taken from their study (Figure 2.16) shows the typical damage caused to a piece of CFC due to a lightning strike. This piece of CFC was damaged with a single current component D strike with a peak current of 50 kA. Notwithstanding the fact that the study by P. Feraboli and M. Miller was conducted with component D whereas G. Reid was conducted with component A and C. The type of damage observed by both of these studies shows very similar results. Feraboli et al. also noticed that inside the CFC there were signs of delamination between the plies [13]. They also noted there were no signs of mechanical damage due to the shock wave. Importantly, comparing this damage with what was seen in metals (Figure 1.4), it is evident that the types of damage caused differ markedly.

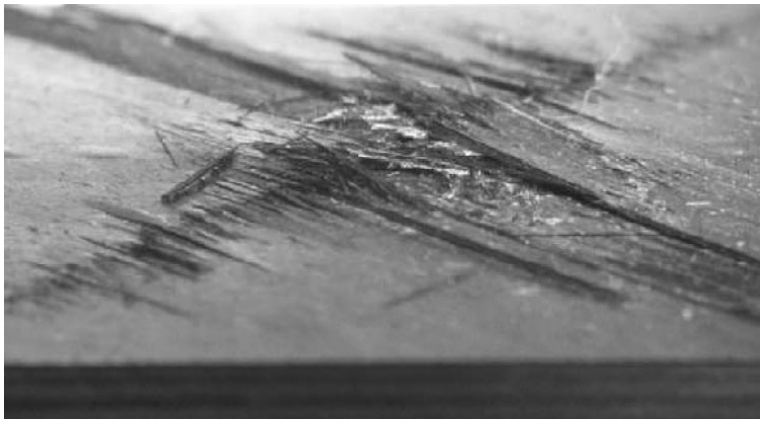

FIGURE 2.16: Typical damage which results from a lightning strike to CFC [13]. The CFC damage has been caused by current impulse with a peak current of 50kA, for a duration of 160ms

Another possible damage mechanism, which has been highlighted for metals, is that of the Lorentz force, created by the strong magnetic field, which surrounds the arc attachment point [9]. This force is akin to the attraction seen between two parallel wires carrying current in the same direction and can cause buckling and deformation of an aircraft's surfaces. Despite this damage mechanisms being reported for metals, having conducted a literature review, there is no mention of this mechanisms damaging CFCs. This can be explained by recognising that CFCs are very stiff and so not easily deformed.

From these discussions, the previous studies indicate, that the majority of the damage is caused by thermo-chemical degradation rather than any mechanical processes.

2.4 Thermo-Chemical Degradation Models

Whilst the discussions presented by both G. Reid et al. [45] and P. Feraboli et al. [13] indicated that the lightning strike damage is prominently a thermo-chemical degradation of the polymer rather than any physical mechanical damage to the panel, the explanations for the damage given by G. Reid and P. Feraboli do not fully explain the physical processes which have occurred to cause the visible damage. In an attempt to gain a better understanding and to investigate the physical processes which cause this damage, this study aims to develop a numerical thermo-chemical degradation model. To this end, the remainder of this chapter considers previous attempts to model numerically the thermo-chemical damage to composite materials. This is done by first presenting an overview of previous numerical models before considering their implementation in more detail.

2.4.1 Existing Lightning Strike Thermo-Chemical Degradation Models

There are three previously published reports of numerical models which have been developed to predict the damage caused by a lightning strike [27, 48, 49]. These models are presented by Hardwick et al. [48], F. Lago et al. [27] and T. Ogasawara et al. [49]. These studies have considered the thermal conduction and chemical degradation within the material due to an energy input. There has been no attempt within these studies to consider any mechanical effects due to a lightning strike. In the work presented by Hardwick et al. [48] and by T. Ogasawara et al. [49], they considered only the energy input from the Joule heat due to the current injection. Whereas the model presented by F. Largo [27] considered the energy input due to both the plasma heat flux and the current injection. By comparing the results from these models, it is evident that whilst the Joule heat does dominate the damage caused, the heat flux from the arc should not be ignored, especially for the continuous components. Both Hardwick [48] and Lago [27] considered the thermo-chemical degradation by defining a critical temperature and stating that if the temperature of the material at any point exceeded this critical temperature, then the material would be degraded at that location. This approach is not a true physical representation of the how a CFC is believed to thermally decompose [50, 51]. Furthermore, this implementation does not consider the change in enthalpy of the system due to the degradation. Both these models assume that the CFC can be modelled using 2D axial symmetry. The limitation with this approach is that it does not accurately represent the conductivity which is present within a CFC. The numerical predictions in [48] and [27] were compared against experimental results. They both independently concluded that the damage depth predictions, from their numerical models, were an over estimate from what had been experimentally determined, and that the damaged areas obtained from the experimental results were also vastly elongated when compared to the numerical predictions. Hardwick et al. concluded that these

differences were most likely due to the assumed symmetry, which incorrectly defines the materials' conductivity. Therefore, due to the anisotropy within a piece of CFC, the thermo-chemical degradation model needs to be considered in 3D. The numerical model developed by T. Ogasawara et al. [49] was implemented in 3D. However, this study only considered the energy input caused by the current injected (i.e. Joule heat). Unlike the models proposed by Hardwick et al. [48], F. Lago et al. [27], which considered a region of current injection, the model proposed by Ogasawara et al. [49] considered a single point current injection, which is not a true representation of a plasma arc. This model, however, did incorporate the chemical reaction via an Arrhenius equation (discussed in Section 2.6.2.3). However the author then decided to limit artificially the maximum temperature allowed in the model to 3000 K, as above this temperature, the carbon fibres are assumed to have degraded. This does not justify the implementation of the maximum temperature.

The discussion presented above, has shown that all these previous studies have limitations. Furthermore, none of these studies made any attempt to consider the internal gas pressure in order to explain the fracturing of fibres seen in Figure 2.16.

2.4.2 Other Thermo-chemical Degradation Models

Although there is a limited number of numerical models which deal with the damage caused due to a lightning strike, there is, however, a vast number of previous studies which have investigated the thermo-chemical degradation of composite materials (fibre glass and carbon-based composites) due to other heat sources. These studies have generally considered the damage caused by fire [52, 53, 54, 55] or laser drilling [56, 57, 23]. The fire based models are focused on the polymer degradation and are, hence, very useful for this investigation. Due to the faster heating rate from a laser beam, the laser drilling studies focus more attention on the fibre degradation than the polymer degradation. As the majority of the damage from a lightning strike appears to be related to polymer degradation, the fire based models are considered further in more detail. The majority of these previous studies are based around very similar sets of equations [52, 53, 54, 55]. The core of these models considers the thermal conduction through the material due to a boundary heat flux. Due to the thermal conduction, the polymer within the composite degrades via pyrolysis. As a result of the degradation, the composition of the composite material changes. These studies considered that the polymer degrades into two new material species, char and gas. A selection of these models also considered the resultant gas transport through the decomposing material [58, 59]. A diagram which illustrates these main processes is shown in Figure 2.17.

Some of these models have been further developed to include mechanical factors such as stress, strain, thermal expansion and shrinkage due to the decomposition [53, 60, 61]. However, as determined by the discussion in Section 2.3, the principle damage due to

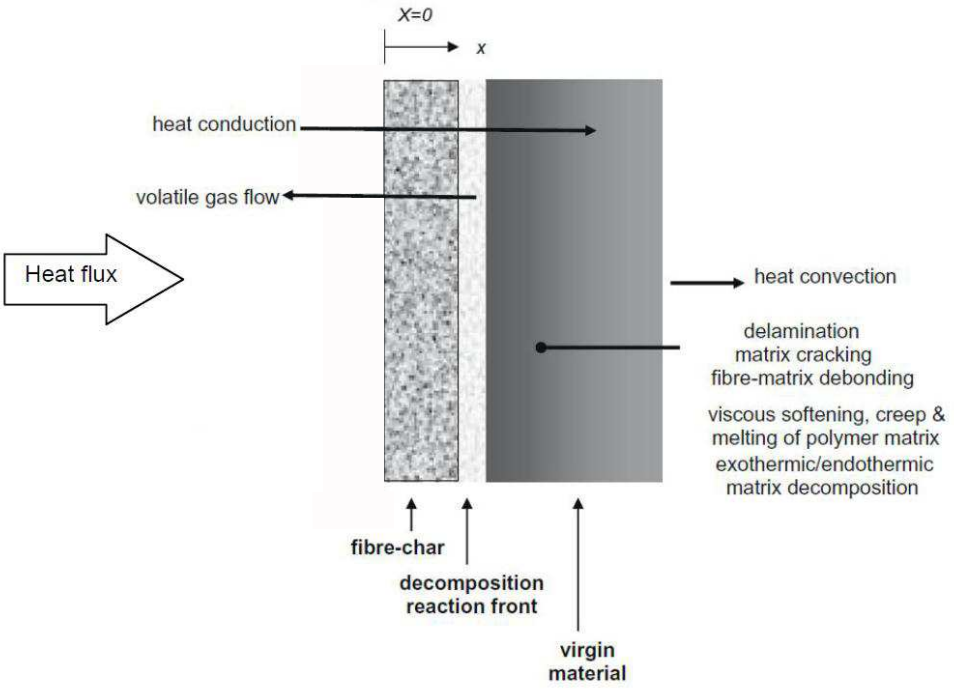

FIGURE 2.17: Schematic of the reaction processes through-thickness, given a uniform heat source at the surface ($x = 0$)[50]

a lightning strike is as a result of the thermo-chemical degradation, and hence these mechanical damage models are not considered further.

It is evident that these fire damage models consider a similar problem to that which is required by a lightning strike thermo-chemical degradation model. It is, therefore, possible to use these models as a basis for our future degradation models. As a result, the physical equations which these models consider and their implementation methods are now considered in more detail.

The remainder of this chapter now explains the numerical implementation method considered by these studies, before outlining the framework required to represent numerically a piece of CFC. The final part of this chapter then considers the equations in detail, which are used by these previous studies to model the degrading CFC.

2.4.3 Model Implementation Methods

Whilst all these methods have been based around a similar set of physical equations, they have been numerically implemented in a variety of different ways. It is important to understand the limitation of these implementation methods as the wrong choice of method can lead to a very inefficient solution time.

The study by F. Lago et al. [27], H. MacManus et al. [61] and J. Florio et al. [58] considered a finite volume approach, whereas the models by R. Sullivan et al. [62] and

N. Jennings et al. [48] considered a finite element approach. The studies by J. Staggs [63, 52] considered a moving boundary formulation. The implementation method for finite element and finite volume methods are very similar. However, the classic formulation and implementation found within many commercially available finite element analysis packages, has an inherent problem, in that it cannot accurately solve for large gradients. The finite volume approach, however, does not share this problem. Therefore, for this study, the Finite Volume approach will be considered. It is, therefore, worth devoting some time to considering how this numerical method operates.

2.4.3.1 Finite Volume Method

The finite volume technique begins by dividing up a geometry into a series of grid points, called elements (i), with discrete non-overlapping cells which have a cell volume (V_{cell}), surrounding each element. The resultant element and cell volumes are generally referred to as a mesh. An illustration for a generic 1D mesh is shown in Figure 2.18.

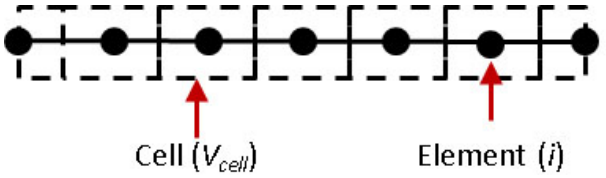

FIGURE 2.18: Idealised mesh [64]

The mesh is then used to represent the dependent variables of the governing equation at each element. The finite volume method considers the governing equations in an integral form to enforce the conservation laws. The general integral form for a finite volume equation is expressed as

$$\iint_{V_{cell}} u(x,t)\, dV_{cell}\, dt + \iint_{A_{cell}} f(u)\cdot n\, dA_{cell}\, dt - \iint_{V_{cell}} S(u,x,t)\, dV_{cell}\, dt \qquad (2.7)$$

This equation states that the rate of change of $u(x,t)$ within a cell volume (V_{cell}) plus the net flux of u through the boundaries (A_{cell}) is equal to the production rate of u given by $S(u,x,t)$. Given a constant uniform cell volume (V_{cell}) and by applying Gauss's theorem the integral form of the general conservation equation can be written in the differential form

$$\frac{\partial u}{\partial t} + \nabla \cdot f(u) - S = 0 \qquad (2.8)$$

This general form can be applied to both the thermal and mass transport. Taking the thermal transport as an example, the finite volume equation to represent the transient 1D thermal conduction problem is

$$\rho C_p \frac{\partial T}{\partial t} - \frac{\partial}{\partial x}\left(\kappa \frac{\partial T}{\partial x}\right) = 0 \qquad (2.9)$$

This equation is taken from the general form shown in Equation (2.8), where now the dependent variable is temperature (T) and the flux across the cell boundary is given by the thermal conduction due to the thermal gradient and the thermal conductivity (κ). For this example, the source term (S) is assumed to be zero. To consider how Equation (2.9) is discretized over a mesh, consider the small mesh region given in Figure 2.19.

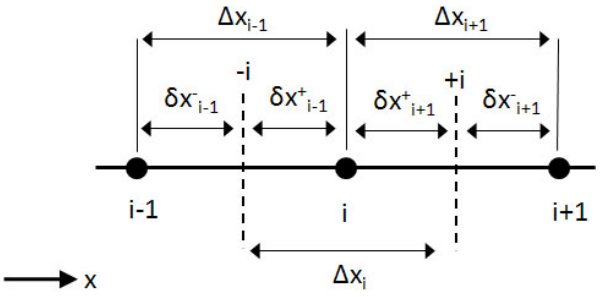

FIGURE 2.19: Example of an element with dimensions to neighbouring elements [64]

For this 1 dimensional case, there is a unit thickness in directions z and y. By integrating Equation (2.9) over a cell volume and by then taking the central difference of the differential equations, the resultant temperature at element 'i' can be defined by [64].

$$\Delta X_i \rho C_v \frac{T^0(i) - T^1(i)}{\Delta t} = \frac{\kappa \left[T^1(i+1) - T^1(i)\right]}{\Delta X_{i+1}} - \frac{\kappa \left[T^1(i) - T^1(i-1)\right]}{\Delta X_{i-1}} \tag{2.10}$$

The thermal conduction equation given in Equation (2.10) gives the temperature for element 'i' based on the temperature at elements '$i+1$' and '$i-1$'. For this example, the thermal conductivity was assumed uniform and constant. The superscript refers to the temperature at the current time step, 1 and the previous time step, 0. The time between these two time steps is given by Δt .

Equation (2.10) can then be used to define the temperature for each grid point within the modelling domain. This generates a set of link equations, which when solved leads to a temperature profile defined at each grid point. There are two main groups of solvers, direct and indirect and an in depth discussion on these is given in [64, 65].

The calculated temperature profile from Equation (2.10), is dependent on the distance between elements (ΔX) and the size of the time step (Δt) taken. As the mesh and time steps are reduced, the numerical results tend towards the correct value. When this happens, the solution is said to have converged. The convergence of the model is linearly dependent on the size of the time step and for a uniform mesh has a quadratic dependence on mesh size. However, if a non-uniform mesh is considered, the temperature convergence becomes linear with decreasing mesh size [64, 65].

Having considered the implementation of the finite volume approach, the discussion now moves on to consider how the previous models represented a composite material, before considering the modelling equations.

2.5 Framework for Modelling CFC Materials

When modelling a CFC, the obvious first choice is to model exactly what is present within the CFC, i.e. to include all the individual fibres, as shown in Figure 2.3. This method has been considered previously for mechanical studies [66, 67, 68], where it has proven to be very reliable. These types of models represent a microscopic approach to modelling. However, this approach is only feasible when considering a very small region with only a few fibres. Since, the thermo-chemical degradation damage is much larger than the size of a few fibres and so the geometry required is considerably larger. Due to the different scale of the problem, it is not possible to use the same microscopic modelling approach for the thermo-chemical degradation model. This is because to represent accurately every carbon fibre within a large geometry, a large number of elements are required. This results in a large mesh, which requires a large amount of computational memory and a long processing time in order to obtain a solution. This makes it impractical and very inefficient to use these microscopic models. To reduce the memory requirements, the previous thermo-chemical degradation models have considered a macroscopic approach [27, 61, 58, 62, 48]. The macroscopic approach considers the composite material to be represented as a homogeneous anisotropic block. This greatly reduces the required mesh and makes the models more efficient to solve.

2.5.1 The Homogeneous Anisotropic Approach

The macroscopic approach considers replacing the complex internal structure of a piece of CFC and numerically representing it as a simple block. This is done by determining the initial volume occupied by each species (carbon fibre, polymer etc.) within the model. Using the volume occupied by each species and the total volume of the material, the volume fraction of each species can be determined. The homogenisation approach then considers that this global volume fraction is the same as the volume fraction of each species within each cell volume. This approach is more generally referred to as homogenisation and an illustration of this approach is shown in Figure 2.20.

As a result of the homogenisation approach, it is important to define the material properties as bulk values for the material. Unfortunately, it is not completely straightforward to predict the bulk properties of composite material. There have been lots of studies which have focused their attention on developing methods, which can be used to predict these bulk properties. Whilst this approach has been used in the previous thermo-chemical degradation models, the homogenisation approach is a whole topic within itself. Only a brief introduction along with some of the most common homogenisation approaches is given here.

Studies have shown that it is possible to model a composite material as a homogeneous anisotropic material [69, 70, 71, 72], and an investigation by P. Korab et al. [73] explained

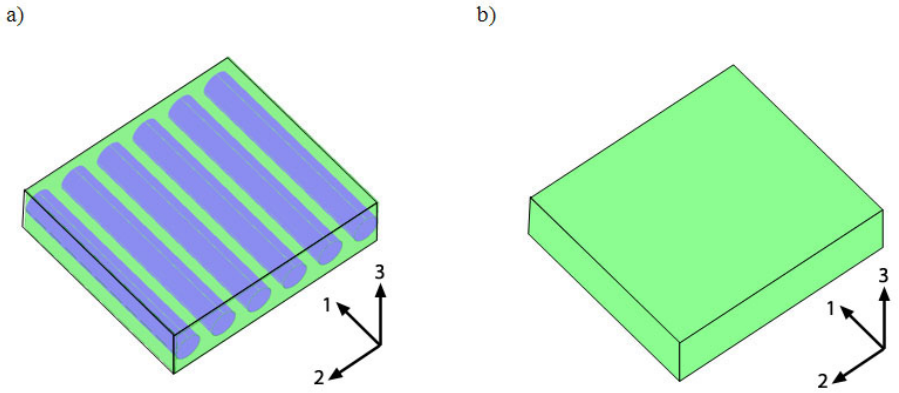

FIGURE 2.20: a) Schematic model of a single ply of CFC including all the carbon fibres b) Schematic model of the same single ply, only now modelled as a homogeneous anisotropic material

that it is possible to model CFCs in this way if the following criteria are met;

- If the sample thickness is much larger than the fibres diameter.
- The fibres are distributed uniformly throughout the polymer.

A typical CFC has a fibre diameter of $8-10\ \mu m$ [7], whilst the panel thickness is typically $5\ mm$. This fulfils the first of the two requirements above. In regards to the second point, previous studies have generally assumed that the fibres are uniformly distributed with similar composite material in [55, 62, 59] and specifically for CFCs in [27, 48, 49]. The relevance of this assumption and a series of methods for determining the bulk properties if CFC do have a non-uniform fibre distribution are considered later. It is also generally assumed that there is a perfect fibre-matrix contact; this is a reasonable assumption as CFC panels are created under very high pressure, which leads to minimal voids within the material, especially at the fibre-matrix interface.

A selection of methods to determine the bulk conductivity are considered below. Whilst there are other material properties apart from the conductivity, these are more straightforward to determine and so are considered in a later section.

2.5.2 Bulk Conductivity of a Homogeneous Anisotropic Material

The discussion here is limited to considering the bulk conductivity for a single ply of CFC. This discussion is kept to a general conductivity rather than focusing on either the electrical or the thermal conductivity. This is done despite the two conductivities being a result of two different physical phenomena, since the two conductivities are analogies to each other and implemented in the same manner within their respective governing equations.

The bulk conductivity for a homogeneous material is defined by the tensor K^{CFC}, using the local axis as defined in Figure 2.20, by

$$K_{ij}^{CFC} = \begin{bmatrix} K_1 & 0 & 0 \\ 0 & K_2 & 0 \\ 0 & 0 & K_3 \end{bmatrix} \tag{2.11}$$

For a single CFC ply only, the non-diagonal terms ($i = j$) are non-zero. The conductivities from the non-zero terms refer to the local axis defined in Figure 2.4.

There are numerous analytical methods to predict the bulk conductivity of a composite material. The different methods vary in mathematical complexity depending on the type of structure inside the composite and the component properties. Two of the most commonly used methods are the Rule of Mixtures [70, 71, 74] and the Eshelby Method [75, 22]. Both of these methods assume that the fibres are distributed perfectly homogeneously throughout the matrix and that there are no voids. More complicated models which attempt to remove some of these assumptions have been investigated by J. Klet et al. [16] and R. Profelhof et al. [76]. However, the increased complexity requires additional knowledge regarding the fibre distribution, volume fraction and distribution of voids etc.. For a generic piece of CFC, this information is not known, and therefore these methods will not be considered any further.

The discussion starts by considering the bulk conductivity for an initially pristine piece of CFC before, considering the application of these methods to a degraded CFC panel. The analytical methods to determine the bulk conductivity parallel to the fibres and perpendicular to the fibres for a pristine piece of CFC are discussed separately below.

2.5.3 Conductivity Parallel to the Fibre Direction

The conductivity parallel to the fibre direction is relatively straight forward to determine and, hence, there is generally only one accepted method. This is called the Parallel Rule of Mixtures [71, 72]. This method is a weighted sum over the components, using the fibre volume fraction as the weighting term, as shown by

$$K_1 = K_f \Phi_f + K_p(1 - \Phi_f) \tag{2.12}$$

Where K_f and K_p are the conductivity of the fibre and polymer, respectively. The fibre volume fraction is given by Φ_f, and is defined as the ratio between the volume occupied by fibres (V_f) and the total volume of the geometry (V).

$$\Phi_f = \frac{V_f}{V} \tag{2.13}$$

It is a necessary requirement that the sum of the volume fractions must always equal unity.

$$\sum_{i=f,p} \Phi_i = 1 \tag{2.14}$$

This implies that if there are no voids in the material then the initial volume fraction of polymer for an undamaged piece of CFC is

$$\Phi_p = 1 - \Phi_f \tag{2.15}$$

This method is akin to calculating the total resistance for resistors connected in parallel.

2.5.4 Conductivity Perpendicular to the Fibre Direction

The bulk conductivity perpendicular to the fibre direction (direction 2 and 3) is not as straightforward to determine. Subsequently, there has been lots of discussions regarding which method is the most appropriate to determine K_2 and K_3 [71, 70, 75, 22]. Below are two commonly used analytical methods which can be used to describe the perpendicular bulk conductivity.

2.5.4.1 Series Rule of Mixtures

The Series Rule of Mixtures, is a continuation of the Parallel Rule of Mixtures, discussed above, and is derived by considering a combination of resistors connected in series. The application of using this method to determine the perpendicular conductivity is considered by Pilling et al. [71] and James B. W. [70]. The conductivity defined by the Series Rule of Mixtures is defined as follows

$$K_3 = K_2 = \left(\frac{\Phi_f}{K_f} + \frac{1 - \Phi_f}{K_p} \right)^{-1} \tag{2.16}$$

2.5.4.2 Eshelby Method

The Eshelby Method has been developed for predicting any material properties within a Laplace equation. Therefore, as well as thermal transport, this method has been proven accurate for calculating the stress and strain in a material due to a foreign body being encased within it [22]. The conductivity tensor for the Eshelby method, as discussed in detail by Khare et al. [75] and Hull and Clyne [22], is given by

$$K_{ab}^{CFC} = \left(K_p^{-1} + \Phi_f \left\{ (K_p - K_f) \left[S - \Phi_f (S_{ab} - \widehat{I}) \right] - K_p \right\}^{-1} (K_f - K_p) K_p^{-1} \right)^{-1} \tag{2.17}$$

Where $\widehat{I}$ is an identity matrix. The Eshelby Method requires knowledge of the shape of the inclusion in the matrix, given by S_{ab} in Equation (2.17). Assuming that the carbon fibres can be represented by long cylindrical rodsr the Eshelby shape tensor (S_{ab}) becomes [22]

$$S_{ab} = \begin{bmatrix} 0 & 0 & 0 \\ 0 & \frac{1}{2} & 0 \\ 0 & 0 & \frac{1}{2} \end{bmatrix} \tag{2.18}$$

By substituting Equation (2.18) into Equation (2.17) and taking $a = b = 1$, the conductivity in the direction parallel to the fibres is obtained. In this case, the derived equation is the same as the bulk conductivity predicted by the Parallel Rule of Mixtures as shown in Equation (2.12). Taking the conductivity along $a = b = 2, 3$, the conductivity perpendicular to the fibres is obtained [22]

$$K_2 = K_3 = K_p + \frac{K_p(K_f - K_p)\Phi_f}{K_p + (1 - \Phi_f)(K_f - K_p)/2} \tag{2.19}$$

2.5.4.3 Validity of the Uniform Fibre Distribution Assumption

All the above models have assumed that the fibres are perfectly uniformly distributed throughout the composite material. An X-ray tomography image of a piece of CFC is shown in Figure 2.21. From this, it is evident that the fibres are not perfectly uniformly distributed. Furthermore, it is noted that there are lots of fibre to fibre contacts. If there are sufficient fibre to fibre contacts, a complete conductive path through the material is created and hence the bulk conductivity will be comparable to that of just the fibres. In this case, the predicted bulk conductivity will be very different from the values predicted by the analytical methods outlined above. It is, therefore, important to try and replicate the true conductivity given by a more realistic CFC fibre distribution. This is investigated by considering the percolation effects within the CFC.

2.5.5 Percolation Effect

Studies have shown that at low volume fractions of the highly conductive material (fillers or fibres), the bulk conductivity behaves similar to what is expected from the analytical methods discussed above, i.e. that there is a gradual increase in bulk conductivity as the volume fraction of the highly conductivity material is increased [78]. However, as the volume fraction increases and reaches a critical value, there is sudden change in bulk conductivity from what is expected by the analytical methods. This critical volume fraction is called the percolation threshold (Φ_{perc}). At this volume fraction, the bulk conductivity rapidly increases towards the conductivity of the inclusion (filler or fibre), as shown in previous studies [78, 79]. The percolation threshold depends on the

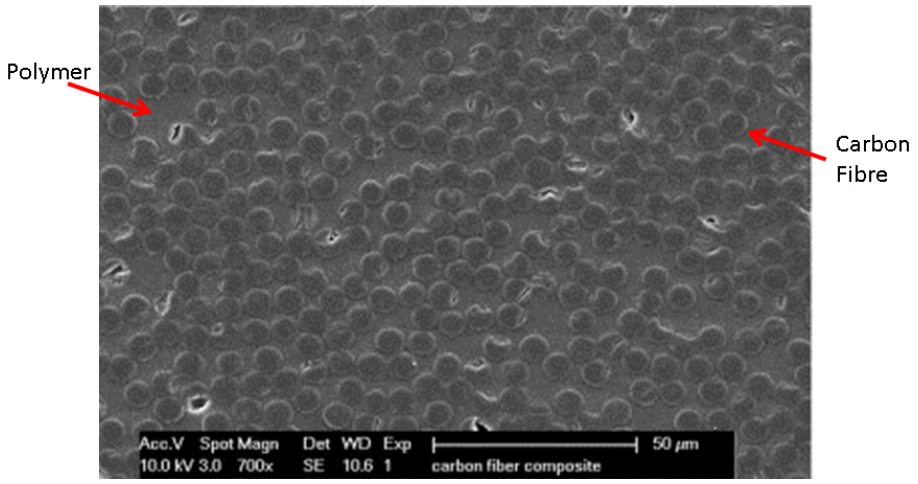

FIGURE 2.21: A SEM image taken of cross section of a piece of CFC. [77]

fibre shape, orientation of fibres and the production process [80, 81]. From previous studies, it has been shown that an empirical power law can be used to describe the bulk conductivity above the percolation threshold. This empirical power law equation is

$$K_2 = K_f(\Phi_f - \Phi_{perc})^{\lambda} \tag{2.20}$$

The power term (λ) and the percolation threshold (Φ_{perc}) are fitted parameters, which need to be determined for each material [78]. A typical graph showing how the bulk conductivity varies as a function of volume fraction, including the percolation effect, is shown in Figure 2.22.

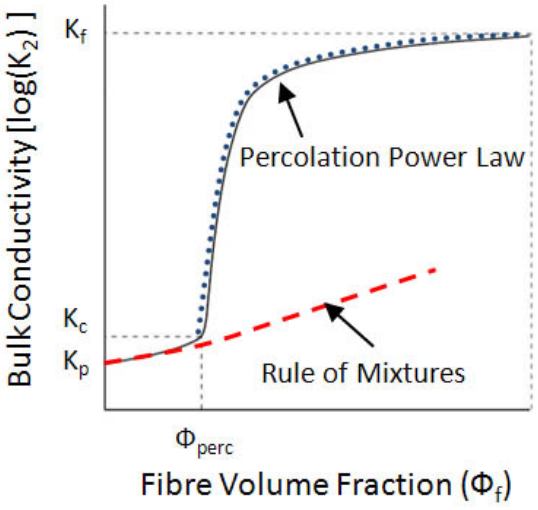

FIGURE 2.22: Typical conductivity trend due to percolation. The blue dots represent the predicted percolation power law, and the red dashed line represents the Series Rule of Mixtures (modified image original from [78])

It has been shown that the fitted parameters are a function of the inclusion shape and its dimensions. Numerical studies by M. Weber [82], M. Kamal and G. Pike and C.

Seager [80] have attempted to determine these parameters for a variety of inclusions. The study by Pike [80] concluded that for 2D circles, the percolation threshold (Φ_{perc}) is 0.68. Due to the symmetry entailed, carbon fibres can be assumed to be 2D circles if they are assumed to be long and straight cylinders. However, in these three studies, no attempt was done to determine the power term (λ).

2.5.6 Homogenisation Approach for Decomposing Composites

So far, the above discussions have considered a pristine piece of CFC with only two species, polymer and carbon fibres. However, as highlighted above, a polymer will decompose into other new species. It is, therefore, important to investigate how the addition of other species affects the choice of method used to the determine the bulk properties. The previous thermo-chemical degradation models have considered using the Rule of Mixtures [27, 48, 49]. One reason for this choice, is that this method has the ability to be expanded to consider any number of different species. This can be done as long as the sum of the volume fraction for each species is equal to unity, as given by Equation (2.14).

However, as it stands, the Eshelby method cannot consider a composite system with more than two species. In its current form, this limits the relevance of this method for these studies. The percolation effects also do not allow for multiple different species, but given that it predicts that only the one species donates the bulk conductivity, the other species are of less importance. However, this model is limited, as it is not able to consider the removal of these dominant species as the empirical power law is only valid above the percolation volume threshold.

2.5.7 Summary of Bulk Conductivity Models

Previous thermo-chemical degradation models have considered using the homogeneous approach to model a composite material. These studies used the Parallel Rule of Mixtures [53, 59, 58] to determine the bulk conductivities. This is a reasonable assumption for their models, as these models consider an isotropic material. P. Korab et al. [73] showed that for a copper matrix with carbon fibres, the predicted bulk conductivity K_1 from the Parallel Rule of Mixtures gave a very good agreement with the experimental data. Therefore, this study will use the Parallel Rule of Mixtures for determining the bulk conductivity along direction 1, i.e. for K_1. However, the choice of method for determining the bulk conductivity in direction 2 and 3 i.e. K_2 and K_3 is not as straightforward. As mentioned above, there is a vast collection of previous methods for determining the bulk conductivity along direction 2 and 3. Two of these analytical methods have been considered above, these are the Series Rule of Mixtures and Eshelby Method. Whilst these methods are well established, there appears to have

been little work published on comparing these methods for long fibre (unidirectional or quasi-isotropic) carbon fibre composite materials. Previous studies have considered carbon-carbon materials [16, 69] and carbon fibres in a copper matrix [73]. The studies by [73, 83] have highlighted that the accuracy of these methods is dependent on the volume fraction of the inclusion (fibres) and the ratio of the conductivity. Korab et al. [73] showed that using the Series Rule of Mixtures to determine K_2 and K_3, there was less agreement when compared with the experimental results.

All the analytical methods assume that the fibres are uniformly distributed, although at large fibre volume fractions, it has been shown that this assumption might not be valid [73], due to clustering of fibres (also as seen in Figure 2.21). Given the large volume fraction of fibres in CFCs, it is important to consider the percolation effects when determining K_2 and K_3. Percolation effects have been seen to have an effect on short fibre CFCs. However, there is no obvious record of the work being conducted for long unidirectional carbon fibre composites. The majority of previous percolation studies have either investigated the bulk conductivity of poorly conductive polymeric materials with different fractions of highly conductive fillers or the percolation effects of short fibre composites [78, 79].

This thesis (in Chapter 6) considers the relative accuracy of the Series Rule of Mixture and the Eshelby Method for use within a pristine CFC for K_2. The accuracy is assessed by conducting a parametric study to investigate how varying the fibre volume fraction and the ratio of the conductivities affects the accuracy. This study also investigates if there are any percolation effects occurring within CFCs and attempts to determine the fitted parameters for a typical CFC. Finally, it has been highlighted that the Eshelby Method is only applicable in composite materials with two species. Therefore, an attempt has been made to adapt the Eshelby Method to permit its application to the thermo-chemical degradation model, by allowing it to consider a composite material with more than two species.

2.6 Modelling Methodology

Having considered the numerical implementation method (Section 2.4.3) and the framework for modelling a CFC (Section 2.5.1), the final aspect to consider is the physical equations which make up the previous thermo-chemical degradation models. The majority of these previous studies considered a 1 dimensional case, due to the isotropic nature of glass fibre composites and the uniform heat source. The following modelling equations discussed here are given for a 1D thermo-chemical degradation case based on the studies given in [52, 53, 54, 55].

2.6.1 Thermal Conduction

Thermal transport is governed by the first law of thermodynamics and written in terms of the conservation of energy. The internal energy is cumbersome quantity to measure in simulations. Therefore, the equation for the thermal conduction is more commonly written in terms of temperature, T [84]. The evolution of the temperature with respect to time, t, is given by

$$\rho C_p \frac{\partial T}{\partial t} = \frac{\partial}{\partial x}\left(\kappa \frac{\partial T}{\partial x}\right) \tag{2.21}$$

Where ρ, C_p, and κ are the bulk density, bulk specific heat capacity at constant pressure, and bulk thermal conductivity, respectively. The methods for predicting the bulk thermal conductivity are discussed in Section 2.5.2. The bulk heat capacity and density are obtained via the Parallel Rule of Mixtures i.e.

$$\rho C_p = \sum_{i=f,p,ch,g} \Phi_i \rho_i C_{pi} \tag{2.22}$$

The 'i' in the sum corresponds to the species of the polymer (p), carbon fibre (f), gas (g) and char (ch) [50, 61, 51]. Note that this is the same principle for determine the bulk conductivity along direction 1.

Equation (2.21) only considers the thermal conduction and does not include any terms which relate to the CFC degradation or gas transport. The next physical process to include is the thermo-chemical degradation.

2.6.2 Thermo-chemical Degradation

The different initial components of a piece of CFC (polymer and fibre) degrade by different physical processes. The degradation processes for carbon fibres and polymers, are discussed separately below along with a numerical modelling approach for each degradation processes.

2.6.2.1 Carbon Fibre Degradation

The first component of the CFC to consider is the carbon fibre, and how they degrade. Given the above models are typically considered for glass fibre composites, there is no discussion of fibre degradation. There is a series of studies which have considered the degradation of carbon fibre. Carbon fibres are known to degrade by two possible mechanisms; oxidisation [7] and phase changes (sublimation) [85, 86]. It has been shown that for a large heat flux, the fibre degradation processes are dominated by phase changes [23], as the oxidation reactions are typically much slower. Carbon fibre sublimation has been considered by Cheng et al. [23] in his paper which discussed laser drilling. In this

study, they developed a 3-dimensional numerical model to predict the spatial extent of the damage caused by the laser drilling to a piece of CFC and metals. This numerical model only considered the damage as a result of sublimation. The numerical model determines the extent of sublimation by a post processing technique after each time step. The post processing technique determines the extent of the sublimation by considering the temperature at every grid point, and if the temperature exceeds the sublimation temperature then the temperature is reduced to the sublimation temperature. The excess heat removed due to the temperature change is recorded in an accumulating sum attributed to each grid point. When the accumulated excess heat at a grid point is equal to the latent heat of sublimation, then the fibres at this grid point are considered to be removed, because sublimation has occurred. The results from this model have been compared against an experimental study, where good agreement was achieved.

2.6.2.2 Polymer Degradation

The two main degradation processes for polymers are via pyrolysis or phase changes [51]. As was mentioned in Section 2.3, Reid et al. [45] noted that typical damage from a lighting strike resembled burning. This damage is actually believed to be pyrolysis rather than burning, although the end appearance from these processes does look similar. This is expected as the typical polymer used in the CFC matrix is a thermosetting epoxy, and hence does not undergo a melting or sublimation phase changes. The previous models thermo-chemical degradation models considered the polymer degradation through pyrolysis [52, 53, 54, 55].

2.6.2.3 Pyrolysis

Pyrolysis is the chemical decomposition of a condensed substance that occurs spontaneously at high temperatures. The mechanism responsible for the pyrolysis of polymers is the breaking of polymer chains [51]. It is known from stoichiometry that a typical epoxy degrades via pyrolysis into 80-90 % by weight into gases, whilst the remaining is decomposed into a highly porous char [51]. The char is typical 85 - 98% carbon, with traces of oxygen, nitrogen and sulphur [62]. The pyrolysis gases produced are mainly carbon monoxide, carbon dioxide, hydrogen, nitrogen, methane and lesser products are given off. The precise chemical products and their relative amounts depend on the specific polymer and heating rates [62]. It has been reported that the heating rate affects the degradation processes [12, 51]. Typically, the higher the heating rate is the less char is produced [87]. Pyrolysis is modelled by using the Arrhenius Equation [50, 53, 88, 58, 59]

$$\frac{dm_p}{dt} = -Am_p(t_0)\left(\frac{m_p(t) - m_p(t_\infty)}{m_p(t_0)}\right)^n \exp\left(-\frac{E_a}{\Re T}\right) \tag{2.23}$$

where the rate of polymer pyrolysis $\left(\frac{dm_p}{dt}\right)$ depends on the temperature T and the activation energy (E_a) of the reaction. Furthermore, A is the pre-exponential factor for the reaction, n is the reaction order and $\Re$ is the molar gas constant. The mass of polymer within a cell volume at time, t, is given by $m_p(t)$. The times t_0 and t_∞, correspond to the initial and final mass of the polymer. The reaction kinetics (A, n, E_a) are obtained experimentally from Thermo-Gravamentic Analysis (TGA) [51, 89, 90].

The majority of these previous models have assumed that the polymer degrades solely into a gas with no char being produced [53, 61, 49]. By considering the conservation of mass, the amount of polymer mass which degrades is equal to the rate at which the mass of gas increases. This leads to an equation which defines the rate of at which the mass of gas is increased i.e.

$$\frac{dm_g}{dt} + \frac{dm_p}{dt} = 0 \tag{2.24}$$

The study by H. McManus et al. [61] considered that the polymer degraded into a gas and a char. Whilst they considered the conservation of mass, it is far from clear in this study how they defined the rate at which the decreases polymer adds to the mass of gas and char.

It has also been reported that the reactants from a degradation process can also go onto cause further degradation processes [87, 90]. To model this, a series of Arrhenius equations are needed. It has been generally assumed that the reaction products do not causes further degradation processes, and hence only one Arrhenius equation is needed [61, 58, 59].

The polymer degradation (Equation (2.23)) is coupled with the thermal conduction equation (Equation (2.21)) in two ways; firstly, by the change in enthalpy (Q_d) and subsequently the temperature due to the polymer degradation, and secondly by a variation in bulk material properties. Due to the inclusion of the chemical degradation, the resultant coupled temperature equation is now given with respect to the mass in each cell rather than the density, as considered within the thermal conduction as given in Equation (2.21) [50, 58, 59]. This coupling is mathematically expressed as

$$mC_p\frac{dT}{dt} = \frac{\partial}{\partial x}\left(\kappa\frac{\partial T}{\partial x}\right)V_{cell} + \frac{dm_p}{dt}(Q_d + h - h_g) \tag{2.25}$$

The change in enthalpy due to the polymer degradation (Q_d) needs to be experimentally determined by Differential Scanning Calorimetery (DSC). The enthalpy of the decomposing composite material and the produced gases is defined by [58, 59]

$$h = \int_{T_o}^{T} C_p T \, dt \tag{2.26}$$

and

$$h_g = \int_{T_o}^{T} C_{p_g} T \, dt \tag{2.27}$$

2.6.3 Thermal Gas Transport

Due to the polymer degradation, gasses are produced within the decomposing material. These gases filter through the decomposing material, causing changes in gas pressure as the gas tries to escape. The filtrating gas also transports thermal energy away from the hot degradation zones. A series of studies by [53, 91, 58] have considered the filtration of the produced gas products through the decomposing material. The discussion will initially focus on how to determine the filtration velocity before considering how the gas transport is incorporated into the model.

2.6.3.1 Gas Filtration Velocity

In the studies by Wu et al. [60], Sullivan et al. [53] and Farakas et al. [91] they considered using Darcy's law for determining the gas filtration velocity. Darcy's law is given as

$$v_g = -\frac{\gamma \nabla P}{\mu \Phi} \tag{2.28}$$

Where P, μ, γ and Φ are the internal gas pressure, viscosity of the gas, the permeability and the porosity of the decomposing material. The porosity defines the fraction of empty space within a material, through which a fluid can flow. The internal gas pressure (P) is calculated by assuming the ideal gas law given as

$$P = \frac{m_g \Re T}{M V_g} \tag{2.29}$$

The gas is assumed to be ideal in the models by [53, 91, 58]. In Equation (2.29), M is the molar mass of gas and V_g is the volume which the gas occupies in a mesh element.

The final outstanding term to determine for Equation (2.28) is the permeability (μ). Previous studies have considered bespoke methods for determining the permeability of glass fibre composites [53, 91, 58]. These methods are not applicable for CFC as they considered composite materials with lower fibre volume fractions. Instead, this study will consider the permeability given by the Blake-Kozeny equation, which is

$$\gamma = \frac{\Phi_g D_H^2}{32\tau} \tag{2.30}$$

Where τ is the torosity and D_H is the hydraulic diameter. The hydraulic diameter is defined as

$$D_H = -\frac{4A_g}{Perimeter} \tag{2.31}$$

Where A_g is the cross sectional area of the gas flow and $Perimeter$ is the perimeter of the gas area. The hydraulic diameter can then be written as

$$D_H = \frac{2r_f\Phi_g}{1.5\,(1-\Phi_g)} \tag{2.32}$$

Where r_f is the radius of a single carbon fibre. From this, the permeability can be written as [92, 93, 94]

$$\gamma = \frac{(2r_f)^2\Phi_g^3}{180\,(1-\Phi_g)^2} \tag{2.33}$$

Throughout this study, the term 'permeability' will always refer to the fluid mechanical concept, of a fluid flowing through a porous media. This term should not be confused with the electromagnetic permeability which in this study will always be referred to as the magnetic permeability.

2.6.3.2 Gas Transport Equations

Gas convection is considered in two parts; firstly by the mass transport and secondly by the thermal convection due to the gas transport. The resultant mass profiles due to the gas filtration are calculated using the mass continuity equation given by [54, 91]

$$\frac{dm_g}{dt} = -\nabla(m_g v_g) - \frac{dm_p}{dt} \tag{2.34}$$

This equation is an expansion of Equation (2.24), with the addition of the gas convection term. The coupling with the thermal conduction equation is done by the inclusion of the thermal convection terms. This is shown by the final term on the RHS of the following thermal transport Equation [58, 59]

$$mC_p\frac{dT}{dt} = \frac{\partial}{\partial x}\left(\kappa\frac{\partial T}{\partial x}\right)V_{cell} + \frac{dm_p}{dt}(Q_d + h - h_g) + m_g C_{p_g} v_g \frac{\partial T}{\partial x} \tag{2.35}$$

The majority of the previous studies [59, 61, 53] have assumed that the gasses are in thermal equilibrium with the remaining solids species. In the paper by Florio et al. [58], they investigated the effect of removing this thermal equilibrium assumption as on the numerical predictions. They concluded that with the thermal equilibrium assumption removed, there was a 16% difference in the predicted temperature profile, which equated to a reduction in predicted damage depth.

2.6.4 Discussion of Existing Thermal Degradation Models

In the studies by Henderson et al. [59] and by Florio et al. [58], they conducted a series of experiments to try and validate the predictions from their numerical model.

These experiments consisted of heating a piece of fibre glass composite with a uniform heat source at one end and then measuring the temperature at distances along the edge of the sample using thermocouples. The temperatures at these locations were then recorded as a function of time whilst the material degraded. The experimentally recorded temperatures were then compared against the numerical predictions. Good agreement was achieved between the experimental and the numerical results. Both of these models also considered the transport of the gas produced by the decomposing polymer. The numerical models predicted that the peak internal gas pressure can be as high as 15 times the ambient pressure in the case of Florio et al. [58] and 50 times that of ambient pressure in the case of Henderson et al. [59]. The differences in predicted internal gas pressure are due to the different permeabilities used in each model. Attempts were made to validate these pressure profiles, however, the authors highlighted that there were issues with the experimental procedure for determining the gas pressure. As a result, the experimentally observed gas pressure was considerably lower than that predicted by the numerical model.

The thermal gas transport model proposed by Florio et al. [58] considered the heat capacity of the gas to be given by the heat capacity at a constant pressure. Yet, the model also considers the gas filtration to be a function of variable gas pressure. Therefore, the use of the heat capacity at constant volume would seem to make more physical sense. Therefore, this study will reconsider the thermal gas transport equations to solve for heat capacity at constant volume.

2.7 Summary of Previous Work

Given the aims outlined in the introduction, the following conclusions can be made, and hence used to define the future content of this study.

It has been shown that a lightning strike can be represented by a current impulse, with the dominant frequencies below 200 kHz [11]. Studies have shown that a lightning strike deposits energy into a material via two mechanisms; Joule heat and a heat flux from the plasma channel. It has been reported that for a CFC, the majority of the energy input comes from the Joule heat, whilst a sizeable amount does still come from the plasma channel [27]. Given a lightning strike is an electrical phenomenon it is important to consider the electrical properties of a piece of CFC. A previous study by Scruggs et al. [26] has shown that a unidirectional CFC can be considered to be a pure resistor, with no capacitive or inductance effects up to 1 MHz. There are no obvious records of this work being conducted for quasi-isotropic CFCs. There is a collection of previous studies which have focused around short fibre CFCs. The results from these studies showed that if the fibre volume fraction is above the percolation threshold, then a CFC can be considered as a pure resistor up to 500 kHz. They explained this result by considering

an equivalent electrical circuit to represent a piece of CFC (discussed in Section 2.1.3.2). Part of this study will aim to determine the electrical impedance of both a unidirectional piece of CFC and a quasi-isotropic CFC.

Previous experimental studies have investigated the damage caused to pieces of CFC using laboratory generated lightning strikes. It is reported that the typical damage to a piece of CFC due to a lightning strike, resembles pyrolysis of the polymer with carbon fibre tufting. Internal damage such as delamination has also been witnessed. The proposed explanation for this delamination, is that a large internal gas pressure is built up within the material due to the rapid polymer degradation (pyrolysis).

To investigate the physical processes which cause this damage, a series of numerical models have been developed. There are only three records of previous attempts to develop numerical models to predict the damage caused to a piece of CFC due to a lightning strike. The models by Lago et al. [27] and Henderson et al. [59] considered a 2D axial symmetric model. The numerical model predictions were compared against previous experimental results. The comparisons showed that the predictions underestimated the damage caused. The main reasons for this could be the use of the axial symmetry which breaks the anisotropy of a true piece of CFC, or due to the method chosen to implement the thermo-chemical degradation. Finally, these models did not consider the gas transport, and so there is no indication of the internal gas pressure, or discussions as to whether it is large enough to cause the delaminations. There are, however, a series of 1-dimensional thermo-chemical degradation models which have been developed to predict the damage caused to composite materials due to surface heat fluxes (fires). Some of these models have been partially verified by comparing the temperature profiles of the decomposing samples with the model. These models have only considered the thermal degradation for fibre glass composite materials. Therefore, these previous models need to be expanded initially into 3-dimensions, to account for the anisotropic nature of CFC. The gas transport model also needs to be reconsidered, given doubt has been cast on the previous methods.

However, before the degradation model can be developed, the framework to model numerically a piece of CFC needs to be considered. Previous studies have considered representing a composite material as a homogeneous block. This same framework is applicable to this study. However, whilst most of the material properties are straightforward to predict, care needs to be taken when calculating the bulk conductivity in directions 2 and 3. A selection of methods for determining the bulk conductivity in these directions has been given above. The accuracy and relevance of each of these methods is considered in the later chapters.

Chapter 3

Experimental Methodology

This chapter outlines experimental methods employed within this study to investigate the damage caused to a piece of CFC due to a lightning strike. To this end, the first half of this chapter considers several experimental techniques required to characterise the material properties of CFCs for use within a numerical model. The required materials properties and their importance have been highlighted in Section 2.1.3 and Section 2.6.2.3. The next part of this chapter considers techniques to damage samples of CFC by either laser ablation (Section 3.4.1) or lightning strikes current impulses (Section 3.4.2). Having obtained the damaged samples, methods to investigate the internal damage, are then considered (Section 3.5).

3.1 CFC Sample

For this study, a single composition of carbon fibres and epoxy will be used. The CFC used in this study consists of $T700s$ carbon fibres from Toray [19] and an epoxy called $M21$ produced by Hexcel [95]. The cured CFC has a fibre volume fraction of roughly 65 %.

Two types of $M21/T700s$ CFC panels have been provided, a unidirectional panel with fibres all aligned in one direction and a quasi-isotropic panel, with the fibres arranged in different directions within each ply (given in appendix A). There is no published record of the material properties for this type of CFC. Similarly, there is no public record of any lightning strike current impulse test having being performed on $M21/T700s$.

3.1.1 Sample Preparation

The provided panels of CFC are much larger than is required by these experiments and, therefore, they need to be cut down to the required size.

For the electrical experiments, the large panels are cut using a water cooled diamond tipped tile cutter. This creates clean, straight, perpendicular sample edges. Before the samples can be used within the proposed electrical experiments, the thin film of polymer which is present on the top and bottom surfaces of CFC panels needs to be removed. This is because as indicated in Section 2.1.3.2, the thin film of polymer does not replicate the bulk properties of the material. The polymer layer is removed by firstly sanding down the top and bottom surface of a CFC sample with a new sheet of 150 grade sand paper. Once it appears that the surface polymer has been removed, a finer clean sheet of sand paper (typical with 280 grade) is used. This finer sheet is used to create a smooth finish. Once the sanding has been completed, a damp cloth is wiped over the surface to remove any polymer or carbon fibre particles which might be left on the surface. Once a damp cloth remains clean after wiping the sample surface, the sample is left to dry for several hours. This allows any water which might be on the surface to evaporate. After this, the sample is then ready to be used for its intended experiment. The thin polymer film for all these studies has been removed in the same way.

For the thermo-chemical degradation experiments, much smaller samples are required, so a sharp clean razor blade is used to remove pieces from the corners and edges of a piece of CFC. It is important to use a clean blade to avoid any contamination. The thin polymer film is not removed from the thermo-chemical degradation sample, because the increase in fraction of polymer mass due to this thin film is so small that the introduced error can be discounted.

3.2 Characterisation of CFC's Electrical Properties

Firstly, the experimental techniques to investigate the electrical properties of CFCs are considered. To this end, techniques have been considered under both alternating current (AC) and direct current (DC) conditions. These experimental techniques consider the bulk properties of the composite material.

3.2.1 Electrical Impedance

The bulk electrical properties of a material under AC condition are given by its impedance (Z), as defined by

$$Z = R + jX \tag{3.1}$$

Where the real part of the impedance is resistance (R) and the complex part (j) is given by the reactance (X). Fundamentally, the resistance of a material is given by its dimensions (thickness, l, and cross sectional area, A_{xs}) and its conductivity i.e.

$$R = \frac{l}{\sigma A_{xs}} \tag{3.2}$$

The reactance within a material can be capacitive (X_c), inductive (X_L) or a combination of the two. The reactance for a capacitor is given by

$$X_c = -\frac{1}{\omega C} \tag{3.3}$$

Where ω is the angular frequency and C is the capacitance of the material. The reactance of an inductor is given by

$$X_L = \omega L \tag{3.4}$$

where L is the inductance of the material. Therefore, the material properties required to describe the electrical behaviour of any material, are the electrical conductivity, σ, the capacitance, C and inductance, L. In the following experimental techniques it is more convenient to discuss the impedance in the polar form, which is given by

$$Z = |Z|e^{j\theta} \tag{3.5}$$

where $|Z|$ is the impedance magnitude and θ is the phase angle. These terms can be more commonly displayed in the following form shown in Figure 3.1

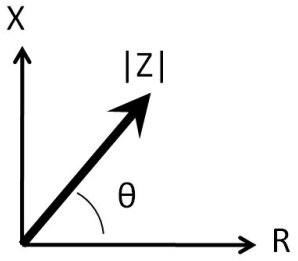

FIGURE 3.1: Impedance phase diagram

From Figure 3.1, it is evident that the impedance magnitude ($|Z|$) can be written as

$$|Z| = \sqrt{X^2 + R^2} \tag{3.6}$$

By considering an AC circuit with a combination of resistor plus a capacitor and/or an inductor, the impedance magnitude can be calculated using

$$|Z| = \frac{|\phi|}{|I|} \tag{3.7}$$

Where $|\phi|$ and $|I|$ are the magnitudes of the voltage and current across the test object. Following on from the circuit discussion, the phase angle is defined as the angular difference between the current and voltage profile. This is written as

$$\theta = 360\, \delta t\, F \tag{3.8}$$

Where δt and F are the time difference between corresponding points on current and voltage profile and the frequency of the applied voltage, respectively. It can, therefore,

be shown that the phase angle relates to the reactance and the resistance through the following trigonometric identity

$$\theta = \tan^{-1}\left(\frac{X}{R}\right) \tag{3.9}$$

Hence, a positive phase angle indicates an inductive affect; whereas a negative phase angle implies capacitive affects.

3.2.1.1 Impedance Measurements Techniques

There are two commonly used experimental methods to obtain impedance measurements, an AC bridge or an AC potential divider network. These two different techniques are now considered in detail.

AC Potential Divider Network

The circuit for a typical potential divider network is shown in Figure 3.2. This circuit comprises a known resistor R_n placed in series with the sample which is under test (Z_x). The CFC sample is then held between two circular flat aluminium electrodes. A high impedance signal generator is used to apply an alternating current to the circuit. A digital oscilloscope is then used to record the voltage profiles across the signal generator and at the known resistor (R_n). From these two voltage profiles, two pieces of important information can be calculated, these are: the potential difference across the sample and the current within the circuit. From these, the impedance magnitude ($|Z|$) and the phase angle (θ) can be calculated using Equation (3.7) and Equation (3.8), respectively.

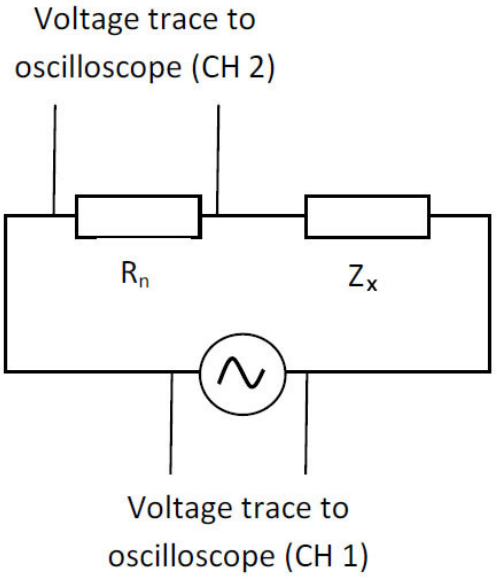

FIGURE 3.2: Circuit for the AC potential divider network

This method is akin to dielectric spectroscopy measurements. Whilst dielectric spectrometers are commercially available, they tend to require highly resistive samples with a minimum of 100 Ω [96]. Given that CFCs are relatively conductive (shown in Figure 2.6), it was decided that these commercially available options were not suitable for this experimental study.

AC Bridge

Another group of experimental methods which can be used to measure the impedance of a sample are called AC bridges. These experiments are similar to the more famous Wheatstone Bridge, which is used in DC conditions to determine the resistance of a sample. There are a wide variety of different AC bridge arrangements depending on what electrical properties the experimenter is investigating. The most common circuits are either the Wien Bridge or the Schering Bridge [97]. All these bridges rely on similar principles. Therefore, it is necessary to devote some time to discussing how one of these bridges works. This is done by considering a Schering Bridge: with a typical circuit diagram for this bridge shown in Figure 3.3.

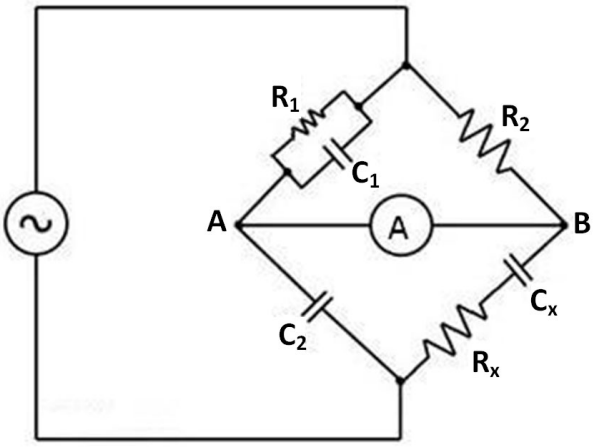

FIGURE 3.3: Circuit diagram of a typical Schering bridge [98]

The Schering Bridge circuit shown in Figure 3.3, comprises two known resistors, R_1 and R_2 and two known capacitors C_1 and C_2. The sample under test is given by R_x and C_x and is introduced into the circuit using the same pair of aluminium electrodes as considered for the previous experiment. To determine the values of R_x and C_x, the values of C_2 and R_2 are fixed, while the values of R_1 and C_1 are varied until the current between points A and B becomes zero. This occurs when the bridge is said to be 'balanced'. When the bridge is balanced, the impedance from the combination of R_1 and C_1 is equal to the impedance of the R_x and C_x combination. By carefully balancing the bridge, a very accurate value for R_x and C_x can be obtained.

3.2.1.2 Discussion of Different Techniques

Before choosing the experimental technique to use in this study, it is necessary to consider the factors which affect the accuracy of each experimental set-up.

The main cause for concern within both experimental set-ups, relates to what the experimentally measured impedance actually refers to. The measured impedance is not solely the actual impedance of the sample under test, but also includes a combination of the electrodes impedance, their contact impedance with the sample and also any other erroneous impedances introduced by other components within the circuit. Each of these possible effects are considered in turn.

Two components have been highlighted as possible causes of erroneous impedance, these are the known resistors (R_n, R_1, R_2, R_3) and the circuit wires. If the resistors used have any inductive effects, then at high frequencies they will create an erroneous reactive effect within the circuit. It is, therefore, important that the resistors used have a low inductance. Similarly, the wires between the different circuit components need to be kept as short as possible, because long wires can produce inductive affects at high frequencies. This inductance can also be reduced by using shielded wires.

Next, the impedance of the electrodes and their contact impedance are considered. For both these experimental set-ups, the sample is introduced into the circuit by being placed between two flat circular aluminium electrodes. It is, therefore, reasonable to assume that the electrode resistance can be neglected, as the resistivity of aluminium is much lower than that of CFC. The contact resistance is, however, much harder to define. Despite careful sample preparation, there is likely to be imperfections on the samples surfaces which are in contact with the electrodes. Such imperfections are mainly caused by the surface of the sample not being perfectly smooth and/or flat. This creates air gaps within the electrical contact, and hence these imperfections lead to an increase in resistance at the interface between the sample and the electrodes. In an attempt to reduce the contact resistance, the sample holder has been designed so a variable pressure can be applied between the two electrodes to improve the electrical contact. The error introduced by the contact resistance is magnified if the conductivity of the sample is high. As the electrical conductivities quoted by F. Uhlig [12], indicate that CFCs are reasonably conductive, it is believed that the contact resistance will be the dominating source of error within this experimental set-up.

Two further sources of errors, which relate to the sample have been identified. Firstly, how uniformly is the current distributed within the CFC and the temperature of the samples. The aluminium electrodes have been designed in accordance with VDE specifications 0303, 0311, 0345. The positive electrode, therefore, includes a guard ring. The guard ring reduces any fringing effects to create a uniform current distribution within the sample. By taking the fringing effects into account, the supplier of the sample holder

defines an effective cross sectional area of a sample which has a uniform current distribution to be 20 cm^2 [99]. Secondly, to what extent does the temperature of the sample vary during the experiment? It has already been shown in Figure 2.6 that the electrical conductivity of a piece of CFC is dependent on temperature [12]. With the available experimental set-up, the temperature of the electrodes can be controlled so they actively maintain a constant predefined temperature. However, there is still the possibility of Joule heat occurring, which can alter the temperature within the material. To reduce the impact from this, care is taken to apply a small current, whilst keeping the voltage large enough to be easily detectable with an oscilloscope.

Whilst accurately balancing the bridge could theoretically produce a more accurate impedance measurement than what is obtained by using the AC divider network, the bridge method is still dominated by the same contact resistance error which is present within the AC potential divider network. This is because whilst the circuit around the sample has changed, the sample is still connected to the circuit in the same way. Hence, despite the extra accuracy from carefully balancing the bridge, the total error contained within the results would be very similar to that obtained from the AC potential divider network. Therefore, as the AC potential divider network is quicker and easier to operate, this method is chosen for the experimental work.

3.2.1.3 Impedance Measurements Methodology

The AC potential divider circuit was set-up as shown in Figure 3.2. For this experiment, the electrodes are held at a constant temperature of 23 $^{\circ}C$. The applied contact pressure between the electrodes is increased until a constant voltage amplitude is recorded on the oscilloscope with increasing pressure. It is assumed that increasing the applied electrode pressure has no variation on electrical properties, as CFCs can be assumed to be incompressible.

When using the potential divider network, care needs to be taken when choosing the value for the fixed known resistor (R_n), as it is important that the potential difference recorded over the known resistor, is not disproportionally small or large when compared against the potential difference across the sample. In order to achieve this, the resistance of the known resistor and the sample under test need to be comparable. A rough idea of the sample's resistance can be calculated by defining the general thickness(l) of a piece of CFC to be 5 mm, the cross sectional area of the sample given by the sample holder i.e. 20 cm^2, and conductivity obtained by F. Uhlig ($\sigma_3 = 1\ Sm^{-1}$) [12]. By putting these values into Equation (3.2), the resistance of the sample is of the order of 4Ω. From this, the chosen known resistor (R_n) had a resistance of 1 Ω.

The signal generator was set to produce a sine wave with a constant peak-to-peak signal. The frequency of the input was varied from 1 Hz to 10 kHz. This maximum frequency

is due to certain parts of the circuit displaying inductive affects when the frequency is increased further. Whilst this frequency range does not cover the entire lightning strike frequency range, it does cover up to the first frequency break point as shown in Figure 2.14. Therefore, the result obtained should provide an indication of the AC behaviour of a piece of CFC during a lightning strike. At each frequency, both voltage profiles measured by the oscilloscope are saved to a Compact Flash card for later analysis. To remove any random experimental errors the frequency range applied to each sample was repeated 3 times, with the voltage profiles at each frequency being recorded for 3 or 4 periods. This allows for many data points to be recorded, which can then be used in the calculations to obtain an averaged result. Once the voltage profiles have been recorded, the data files are uploaded onto a computer, and the impedance is calculated as outlined in Section 3.2.1.

3.2.2 DC Conductivity Measurements

The main uncertainty with the above experimental technique is due to the contact resistance between the sample and the electrodes. Whilst it has not been possible to remove this source of error under AC conditions, it is possible to reduce this error under DC conditions, by using the four probe method. The four probe method has proven very useful for reducing the contact resistance when measuring the electrical conductivity of composite materials [100, 101].

Four Probe Method

The experimental set-up developed by the author of this study, for the four probe method is similar to that seen above with the AC potential divider network. The differences are that the signal generator has been replaced by a DC power supply and the oscilloscope and known resistor have been removed. A circuit diagram of the four probe experimental set-up is shown in Figure 3.4

From this experimental set-up, the bulk electrical conductivity is calculated by firstly measuring the potential difference (V_{CFC}), between two points on the samples surface, using the two measuring electrodes shown in Figure 3.4. The measuring electrodes are sharp razor blades which are connected to a digital voltmeter. Sharp razor blades are used as they allow for a good electrical contact with the sample. The distance between the two measuring electrodes (D) can then be varied. By then measuring the current within the circuit, it is straightforward to determine the resistance and, hence, the apparent bulk conductivity of the sample using

$$\sigma = \frac{DI}{V_{CFC}A_{xs}} \tag{3.10}$$

This equation is a modified form of Equation (3.2), where here the resistance (R) is

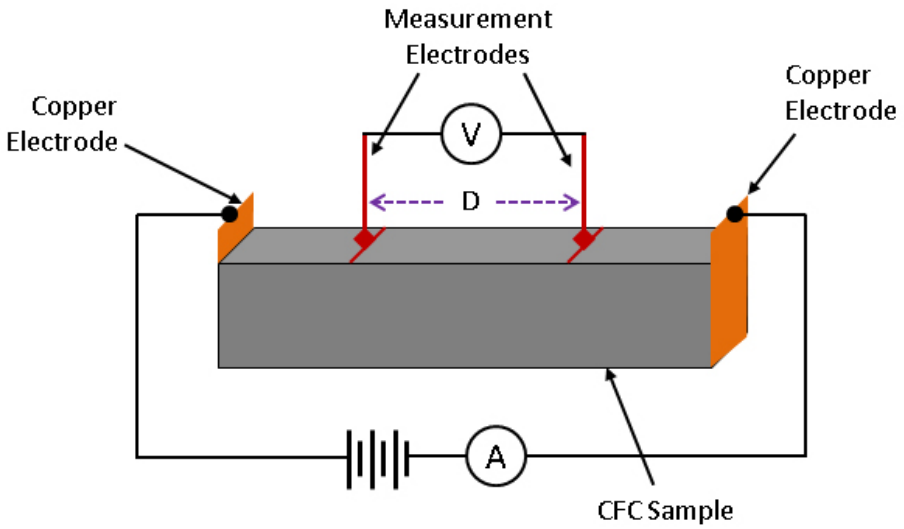

FIGURE 3.4: Circuit diagram of the Four Probe method

given by the ratio of voltage (V) and current (I), as stated in ohm's law and the length of the sample l is now replaced by D, the distance between the electrodes.

3.2.2.1 Experimental Method

The sample is connected to the circuit via two copper electrodes. The copper electrodes are formed by cutting a thin sheet of copper so that the electrodes surface area is just larger than the sample's cross sectional area. The electrodes are then attached to the sample using silver conductive paste. As well as helping to attach the cooper electrodes to the samples the paste also helps to reduce the contact resistance. The silver conducting paste is not designed as a glue, and so a metallic clamp with plastic feet is also used to help keep the electrodes attached to the sample. The clamp is only designed to keep the electrodes in contact with the sample and so only a small pressure is applied to the electrodes via the clamp. The copper electrodes are then connected to the circuit via crocodile clips.

It is reported on the technical sheet supplied with the silver conducting paste [102], that the conductivity of the paste does vary as it dries. Therefore, once the electrodes have been attached to the CFC sample, they are left to dry for an hour. Once the silver paste has dried, a potential difference is then applied across the sample. The potential difference between the measuring electrodes is recorded as a function of the distance between the measurement electrodes (D). The distance 'D' is defined to be zero when both measurement electrodes are in the middle of the sample, equidistant from the copper electrodes. The distance between the measurement electrodes is then increased symmetrically outwards from this mid-point. To determine the spacing between the measurement electrodes, a threaded plastic rod is placed between the clamps, but not touching the CFC sample. This rod, has been marked, to guide the position

of the measurement electrodes accurately and further allowing for the electrodes to be easily placed at the same location for each experimental trial. The potential difference is then measured as a function of D to investigate at what point the potential difference within the material becomes uniform. The uniform potential difference is required to obtain a true bulk electrical conductivity value of the sample under test. A non-uniform potential difference can be created near the interface between the sample and the electrodes, if there are imperfections in the electrical contact. A region of uniform potential difference is defined by a linear increase in potential difference with increasing D. By then only considering the uniform potential difference as a function of electrode spacing, the bulk electrical conductivity can be calculated for each data point by using Equation (3.10). For this, the current in the circuit needs to be accurately measured with ammeter positioned in series in the circuit. The ammeter chosen has a resolution of 'mA', which is sufficient for an accurate reading for this experiment. To remove any random errors, which might occur during the experiment, the calculated bulk conductivities are combined to obtain an average conductivity.

3.2.2.2 Discussion

Having outlined the experimental methodology, it is necessary to discuss the possible sources of error which might occur during this experiment. Whilst conducting this experiment, it was important to minimise any Joule heat which might occur within the sample. This error can be controlled by carefully limiting the maximum allowed current, whilst keeping the applied potential difference large enough so that it can be accurately measured by the digital voltmeter. To further reduce the possibility of Joule heating, between measurements the power supply is switched off. Limiting the Joule heating is of principal importance when measuring the conductivity along direction 1. This is because the electrical conductivity in this direction is at its highest and so the largest current will hence be applied to the circuit and so the most amount of Joule heating will be generated.

Another possible limitation of this experimental set-up is the resistance of the silver conducting paste and the electrodes. For this set-up, the sample under test needs to have a resistance of at least 2 orders of magnitude greater than everything else in the circuit. Therefore, the worst case scenario for the proposed experiments occurs when measuring the resistance along fibre direction. Taking the along fibre electrical conductivity from Figure 2.6 to be $16 \times 10^3\, Sm^{-1}$, it is important to determine the electrical conductivity of the silver paint and the copper electrodes. The reported electrical conductivity for the silver paste is $1 \times 10^5\, Sm^{-1}$ [102] and the electrical conductivity of copper is $5.96 \times 10^7\, Sm^{-1}$. Given that the electrical conductivity of these components is at least an order of magnitude greater than the along fibre conductivity and as the thickness of these components (paint region and copper electrode) are much thinner than the CFC samples,

it is reasonable to assume that the resistance introduced by the silver conducting paste and the electrodes will have a negligible impact on the measured resistivity of the CFC.

3.3 Characterisation of CFC's Degradation Mechanisms

It has been highlighted in Section 2.6.2.3 that to represent numerically the thermo-chemical degradation of CFC, a series of parameters is required. These parameters can be obtained by two experimental techniques; Thermal Gravimetric Analysis and Differential Scanning Calorimetry.

3.3.1 Thermal Gravimetric Analysis

Thermal Gravimetric Analysis (TGA) is a technique whereby it is possible to investigate the decomposition chemistry of a particular material at elevated temperatures. It is then commonly used to determine over what range of temperatures a given material is stable and unstable [103]. There are two commonly used modes in which a TGA can operate. The first method considers a sample placed in an open crucible which is then held at a fixed temperature. The mass of the sample is then recorded over time as the sample degrades. This method is called isothermal TGA. This method can be very time consuming depending on the reaction rate, and also there are limitations in bringing the sample and apparatus to the specified temperature without part of the decomposition having occurred [104, 103]. To avoid these complications, a second TGA experimental method can be considered. This second method involves placing a sample in an open crucible which is then heated at a predefined constant heating rate (β). During the heating, the mass of the sample is constantly being monitored and recorded. In this study, the second TGA technique will be considered [105]. It is also worth noting that the atmospheres in which the samples are heated in can be carefully controlled to contain different gasses. The raw data obtained from these TGA experiments is the mass of the decomposing sample as a function of temperature. As the sample degrades, it gives off gaseous products, which are free to escape, and hence the mass of the sample is reduced. It is not very useful to compare directly the decomposing mass of each sample, as each sample is likely to have a different initial mass. It is more useful to compare the remaining mass fraction of each sample as a function of temperature. The remaining mass fraction (Γ) is defined as

$$\Gamma = \frac{m_{cfc}(T)}{m_{cfc}(T_i)} \tag{3.11}$$

where $m_{cfc}(T)$ is the mass of the sample at a given temperature, T. The denominator represents the initial mass of the sample at the initial temperature, T_i. A generic TGA curve showing the variation in mass of an organic material as it is heated is shown in Figure 3.5.

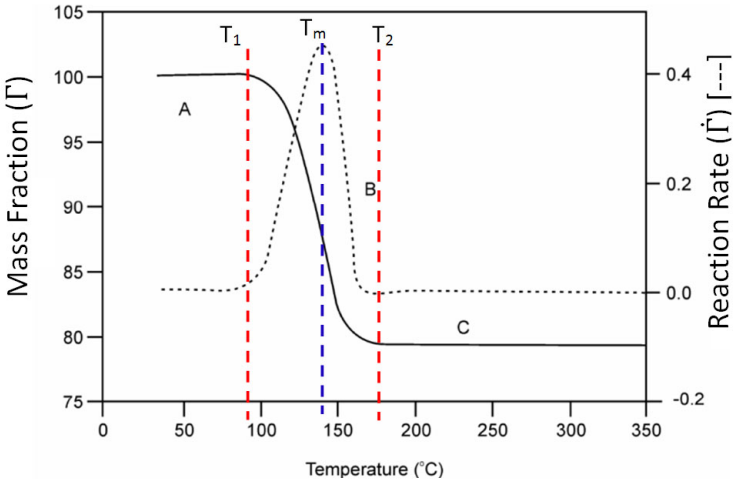

FIGURE 3.5: Generic fraction of mass during heating, overlaid with the derivative of the variation in the fraction of mass

With reference to Figure 3.5, as the sample is initially heated, there is no variation in mass (region A). Once the temperature of the sample becomes high enough (T_1), it begins to decompose, as shown by the decreases in the mass fraction (region B). There is then a point where all the mass that is going to degrade will have degraded, and so another plateau region forms at T_2 (region C). The variation in mass can be described by the derivatives of the mass variation and is termed reaction rate ($\dot{\Gamma}$). The reaction rate is shown by the dotted line in Figure 3.5, and is mathematically defined by

$$\dot{\Gamma} = \frac{d\Gamma}{dt} \tag{3.12}$$

From this, it is possible to define the temperature at which the maximum degradation rate occurs; this is given by T_m in Figure 3.5.

3.3.1.1 Reaction kinetics

From these TGA results, it is possible to calculate the reaction kinetics. The reaction kinetics are parameters used by the Arrhenius equation (Equation (2.23)) to model the degradation of a material. There are three reaction kinetics: activation energy (E_a), pre-exponential factor (A) and the reaction order (n). Several studies have been published, which outline different methods to determine these parameters from the TGA results [106, 107, 105, 108]. Care needs to be taken to choose the correct method, as different methods make different assumptions, which might not be relevant for the degradation under investigation e.g. the ASTM E-1641 assumes first order kinetics [108, 106]. Methods to determine each reaction kinetic are now considered in turn.

(i) Activation Energy

The activation energy (E_a) defines the amount of energy which must be overcome in order for a reaction to occur. There are several methods which can be used to determine the activation energy [106, 107, 109]. For this study, the method outlined by Kissinger [107] will be considered. This method is chosen as it does not require knowledge of the reaction order whilst not assuming it to be 1. Using this method, the activation energy for a single stage reaction can be determined by

$$\frac{d\left(ln\frac{\beta}{T_m^2}\right)}{d\left(\frac{1}{T_m}\right)} = -\frac{E_a}{\Re} \tag{3.13}$$

The complete derivation for this method is outlined in [107].

(ii) Reaction Order

The reaction order defines how the concentration (mass) of the decomposing material affects the reaction rate. There are several different forms which the reaction order can take [103]. For the typical epoxies used within composite materials, it is generally assumed that an nth reaction order can define the reaction kinetics accurately [50]. An nth reaction order is implemented into the Arrhenius equation as shown in Equation (2.23). A method for determining the nth reaction order has been proposed by Kissinger [107]. It has been shown that this method is only valid if the topology of the reaction rate is independent of heating rate and when the reaction kinetics (E_a and A) are constant [107]. If these are true, the reaction order can be determined by considering the degree of symmetry in the reaction rate around T_m. The symmetry of the reaction rate is defined by the shape index S, which is given by

$$S = \left| \frac{\frac{d^2\Gamma}{dt^2}|_1}{\frac{d^2\Gamma}{dt^2}|_2} \right| \tag{3.14}$$

Where the index 1 and 2 on the nominator and denominator refer to the left and right hand side of the reaction peak, respectively. This is quantitatively determined by considering the reaction rate gradient on either side of the peak reaction rate [107]. A representative example of this is given in Figure 3.6

The reaction order can then be determined from the shape index by use of

$$n = 1.26\sqrt{S} \tag{3.15}$$

(iii) Pre-exponential Factor

The final reaction kinetic to consider is the pre-exponential factor (A). This parameter

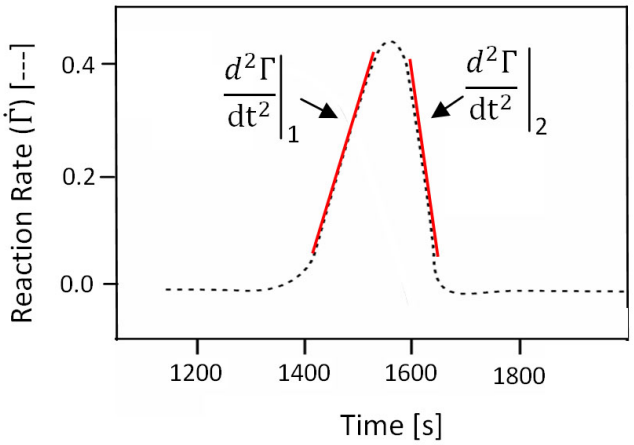

FIGURE 3.6: Slope of reaction rate to determine the reaction order

is used to define the rate at which the reaction occurs. In the study by Kissinger [107], they showed that given the activation energy (E_A) and the reaction order (n), the pre-exponential factor (A) can be determined by

$$A = \frac{\frac{E_a \beta}{\Re T_m^2}}{\left[1 + (n-1)\frac{2\Re T_m}{E_a}\right] e^{-\frac{E_a}{\Re T_m}}} \tag{3.16}$$

3.3.1.2 Previous TGA Studies

TGA is a well document experimental technique for determining the reaction kinetics of degrading polymers [109, 110], polymer based composites [111, 112, 113] and specifically CFCs [12]. It is evident from these studies that there is a wide variety of different polymers and epoxies, which each have very different reaction kinetics. These reaction kinetics can be used to describe the polymer pyrolysis.

The most notable TGA studies which considered similar composite systems were conducted by F. Ulhig [12] and T. Ogasawara [49]. The TGA experimental results presented in [12] had a temperature range of 297 K to 1273 K, with the majority of the polymer pyrolysis occurring between 570 K and 773 K. The TGA results given in [49] were conducted from 293 K to 1073 K, with the majority of the degradation occurring between 680 K and 780 K. Whilst the TGA results presented by T. Ogasawara [49] were used to calculate the reaction kinetics, there was no attempt by F. Ulhig [12], to determine the reaction kinetics. Instead the TGA results presented by F. Ulhig [12] were only used to indicate the temperature range over which the degradation occurred and to consider how much char was produced by the degradation. Despite this, F. Uhlig did reach some very interesting conclusions, which will be used to aid this study. F. Uhlig showed that for slow heating rates, 5 $K\text{min}^{-1}$, in an air atmosphere, the oxygen which is present

leads to secondary reactions occurring with the char based pyrolysis by-products. He then later showed that as the heating rate is increased to 60 $K\text{min}^{-1}$, these secondary reactions become less noticeable. The study concluded that this is due to the slow reaction kinetics which were driving the oxygen based reactions not having sufficient time to occur. The study then conducted the same experiments in a nitrogen rich atmosphere for both a slow heating rate, 5 $K\text{min}^{-1}$, and a high heating rate, 60 $K\text{min}^{-1}$. Both these experiments gave very similar results to that of the higher heating rate experiment conducted in an air atmosphere. They concluded that this similarity was due to the lack of oxygen to cause the secondary reactions, and so the degradation witnessed is solely due to the polymer pyrolysis.

3.3.1.3 TGA Experimental Methodology

Based on the conclusions from previous studies, the experimental methodology conducted within this study can now be outlined. CFC samples are obtained by following the procedure outlined in ection 3.1.1, and are then placed in open crucibles and put in the TGA. By assuming that the degradation properties for M21/T700 are comparable to those epoxies considered in the studies presented by S. Montserrat [114], F. Ulhig [12] and T. Ogasawara [49], the TGA experiments for this study are conducted from 297 K to 1073 K. This temperature range is chosen, as based on the previous studies, it should encompass the entire pyrolysis. Once the sample has reached 1073 K, they are then cooled back to room temperature whilst continuing to record the mass of the sample. This is done to check that there are no temperature reversible reactions occurring within the CFC samples.

The available TGA equipment is not able to obtain the high heating rates associated with a lightning strike. Therefore, based on the conclusion of the study by F. Uhlig [12], the experiments conducted here are done under a nitrogen rich atmosphere at lower heating rates. The TGA experiments are repeated for a series of heating rates. This is required to determine the reaction kinetics as discussed in Section 3.3.1.1.

3.3.2 Differential Scanning Calorimetry

As well as the reaction kinetics, the numerical model also requires the change in enthalpy due to the reaction (Q_d). This parameter is used to couple the chemical degradation with the internal energy. A commonly used experimental technique to determine this parameter is Differential Scanning Calorimetry (DSC). DSC studies have been considered in previous investigations [115, 116, 12].

3.3.2.1 Experimental Methodology

Based on these previous investigations, the DSC experimental methodology conducted is as follows. CFC Samples are obtained, by following the procedure outlined in Section 3.1.1. These samples are then placed within an aluminium crucible and sealed with an aluminium lid. A second identical empty crucible is then also sealed, this is to be used as a reference crucible. These two crucibles are then placed upon two independent heating elements. The two crucibles are then heated independently, so that they both achieve a predefined constant rate of temperature increase. For both containers to achieve the same required rate of temperature increase, the crucible containing the sample, requires a different heat flux to that of the empty crucible. It is this difference in heat flux which is recorded. The DSC trace for a sample of indium taken from the experimental set-up used in this study is shown in Figure 3.7.

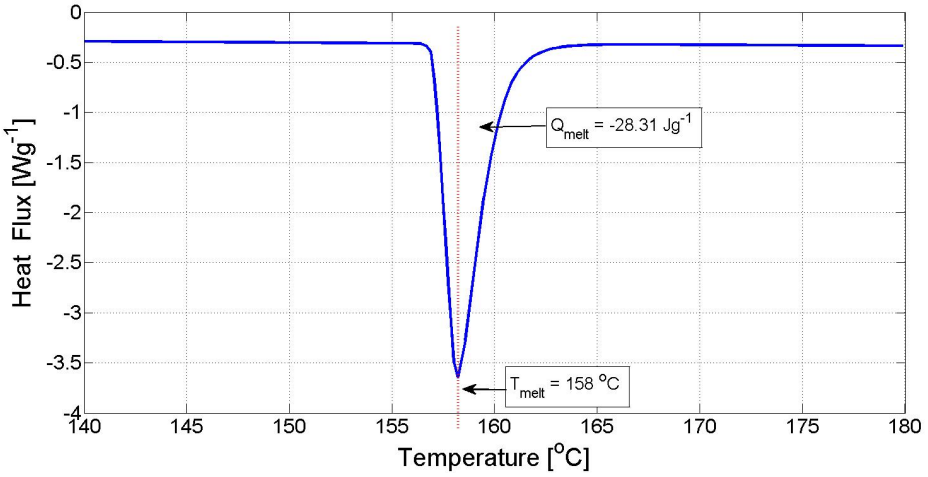

FIGURE 3.7: Differential Scanning Calorimetry result for sample of Indium

As the sample undergoes degradation or a phase change, either heat is expelled (exothermic reaction) or absorbed (endothermic reaction or phase change) by the sample under test. This further changes the heat flux required to maintain the constant heating rate within the crucible which contains the sample. The difference in heat flux from the reaction leads to a peak or dip occurring within the DSC trace. By considering the difference in heat flux for the indium sample, shown in Figure 3.7, there is a dip occurring at 158 $^{\circ}C$. By integrating the area of this peak, the latent heat of fusion can be calculated to be $Q_{melt} = 28.31\, Jg^{-1}$. It is known that this result is due to a melting phase change. The accepted values for this phase change are that it occurs at $156.63^{\circ}C$ and $Q_{melt} = 28.53\, Jg^{-1}$ [117]. Due to the good agreement between these results, it can be stated that the experimental set-up used for this study is working correctly and accurately. This experiment is repeated for several samples so an average change in enthalpy can be obtained.

3.4 Experimental Damage

For this study, two experimental techniques will be used to damage pieces of CFC. The first is laser ablation and the second is lightning strike current impulse tests. The lightning strike impulse tests are important, given the aim of this study is to investigate the damage caused to a piece of CFC due to a lightning strike. These experiments are conducted, as the aim is to compare these experimental results with the predictions from the bespoke thermo-chemical degradation model.

3.4.1 Laser Ablation

Laser ablation is a technique whereby a high power laser beam is irradiated onto the surface of a sample. The laser beam causes the sample to heat up and hence degrade. Laser ablation of composite materials has been widely documented previously [118, 119, 86, 120]. These papers considered laser drilling or cutting of CFC panels using short pulse lasers. In these studies, they describe two damage mechanisms; carbon fibre ablation and polymer degradation i.e. pyrolysis. This polymer pyrolysis can be likened to the polymer degradation caused by a lightning strike impulse test.

Laser ablation has been considered as it decouples the thermal effects from the electrical affects, and hence makes for a simpler set of physical damage mechanisms. Also, the thermal input from a laser beam can be very accurately controlled, which makes it an ideal experiment to try and verify the model against.

3.4.1.1 Experimental Methodology

The laser ablation experiment, is conducted using a 6 Watt pumped diode laser from Coherent [121]. This laser was operated in (0,0), which produces a Gaussian beam as its output, with a beam radius (Λ) of 1.125 mm. The beam has a wavelength of 532 nm and a divergence of less than 0.5 $mrad$. The sample of CFC was placed in the laser beam at a distance of 0.75 m away from the output port. No lenses were used to focus the beam, but given this distance, it is reasonable to assume that there is minimal beam divergence, and so it can be further assumed that the sample is irradiate with the same Gaussian beam, as that which left the laser's output port. The samples were placed on a 3-axis optical stage, which allowed the position of the sample to be adjusted and aim accurately the laser onto the middle of the sample surface. Having the beam aimed at the centre of the sample means the edges are equidistant from the peak heat flux so that the damage should be symmetrical. The CFC was irradiated for a predefined time duration. After each ablation, the sample is moved before irradiating the sample again at a new undamaged location for a new ablation duration. The distance between the laser ablation regions was kept large enough to avoid any effects being

caused by neighbouring damaged regions. To keep the laser beam from moving during the ablation experiment, the experimental apparatus is mounted on an optical bench. As a precautionary measure the experiment was conducted with an extractor fan placed just above the samples. This was used to extract any harmful gases which might be produced due to the polymer pyrolysis.

3.4.2 Lightning Strike Current Impulse Experiments

The lightning strike impulse tests were conducted at Cobham in UK and at the Morgan-Botti Lightning Laboratory in Cardiff. Before considering the experimental methodology used for the lightning strike current impulse tests, it is first necessary to discuss how the lightning strike current impulses are generated. However, before this, a brief precis on previous lightning strike current impulse tests is given.

3.4.2.1 Previous Lightning Strike Experiments

Whilst this type of experimental study is not new and a collection of similar previous studies has already been discussed in Section 2.3 [45], there is no published record of any lightning strike tests being conducted on a carbon fibre composite materials constructed from M21/T700s. The type of CFCs used in these previous experiments is not important, as the aim for this study is not to compare the experimental results, but instead use these previous studies to help direct the study conducted here.

All published lightning strike current impulse studies have been conducted on small test panels, rather than on full size aircraft structures [122, 13, 123, 124, 45]. This is because the same information can be gained from the small test panels, as that of damaging a small region on an entire CFC aircraft. The benefit of using these small panels is that they are much cheaper to make, and also given their small dimensions much easier to handle [9].

The studies by Y. Hirano [122], and G. Reid [124, 45] considered the damage caused due to component A and also for component C in G. Reid's studies. These studies were both conducted for different types of quasi-isotropic CFC materials. Y. Hirano et al. [122] showed that there was minimal variation in damage dimensions as the panel thickness was varied. This implies that the majority of the thermal/electrical affects occur within the top few plies. These studies also demonstrated that there appears to be a linear increase in damage depth and area as the charge transfer for component C and the action integral for component A are increased.

Whilst the primary aim for these current impulse tests is to investigate the damage caused by a current injection, the following specific questions will be investigated:

- How does the damage caused by the different lightning strike current impulses differ?
- How does the damage caused by a combination of lightning strike impulses compare with the damage cause by the separate components?

These questions have arisen based on the conclusion from the results presented in the previous studies.

3.4.2.2 Lightning Strike Generator

The large currents, required for a lightning strike impulse are generated using surge generators. These comprise of a series of large capacitors, connected in parallel, as shown in Figure 3.8.

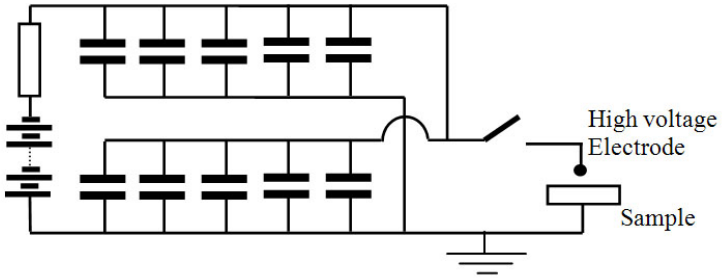

FIGURE 3.8: Circuit diagram for a generic surge generator. Circuit diagram modified from [9]

The sample under test, with dimensions L_x, L_y and L_z, is placed between two metal plates. These two plates are held together by a series of metallic bolts. The bolts are tightened to secure the test panel in place during testing. The bottom of these two plates is directly connected to ground, and through the metallic bolts, the top plate is also indirectly connected to ground. These metal plates provide the only connection to ground for the sample which is under test. This results in two small grounding regions on the top and bottom surfaces on the sample. This is illustrated in Figure 3.9 and Figure 3.10

A high voltage electrode, connected to the surge generator, is positioned 100 mm above the surface of the sample, as shown in Figure 3.10. Screwed onto the end of the high voltage electrode is a jet diverter. The jet diverter is a nylon ball with a diameter of 2.5 cm. This is used to direct the ejected particles from the formation of the electric arc away from the samples test surface. To help direct the arc attachment to a specific point on the CFC surface, a fine metallic fuse wire, with a diameter of 0.1 mm, is used [34]. This is wrapped around the high voltage electrode just above the jet diverter and is then fixed to the surface of the sample with a small piece of insulating tape. A lightning

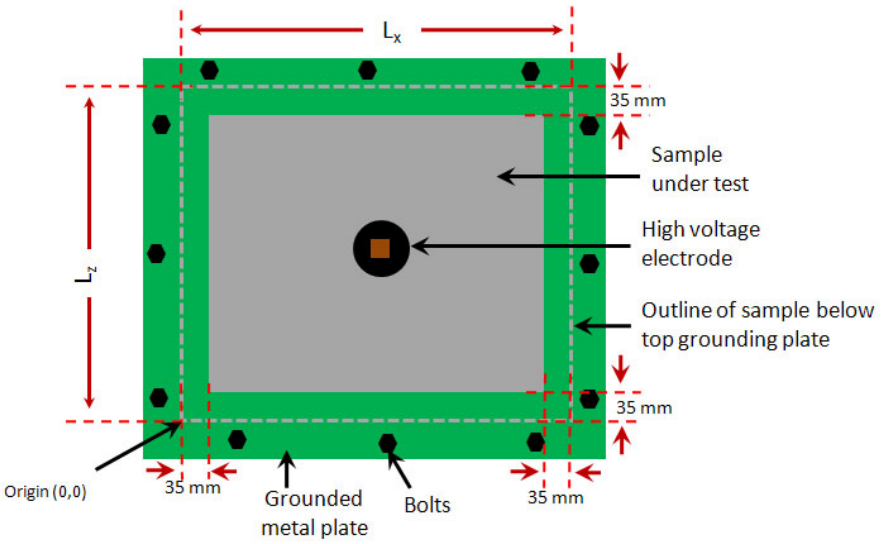

FIGURE 3.9: A top down view diagram which summaries the experimental.

strike arc is known to wander around the surface [9]. To help confine the arc to a region on the samples surface, a plastic insulating mask is placed around the region of interest. The masked region is formed by placing sheets of plastic around the fuse wire. The size of the masked region varies for the different current impulses. There is no standard size for the mask for each current component, and the size of the masked region is normally left down to the experimenters experience. Whilst there is no problem with having the mask too large, if the masked region is too small, the arc is likely to avoid the test panel and connect straight to the ground electrode and not damage the sample under test. As a rough guide for these experiments, the mask has dimensions of 9 cm by 9 cm for component D and 2 cm by 2 cm for component C.

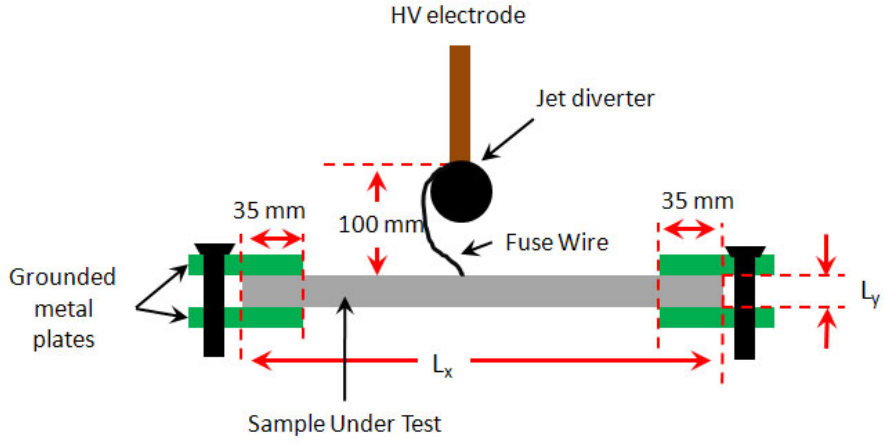

FIGURE 3.10: Cross section view of the experimental set-up

To generate the current impulse, the capacitor banks are charged up using a high voltage power supply. When the capacitors are charged and with the test sample placed in the sample holder correctly, the switch shown in Figure 3.8 is then closed. This creates a high

current arc to form from the high voltage electrode. Due to the sample's connection to ground, its proximity to the electrode and the fuse wire, the arc attaches to the sample's surface. This allows the capacitors to discharge through the sample to ground.

The shape of the discharge current is a function of the circuit design. To generate the correct double exponential current waveform, as defined for a lightning strike by ED-84 [11], the inductance and resistance of the experimental circuit need to be carefully controlled. As an example, the peak current delivered by the surge generator is dependent on the circuits internal inductance [9], with the lower the internal inductance, the larger the peak current. There are a variety of different circuit techniques to improve the relationship between the theoretical current profile, as given by ED-84, and the experimental observed current profile from the surge generator. A discussion on the different methods is presented in [9].

3.4.2.3 Experimental Method

Based on the previous lightning strike tests and the available experimental equipment, the following experimental methodology was conducted. The dimensions of the CFC panels required by this experimental set-up are $L_x = 530\,mm$, $L_z = 530\,mm$. For this experimental study, the following lightning strike components were available: D, B and C^*. Component D is a reduced form of the initial return stroke i.e. component A, and is typically used to represent a subsequent return stroke [11]. Current impulse B is the intermediate current and component C^* is a reduced form of component C.

The CFC panels are damaged at 6 different locations, with each location being damaged by a different lightning strike. The 6 different regions were damaged separately, and the panel was then left for 5-10 minutes before conducting the next lightning strike impulse. The duration between subsequent lightning strikes was set to allow the panels to return back to an ambient temperature. The damage locations are illustrated in Figure 3.11 with the exact coordinates defined in Table 3.1. These damaged locations were defined to be far enough away from other damage locations to avoid any interaction with previous damaged locations.

The quoted positions given in Table 3.1 are based on having placed the origin in the bottom left corner of the panel as shown in Figure 3.11.

Current component	Position (x,y) $[mm]$
D	400,425
$D^{\dagger}$	150,425
B	150,275
C^*	150,150
$D + B + C^*$	275,275
$B + C^*$	400,150

TABLE 3.1: Positions of the different damage locations are given above

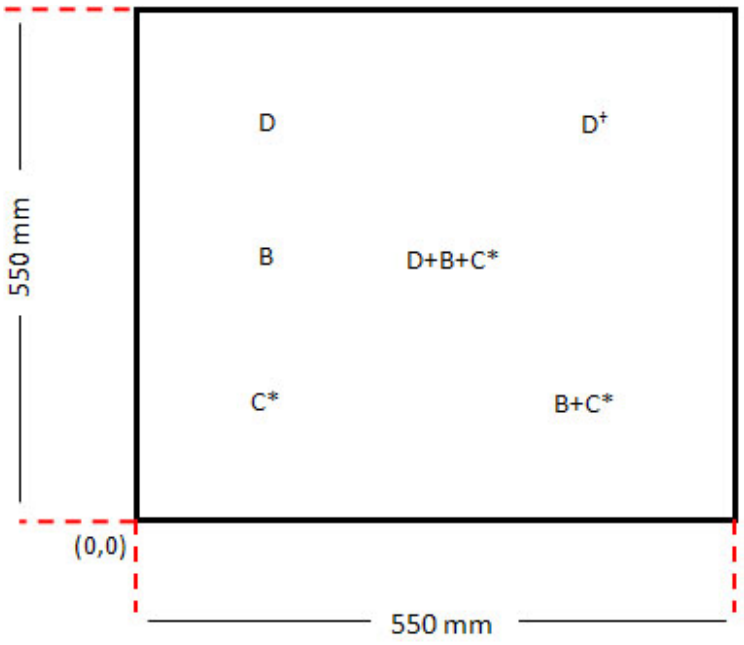

FIGURE 3.11: Lightning strike locations for each CFC panel

Whilst the discharge profile of the current impulse is carefully defined by the corresponding standards, there is still a chaotic aspect to a current impulse arc, due in part to the arc wandering. Therefore, to negate these random fluctuations, this experiment has been conducted with three different panels, so that a set of average damage dimensions can be obtained.

The measured current waveforms from the experimental study at Cobham, for component D and C^*, are shown in Figure 3.12. The experimentally produced current impulse for component D, B and C^* are in accordance with the current profiles outlined in ED-84 [11]. This can be shown by comparing the action integral for component D and the total charge transfer for component B, measured from the experimental set-up, shown in Table 3.2, with the values quoted in ED-84 which have been previously discussed in Section 2.2.3.1. The current impulse for component C^* is defined by ED-84 as a square wave. Experimentally, it is not possible to produce a perfect square wave with such a large current output, and so the current waveform shows a slightly decreasing current over time. As a result, ED-84 [11] defines a total charge transfer for the current component. The measured total charge transfer for component C^* generated for this experiment is shown in Table 3.2, and the current profile is shown in Figure 3.12(b).

Current component	Peak Current [kA]	Action Integral $[MA^2s^{-1}]$	Total Charge Transfer [C]
D	102	0.25	N/A
$D^\dagger$	85	0.19	N/A
B	3.6	N/A	9.5
C^*	N/A	N/A	17.7

TABLE 3.2: Measured current impulse parameters from the experimental set-up

The additional D component given by $D^{\dagger}$, corresponds to a D current impulse conducted at the lightning laboratory in Cardiff. Table 3.2 shows that $D^{\dagger}$ has a lower action integral than component D, and so there should be less damaged caused by this current impulse, than the D component conducted at Cobham.

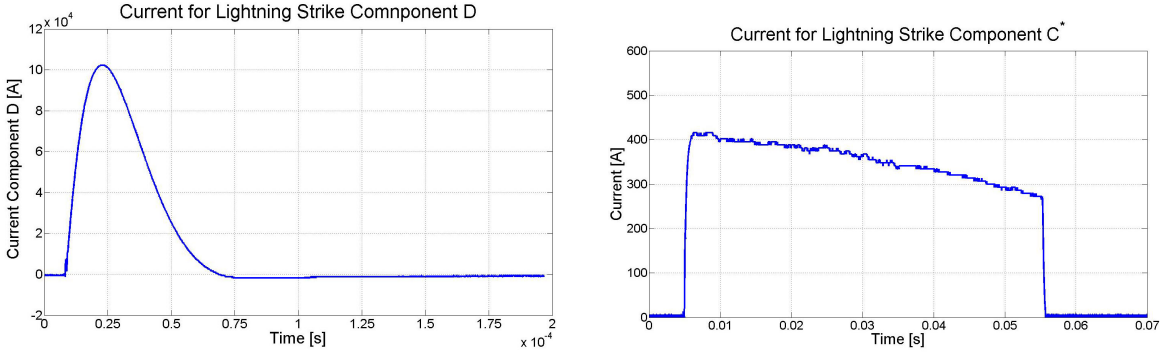

(a) (b)

FIGURE 3.12: Experimentally measured lightning strike current for a) Component D b) Component C^* from Cobham

As well as being able to damage a sample using each separate current waveform, it is also possible to conduct experiments using a combination of current waveforms. The combination of different components allows for an investigation to determine if the damage caused by a lightning strike is a correlated sum of damage caused by each of the separate lightning strike components. The combinations chosen for this experimental study were $B + C^*$ and $D + B + C^*$.

3.5 Damage Characterisation

Once the CFC samples have been damaged, either by laser ablation or by a current impulse test, they need to be investigated to determine the spatial extent of the damage. The following methods have been considered, Visual inspection, X-ray tomography and Ultrasonic C-scan. Each of these methods is now considered in detail.

3.5.1 Visual inspection

From the visual inspection, it is possible to determine the extent of the damage on the surface of the sample. This includes determining to what extent the carbon fibres have been lifted up and also if there has been any fibre or polymer degradation. This method is, however, unable to investigate the extent of the internal damage caused to the sample.

3.5.2 X-ray Tomography

By using X-ray tomography, it is possible to investigate the internal damage caused to a sample. The basic principles behind X-ray tomography are relativity simple and a simplified example of the experimental set-up is shown in Figure 3.13 [125]. X-ray tomography is a technique where an X-ray beam is directed at a sample. The resultant X-ray beam which has passed through the sample is then recorded by a detector. Due to the different densities contained within a sample an image will appear on the detector comprising of light and dark regions. The denser a particular region of the material, the more of the X-ray source is absorbed by the sample, and so a darker region is formed. The sample is then rotated on a turntable by a small angle and another X-ray image is taken. This is repeated until the sample has been rotated through a complete 360 degrees of rotation. By recording the angular rotation of the sample, it is then possible to manipulate all these images and reconstruct a 3D image of the sample. Using this reconstructed image, it is possible to investigate the internal structure of the sample.

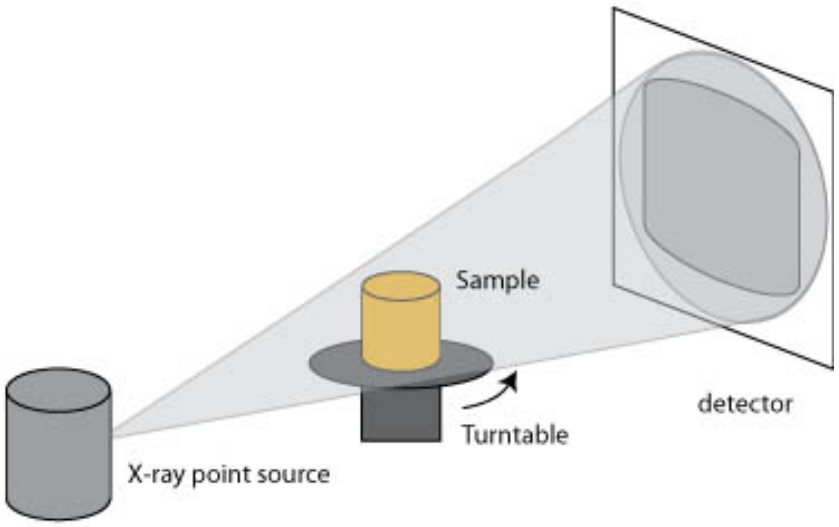

FIGURE 3.13: Illustration of X-ray tomography

The maximum resolution of the available experimental set-up is 1 μm. This resolution is, however, dependent on the largest dimension of the sample, which is being scanned and the number of pixels in the detector. Therefore, the larger the sample is, the lower the resolution will be [125].

3.5.3 Ultrasonic Inspection Technique

Another method which is able to investigate the internal damage of a sample is Ultrasonic inspection. Whilst a brief explanation of the physics behind ultrasonic c-scan technique is given here, a more exhaustive review of the technique is provided by The Non-Destructive Testing (NDT) Resource Centre [126] and by T. Hasiotis et al. [127]. The process starts

by placing the panel's damaged side down and placing the ultrasonic transducer on the undamaged top surface. A high frequency ultrasonic wave is then generated from a piezoelectric crystal with the transducer. The generated wave propagates through the sample under test. When the wave encounters a discontinuity, such as a crack or a void in the sample, part of the wave is reflected back. The magnitude of the reflected wave is related to a function of acoustical impedance on either side of the discontinuity. The reflected wave travels back through the sample towards the transducer. The time taken for the signal to leave and then return back to the transducer is measured. From the measured time, it is possible to calculate directly the undamaged thickness of the sample and, hence, as the undamaged sample thickness is known, it is then straightforward to determine the damage depth. This experimental set-up is summarised in Figure 3.14.

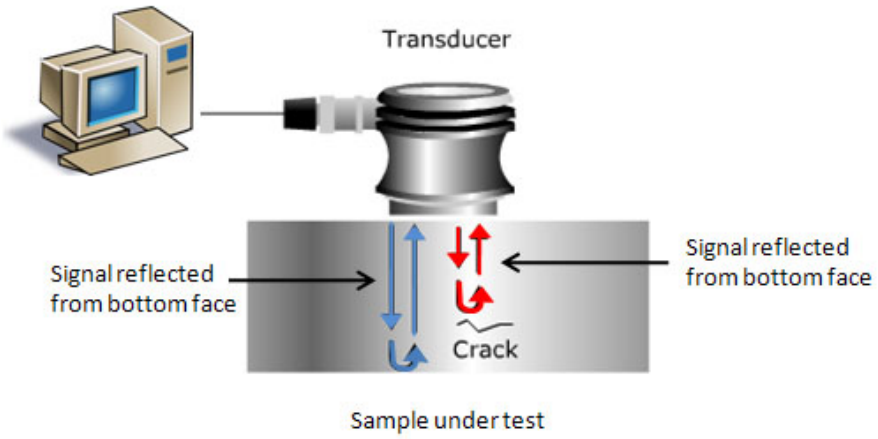

FIGURE 3.14: A diagram which illustrates how the ultrasonic c-scan experimental set-up. Image modified from [126]

The transducer is then moved across the surface of the sample taking regular measurements at different positions. By recording the position of each measurement, the internal damage of the entire sample can be mapped out. This method is, therefore, not able to generate a 3D image to investigate the internal structure of the damage. The surface spatial resolution of the available ultrasonic inspection equipment is $0.5\,mm$ [128]

3.5.4 Discussion of Damage Measurement Techniques

It is now important to consider how relevant these different methods are for investigating the damage caused by both the laser ablation and the lightning strike current impulse test.

All the damaged samples are initially examined using visual inspection. The laser ablated samples are then further investigated with X-ray tomography. X-ray tomography has been considered, as it is expected that the damage dimensions will be roughly comparable to that of the laser beam diameter ($2.25\,mm$). Therefore, these small damage

dimensions and the small size of the samples used makes X-ray tomography an ideal inspection tool for the laser ablated samples. The ultrasonic inspection technique will not be used here due to the small size of the laser ablation damage.

As the damage caused by the current impulse test is expected to be much larger, the damage on these panels is investigated by the ultra-sonic inspection technique. This inspection method has proven to be a very accurate and reliable for measuring the internal damage of composite panels [122, 13, 127]. This is because given the typical damage area for component D is 2000 mm^2 [45, 122], which is sufficient for the spatial resolution of the ultrasonic inspection method. X-ray tomography has not been considered, because due to the large panel dimensions (and damage dimensions), the resolution of the X-ray tomography would be reduced, to a level similar to that which can be achieved by the ultrasonic scan. Therefore, given the minimal extra information which would be gained by using this method, it was decided to only consider the ultrasonic inspection method for these panels.

3.6 Summary

A series of experimental techniques has been outlined to determine the electrical properties of CFCs. Within the above discussions, a selection of experimental methods have been identified along with their limitations. As a result, a potential divider network has been chosen to measure the through thickness impedance and the four probe method has been chosen to measure the in-plane electrical conductivity. Based on the models used to represent the thermo-chemical degradation of the CFC, a series of experimental techniques required to determine the reaction kinetics for the Arrhenius equation has been considered. These discussions have also outlined an experimental methodology, using conclusions from previous studies.

The final section of this chapter has described two experimental techniques to thermo-chemical damage samples of CFC. These techniques are lightning strike current impulse testing and laser ablation. To investigate the damaged samples, a series of non-destructive testing techniques has been considered along with the limitation and benefits of each approach.

Chapter 4

Material Properties of Carbon Fibre Composites

This chapter presents experimental results from a series of material characterisation experiments. The results from these experimental studies are required for the numerical models, which are discussed in later chapters. The accuracy of the material characterisation is important if the numerical predictions are to be accurately compared against the experimental studies. This chapter first presents results for the electrical properties for CFCs, before presenting the parameters required to model the thermo-chemical degradation process.

4.1 Electrical Properties - Background

As a lightning strike is principally an electrical phenomenon, it is important to understand the electrical properties of any material with which it might interact. This is of principal importance for CFCs, as it is believed that the Joule heating, which results from the injected current, is the dominant source of heat (Section 2.2.4.3). It is, therefore, important to understand how an electric current is distributed throughout a CFC panel.

The current impulse from a lightning strike is equivalent to a series of frequencies (Section 2.2.3.1). As a result, this discussion also needs to consider if there are any reactive effects within CFC panels, as these effects would influence the amount and rate of Joule heat released. Previous studies (Section 2.1.3.2), have demonstrated that short fibre CFC have an impedance which is independent of frequency below 500 kHz [28]. However, very little work has been published on investigating the electrical properties of long fibre (unidirectional or quasi-isotropic) CFCs. Therefore, to gain an understanding of the electrical properties within both unidirectional and quasi-isotropic CFCs, a series of

experimental studies have been conducted using the experimental techniques outlined in Section 3.2.1.1. Before considering any experimental results, the discussion first considers whether there are any skin depth effects which might occur within a piece of CFC due to a lightning strike. This is important as it is known that skin depth effects have a dominant effect within metals [129, 130].

4.1.1 Skin Depth

Skin depth demonstrates the ability for an alternating current to distribute itself through a material [129, 130] and implies that as the frequency increases, the effective cross section of the conductor is decreased, which in turn increases the effective resistance of the material. The skin depth (δ) for an isotropic material is defined by

$$\delta = \sqrt{\frac{2}{\sigma \omega \mu_m}} \tag{4.1}$$

where σ is the materials electrical conductivity, μ_m is the magnetic permeability and ω is the angular frequency. The magnetic permeability for a piece of CFC can be considered to be that of free space $4 \times 10^{-7} Hm^{-1}$. Given that skin depth effects dominate at high frequencies, it is important to consider the maximum frequency which occurs within the lightning strike current impulse. As stated in Figure 2.14, the majority of the dominant frequencies are below $200\,kHz$ [11].

Skin depth is typically considered for isotropic materials, but CFCs are highly anisotropic. As a result, the skin depth for CFCs is calculated for a range of electrical conductivities, which are given by the conductivities in the different principle directions. For this investigation, the electrical conductivities used are those presented by F. Uhlig [12] and shown in Figure 2.6 i.e. $\sigma_1 = 15.5 \times 10^3 Sm^{-1}$ and $\sigma_2 = \sigma_3 = 1\ Sm^{-1}$ at $25\ ^\circ C$ [12]. By considering the maximum frequency present with a lightning strike ($200\,kHz$) a skin depth of 16 mm and 2 m, are obtained for directions 1 and 2, respectively. As both these depths are greater than the typical thickness of a CFC panel (i.e, 5 mm), it suggests that there are negligible skin depth effects occurring within a piece of CFC during a lightning strike.

4.1.2 Electrical Impedance

The next aspect to consider is the impedance of CFCs as a function of frequency. This discussion is split into two sections. Firstly, experimental work is conducted to determine the impedance in the through thickness direction (direction 3). Using these results, an attempt is made to apply the short fibre equivalent circuit [28], as discussed in Section 2.1.3.2, to the long fibre CFCs results obtained here. The second half of this section considers the electrical impedance along the two remaining directions (1 and 2).

The discussion begins with direction 3 because it is believed that this direction is the most affected by the dielectric polymer between the fibres, as seen in Figure 2.21. Therefore, if the impedance is independent of frequency (i.e. no reactive effects) in this direction, it can be assumed that the impedance is frequency independent in the remaining two directions.

4.1.3 Electrical Impedance - Direction 3

The experimental study to determine the impedance in direction 3 has been conducted following the AC potential divider network and experimental methodology outlined in Section 3.2.1.3.

4.1.3.1 Samples

This experiment was conducted for two different samples, a unidirectional CFC sample and a quasi-isotropic CFC sample. Both these samples have been prepared as outlined in Section 3.1.1. The dimensions of the unidirectional panel is $113\,mm$ x $116\,mm$ x $4\,mm$ and the dimensions of the quasi-isotropic panel is $112\,mm$ x $114\,mm$ x $5.2\,mm$. After each experimental trial, the CFC samples are removed from the electrodes and turned over before being placed back in between the electrodes i.e. each sample is tested more than once.

4.1.3.2 Experimental Results - Impedance in Direction 3

With the potential divider circuit set-up, the signal generator was set to produce a $3\,V$ peak-to-peak signal. A selection of raw results from this experiment, taken at different frequencies, recorded by the oscilloscope, are shown in Appendix B. The phase angle (θ) and the impedance magnitude ($|Z|$) for the quasi-isotropic panel are shown in Figure 4.1 and Figure 4.2, respectively. The results for each of the 3 trials shows a good repeatability with only a small spread between results. The results show that over the given frequency range there is no change in impedance magnitude and that the phase angle is zero. This implies that within this frequency range, there are no reactive effects within a quasi-isotropic piece of CFC. Therefore, a quasi-isotropic piece of CFC can be treated as a pure resistor up to $10\,kHz$. This result implies that the electrical impedance of CFCs is dominated by fibre to fibre contacts within this frequency range.

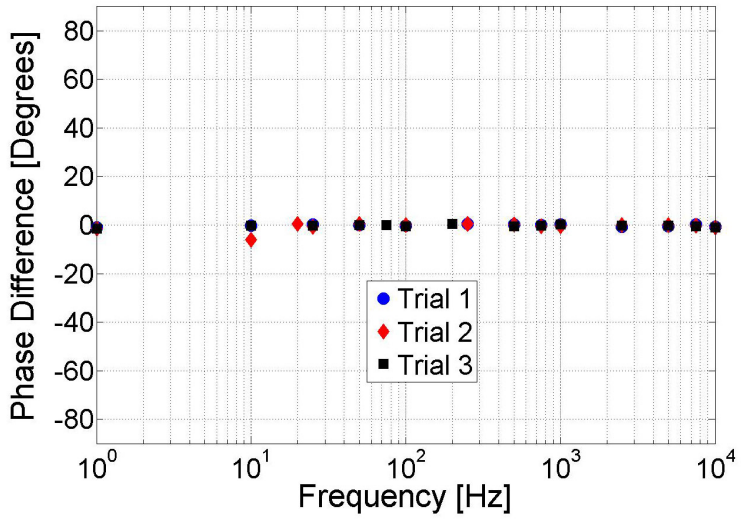

FIGURE 4.1: Phase angle for a quasi-isotropic piece of CFC as a function of frequency

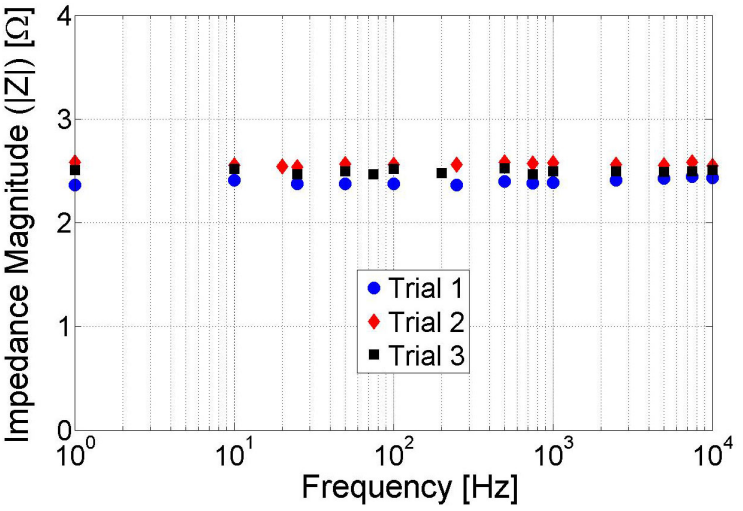

FIGURE 4.2: Impedance magnitude for a quasi-isotropic piece of CFC as a function of frequency

Using the same experimental set-up as above, with now a unidirectional CFC sample, the signal generator was set to produce a 10 V peak-to-peak signal. A selection of raw results from this experiment, taken at different frequencies, recorded by the oscilloscope, are shown in Appendix B. The phase angle (θ) and the impedance magnitude ($|Z|$) for this unidirectional panel are shown in Figure 4.3 and Figure 4.4, respectively. The unidirectional panel shows a constant impedance magnitude up to 1 kHz. At higher frequencies, there is a slight increase in phase angle as the frequency approaches 10 kHz. This implies that for a unidirectional CFC panel, the fibre to fibre contacts dominates the electrical properties up to 1 kHz, and above this, there are slight reactive affects. From the magnitude of the phase angle, these reactive effects are believed to be inductive.

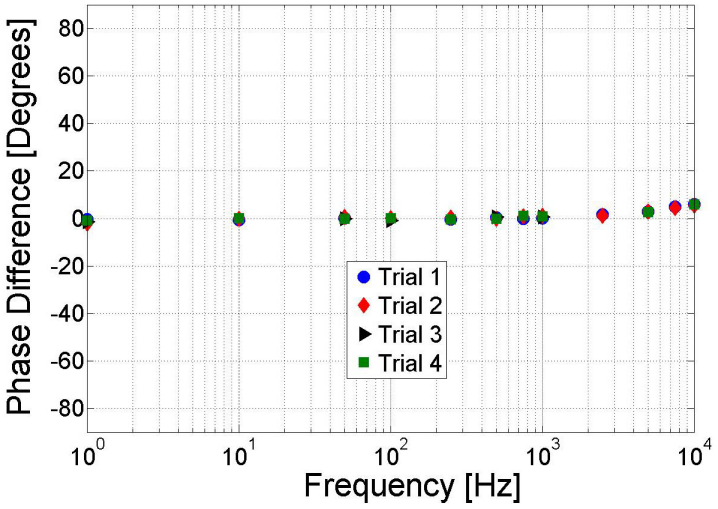

FIGURE 4.3: Phase angle for an unidirectional piece of CFC as a function of frequency

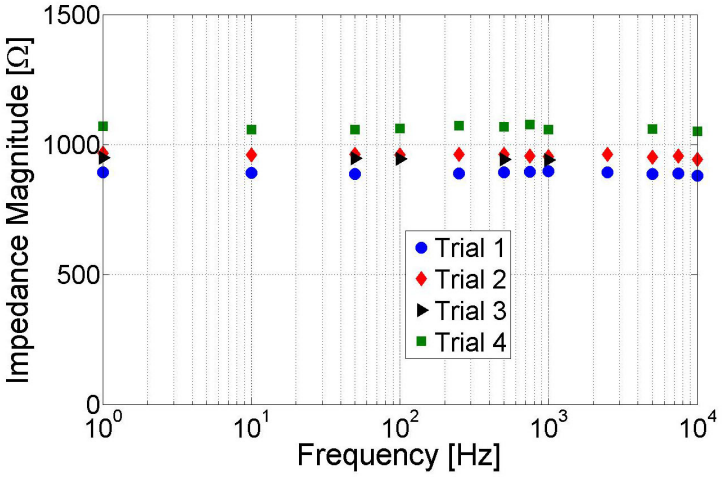

FIGURE 4.4: Impedance magnitude for an unidirectional piece of CFC as a function of frequency

4.1.3.3 Electrical Conductivity in Direction 3

The results presented above show that the impedance is constant with frequency below $10kHz$ for the quasi-isotropic panel and below $1\,kHz$ for the unidirectional panel. Furthermore, it has also been demonstrated in Section 4.1.1 that there are no skin depth effects occurring within CFCs. Therefore, within these frequency ranges, the impedance magnitude can be directly equated to the bulk resistance for each CFC sample. From this conclusion, the bulk electrical conductivity of each sample can be calculated from Equation (3.2), where the resistance (R) is replaced by the impedance magnitude ($|Z|$).

To obtain a more accurate bulk conductivity, the impedance magnitude at each frequency can be averaged together to determine an average bulk conductivity. The aver-

aged bulk electrical conductivity along direction 3 for the quasi-isotropic panel and the unidirectional panel are $0.96 \pm 0.03\ Sm^{-1}$ and $2.08 \pm 0.14 \times 10^{-3}\ Sm^{-1}$, respectively.

4.1.3.4 Equivalent Circuit

As mentioned in Section 2.1.3.2, a previous attempt has been made to derive an equivalent circuit which can explain the impedance results obtained for a short fibre composite material [28]. The results presented for the quasi-isotropic panel show no signs of any reactive effects occurring within the given frequency range. It is, therefore, not possible to fit this equivalent circuit to these results.

The results presented for the unidirectional panel on the other hand, do show a slight variation in phase angle, which could account for the initial stages of an inductive effect. However, the increase in phase angle is relatively small and so a further study with higher frequencies is required before this equivalent circuit can be realistically applied to these results.

Therefore, given the frequency limitation of the experimental set-up, there is not sufficient evidence to state conclusively if this equivalent circuit can or cannot be applied to long fibre CFCs. A series of future experiments with a higher frequency range is required to investigate fully the application of this equivalent circuit to long fibre composites.

4.1.3.5 Discussion on Through Thickness Impedance Results

The experimental results presented above show good repeatability with minimal scatter between the experimental trials. The systematic errors highlighted in Section 3.2.1.2 have been addressed, with efforts made to minimise them. Therefore, these results are believed reliable. There is, however, a noticeable discrepancy between the results for the two different types of CFC panel. This is shown by the impedance magnitude for the unidirectional panel being 3 orders of magnitude greater, than that of the quasi-isotropic panel. Also, there is a slight increase in phase angle for the unidirectional panel, as the applied frequency approaches $10\,kHz$, which was not seen with the quasi-isotropic panel.

The inductance affects observed at high frequencies, could be caused by the wires within the experimental circuit. The possible inductance affects created by the wires, was highlighted in Section 3.2.1.2, with attempts then made to this source of error by using short shield wires. This does not totally remove the possibility of mutual inductance, and so, if this experiment were to be conducted again, an extra third channel would be included to measure the voltage profile across the sample. With the voltage profiles across, the sample, the known resistor and signal generator, it is possible to split the sample impedance from the any inductive affects produced within the wires.

Remembering that the constituent components of both CFC panels are the same, the following reasons could also explain the difference in the results. The different fibre arrangement could affect the results, as it could alter the number of fibre to fibre contacts within the panel. This could occur because in the quasi-isotropic panel the fibres are not all parallel, and so a single fibre could pass over many fibres, whereas within the unidirectional panel the fibres are all parallel to each other and so they can only touch the fibres above and below themselves. Therefore, a quasi-isotropic panel could have more fibre to fibre contacts and a more uniform distribution of current. Furthermore, the increase in fibre contacts can also explain the 3 orders of magnitude difference between the impedance magnitudes, by considering percolation effects, as discussed in Section 2.5.5. Percolation theory states that if the volume fraction of conductive medium is close to the percolation threshold, then a small increase in volume fraction will result in a large increase in conductivity. It has already been shown that for CFCs, the fibre volume fraction is around the theoretical percolation threshold, and so any small increase in the number of fibre to fibre contacts, could cause this large variation in impedance magnitude. The different fibre layout, could also explain the noticeable increase in phase angle by two explanations. Firstly, if the resistance of the panel is lower, then the capacitive effects will not affect the conduction until higher frequencies. Secondly, inductive effects could be caused by parallel conductors with a dielectric in between. Therefore, the fewer parallel conductors in the quasi-isotropic panel would reduce these inductive affects.

Despite careful sample preparation, the difference between the experiments could be as a result of the contact resistance between the two samples being different. Whilst every effort was made to reduce this possible error, the error could still remain.

Before concluding on what could have caused these differences, these results are compared against results presented by F. Uhlig [12] and Y. Hirano [122]. The bulk conductivity in the through thickness direction presented by F. Uhlig for a sanded quasi-isotropic panel of T300/1914 was 11 Sm^{-1}. In the study presented by Y. Hirano et al. [122], they showed that for CFC IM600/133, the through thickness electrical conductivity was $1.8 \times 10^{-3} Sm^{-1}$. The low value of through thickness electrical conductivity presented by Hirano, was put down to the thicker polymer layer which is present in the aerospace grade CFC which they were investigating. The bulk conductivity from the quasi-isotropic panel obtained in this study, is one order of magnitude less than that obtained by [12], whilst the unidirectional bulk conductivity is 3 orders of magnitude less. However, interestingly the unidirectional bulk conductivity results do agree well with the results presented in [122]. A slight difference in conductivity is expected as these experimental results are for a different composite material. The lower bulk conductivity presented in [122] was put down to a thin polymer layer between each ply. Therefore, the difference in conductivity between the two samples is believed to be due to a difference in fibre to fibre contacts due to a combination of fibre layout and a possible increase in

polymer gap between the plies.

Despite the difference in the results and the possible reasons for this differences, both the unidirectional panel and the quasi-isotropic sample displayed no capacitive or inductive affects below 1 kHz and 10 kHz, respectively, hence it is possible to treat CFC as a pure resistor within this frequency range. This implies that the fibre to fibre contacts dominate the electrical conduction within the CFC along direction 3 below 10 kHz.

4.1.4 Electrical Properties - Direction 1 and 2

Having considered the electrical properties in direction 3, the next aspect to consider is the electrical impedance in the two remaining directions. This investigation is simplified by the results from the previous section i.e. CFCs can be treated as a pure resistor. As a result, these experiments can be conducted under DC conditions rather than the more complicated AC conditions. Hence, the purpose of these experiments is to measure only the bulk conductivity. Therefore, for these experiments the four probe method, as outlined in Section 3.2.2.1, is considered.

4.1.4.1 Samples

To determine the bulk conductivity along directions 1 and 2, two separate experiments are conducted using the four probe method. These two experiments are termed 'Direction 1' for determining the bulk conductivity along direction 1 and 'Direction 2' for determining the conductivity along direction 2. The difference between these experiments is solely due to the samples dimensions relative to the fibre direction.

For this experiment, only the unidirectional CFC panel is considered. The quasi-isotropic panel is not considered, as due to the fibre layup, it is not possible to measure the electrical conductivity along the principle directions 1 and 2. As stated previously, all the uncut surfaces have been sanded down to remove any thin polymer layers. The two types of samples used in this study are illustrated in Figure 4.5.

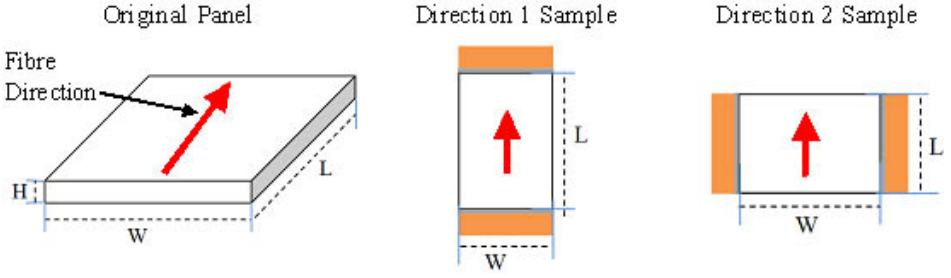

FIGURE 4.5: Illustration of the samples used in the two four probe experiments. The red arrow line indicates the fibre direction

For this study, one direction 1 panel was made with dimensions of 185 mm x 10 mm x 5 mm (L x W x H). For direction 2, three samples were made each with the same dimensions 9 mm x 100 mm x 5 mm (L x W x H). Notice that the bulk conductivity is always measured along the longest sample dimension. It was only possible to make one sample for the 'Direction 1' experiment due a limitation on the available material.

4.1.4.2 Results

The results for each of these experiments are considered separately below.

Direction 1

The four probe experiment was conducted 4 times with the sample described above. For this experiment, a potential difference was fixed at 0.355 V. During the experiment, the measured current varied from 0.88A to 0.98A. This variation in current can be explained by the heating up of the sample during the experiment which affects the conductivity.

The resultant potential difference between the measurement electrodes as a function of measurement electrode spacing (D) is shown in Figure 4.6. From Figure 4.6, it is evident that there is a uniform potential profile in the centre region of the sample and as the electrode spacing is initially increased. When the electrode spacing is greater than 0.1 m, the potential difference becomes non-uniform, as shown by the variation in the potential difference gradient. As stated in Section 3.2.2.1, the non-uniform potential profile near the interface with the electrodes is due to imperfections with the electrical contact. As a result the bulk conductivity is only considered when the electrode spacing is less than 0.1 m.

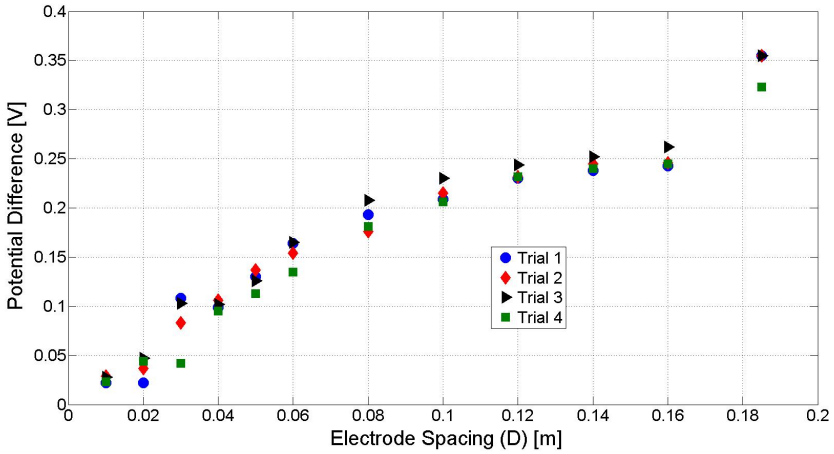

FIGURE 4.6: Potential difference as a function of electrode spacing along direction 1

By considering only the results in the uniform potential difference region and by considering Equation (3.10), the bulk electrical conductivity as a function of electrode spacing

can be calculated. Given the bulk conductivity is constant within this region, the average bulk conductivity for direction 1 can be calculated to be $7.32 \pm 0.8 \times 10^3\ Sm^{-1}$.

Direction 2

The four probe method along direction 2 was conducted 3 times for each of the three samples. For this experiment a constant potential difference of $5.35V$ was applied. Whilst the applied current remained constant for each sample throughout the experiment, there was a variation in applied current between the samples. The applied current for samples 1, 2 and 3 are $0.28\,mA$, $0.30\,mA$ and $0.16\,mA$, respectively. The variation in applied current is either due to the slight imperfections in the electrical contact between the electrode and the sample, or down to small variations within the CFC itself. The average measured potential difference for each of the samples as a function of measurement electrode spacing is shown in Figure 4.7. Figure 4.7 shows a near linear increase in potential difference as the measurement electrode spacing increases. From these results, it is evident that there is no sign of a non-uniform potential difference region, as was noticed for direction 1 (Figure 4.6). This is expected, because even if there are regions of poor electrical contact (between the electrode and the sample), having the principle direction of conductivity parallel to the electrodes, causes the applied potential to become uniform along the highly conductive fibres.

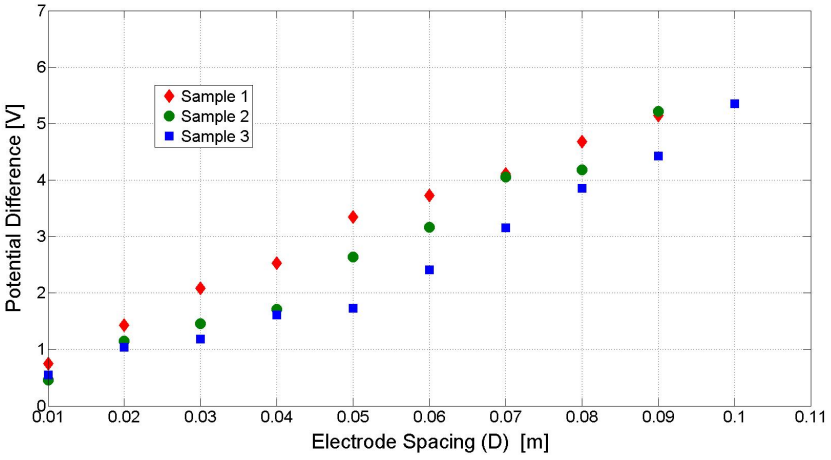

FIGURE 4.7: Potential difference as a function of electrode spacing along direction 2

The bulk electrical conductivity has been calculated by applying Equation (3.10) to the results presented in Figure 4.7 to be $0.100 \pm 0.008 Sm^{-1}$.

4.1.4.3 Bulk Conductivity Discussion

A series of experiments has been conducted to determine the bulk conductivity along directions 1 and 2. These experiments were conducted using the four probe method to reduce the impact of the contact resistance. The bulk conductivity along direction 1 is

$7.32 \pm 0.8 \times 10^3\, Sm^{-1}$ and the bulk conductivity along direction 2 is $0.100 \pm 0.008 Sm^{-1}$. The bulk conductivity along direction 1 is 4 orders of magnitude greater than the bulk conductivity along direction 2. This is expected due to the CFC layup and that the fibres have a much higher conductivity than the polymer.

The experimental results are believed to be reliable, as attempts have been made to minimise all the possible errors highlighted in Section 3.2.2.2. It was, however, noticed that the applied current did vary throughout the experiment to determine the conductivity in direction 1. This is believed to be caused by the thermal variation in electrical conductivity, due to the Joule heating caused by the relatively large current. Despite the variation in current, the variation in average bulk electrical conductivity for direction 1 is not significant. Due to the smaller current used in the direction 2 experiments, there was no evidence of heating. All the results are repeatable given the reasonably small scatter between the experimental results. To further reduce the effect of any scatter, each experiment has been repeated a number of times to calculate an average conductivity.

By considering the experimental measured σ_3 and σ_2 for the unidirectional panel, it is evident that there is a factor of 50 difference between these bulk conductivities. This difference is initially a surprise, given that the conduction in both directions 2 and 3 is believed to be dominated by fibre to fibre contacts. Therefore, if the fibres in both panels are evenly distributed, then the bulk conductivity in these directions should be similar. The difference in conductivity could be explained by a small polymer region in between the plies, which would reduce the number of fibre to fibre contacts between the plies.

Confidence in these results can be gained by comparing the measured values for σ_1 and σ_2 against previous experimental studies conducted by F. Uhlig [12] and Y. Hirano et al. [122]. The electrical conductivity presented by Y. Hirano for CFC IM600/133 are $\sigma_1 = 36 \times 10^3\, Sm^{-1}$ and $\sigma_2 = 1.15\, Sm^{-1}$. The bulk conductivity along direction 1 measure by F. Uhlig for T300/914 is between $15 - 17 \times 10^3\, Sm^{-1}$ (shown previously in Section 2.1.3.2). There was no attempt by F. Uhlig to measure the electrical conductivity in direction 2. By comparing these conductivities, there is a reasonable agreement between the studies. The differences in results can readily be explained by the different CFCs used in in each study.

4.1.5 Summary of Electrical Properties

A series of experiments has investigated the electrical properties for a unidirectional and a quasi-isotropic piece of CFC. The studies have shown that a piece of CFC can be treated as a pure resistor up to $1\, kHz$ for a unidirectional panel and $10\, kHz$ for a quasi-isotropic panel. Whilst it has not been possible to consider the entire frequency range of a lightning strike current impulse, it has been possible to consider the frequencies up to

the first break point. The results for both the unidirectional panel and the quasi-isotropic panel, indicate that there are minimal reactive effects up to this first break point. This implies that the current conduction is dominated by the fibre to fibre contacts and that the injected current leads solely to the Joule heating.

The electrical conductivities in the different directions have then been investigated. The experimental results for the unidirectional panel show that each principal direction has a unique electrical conductivity. The bulk electrical conductivity values agree well with previously published studies. This, combined with the efforts to address and minimise any possible sources of errors, allows to state that it is believed that the results presented here are accurate.

4.2 Polymer Degradation

As discussed in Chapter 2, when epoxies are exposed to high temperatures, they decompose. This decomposition can be numerically represented by the Arrhenius equation. In Chapter 2, experimental techniques were outlined to determine the required parameters to model accurately this decomposition. The results from these experimental studies are now presented.

4.2.1 Thermal Gravimetric Analysis

A thermal Gravimetric Analysis (TGA) study has been conducted following the experimental methodology outlined in Section 3.3.1.3.

4.2.1.1 TGA Samples

Following the experimental methodology outlined in Section 3.3.1.3, three samples were cut from a pristine piece of quasi-isotropic CFC. It is, therefore, worth emphasising that these samples also contain carbon fibres as well as epoxy. Each of these samples was then heated at a different heating rate (β). The initial mass and heating rate of each sample is contained within Table 4.1 .

Sample ID	Initial Mass [mg]	Heating Rate (β) [K/min]
CFC_5	14.56	5
CFC_{10}	7.48	10
CFC_{20}	9.93	20

Table 4.1: TGA sample details

4.2.1.2 Raw Experimental Results

As mentioned in Section 3.3.1, no meaningful comparisons can be gained by comparing the raw mass Vs. temperature graphs from the TGA, for each sample. Therefore, the fraction of remaining mass (Γ) is calculated using Equation (3.11) for each sample and is shown in Figure 4.8.

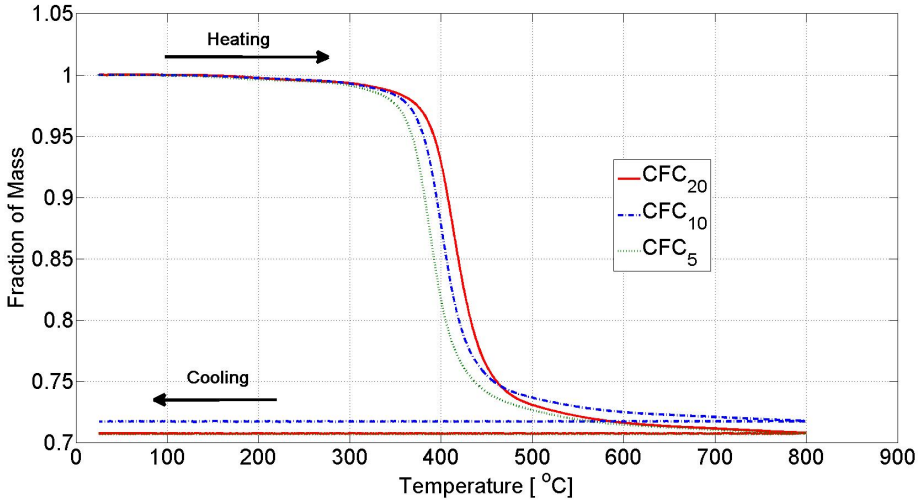

FIGURE 4.8: Comparison of the fraction of mass from the TGA experiment for M21/T700s

The results in Figure 4.8 show that the onset temperature for decomposition is around 300 $°C$ for each of the samples. For all the samples, the majority of the decomposition appears to have been completed by 500 $°C$. As the samples are cooled from 800 $°C$ back to room temperature, there is no change in the remaining fractional mass. This indicates that there are no temperature reversible reactions occurring.

The results for the different samples indicate that as the heating rate is increased, the onset temperature at which the decomposition begins is shifted to slightly higher temperatures. This is because, at any given temperature, the degree of decomposition is greater for a slower heating rate. Whilst the different fraction of mass profiles gives good agreement below $450°C$, there is a noticeable difference between CFC_{10} and the rest above this temperature. It appears that the final fraction of mass for CFC_{10} is slightly greater than for the other samples. This is most likely due to there being a slightly lower initial volume fraction of polymer within this sample. This probably occurred whilst the samples were being cut from the large CFC panel. The likely cause for this error is that some of the polymer around the edges of the sample may have crumbled away leaving fibres behind. This, therefore, affects the initial polymer volume fraction. Despite this, the main degradation region from 350 to $450°C$ fits well with the other profiles. Therefore, the discrepancy with CFC_{10} above 450 $°C$ should not have a great effect on the predicted degradation kinetics which are obtained from this data. The results in Figure 4.8 match the expected trends, as seen in other studies [49, 12], and so

these experimental results will be used to determine the reaction kinetics.

Before considering the reaction kinetics, it is first possible to obtain an indication for the fraction of gas and char which is produced by the pyrolysis. To do this, first the initial mass fraction of the carbon fibres within a piece of CFC needs to be calculated using

$$\Gamma_f = \frac{\rho_f \phi_f}{(\rho_f \phi_f + \rho_p [1 - \phi_f])} \tag{4.2}$$

Where ρ, ϕ_f and V are the density, volume fraction of fibre and volume of the sample, respectively. The density of polymer (ρ_p) is 1200 kgm^{-3} and carbon fibre density (ρ_f) is 1800 kgm^{-3} [19, 131]. The initial fibre volume fraction (ϕ_f) is 0.65. From this, the initial fibre mass fraction (Γ_f) within CFC is 0.73. If it is then assumed that at the end of the degradation all the polymer has been degraded, then any excess mass fraction above the fibre mass fraction, can be assumed to be related to the mass of the char. The final mass fraction from our samples is approximately 0.72. This final fraction is less than the initial fibre mass fraction, which is slightly concerning. However, the density values used in this calculation are taken from literature and so there is some uncertainty in these values. Despite this, it is still reasonable to assume that there is minimal char produced and left within the CFC due to the degradation.

4.2.1.3 Reaction Rate

Using the data presented in Figure 4.8 and considering Equation (3.12), the reaction rate ($\dot{\Gamma}$) for the three samples can be calculated. These reaction rates are shown in Figure 4.9.

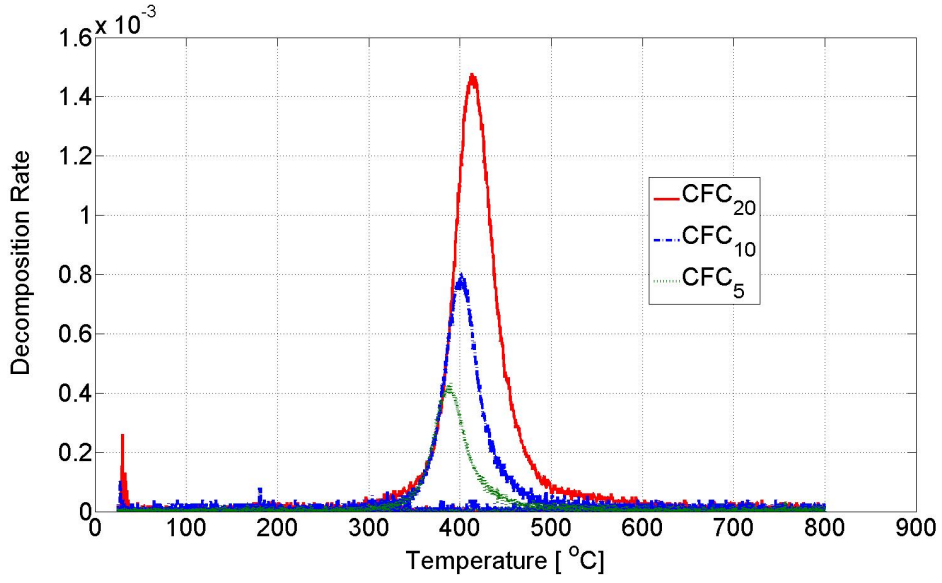

FIGURE 4.9: Polymer reaction rate for M21/T700s

Figure 4.9 shows that the temperature at which the reaction begins, is the same regard-

less of the heating rate. From Figure 4.9, it is also evident that the topology of the reaction rate is independent of heating rate. The heating rate only appears to scale the reaction rate up or down. This is evident in Figure 4.9, as when the heating rate is increased, the temperature of the peak reaction rate (T_m) increases, as shown in Table 4.2.

Sample ID	T_m [$^\circ C$]
CFC_5	386
CFC_{10}	402
CFC_{20}	414

TABLE 4.2: Temperature at the peak reaction rate for each sample

4.2.2 Determination of the Reaction Kinetics

From the TGA results and the discussions in Section 3.3.1.1, the reaction kinetics for this type of CFC can be determined.

Activation Energy

The activation energy (E_a) is calculated by solving Equation (3.13). This is done by determining the gradient of the fitted line of the nominator plotted against the denominator. The corresponding data points for each sample have been calculated, and the resultant graph is shown in Figure 4.10.

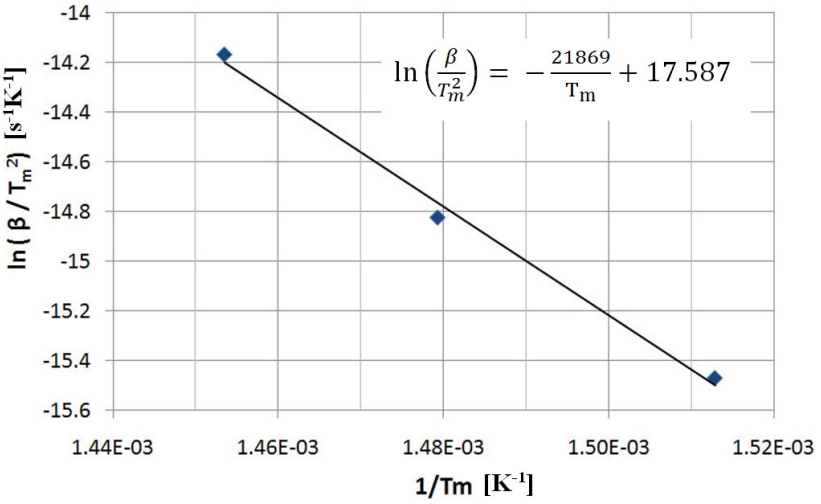

FIGURE 4.10: Activation energy (E_a) for the decomposing CFC is calculated from the gradient of the plotted line

By considering the RHS of Equation (3.13) and using the gradient of the fitted line shown in Figure 4.10, the activation energy is calculated to be 181.73 $kJmol^{-1}$.

Reaction Order

The next aspect to consider is the reaction order (n). A method to determine this has been discussed previously in Section 3.3.1.1. During this discussion, it was stated that this method is only valid if the topology of the reaction rate is independent of heating rate. Section 4.2.1.2 has previously discussed that the topology of the reaction rate is indeed independent of heating rate. Hence, this method is applicable for these epoxy samples. By using the raw results obtained from the TGA experiments, the reaction order for the CFC samples is summarised in Table 4.3.

Sample ID	n
CFC_5	1.357
CFC_{10}	1.288
CFC_{20}	1.388

TABLE 4.3: Calculated reaction orders (n) for each of the samples

Table 4.3 states that CFC_5 and CFC_{20} give similar reaction orders, whilst the results for CFC_{10} are slightly different. It has already been discussed that there is a slight discrepancy with the raw results for CFC_{10}, and this could certainly be the source for the slight difference in these results. Given that the variation is only slight, all these values can be used to obtain an average reaction order. By considering all the results in Table 4.3, the average reaction order for this CFC is 1.344 ± 0.05.

Pre-Exponential Factor

The final reaction kinetic to consider is the pre-exponential factor (A). A method for determining this has been outlined previously in Section 3.3.1.1. By using the reaction kinetics calculated above, the pre-exponential factor can be obtained using Equation (3.16). The pre-exponential factor obtained for each sample is shown in Table 4.4.

Sample ID	A (s^{-1})
CFC_5	3.17×10^{11}
CFC_{10}	3.12×10^{11}
CFC_{20}	3.16×10^{11}

TABLE 4.4: Calculated pre-exponential factor for each sample

As with the previous results for the reaction kinetics, the results for CFC_5 and CFC_{20} give close agreement. Whereas the results for CFC_{10} are slightly adrift, due to the discrepancy which has been mentioned with the raw results. Given that there is only a small variation in these results, an average pre-exponential factor can be calculated from all three results to be $3.15 \pm 0.03 \times 10^{11}\ s^{-1}$.

4.2.2.1 TGA Discussion

From the above discussion, a complete set of reaction kinetics for T700/M21 have been obtained and are summarised in Table 4.5. Whilst these results are presented for the

degradation of a composite material, given that the remaining mass fraction at the end of the decomposition is very similar to the initial carbon fibre mass fraction, it is assumed that only the polymer has degraded. Hence the present reaction kinetics can be assumed to be for the epoxy, M21.

Parameter	Value
E_a $[kJmol^{-1}K^{-1}]$	181.73
n	1.344 ± 0.05
A $[s^{-1}]$	3.15×10^{11}

TABLE 4.5: The reaction kinetics for M21

Confidence in the experimental results is obtained as the different experimental samples (CFC_5, CFC_{10}, CFC_{20}) give good repeatability with only a small experimental uncertainty. To gain further confidence in these results, a comparison is drawn with previous experimental studies presented by F. Uhlig [12] and T. Ogasawara [49]. By considering first the topology of Γ, these previous studies both showed a single stage degradation occurring between $300°C$ and $550°C$. The topology of Γ and these temperatures agree well with the experimental results presented here. The temperature range of degradation is only an indicator given this depends on the heating rate. The study conducted by T. Ogasawara then went on to calculate the reaction kinetics from their TGA results [49]. In this study, the reaction kinetics were calculated to be $n = 3.5$, $A = 8.33 \times 10^{11} s^{-1}$ and $E_a = 180\, kJmol^{-1}K^{-1}$. Apart from the reaction order (n), these results give a surprisingly very good agreement with the experimentally measured reaction kinetics. The difference with the reaction order is not a significant concern as it can be put down to their experiments being conducted with a different epoxy.

4.3 Differential Scanning Calorimetry

The final parameter to consider is the change in enthalpy due to the epoxy degradation. As outlined in Section 3.3.2, this change in enthalpy can be measured from Differential Scanning Calorimetry (DSC). The DSC experiments conducted here follow the experimental methodology outlined in Section 3.3.2.1.

4.3.1 DSC - Samples

For this experiment 6 samples were cut from the same pristine piece of quasi-isotropic CFC, which has been used for the TGA experiments. Each of the different samples was heated to 550 K. This maximum temperature was chosen as the TGA results showed that the majority of the chemical degradation had occurred by this temperature (shown in Figure 4.8). The six samples and their masses are summarised in Table 4.6.

Sample ID	Mass [mg]	Heating Rate [K/min]
1	3.82	15
2	4.11	15
3	4.15	20
4	3.95	20
5	3.87	10
6	9.79	10

TABLE 4.6: Mass of each DSC sample and its heating rating

4.3.2 Experimental Results

A typical DSC trace, taken from the results is shown in Figure 4.11. This graph shows two regions of interest. Firstly, there are a series of small dips at 150 $°C$ and 210 $°C$. These are phase transitions which are occurring within the epoxy. It is evident that these are not related to the polymer degradation as at these temperatures, the TGA results showed no change in mass. The second region of interest is the large peak around 390 $°C$. This relates to the change in enthalpy of the system due to the thermo-chemical degradation. The temperature at the peak change in enthalpy, gives reasonable agreement with the temperature at the peak reaction rates given in Table 4.3.

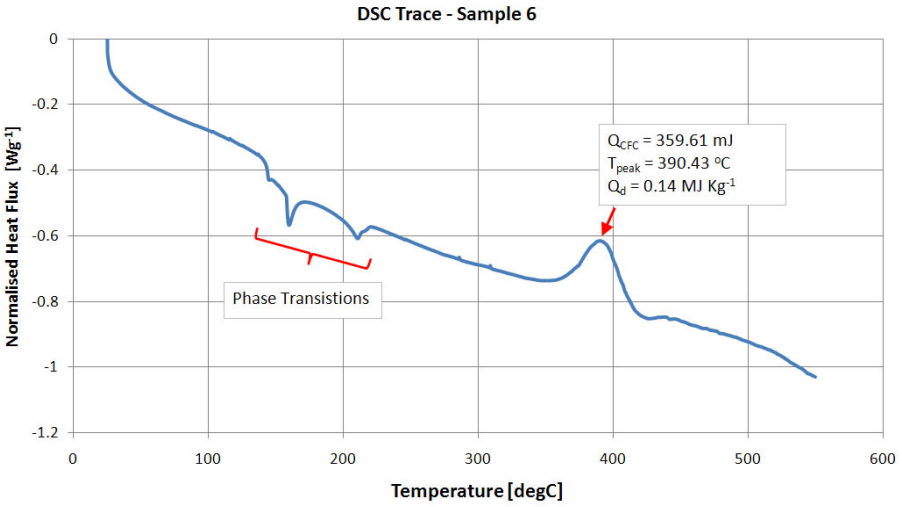

FIGURE 4.11: DSC results for CFC sample 6

For this peak, the total change in enthalpy (Q_{CFC}) for the sample has been calculated to be 359.61 mJ. To compare these values with the different samples, this value first needs to be normalised against the mass of the decomposing sample. Remembering that the sample here also contains fibres and polymer and that the fibres are inert, it is important to calculate the initial mass of just the polymer. This is achieved using the polymer volume fraction along with density of the fibre and polymer as stated in appendix C. The normalised change in enthalpy (Q_d) for the decomposing polymer in sample 6 is 0.14 $MJkg^{-1}$. These values have been calculated for each of the other samples and are shown in Figure 4.12.

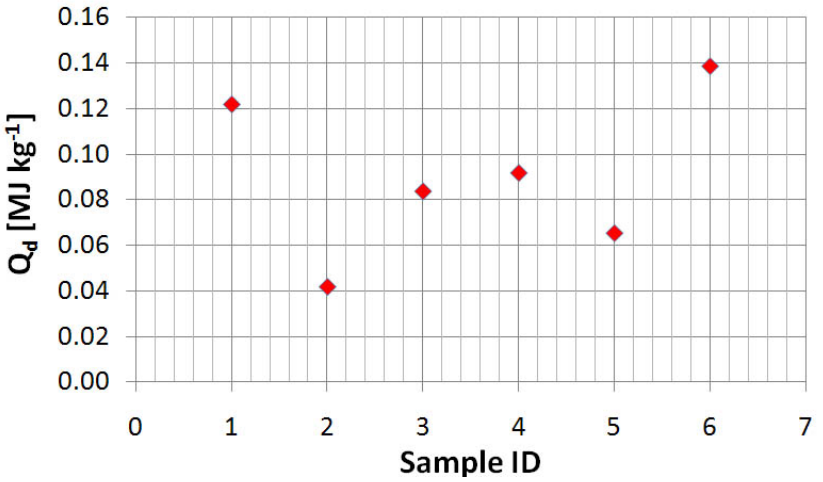

FIGURE 4.12: Change in enthalpy for polymer degradation (Q_d) for each of the samples

From Figure 4.12, it is evident that there is large scatter between the different calculated changes in enthalpy. Despite this variation, it is still possible to obtain an average change in enthalpy due to the pyrolysis. The averaged normalised change in enthalpy is $0.09MJkg^{-1}$.

4.3.3 DSC Discussion

A series of DSC experiments has been conducted to determine the change in enthalpy due to the polymer pyrolysis. The experiment was conducted for six samples at varying heating rates. The results from these experiments have shown a large scatter (Figure 4.12). This scatter is believed to be caused by crucibles rupturing due to the large gas pressure which builds up inside the sealed crucibles due to the polymer pyrolysis. Unfortunately, this error was unavoidable with the available experimental set-up. However, from the 6 trials, it is still possible to obtain an average normalised change in enthalpy for the decomposing polymer.

The positive normalised change in enthalpy indicates that the reaction is exothermic i.e. that the reaction produces heat. This is a little surprising given that it is generally assumed that the polymer decomposition is an endothermic reaction [51]. Whilst this is assumed for a general polymer, it has already been shown previously that for a comparable CFC with an epoxy matrix that the reaction is exothermic [12]. The exothermic change in enthalpy could be caused by a burning degradation rather than a true pyrolysis. This is possible as the experiment was conducted in an air atmosphere, whereas the TGA conducted previously, was conducted in an inert nitrogen rich atmosphere. In the study by F. Uhlig [12], he presented that the normalised change in enthalpy from their type of CFC to be $0.9MJkg^{-1}$. There is an order of magnitude difference between the results obtained by F. Uhlig and the results presented in this study. This order of magnitude difference, could likely be explained by the use of a different epoxy in each

case.

4.4 Summary

This chapter has presented experimental studies to determine a series of material properties which are required by the numerical models which are considered later. The first half of the chapter considered the electrical properties whilst the second half considered the degradation of CFC. It was important to conduct these studies given that there is no published record of the required material properties for this CFC. A summary of the experimentally obtained values is given in Table 4.7.

Parameter	**Value**	**Units**
σ_1 (unidirectional panel)	7.32×10^3	Sm^{-1}
σ_2 (unidirectional panel)	0.1	Sm^{-1}
σ_3 (unidirectional panel)	2.08×10^{-3}	Sm^{-1}
σ_3 (Quasi-isotropic panel)	0.96	Sm^{-1}
E_a	181.73×10^3	$Jmol^{-1}$
A	3.15×10^{11}	s^{-1}
n	1.344	
Q_d	0.9×10^6	Jkg

TABLE 4.7: Summary of the experimental obtained material properties for CFC M21/T700

All the results presented above show reasonable agreement with the relevant previous studies. So, whilst the experimental work conducted here has not be conducted before for this composite material, it is evident that these results are at least sensible. Therefore, the experimentally determined values will be used within the numerical studies in future chapters. The only experimental result that carries doubt, is the change in enthalpy of the polymer. With the uncertainties in the obtained results and the fact that doubt has been cast on what change in enthalpy is actually being recorded, future numerical work will consider a parametric study to determine how sensitive the numerical predictions are to the accuracy of these obtained results.

Chapter 5

Experimental Damaged Samples

This chapter presents results from a series of experimental studies, which has been designed to damage panels of CFC, to provide a comparison against any proposed numerical model. Two damage techniques have been considered, laser ablation and lightning strike current impulse tests. Both these experimental techniques and the methods for investigating the damage have been outlined in Chapter 3.

5.1 Laser Ablation - Samples

A series of laser ablation experiments has been conducted as proposed in Section 3.4.1.1. The CFC samples used in this experiment were strips of M21/T700, cut from a pristine quasi-isotropic panel (fibre layout as defined in Appendix A). The dimensions of the CFC samples are shown in Figure 5.1.

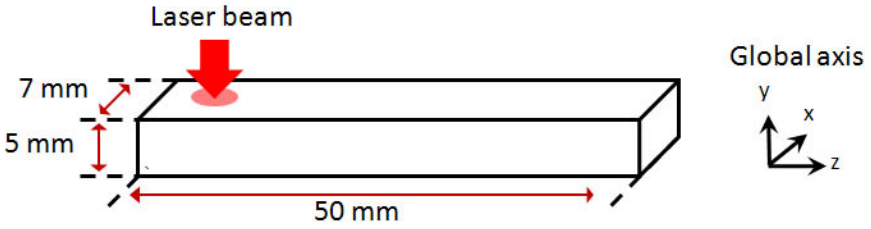

FIGURE 5.1: Diagram of the CFC sample which has been laser ablated

The CFC samples were ablated for the following durations 10, 30, 60, 90, 120, 150, 180 seconds. Three laser ablations regions were established per sample. The limit of three damaged regions per sample, was set to avoid any damage caused, being affected by neighbouring damage sites. For this study, 4 CFC strips were used.

5.1.1 Results

During the ablation, it was noticed that the decomposing CFC samples gave off a large amount of clearly visible grey gas. As discussed in Section 3.5.4, the ablated samples were then scanned using X-ray tomography to investigate the spatial dimensions of the damage. An example of a reconstructed X-ray tomography image, for the 180 seconds ablated CFC sample is shown by a top down view in Figure 5.2 and a cross section through the middle of the damage region in Figure 5.3. The X-ray tomography images show three distinct regions. The solid grey regions represents the undamaged material, the grey streaky region depicts where the polymer has been removed, but the fibres still remain, and the black region indicates where there is no material present. The distances between damage sites was sufficiently large to avoid neighbouring damaged locations affecting new damage sites, this is shown by the symmetrical appearance of the damage.

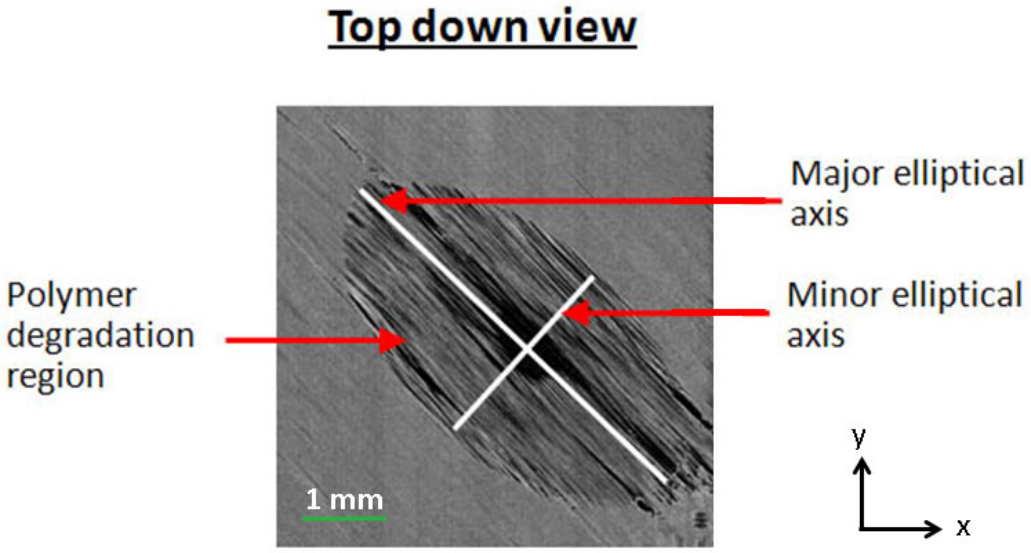

FIGURE 5.2: X-ray tomography image of a laser ablated sample. The damage shown is for an ablation time of 180 seconds

By considering the damage on the top surface first, it is evident from Figure 5.2 that the polymer damaged region resembles an ellipsoid, with the major elliptical axis being at -45 deg to the x axis. This corresponds to the fibre direction in the top ply, as given in Appendix A. This elongated damage along the fibre is expected since it has been shown in previous studies [56, 57, 132]. The small dark region in the centre indicates that some fibre removal has also occurred. The cross section results presented in Figure 5.3 are now considered. This cross section slice is taken in the middle of the damaged region, where the maximum damage depth is observed.

In Figure 5.3, the polymer degradation and the fibre removal region are again visible. This image also indicates that there is cracking or de-lamination occurring just below the polymer degradation region. This is shown by the small straight black regions. A

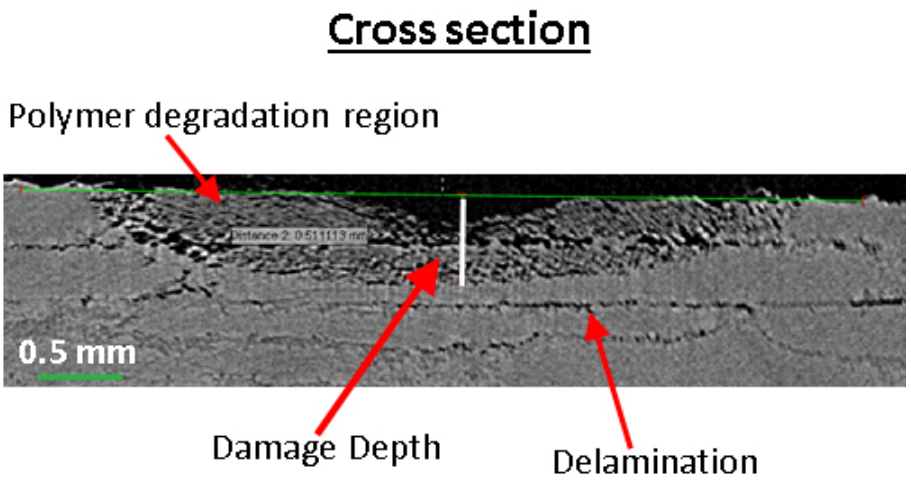

FIGURE 5.3: X-ray tomography image of laser ablated sample. The damage shown is for an ablation time of 180 seconds

scan of the panel was not conducted before the ablation experiments, so there is no way to categorically state that these artefacts are as a result of the laser ablation. However, given there are no signs of other cracks or delaminations within the undamaged regions of the CFC sample, it is believed these cracks or delaminations are due to the laser ablation. These cracks and delaminations could either be caused by a large build-up of internal gas pressure due to the decomposing polymer, or as a result of a mechanical fracture due to differential thermal expansion.

For this investigation, three parameters were defined to record the damage dimensions. These are the major and minor axis of the ellipsoid, measured from the top surface as shown in Figure 5.2 and the maximum internal damage depth, as shown in Figure 5.3. These parameters can be defined for both the polymer damage and the fibre damage. As the proposed model does not consider the fibre degradation, only the polymer degradation dimensions are considered further. The major and minor length of the polymer damage as a function of time is shown below in Figure 5.4.

The individual data points in Figure 5.4 (and Figure 5.5) refer to the measured damage dimensions at each individual damage site. At some durations, there is more than one data point, this is because the experiment was conducted on two different dates and, therefore, it was important to verify the experimental set-up between the two experiments was the same. The results presented in Figure 5.4 show that the damage along the major axis has a greater rate of increase than the minor axis. This result is not a surprise, as the thermal conductivity along the major axis is greater than in the minor axis direction. The reason for this is the majority of the heat will travel along the major axis and so more thermal degradation will occur in this direction [56, 57, 118]. The damage depth of the ablated sample as a function of time is given in Figure 5.5.

The results for the damage depth (Figure 5.5) show that at earlier times (less than 10

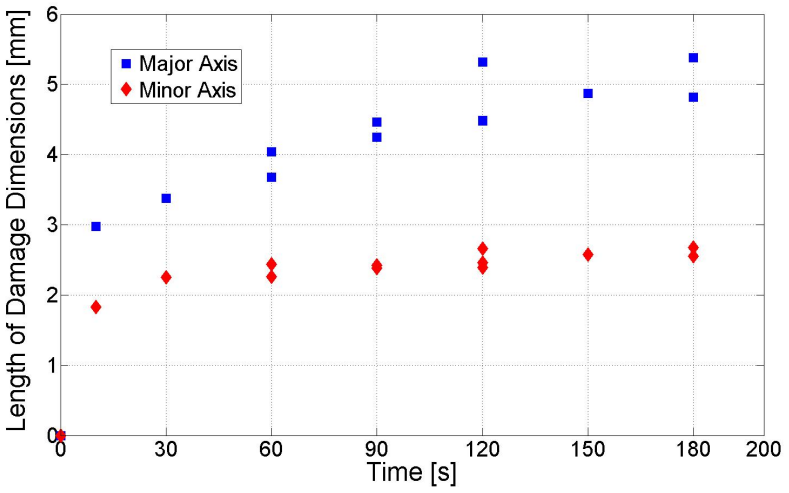

FIGURE 5.4: Resultant damage dimensions for the major and minor axis on the top CFC surface, obtained from the X-ray Tomography scans

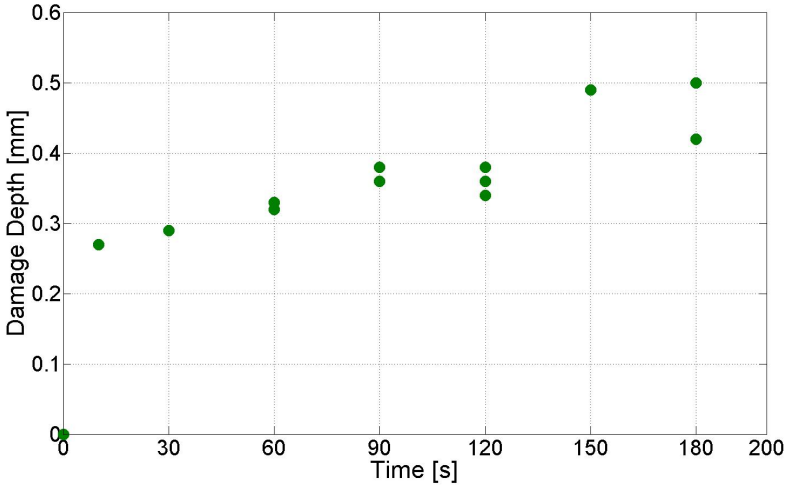

FIGURE 5.5: Maximum damage depth as a function of ablation duration

seconds), there is a sudden increase in damage depth, after which there is a more gradual trend in increasing damage depth. The damage depth appears to be limited to the top two plies (ply thickness 0.25 mm).

5.1.2 Discussion

A series of laser ablation experiments with variable ablation times has been conducted on a quasi-isotropic piece of CFC. To determine the damage dimensions, these samples have been scanned using X-ray tomography. The polymer degradation shows an ellipsoidal shape, which is due to the anisotropic nature of the CFC. The majority of the damage occurs along the direction of the carbon fibres, as this is the direction of highest thermal conductivity. Cracks and de-laminations have also been witnessed within the damaged

CFC. These are believed to be caused by a large internal gas pressure, which occurs due to the gasses produced by the polymer pyrolysis. The internal gas pressure is assumed to dominate over the differential thermal expansion for two reasons. Firstly, it has been reported that the thermal expansion of a typical CFC is very small, with minimal cracking and delamination occurring [7, 133]. Secondly, it has also been reported that the internal gas pressure can reach 50 atmospheres [58, 59], which is thought to be sufficient to cause cracks and de-lamination.

The results presented here are believed to be reliable as possible sources of errors have been considered and minimised, discussed in Section 3.5. As a result, it is believed these results are accurate. The resolution of the damage dimensions are controlled by two experimental parameters which have been carefully controlled. Firstly, the duration of the ablation, which is controlled with a digital stop-watch and, therefore, are accurate to within a second. Secondly, the damage dimensions measured with the X-ray tomography are measured to a resolution of 10 μm.

5.2 Lightning Strike Experiments

A series of lightning strike current impulse tests has been conducted, based on the experimental procedure outlined in Section 3.4.2.3.

5.2.1 CFC Panels

For this experimental study, three M21/T700 CFC panels were made. These panels had a bare top surface with no lightning strike protection or paint applied to the surface. All of the panels had top surface dimensions, as defined by the experimental apparatus in Section 3.4.2.3 ($L_x = 530\ mm$, $L_z = 530\ mm$). Two of the panels were constructed from 20 unidirectional plies of CFC, which resulted in a thickness (L_y) of 5 mm. These panels are refereed to as '202' and '203'. The third panel referred to as '205', was constructed with 14 unidirectional plies and, hence, has a thickness of 3.5 mm. The order in which panels '202' and '203' were damaged are, $D + B + C^*$, D, $B + C^*$, C^* and B. For panel '205', this order was reversed, to investigate if there are any changes to the damage caused by the order in which the panels are damaged.

5.2.2 Ultrasonic C-scan Results

As discussed in Section 3.5.4, after the CFC panels were subjected to a series of current impulse tests (lightning strikes), the damaged panels were scanned using an ultrasonic C scan. The results from the ultrasonic C scan for panel '205' are shown in Figure 5.6. The different damaged locations have been annotated with the corresponding current

impulse which caused the damage. These locations correlate to the proposed damage locations given in Figure 3.11, but in this case, the damage locations here are reversed as the panels has been flipped upside down before taking the ultrasonic measurements. Figure 5.6 also shows regions of damage which do not correspond to lightning strike test sites; these have been highlighted with red circles. These damage locations are caused by the current leaving the panel and making contact with the grounding plate, i.e. these locations are under the metal grounding plates. These unplanned damaged regions are relativity small and shallow and so should not have any impact on the experimental results; hence they have been ignored for the remainder of this study.

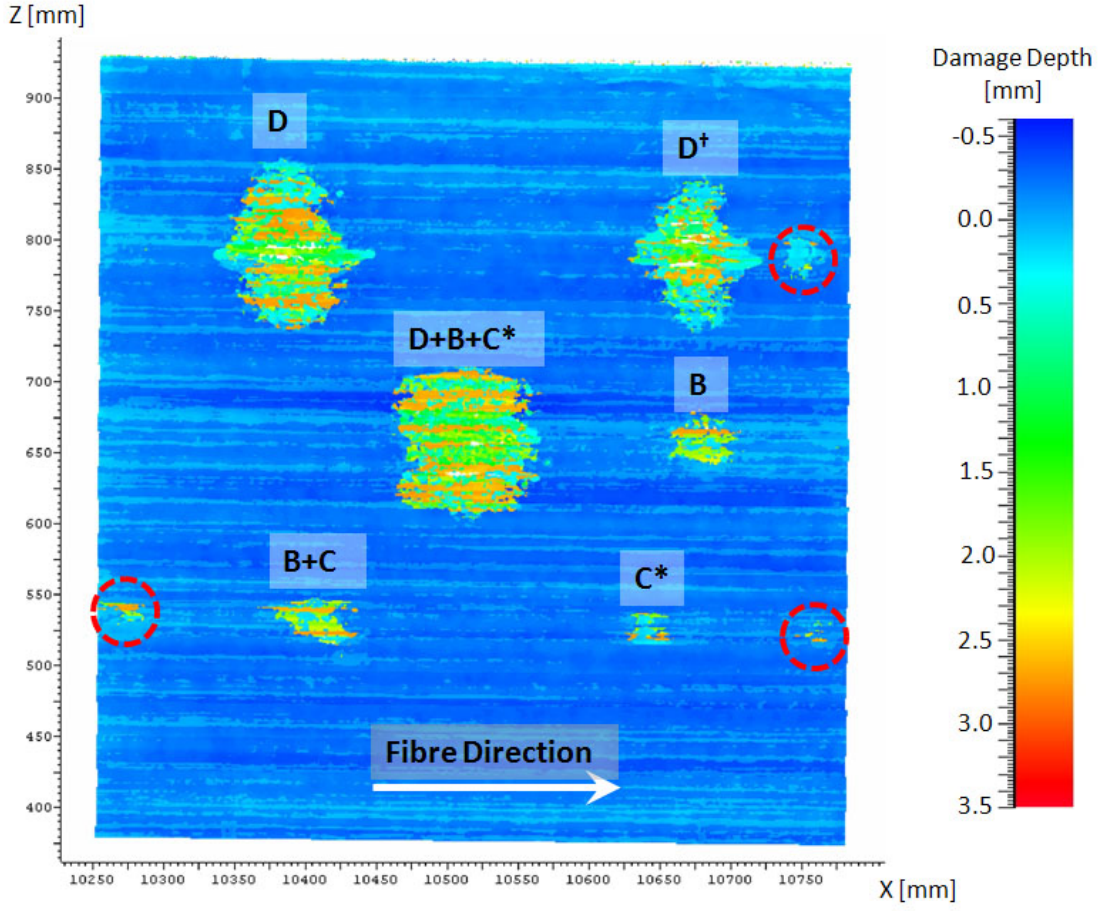

FIGURE 5.6: Ultrasonic C-scan results for panel '205' after the lightning strike current impulse test

From the ultrasonic C scan results, the following parameters can be defined for each damage location on each panel: the major damage axis, which is given as the maximum damage along the fibre direction, the minor damage axis which refers to the maximum damage perpendicular to the fibre direction and the average damage depth. The damaged area can also be calculated for each damaged location. This is achieved by first drawing a polygon around the perimeter of the damage region and then calculating the enclosed area.

5.2.2.1 Component D

The damage caused by component D is considered first. A photograph of the damage seen on the top surface of panel '205' is shown in Figure 5.7, with the corresponding ultrasonic C scan results for the same panel shown in Figure 5.7(b). From Figure 5.7(a), it is evident that the damage caused by component *D* appears as fibre splitting and lifting up from the surface. The raised and split fibres are believed to be caused by the large internal gas pressure which is produced within the CFC, due to the rapidly decomposing polymer. The visible damage extends further, perpendicular to the fibre direction, than along the fibre direction. The physical mechanism behind why this has occurred is not clear, but the most likely explanation is that it results from the arc wandering. It was also noticed that around the fibre splitting region, there are signs of polymer degradation. Finally, there are minimal signs of fibre removal.

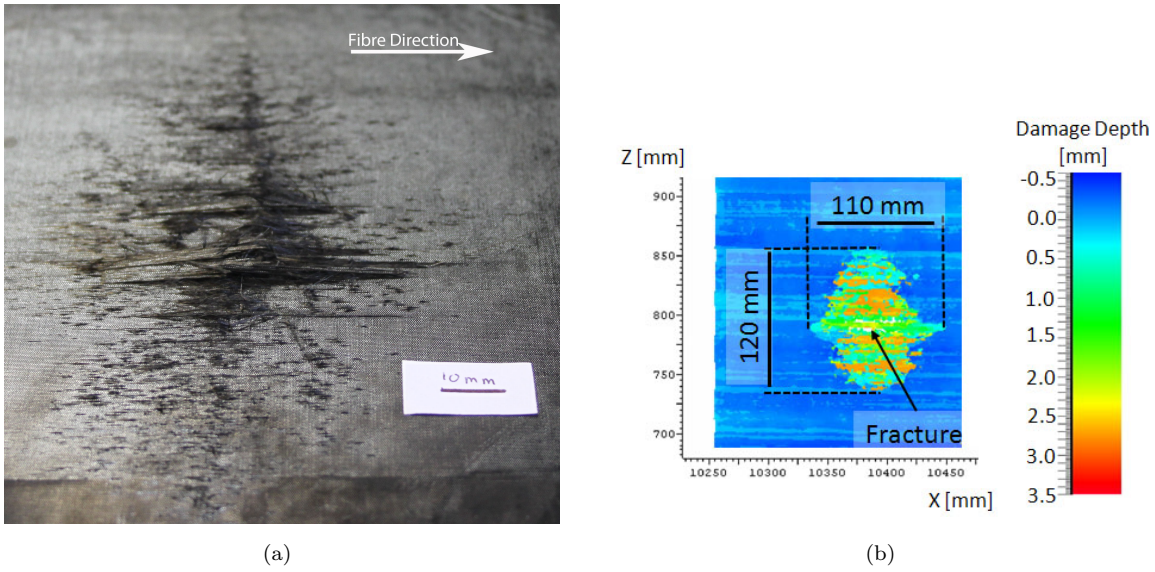

(a) (b)

FIGURE 5.7: Results for panel '205' for component D shown for a) Photograph of the surface damage b) Ultrasonic C-scan Result

By visually comparing the damage observed here with the results from previous studies, it is evident the type of damage observed is very similar. This can be seen by considering an example of the damage observed by F. Lago as shown in Figure 1.4. The damaged witnessed in Figure 1.4 shows a damage region spread along the fibres, with lifting of fibres from the surface, and a narrow line of damage perpendicular to the fibre direction [122, 13].

It is evident from Figure 5.7(b) that there is a roughly uniform damage depth. In the middle of damage region, the ultrasonic C-scan shows a white region which runs parallel to the fibres. This is caused by the splitting of the unidirectional panel, and is visible on the underside of the panel. The fracture is believed to be caused by the shock wave which is known to occur at the initialisation of component D [9]. Fracturing has not

been reported in previous studies [122, 13, 123, 124, 45]. This is because the majority of previous studies have been conducted using quasi-isotropic panels (not uni-directional panels). These quasi-isotropic panels are more resilient to impacts, as the fibres can distribute the mechanical load more evenly over the panel. From these results, it is not possible to determine what effect this fracturing will have on the damage dimensions, but it is worth noting when these experimental results are compared against previous experimental results.

Having considered the damage caused to panel '205' in detail, the damage parameters for the remaining panels are now considered. The damage dimensions for each of the panels caused by component D are given in Table 5.1

Panel	Major $[mm]$	Minor $[mm]$	Damage area $[mm^2]$	Maximum Damage Depth $[mm]$	Average Depth $[mm]$	Noticeable Split
202	120	120	8429	3.90	2	Yes
203	90	115	7979	4.25	1.8	Yes
205	110	120	8599	2.75	2.2	Yes

TABLE 5.1: Measured damage dimensions for each panel of CFC tested with component D

The surface damage (major and minor) dimensions for panel '202' and '205' give reasonable agreement, whilst the surface dimensions for panel '203' are slightly different. The variation in these results is not surprising, as some variation is expected given the chaotic nature of the arc wander. The maximum damage depth for panel '205' is considerably less than that for '203' and '202', whilst the average damage depth and damaged area is more comparable between the test panels. This implies that the maximum damage depth is related to the panel thickness whilst the average damage depth is less affected by panel thickness and is more a function of the lightning strike. However, future experiments with more panels is required to confirm this conclusion.

5.2.2.2 Component $D^{\dagger}$

The type of damage witnessed for component $D^{\dagger}$, is very similar to that which is observed for component D as shown in Figure 5.7(a). However, due to the reduced peak current and action integral of $D^{\dagger}$ (shown in Table 3.2), the damage dimensions for component $D^{\dagger}$ are considered separately and summarised in Table 5.2

Panel	Major $[mm]$	Minor $[mm]$	Damage area $[mm^2]$	Maximum Damage Depth $[mm]$	Average Depth $[mm]$	Noticeable Split
202	70	100	6491	3.95	2.3	Yes
203	80	105	6438	4.25	2.4	Yes
205	95	110	6285	2.75	1.7	Yes

TABLE 5.2: Measured damage dimensions for each panel of CFC tested with component $D^{\dagger}$

Table 5.2 shows that whilst the minor axis of damage is comparable in length to that observed for component D, the major length is reduced from that seen for component D. The similar minor damage length can be explained by realising that despite the lower action integral in $D^{\dagger}$, the duration of the impulse is the same, and so assuming that arc wandering is independent of arc current, the amount of wander in D and $D^{\dagger}$ should be comparable. Hence, if the size of the minor damage is dominated by arc wandering then the minor axis damage dimension should be more comparable. The reduction in major damage length witnessed for $D^{\dagger}$ can be explained by considering that the action integral and the peak current measured for $D^{\dagger}$ is less than that for component D.

5.2.2.3 Component B

A photograph of the damage caused by component B on the top surface is shown in Figure 5.8(a), with the ultrasonic C-scan results for the same panel ('205'), given in Figure 5.8(b). From the photograph it appears that there are signs of polymer degradation on the top surface which has exposed bare fibres. The fibre damage manifests itself as many small regions of fibres tufting. It has not been possible to determine if there has been any fibre degradation due to the significant amount of fibre tufting.

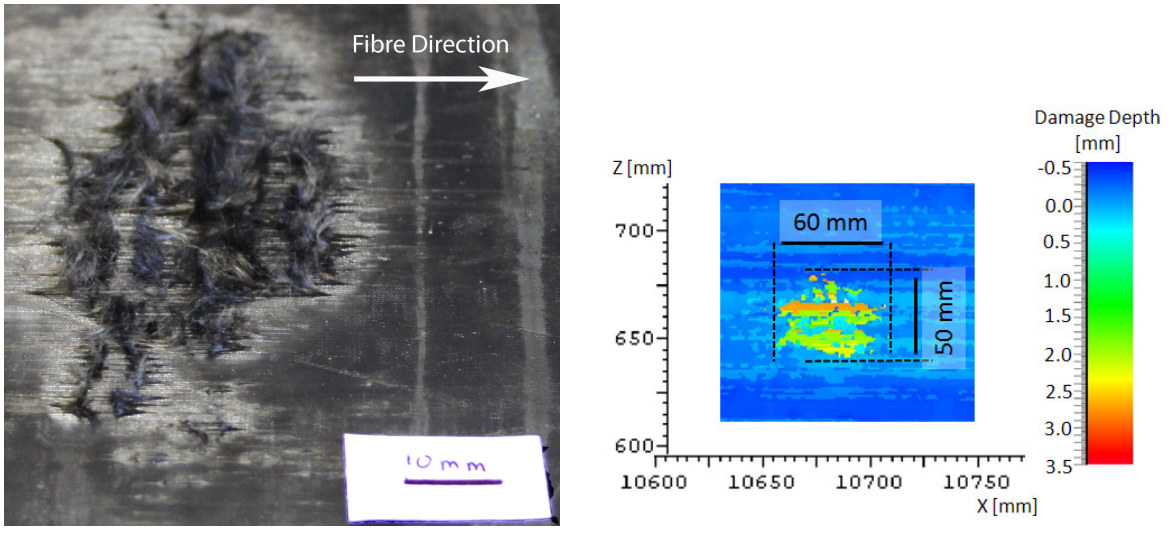

(a) (b)

FIGURE 5.8: Results for panel '205' for component B shown for a) Photograph of the surface damage b) Ultrasonic C-scan Result

The ultrasonic results in Figure 5.8(b) indicate similar damage dimensions to that in Figure 5.8(a). The measured damage depth from the ultrasonic C-scan shows a deeper damage depth than expected based on visual inspection of the panel.

Having investigated the damage on panel '205' in detail, the measured damage dimensions for each panel damage by component B are now compared. Due to a problem whilst conducting the experiment, panel '203' was not damaged with component B.

The type of damage caused to each of the panels is very similar. It is evident from Table 5.3, that the surface damage dimensions (major and minor) are in reasonable agreement, but the damage area and damage depth for the different panels are different.

Panel	Major $[mm]$	Minor $[mm]$	Damage area $[mm^2]$	Maximum Damage Depth $[mm]$	Average Depth $[mm]$	Noticeable Split
202	44	33	1518	3.98	3.4	No
205	55	45	2040	2.75	1.9	No

TABLE 5.3: Measured damage dimensions for each panel of CFC damaged with component B

Due to this variation and having only conducted two tests, more experimental results are required before any conclusive results can be gained regarding the damage caused by component B.

5.2.2.4 Component C^*

The final component which is considered separately is component C^*. A photograph of damaged caused to panel '205' is shown in Figure 5.9(a) and the results from the ultrasonic C-scan are given in Figure 5.9(b). The damage for component C^* resembles a rectangular shape with the longest sides orientated perpendicular to the fibre direction. Along these long edges, there are many fibres sticking out vertically from the panel's surface. In the middle of the rectangle, there are signs of polymer degradation which has exposed bare undamaged fibres. There are signs of polymer degradation along the long edges, where the fibres go from vertical to being flat. Figure 5.9(b) shows that the damage depth is generally relatively shallow.

Having considered the damage to panel '205' in detail, the damage dimensions for each of the panels are shown in Table 5.4

Panel	Major $[mm]$	Minor $[mm]$	Damage area $[mm^2]$	Maximum Damage Depth $[mm]$	Average Depth $[mm]$	Noticeable Split
202	25	22	841	3.8	0.4	No
203	25	26	814	4.22	0.4	No
205	30	25	835	2.75	0.5	No

TABLE 5.4: Measured damage dimensions for each panel of CFC tested with component C^*

Table 5.4 shows that the damage dimensions for the different samples are reasonably similar given the wandering nature of an arc. Similar damage has been observed for each of the CFC test panels. Furthermore, there are no signs of the panels fracturing due to component C^*. The maximum damage depths show significant variation from the average depths. This is caused by single isolated points within the ultrasonic results showing a large damage depth, whilst the main surrounding damage is much shallower.

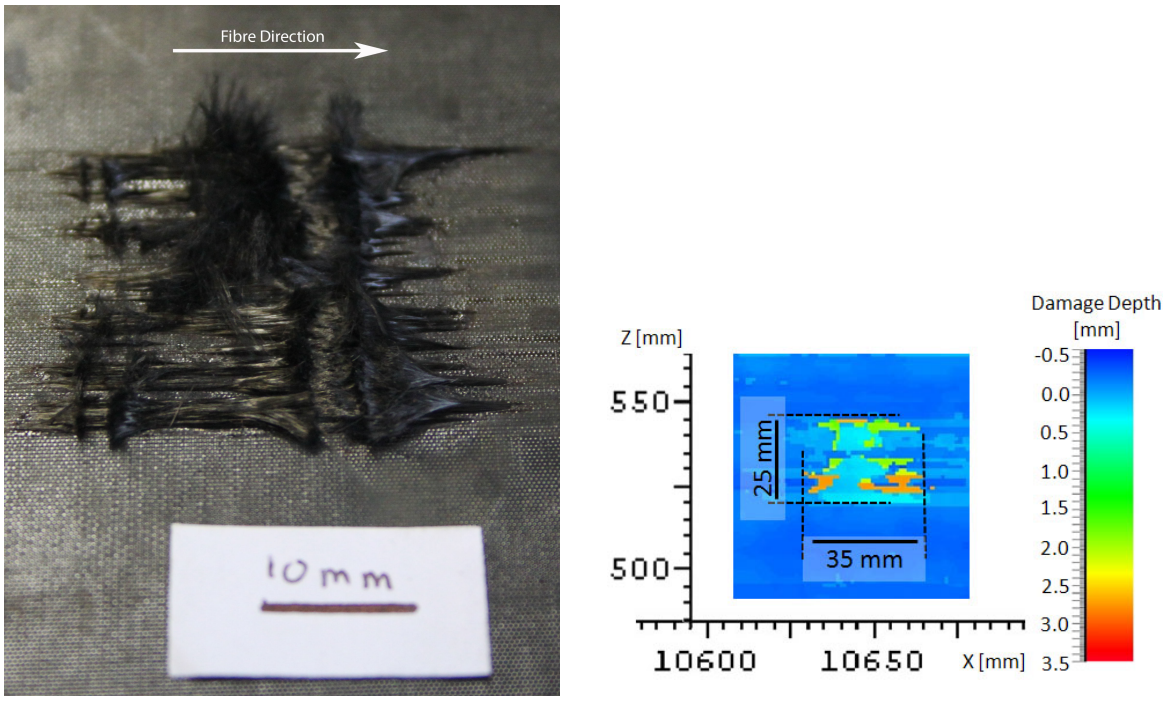

(a) (b)

FIGURE 5.9: Results for panel '205' for component C^* shown for a) Photograph of the surface damage b) Ultrasonic C-scan Result

Having considered the damage caused by each of the components separately, the next aspect to consider is the damage caused by the combination of lightning strike components.

5.2.2.5 Component $B + C^*$

The first combination of impulse currents considered is component $B+C^*$. A photograph of the damage caused to panel '205' is shown in Figure 5.10(a), with the corresponding ultrasonic C-scan results shown in Figure 5.10(b). Figure 5.10(a) shows that the damage caused by the combination of $B + C^*$ in part resembles that of the damage caused by component C^*, with a rectangular region of polymer degradation surrounded by a row of tufting fibres. The damage observed is, however, much larger than that caused by component C^*, with more fibres having been tufted. This larger damage area is more akin to the damage caused by component B. The damage observed can be explained by considering the order in which the damage has been caused. Component B happens first and causes lots of fibres to be tufted up which explains why the damage area is comparable to that of solely component B. Then, when the longer component C^* begins the arc can wander more easily, as it can directly attach to any of the exposed conductive fibres. Therefore, the rectangular damage shape can be seen as a record of the path the arc followed. Strangely, the damage dimensions along the fibre direction seem

much longer in the ultrasonic C-scan, than from what is visible within the photograph in Figure 5.10. This indicates that there is polymer degradation occurring below the surface, which is not visible from the surface.

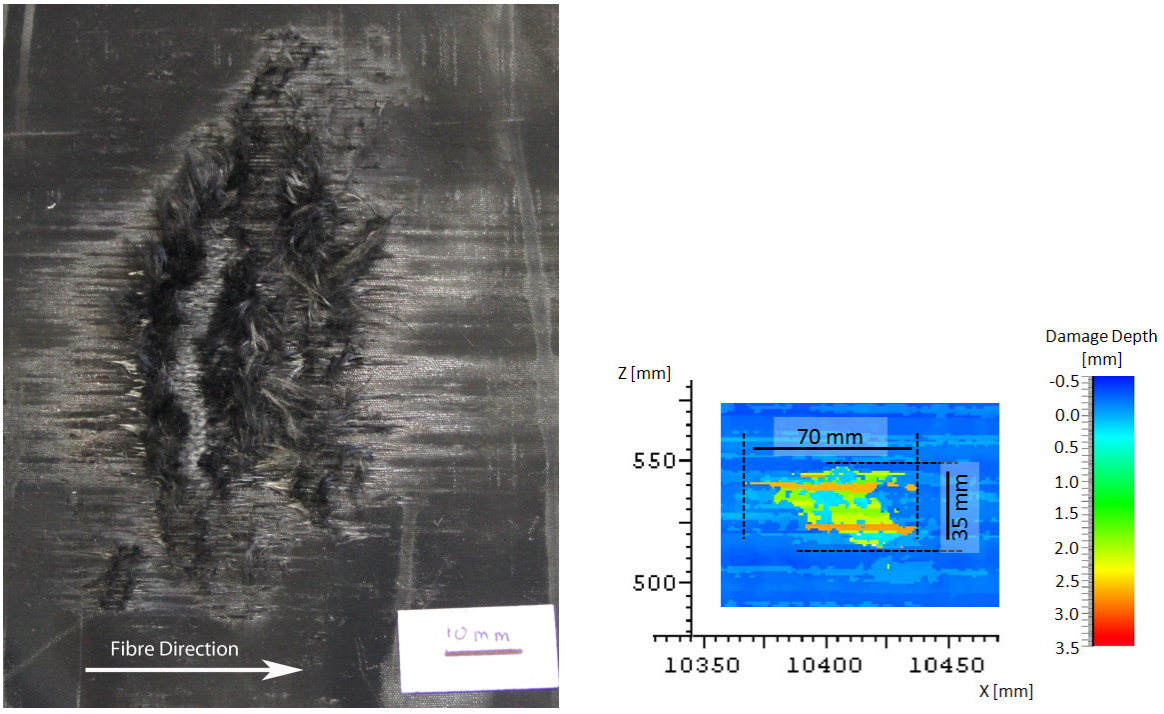

(a) (b)

FIGURE 5.10: Results for panel '205' for component $B + C^*$ shown for a) Photograph of the surface damage b) Ultrasonic C-scan Result

The measured damage depth from the ultrasonic C-scan shown in Figure 5.10(b) shows a damage depth more akin to component B rather than component C^*. The reason for this is that with this current combination, component C^* has wandered much more, than when component C^* was considered separately. This increase in wandering, reduces the energy density imparted by component C^* and reduces the additional damage caused by combining of the small damage depth of component C^*, with that already caused by B.

Having considered the results in detail for panel '205', the damage dimensions for each of the samples is given in Table 5.4. These damage dimensions show that the damage is comparable between all three damaged panels.

Panel	Major $[mm]$	Minor $[mm]$	Damage area $[mm^2]$	Maximum Damage Depth $[mm]$	Average Depth $[mm]$	Noticeable Split
202	50	45	2442	4.01	2	No
203	45	35	1671	3.83	2	No
205	70	37	2053	2.75	1.7	No

TABLE 5.5: Measured damage dimensions for each panel of CFC tested with component $B + C^*$

5.2.2.6 Component $D + B + C^*$

The final combination of lightning strike current impulses to consider is the combination of components $D + B + C^*$. A photograph of the damage caused to panel '205' is shown in Figure 5.11(a), with the corresponding ultrasonic C-scan result shown in Figure 5.11(b). The damage caused here resembles two distinct arc attachments. There is the damage caused by the combination of components $D + B$, seen by the fracturing and lifting of fibres which is typical of component D. Then, there is a separate damage region which resembles the damage caused solely by component C^*; the rectangular shape, with the large region of tufting up of fibres. The ultrasonic results do not appear to show the distinct regions of the damage which are witnessed on the surface of the CFC. This indicates that there must be some degradation occurring between the two regions, below the surface.

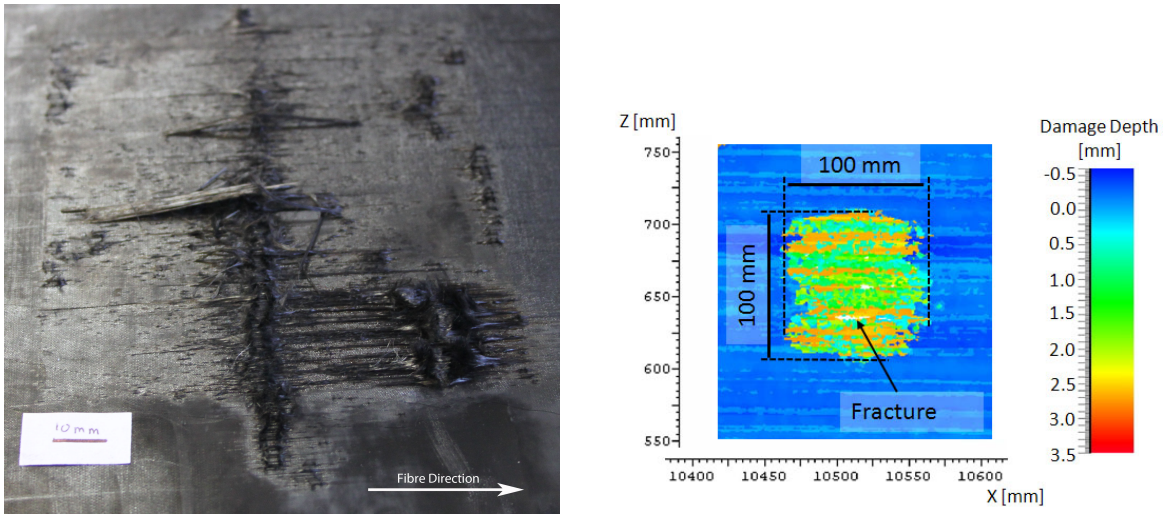

(a) (b)

FIGURE 5.11: Results for panel '205′ for component $D + B + C^*$ shown for a) Photograph of the surface damage b) Ultrasonic C-scan Result

The damage depth resembles that of the damage caused by component D only. This implies that there is no increase in damage depth by combining components $D + B + C^*$ together. It is evident though that the damage area is increased when compared against the damage caused solely by component D. Having considered the damage to panel '205', the damage dimensions for all the panels are shown in Table 5.6.

Panel	Major $[mm]$	Minor $[mm]$	Damage area $[mm^2]$	Maximum Damage Depth $[mm]$	Average Depth $[mm]$	Noticeable Split
202	100	120	11097	4.25	2.8	Yes
203	100	120	11039	4.2	2.5	Yes
205	105	110	10023	2.75	2.3	Yes

TABLE 5.6: Measured damage dimensions for each panel of CFC tested with component $D + B + C^*$

From Table 5.6, it is evident the damaged area on the surface of each panel is consistent. These results also show signs of fracture in each of the samples due to the shock wave, which is consistent with the damage caused by component D. The maximum damage depth is greater for the two thicker panels than observed for the thinner panel '205'. However, the average damage depth between all these panels is far more comparable.

5.2.3 Discussion - Lightning Strike Damage

Having considered the lighting strike current impulse results separately, conclusions can now drawn on the overall results. It is evident that neighbouring damage locations do not impact on each other, as the results for all the panels show comparable damage dimensions despite the order of the impulse test being reversed for panel '205'. Furthermore, the symmetrical damage indicates that the varying proximity to the grounded surfaces had no effect on the observed damage.

Excluding the maximum damage depth, the results present above show comparable damage dimensions between each panel, despite panel '205' being thinner. This conclusion is in accordance with the findings of Y. Hirano et al. for quasi-isotropic panels [122]. This result implies that the majority of the thermal damage occurs within the top few plies, with the remainder of the plies conducting minimal current.

The average damage dimensions for each component are summarised in Table 5.7. By initially considering the lightning strike components separately, it is evident that the largest damage area is caused by component D, followed by component B and finally component C^*. The average damage depth caused by component D and B are very similar, whilst the damage depth caused by component C^* is much shallower. It has also been shown that the damage caused by each component exhibits very different characteristics.

Component	Major $[mm]$	Minor $[mm]$	Damage area $[mm^2]$	Average Depth $[mm]$	Noticeable Split
D	107	118	8335	2	Always
$D^\dagger$	82	105	6404	2.13	Always
B	50	40	1779	2.65	No
C^*	27	24	830	0.4	No
$B + C^*$	55	38	2055	1.9	No
$D + B + C^*$	102	116	10719	2.5	Always

TABLE 5.7: Maximum damage dimensions for each lightning strike

The damage caused by the combinations of current impulse components, show signs of the damage caused by the separate impulse components. It is also evident from Table 5.7 that there is no linear increase in damage depth or the major or minor axis, as the current impulses are combined.

The characteristic damage observed for component D has already been compared against

previous studies in Section 5.2.2.1. There, is however, no images of the damage caused by component C^* (or C) or B in the literature review and so it has not been possible to compare the visible damage observed with previous studies. It is, however, possible to compare the experimentally measured damage dimensions presented with previous experimental studies for both component D and C^*.

The damage dimensions are first compared for component D. Whilst no study has been conducted with similar lightning strike current impulses, it is still possible to obtain a comparison between these results and those presented in previous studies. The study by Y. Hirano, observed a damage area of 2000 mm^2, which had been caused by a reduced form component A, with a peak current of 40 kA and an action integral of 22 kA^2s^{-1} [122]. The study presented by P. Feraboli [13] used a similar modified component A with peak current 50 kA and an action integral 50 kA^2S^{-1}, in this study they measured a damage region of 1612 mm^2. Finally, G. Reid measured a damage area of area of 3000 mm^2, for a peak current of 75 kA and an action integral of 180 kA^2s^{-1} [124]. All these previous studies have observed a smaller damage area than was measured in these experiments. However, the component D used here had a greater peak current and action integral, as shown in Table 3.2, than the current impulses considered in these earlier studies. Therefore, as both the peak current and the action integral are larger than what has been used in the previous experiments, it is no surprise that the previous studies have observed smaller amounts of damage.

A comparison of the results for component C^* is now considered. Only one previous study, by G. Reid, has conducted experimental damage using a continuous current component, such as C^*. In this study, G. Reid observed that a linear trend line could be fitted between the damaged area as a function of charge transfer [124]. By reading off the predicted damage area from the fitted trend line in [124] with the total charge transfer used in this study, a predicted damage area of 700 mm^2 is obtained. This damage area is in good agreement with the results measured in this experiment.

5.3 Summary

A series of CFC samples has been damaged by laser ablation and lightning strike current impulse tests. The results from the current impulse tests show that the different lightning strike components, cause different types of damage. However, the underlying physical processes of polymer degradation which exposes bare carbon fibres appears to be consistent for each current component. Furthermore, this damage indicates the same physical processes which have been observed in the laser ablation experiment. As well as the polymer degradation, current component D also showed splitting and lifting up of carbon fibres. This is believed to be caused by the same physical mechanisms which caused the cracking and de-lamination from the laser ablation experiment. This damage

is believed to be caused by a build-up in internal gas pressure caused by the polymer ablation.

The remainder of this study is devoted to developing a numerical model designed to investigate these damage mechanisms. However, it has been shown that the arc wandering, which occurs in the current impulse tests, plays a dominant role in the damage caused. Within the current state of the art knowledge, there is no equation to model this arc wandering. Fortunately, the same limitation does not exist when modelling the laser ablation experiment, as the heat input from the laser beam is very well defined. Therefore, this research will develop a numerical model designed to investigate the damage caused by a laser ablation. Whilst the energy input from the laser beam is considerably less than that of the lightning strike, the results from this model can still provide a useful insight into the thermal damage caused by a lightning strike, as it has been demonstrated that the observed damage mechanisms are similar.

Chapter 6

Homogenisation Framework

Having investigated the experimental damage and outlined the requirements for a numerical model to investigate the observed damage, the next step is to develop this numerical model. To this end, the first aspect to consider is the homogenisation approach, which is used to represent numerically a piece of CFC. Whilst a series of homogenisation approaches have already been discussed in Section 2.5.1, these methods have not been fully investigated to consider their accuracy and relevance when applied to CFCs. Therefore, in this chapter the relevance of each of these methods for modelling CFC is discussed.

6.1 Overview of Homogenisation Approach

As stated in Section 2.5.1, it is not possible to represent numerically the internal structure of a piece of CFC. This is due to the large mesh which is required to represent such a material accurately. Therefore, a common method to avoid this problem is to consider an homogenisation approach, whereby material is modelled as a homogeneous uniform block. When modelling a composite in this way, care needs to be taken to predict the bulk material properties which accurately represent the composite material.

The fundamental aspect of the homogenisation approach is that it considers within each mesh element there is a uniformly distributed amount of each species. For this study, it is evident that two initial species are required; these are polymer (p) and carbon fibre (f). Two further species are required in order to consider the thermo-chemical degradation of the polymer; these are the produced gas (g) and char (ch). The amount of each species present within each cell is given by the volume fraction of each species. This is defined at any point during the solution by

$$\Phi_i = \frac{V_i}{V_{cell}} \tag{6.1}$$

It is evident that to calculate the volume fraction of a species, one first needs to calculate

the volume occupied by each species (V_i) in a cell. This is straightforward to calculate for the solid species such as carbon fibre, polymer and char, as these species are assumed to be incompressible. Hence, only the mass and density of each species is required to determine the species volume by considering

$$V_i = \frac{m_i}{\rho_i} \tag{6.2}$$

However, the volume of gas is not as simple to calculate, as the gas is considered to be compressible and so the above method is not applicable. Instead, the gas volume is calculated by determining the remaining volume within each cell which is not occupied by a solid species. This is expressed by

$$V_g = V_{cell} - (V_{ch} + V_p + V_f) \tag{6.3}$$

Having determined the volume which the gas occupies, the volume fraction of gas can be calculated by Equation (6.1). Based on this discussion, the numerical model will consider the mass of each species within each cell to be as dependent variables within the relevant physical equations.

6.2 Required Bulk Material Properties

From the discussions in Section 2.5.1, it is evident that the following bulk material properties are required;

- Bulk heat capacity and density.
- Bulk Thermal Conductivity.
- Bulk Electrical Conductivity.

It is straightforward to predict the bulk density (ρ) and heat capacity (C_V), by using the Parallel Rule of Mixtures, expressed as

$$\rho C_V = \sum_{i=f,p,ch,g} \Phi_i \rho_i C_{V\,i} \tag{6.4}$$

Where the respective volume fractions of each species (Φ_i) is calculated using Equation (6.1). This is the same method as that used in previous studies, where it has proven to be an accurate approach for predicting their bulk material properties [52, 53, 54, 55].

However, to predict the bulk thermal and electrical conductivity, extra care is required. This is because these terms need to be defined for each of the principle directions within

a CFC panel. As an example, the bulk thermal conductivity tensor is defined as,

$$\kappa = \begin{bmatrix} \kappa_1 & 0 & 0 \\ 0 & \kappa_2 & 0 \\ 0 & 0 & \kappa_3 \end{bmatrix} \tag{6.5}$$

The bulk electrical conductivities are given by a tensor of similar form to that given in Equation (6.5). It has been stated in Section 2.5.4 that it is relativity easily to predict the bulk thermal and electrical conductivity along the fibre direction (direction 1) by considering Equation (2.12). However, it is not as simple to predict the bulk conductivity along directions 2 and 3.

6.2.1 Bulk Conductivity in Direction 2

This study focuses on a series of methods for predicting the bulk conductivity along direction 2. Only direction 2 is considered, as it is assumed that the conductivity in direction 2 and 3 are equivalent. Whilst in Section 4.1.4.3 doubt was cast on this assumption, for now, the assumption will be made with the implications of this assumption being addressed in Section 6.4. The discussion presented here, first considers the thermal conductivity for a general fibre matrix system, before focusing on the bulk electrical and thermal conductivity for a realistic piece of CFC. This can be done despite the two conductivities being as a result of two different physical phenomena, because the two conductivity terms are analogies to each other and implemented in the same manner within their respective governing equations. After discussing methods for predicting the general bulk conductivity, conclusions will be drawn by applying these methods to the thermal and electrical conductivities separately.

This study will first consider two analytical methods for predicting the bulk conductivity along direction 2. These analytical methods assume the fibres are uniformly distributed throughout the material which, for CFCs, might not be a valid assumption to make. Therefore, the next part of this section will consider the bulk conductivity for a non-uniform fibre distribution.

6.2.2 Analytical Methods for Bulk Conductivity

The two analytical methods considered for predicting the bulk conductivity are the Series Rule of Mixtures and the Eshelby Method. A detailed description of each of these methods can be found in Section 2.5.4.2 and Section 2.5.4.1. For this study, the general b ulk thermal conductivity along direction 2 is referred to as K_2. To determine the accuracy of the predicted bulk conductivity obtained from the analytical methods, reference values are required. These are obtained by constructing a numerical model

which represents a true piece of CFC. Then, from this numerical model, the true bulk conductivity can be determined. Using the results from this numerical model, the relevance and accuracy of these analytical methods is considered by conducting a parametric study. Before considering the parametric study, the numerical model is first considered in detail.

6.2.3 Numerical Model

Whilst it is not feasible to model the entire internal structure of a piece of CFC using a Finite Element or Finite Volume approach (due to the large mesh required), it is possible to model a small unit cell representation of a piece of CFC. This is because these models consider a much smaller geometry i.e. on the scale of a few fibres, and so the required mesh is relatively small. This reduces the computational memory and processing time required to obtain a numerical solution. The general thermal conductivity is determined using a two dimensional steady state thermal conduction model. The model solves the standard Laplace equation,

$$\nabla \cdot (K \nabla T) = 0 \tag{6.6}$$

Where K is the generalised thermal conductivity tensor. A triangular mesh was generated using the inbuilt automatic mesh generation tool found within COMSOL [84]. A linear first order discretisation was used between elements. The resulting equations were solved using a direct solver called UMFPACK [134].

6.2.3.1 Geometry and Boundary Conditions

By considering a thick single layer ply with perfectly straight cylindrical carbon fibres of constant radius, all orientated in the same direction, the conduction problem can be modelled as a 2D cross sectional slice. This can be done due to the symmetry entailed. Given the assumption that the fibres are uniformly distributed, a unit cell can be obtained, as shown in Figure 6.1. The conductivity of the fibre (κ_f) and polymer (κ_p) are entered into the numerical model. The boundaries are defined such that the top and bottom boundaries are held at a fixed constant temperature, with the temperature on the top boundary (T_{top}) being greater than the temperature on the bottom boundary (T_{bottom}). The remaining boundaries are defined with a periodic boundary condition. From the numerical solution the bulk conductivity can be predicted. This is done by considering the Fourier Equation [75],

$$q_y = -K_2 \frac{dT}{dy} \tag{6.7}$$

Where q_y is the heat flux normal to the top boundary at each element in the numerical model. To predict the bulk conductivity of the sample, the average heat flux is required.

This is calculated by integrating the heat flux along the top boundary and then dividing this by the length of the heat flux boundary, this is expressed mathematically by

$$\bar{q_y} = \frac{\int q_y dz}{L} \tag{6.8}$$

As the unit cell is considered to be square, the length of all the boundaries are the same and hence the parameter L, shown in Figure 6.1, is defined as the length of the heat flux boundary. By assuming the temperature profile is uniform and linear, the differential term in Equation (6.7) can be equated as a simple difference equation, where

$$\bar{q_y} = -K_2 \left(\frac{T_{top} - T_{bottom}}{L} \right) \tag{6.9}$$

Using the heat flux obtained from the numerical results, it is therefore possible to solve Equation (6.9) for the bulk conductivity, (K_2).

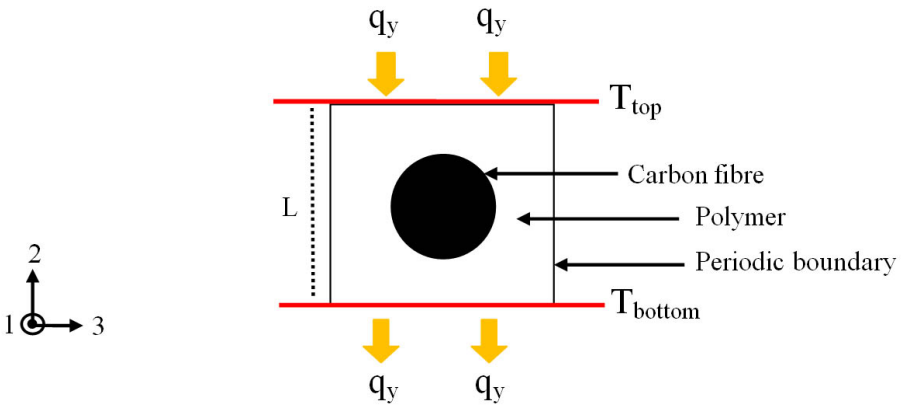

FIGURE 6.1: Illustration of the unit cell used within the numerical model to predict the bulk conductivity

6.2.4 Parametric Study of Predicted Bulk Conductivity

A parametric study has been conducted to investigate the accuracy of the two analytical methods for predicting the bulk conductivity, K_2. This study considers the following parameters: volume fraction of fibre (ϕ_f), ratio of polymer and fibre conductivity (κ_p / κ_f) and the homogeneity of fibre distribution. The accuracy of the analytical models is obtained by comparing their values against the predicted conductivity values calculated from the numerical model outlined above.

6.2.4.1 Variation in Fibre Volume Fraction

The fibre volume fraction is controlled by considering a fixed polymer box and varying the radius of the fibre. The bulk conductivity (K_2) as a function of volume fraction (ϕ_f)

is shown in Figure 6.2. For this investigation, the conductivity of the polymer (κ_p) is 0.425 $Wm^{-1}K^{-1}$ and the conductivity of the fibre is (κ_f) 230 $Wm^{-1}K^{-1}$.

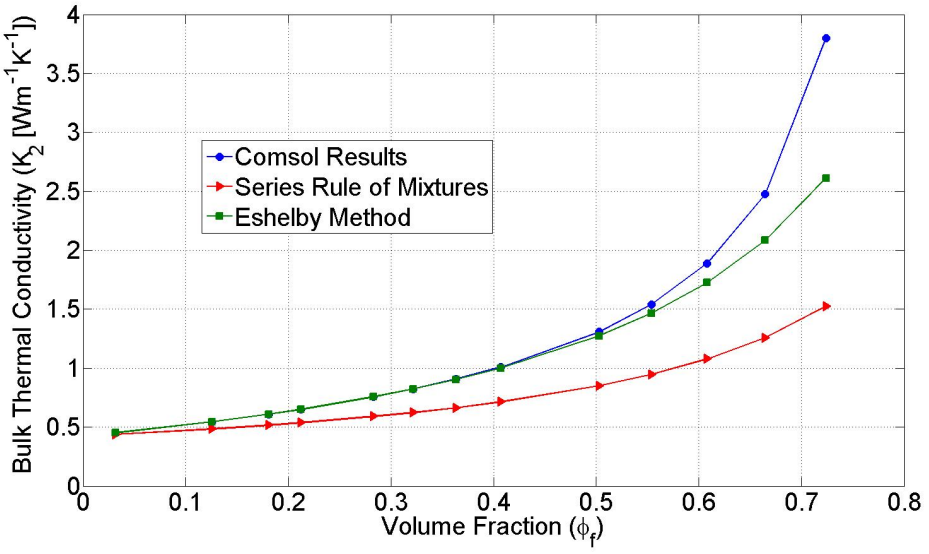

FIGURE 6.2: Effect of fibre volume fraction on the predicted bulk conductivity of the composite material. Ratio of conductivities 1.84×10^{-3}

The results shown in Figure 6.2 reveal that as the volume fraction of fibres increases the bulk conductivity increases, as expected. From Figure 6.2, it is also noticeable that at low volume fractions all the models converge to the same conductivity. However, as the volume fraction is increased, the accuracy of the Series Rule of Mixtures decreases as it diverges away from the COMSOL results. The Eshelby Method remains relatively accurate as the fibre volume fraction (ϕ_f) increases up to approximately 0.55. Above this fibre volume fraction, the Eshelby Method results also diverge away from the COMSOL results. Given the typical volume fraction for CFC is around 65%, it is evident that the Eshelby Method is more representative than the Rule of Mixtures for predicting K_2.

6.2.4.2 Variation in the Conductivity Ratio

Next the ratio of polymer conductivity to fibre conductivity is considered. The comparison between the analytical methods and the COMSOL results for the bulk conductivity (K_2) is shown in Figure 6.3. With reference to Figure 6.3, as the ratio of the conductivities tends to 1, all the models converge to the same value of conductivity. This is expected as when κ_p/κ_f equals one, the material is isotropic, and so the bulk conductivity is easy to predict. As the ratio of the two conductivities tends to zero, the Series Rule of Mixtures is not very accurate compared to the COMSOL method. The accuracy of the Eshelby Method compared with COMSOL remains relatively unaffected by varying the conductivity ratio given a uniform fibre distribution.

The ratio of conductivities for the thermal and electrical properties are 0.01 and 1×10^{-6},

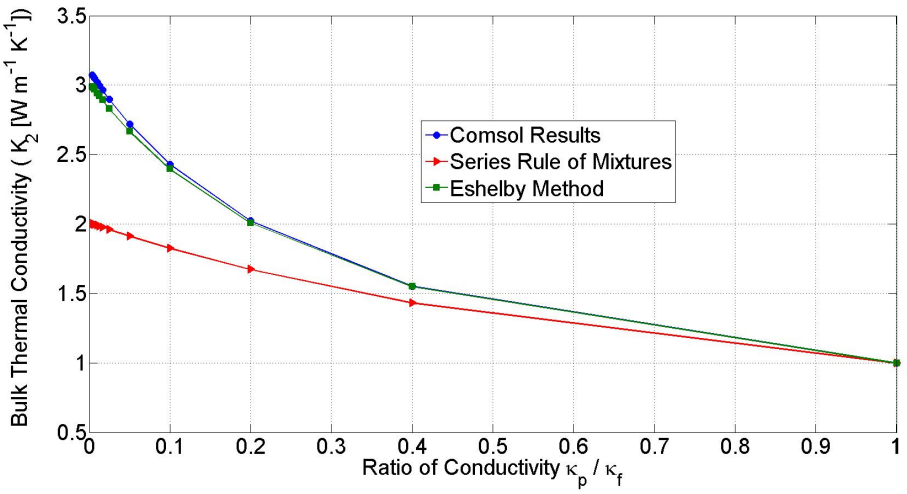

FIGURE 6.3: Effect of the ratio of conductivities on the predicted bulk conductivity for each of the different methods. The volume fraction was kept constant at 0.5 and $\kappa_p = 1\ Wm^{-1}K^{-1}$

respectively [19, 131]. Using these conductivity ratios and the results presented in Figure 6.3, it is evident that the Series Rule of Mixtures is not very accurate. However, at the same conductivity ratios, the Eshelby Method remains relatively accurate as there is minimal variation from the COMSOL result.

6.2.4.3 Variation of Carbon Fibre Distribution

In the two previous studies, the geometry used in the numerical model assumed a uniform fibre distribution. Now, the discussion moves on to see what effect the non-uniform fibre distribution has on the bulk conductivity and how a non-uniform fibre distribution affects the accuracy of the two analytical methods. For the purpose of this investigation, the same numerical model as developed above is considered, but a new geometry shown in Figure 6.4 is considered. The fibre distribution is investigated by varying the separation of the fibres $\triangle Z$, whilst keeping $\triangle Y$ constant. The boundary properties and the method for determining the bulk conductivity remain unchanged. The conductivity of the carbon fibres was taken to be 230 $Wm^{-1}K^{-1}$ and 0.425 $Wm^{-1}K^{-1}$ for the polymer. The fibre volume fraction was kept constant at (ϕ_f) 0.5.

The bulk conductivity in both the z and y directions are investigated as a function of $\triangle Z$. To predict the bulk conductivity in the z direction, the boundary conditions for the top and bottom were swapped with the sides and vice versa. The results for this investigation are shown Figure 6.5, where the bulk conductivity is plotted as a function of $\triangle Z/\ \triangle Y$.

The conductivities predicted by the two analytical methods remain constant despite variations with $\triangle Z/\triangle Y$. This is because the analytical methods consider a uniform

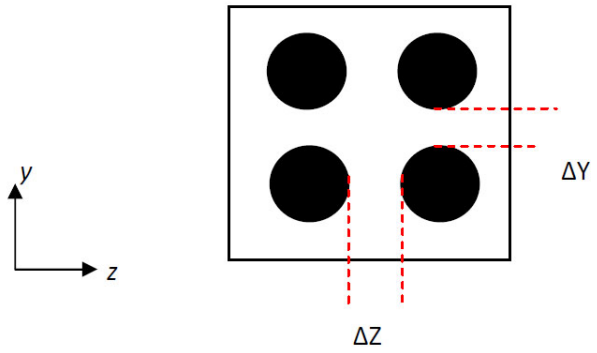

FIGURE 6.4: 2D schematic diagram of the model designed in COMSOL. The separation between the fibres along the z direction was varied ($\triangle Z$), whilst keeping $\triangle Y$ constant.

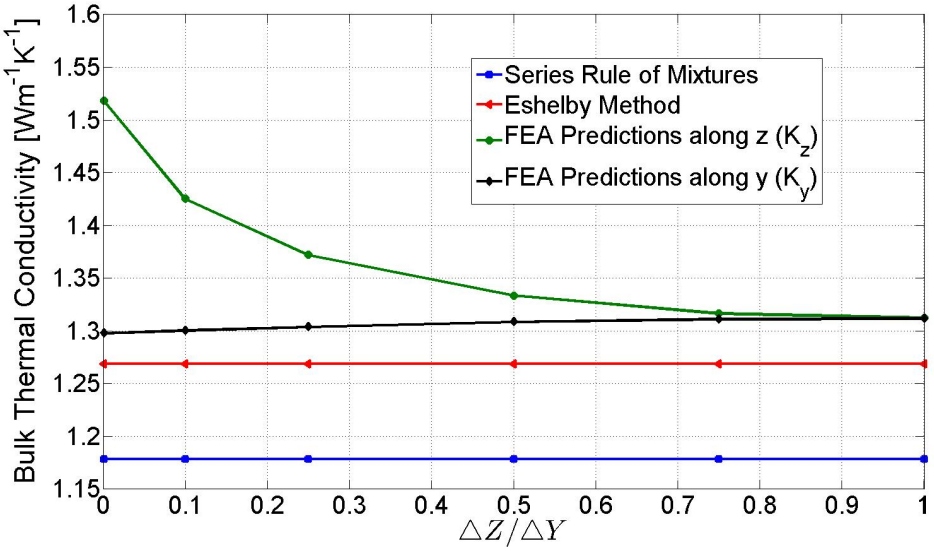

FIGURE 6.5: Bulk conductivity dependency on the carbon fibre separation ($\triangle Z$). Ratio of conductivities 1.84×10^{-3}, fibre volume fraction of 0.5

fibre distribution i.e. there is no dependence on fibre distribution considered. When the fibres are uniformly distributed (i.e. $\triangle Z/\triangle Y = 1$), the bulk conductivity calculated for the z and y directions are equal. As $\triangle Z/\ \triangle Y$ tends towards zero, the conductivities calculated from the numerical models diverge away from the analytical solutions. The conductivity in the y direction shows a slight decrease, whereas the bulk conductivity in the z direction increases more rapidly. This increase in bulk conductivity in the z direction is due to the highly conductive fibres coming into contact with each other. Despite the divergence in K_z, the magnitude of the variation is only a small fractional difference from the conductivity of the uniform fibre distribution. This is due to the large band of polymer which remains above and below the fibres, which dominates the bulk conductivity. This large band of polymer is not likely to be present in a typical CFC. Therefore, despite the small variation in conductivity, Figure 6.5 does indicate that there is an effect, on the bulk conductivity in the through thickness direction, as

the fibre distribution becomes less uniform. This conclusion is re-considered in more detail in the next section.

6.3 Percolation Effects on Bulk Conductivity

From the previous section, it is evident that a non-uniform fibre distribution can increase the through thickness bulk conductivity (K_2), in the event of fibre to fibre contacts. In this section, a series of numerical models has been developed which consider in depth how the variation in non-uniform fibre distribution affects the bulk conductivity. These models have been used to investigate what effect percolation has on the bulk conductivity. Percolation effects have already been discussed in detail in Section 2.5.5.

6.3.1 Modelling Strategy

The numerical model is again taken to be a 2D stationary conduction model based on Equation (6.6). The only difference with these models is that the geometry is changed. To create the geometry, a bespoke numerical subroutine has been developed which aims to simulate the realistic CFC fibre distribution, as shown in Figure 2.21. To achieve this, fibres are arranged randomly within a section of polymer using Monte Carlo based simulation techniques. Two different Monte Carlo based approaches for generating the geometry are considered.

6.3.1.1 Monte Carlo Fibre Placement Model

This method generates a fixed number of circles randomly placed within a block of polymer. Due to the fixed number of fibres, the volume fraction is controlled by the fibre radius. All the fibres within the model have the same radius. This is a valid method to use, as it has been reported by [82] that the fibre radius does not have a significant effect on the percolation threshold. The polymer is depicted by a rectangular box with unit dimension in directions 2 and 3. The carbon fibres are placed within this rectangular box. Each circle is positioned by generating two random numbers which are used to describe the centre of the circle. When placing each new circle, its location is checked against each of the previously placed circles to determine if its location is valid. The validity is determined by checking that the entire circle lies inside the bounds of the polymer, and that if two or more circles do overlap, it is limited to 10% of the circles radius. This process is repeated until a predefined number of fibres (i.e. circles) have been placed within the polymer. A geometrical representation of this model is shown in Figure 6.6.

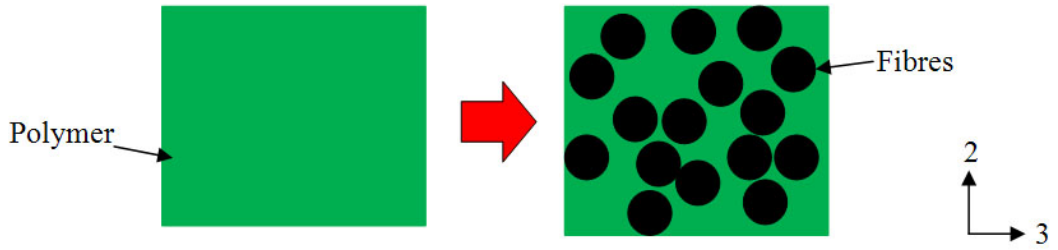

FIGURE 6.6: Typical geometry created by the Monte Carlo code for random fibre placement. (left) initial empty polymer matrix, (right) matrix with a predefined number of fibres randomly placed within

The numerical model allowed fibres to overlap, as the model assumes the fibres to be perfect circles, and so at most there will only ever be a single point of contact, between two touching fibres. This is considered to be unrealistic, as carbon fibres are not perfect circles and due to their surface roughness, there is likely to be a much larger contact region between neighbouring fibres. Furthermore, it is numerical difficult to accurately model a single point of electrical contact between two highly conducting circles in a poorly conducting matrix. To address both of these issues, the fibres where allowed to overlap by 10% of the circles radius. This overlap leads to 1.3% of the area of one fibre, overlapping with the area of another fibre. This small overlap fraction was considered to be large enough to remove any numerical errors whilst small enough to account for the physical contact between fibres.

Using this method, it is difficult to obtain a fibre volume fraction above approximately 65%. This is due to the methods inability to pack tightly lots of fibres close together. To obtain a higher fibre volume fraction, a second Monte Carlo based approach has been considered.

6.3.1.2 Monte Carlo Fibre Removal Model

This model starts with a perfect fibre packing arrangement which produces the highest possible fibre volume fraction. Then, a specified number of randomly selected circles (fibres) are removed leaving polymer in their place. In this model, the fibre volume fraction is controlled by varying the number of fibres which are removed. An illustration of this model is shown in Figure 6.7.

The initial tightly packed fibres are again allowed to overlap by the same amount as used within the 'Monte Carlo fibre placement model', outlined above.

6.3.2 Governing Equations and Boundary Conditions

The initial conductivities for this study were taken to be $\kappa_f = 1 \times 10^5\, Wm^{-2}K^{-1}$ and $\kappa_p = 1\, Wm^{-2}K^{-1}$, and the temperature difference across the sample was 1000 K. The

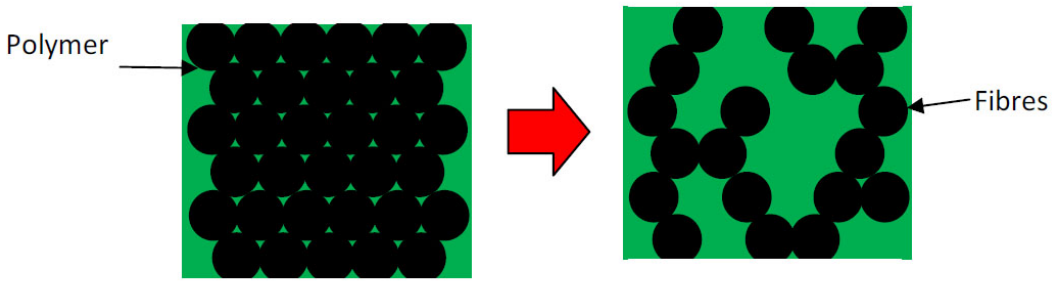

FIGURE 6.7: 2D representation of the fibre removal geometry. Left) Initial maximum packing arrangement. Right) After a random number of fibres have been removed.

bulk conductivity of the different geometries was calculated using the same method as that outlined previously by Equation (6.9). Due to the random nature of the Monte Carlo based simulations, it is important to collect a large number of results for each specified volume fraction, in order that an average conductivity can be calculated.

6.3.3 Comparison of Different Models

The results for both of the different Monte Carlo based models are shown in Figure 6.8. Each data point shown on the graph represents an average conductivity obtained from the repeated simulations for a given fibre volume fraction. The vertical bars which surround each data point are the range bars, which represent the variation in predicted conductivities for each specific volume fraction. This figure also includes the bulk conductivity predicted from the two analytical methods considered previously e.g. Series Rule of Mixtures (green) and the Eshelby Method (red).

With reference to the results in Figure 6.8, consider initially the results for the Monte Carlo fibre placement model. For low fibre volume fractions, the predicted bulk conductivity from this model shows minimal variation from the values predicted by the analytical methods. As the fibre volume fraction increases, the average conductivity predicted by the fibre placement model shows that there is a divergence away from the analytical methods. When the fibre volume fraction is greater than 0.6, the bulk conductivity shows a more dramatic increase. Whilst this in itself does not prove the existence of percolation affects, further information can be gained by considering the range bars. These show that the maximum predicted conductivity suddenly and dramatically increases at this volume fraction. This demonstrates that within some of the randomly created geometries, percolation effects did occur. When the fibre volume fraction (ϕ_f) is greater than 0.6, the bulk conductivity shows a more gradual increase in bulk conductivity towards the conductivity of the fibre. Now, the predicted bulk conductivity from the fibre removal model is considered. These results show that, at low volume fractions, there is a strong agreement with the predicted bulk conductivity determined

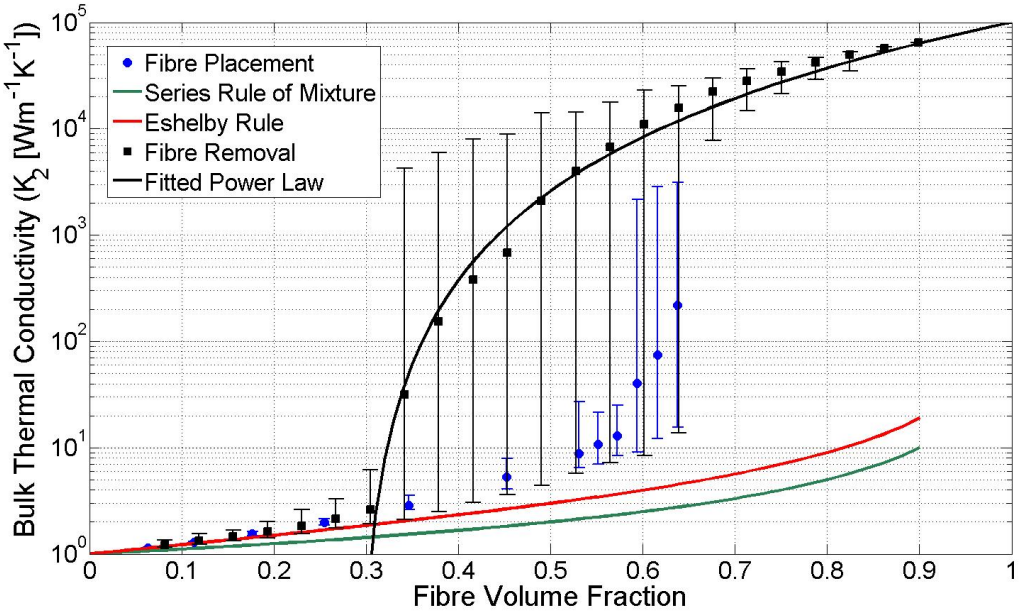

FIGURE 6.8: Predicted bulk conductivity as a function of fibre volume fraction for two Monte Carlo methods and the two analytical methods

by all the previous methods. As the fibre volume fraction (ϕ_f) increases beyond 0.3, the dramatic increase in average bulk conductivity and the sudden increase in the size of the range bars, indicates that percolation affects are occurring. Furthermore, the range bars indicate that percolation effects were highly variable within the simulation results when the fibre volume fraction is greater than 0.3 but less than 0.6. Either side of this volume fraction range, there is a sudden decrease in the range of predicted conductivities, which implies that when the fibre volume fraction (ϕ_f) is less than 0.3, the percolation effects never occur and when the fibre volume fraction is greater than 0.6, the percolation effects usually occur.

An attempt is now made to fit the empirical percolation power law given in Equation (2.20) to the results from the fibre removal model. The fitted line is shown in Figure 6.8. The fitted curve parameters are ϕ_{perc} equal to 0.29 and α equal to 3. The percolation threshold obtained is much lower than the theoretical value given by [82, 80]. This is due to the initially tightly packed fibre arrangement which forces an increase in the number of percolation paths. As a result, this indicates that the removal model is not suitable for predicting the percolation threshold. It is not feasible to try and fit the same percolation power law to the fibre placement results, as only 5 points show any sign of percolation, and this is not enough get an accurate line fit.

6.3.3.1 Effect of Fibre Overlap on Percolation Models

In the above discussions, the numerical models considered a maximum fibre overlap of 10% of the fibre radius. The affect of varying this maximum allowed fibre overlap is now considered by using the fibre removal model. The predicted bulk conductivity for a maximum overlap of 10% and 5% is shown Figure 6.9.

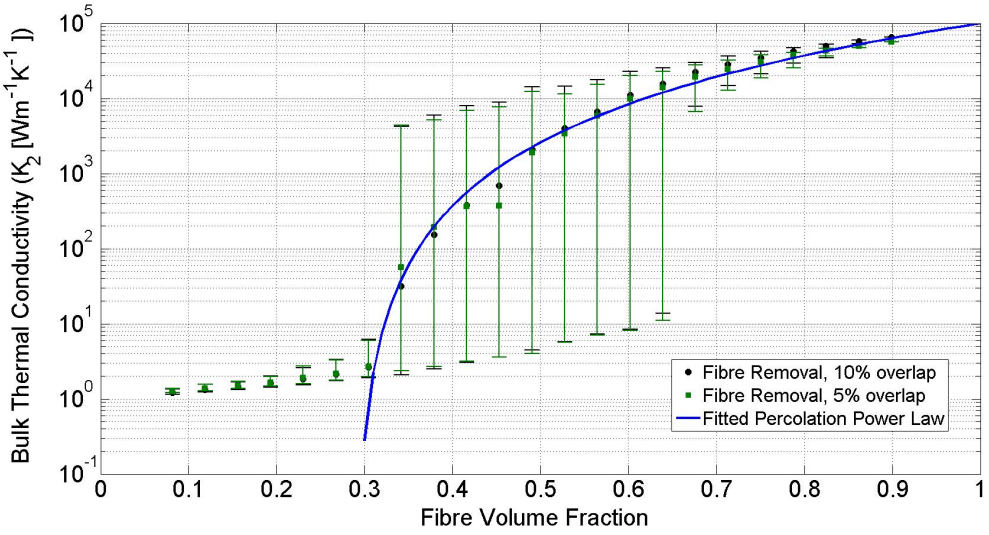

FIGURE 6.9: Predicted bulk conductivity from the fibre removal model as the maximum fibre overlap is varied

It is evident from Figure 6.9, that there is a minimal variation in bulk conductivity as the overlap is varied. This can be explained, by considering that once there is sufficient overlap to cause a good fibre to fibre contact, varying the overlap further does not affect bulk conductivity.

6.3.3.2 Reviews of Percolation Models

The two numerical percolation models discussed above, show that a non-uniform fibre distribution does affect the bulk conductivity of a material even when the fibre volume fraction is below the percolation threshold. By considering the model geometries and the numerical results, it is believed that the fibre placement model gives a more realistic fibre arrangement than the fibre removal model. Whilst it is not possible to fit the empirical percolation power law to the random fibre placement model, it is still possible to get a prediction for the percolation threshold (Φ_{perc}) to be approximately 0.6. This percolation threshold value is slightly lower than the theoretical value of 0.68 predicted by [82, 80]. An underestimate of the percolation threshold is expected as the fibres here were allowed to overlap by 10%. The fibre removal model severely underestimates the percolation threshold, due to its initially tightly packed arrangement. Despite this

the fibre removal model is still of interest, as it demonstrates how the bulk conductivity would behave near and above a percolation threshold. This is something that the random fibre placement model cannot do. It is possible to use the random fibre removal results to predict the bulk conductivity for the fibre placement model. Since the fibre removal model and the fibre placement model give similar trends and conductivities around their respective percolation thresholds. Finally, by recognising that the initial fibre volume fraction for CFCs ($\Phi_f(t_0)$) is 0.65, it is evident from the fibre placement model that the percolation effects will affect the bulk conductivity in a real piece of CFC. The extent to how much percolation affects the conductivity when compared with the other numerical model is considered in the next section, for the thermal and electrical conductivities separately.

6.4 Relevance of these Bulk Conductivity Methods to the Thermal and Electrical Conductivity of CFCs

Having considered two different methods for predicting the bulk conductivity, it is now worth considering how realistic each of these methods is for predicting the bulk thermal and electrical conductivity of a pristine CFC sample. It is important to understand the relevance of each of these methods as they will be used within the thermo-chemical degradation model.

For the above methods to be considered, a series of material properties are required. This study considers a CFC which is comprised of a carbon black filled epoxy called M21 and a carbon fibre called T700s. For the fibre, T700s, there is a published data sheet which states that the thermal conductivity (κ_f) is 9.37 $Wm^{-1}K^{-1}$ and the electrical conductivity (σ_f) is 62×10^3 Sm^{-1} [19]. There is no data sheet available for the epoxy M21. However, we can take solace from average epoxy properties published in [131, 135]. Given an epoxy with a carbon black filler, the typical electrical conductivity (σ_p) is $1 \times 10^{-6} Sm^{-1}$ and a typical thermal conductivity (κ_p) is between 0.1 and $0.2 Wm^{-1}K^{-1}$. The published fibre volume fraction ($\Phi_f(t_0)$) for this CFC is 0.65.

6.4.1 Electrical Bulk Conductivity

The electrical conductivity is considered first, as it is possible to make a direct comparison between the experimental results, presented in Chapter 4, and the numerically predicted values. Recall that the electrical conductivity for the unidirectional panel are σ_2 equal to $0.1\,Sm^{-1}$ and σ_3 is equal to $2 \times 10^{-3}\,Sm^{-1}$. The through thickness electrical conductivity for the quasi-isotropic panel (σ_3) was $0.96 Sm^{-1}$. By considering the material properties given above (i.e. σ_f is equal to $62 \times 10^3\,Sm^{-1}$ and σ_p is $1 \times 10^{-6}\,Sm^{-1}$),

the predicted bulk electrical conductivity from the different methods are shown in Figure 6.10.

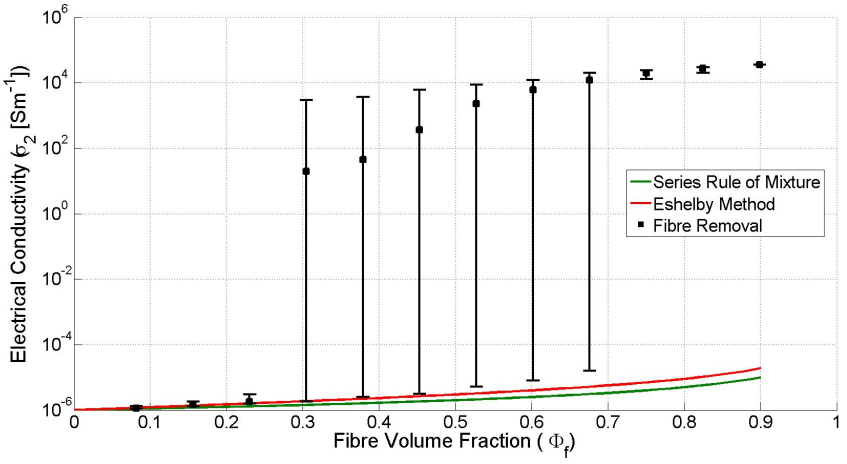

FIGURE 6.10: Results for the bulk electrical conductivity from the two numerical modelling approaches are shown

Figure 6.10 shows that the analytical methods, Series Rule of Mixtures and the Eshelby Method, drastically underestimate the bulk electrical conductivity. This is because of the percolation effects which affect the bulk conductivity. The percolation threshold is noticeable in these results by the sudden jump in bulk conductivity, predicted by the fibre removal model when the fibre volume fraction (Φ_f) is approximately 0.3. It has not been possible to consider the fibre placement model here, as due to the very low conductivity of the polymer, the numerical model was unable to conserve the current density and so the numerical results were erroneous. However, as has already been discussed, it is possible to use the bulk conductivity values predicted by the fibre removal method around the percolation threshold to obtain a bulk conductivity for when Φ_f is approximately 0.65. By considering the range of bulk conductivity values at the percolation threshold, it is evident that the experimental results can be explained by the percolation effects predicted by this model. The range of conductivities around the percolation threshold is considered as the fibre volume fraction of the samples used in the experiment are not thought to be sufficiently above the percolation threshold to show a constant conductivity dominated by the percolation effects.

6.4.2 Thermal Bulk Conductivity

Whilst there are no experimental values for the bulk thermal conductivity for comparison purposes, it is still important to see how the predicted bulk thermal conductivity from the different models compare. The thermal conductivities predicted by the above methods, using the thermal conductivities stated in Section 6.4 (i.e. κ_f is $9.37\,Wm^{-1}K^{-1}$ and κ_p is $0.1\,Wm^{-1}K^{-1}$) are shown in Figure 6.11.

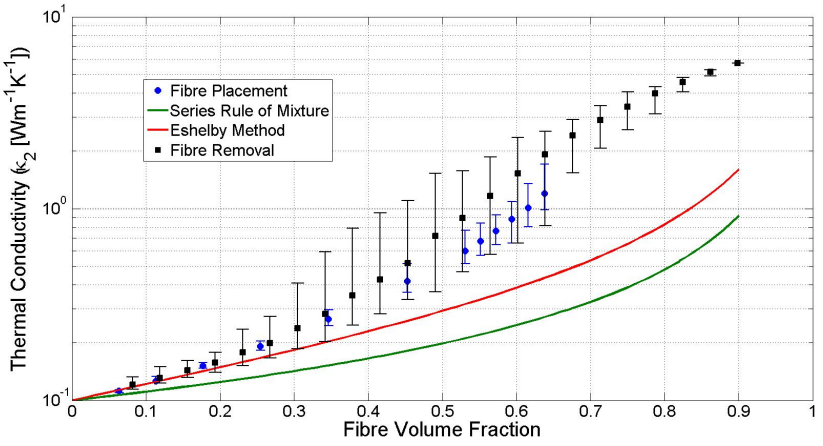

FIGURE 6.11: Results for the bulk thermal conductivity from the two numerical modelling approaches are shown

The predicted thermal conductivities given by the numerical model and the two analytical methods give a much closer agreement than has been observed for the electrical conductivity above. This is due to the CFCs constituent components having similar thermal conductivities, and because of this, the percolation effects are greatly diminished. Despite this, there is still a noticeable divergence in predicted bulk thermal conductivity from the analytical methods and the Monte Carlo percolation models. The slight percolation effects which are observed through the variation in the range bars when ϕ_f is 0.5, are believed to be exaggerated due to the 10% overlapping of fibres, which decreases the thermal contact resistance of the fibre to fibre contacts. Given there is less than an order of magnitude difference between all the predicted thermal conductivities when ϕ_f is equal to 0.65, the choice of method for predicting the bulk thermal conductivity is less critical than for the electrical conductivity. Future numerical studies will consider the sensitivity of the numerical predictions to increasing the bulk thermal conductivity by artificially varying the thermal conductivities of the fibre and polymer. This achieves an increase in the thermal conductivity predicted by the Eshelby Method which brings it closer to the predicted values from the Monte Carlo percolation methods.

6.4.3 Summary

The discussion presented above has shown that to predict accurately the bulk electrical conductivity in direction 2 and direction 3, the percolation effects cannot be ignored. However, for the thermal bulk conductivity the percolation effects have much less of an impact on the bulk conductivity. Furthermore, it is also evident that the effects of the polymer degradation i.e. the increase and gas and char, will have an effect on the bulk thermal conductivity, but not the electrical conductivity. It is not possible to include in the Monte Carlo based percolation method the effects of gas and char. Therefore, whilst the percolation theory can be used to predict the bulk electrical conductivity,

for the bulk thermal conductivity the only available methods are the Rule of Mixtures and the Eshelby Method. However, as it stands currently, the Eshelby Method is only applicable for two composite materials with two species. An expansion of the Eshelby Method which allows it to consider a composite system with more than two species is outlined below.

6.4.4 Bulk Conductivity for a Decomposing CFC

It is only important to consider the bulk thermal conductivity as the CFC degraded. This is because the electrical conductivity during the polymer degradation is kept constant, as the fibre contacts continue to dominate the bulk electrical conductivity. Considering just the thermal conductivity, the results presented above indicate that the constituent components of the decomposing polymer have a dramatic effect on the bulk thermal conductivity. The previous thermo-degradation models have generally considered the Rule of Mixtures to predict the bulk conductivity, due to its ability to consider a composite with any given number of constituent components. However, the results presented in this chapter have shown that the Series Rule of Mixtures is not as accurate as the Eshelby Method for predicting the bulk thermal conductivity of a pristine piece of CFC. Therefore ideally, the Eshelby Method would be used to predict the bulk thermal conductivity within the thermo-chemical degradation model. However, the Eshelby Method is limited to only being able to consider two components within a composite material. Therefore, this method needs to be expanded to allow for the inclusion of the polymer degradation products (char and gas).

The expansion is achieved by considering that the volume which surrounds the fibres, contains a uniformly distributed amount of char, gas and polymer. This can be mathematically modelled by using the Rule of Mixtures. Based on this, the new modified Eshelby Method is given by

$$K_2 = K_{mix} + \frac{K_{mix}(K_f - K_{mix})\Phi_f}{K_{mix} + (1 - \Phi_f)(K_f - K_{mix})/2} \tag{6.10}$$

Where the conductivity of the polymer (K_p) used in the original Eshelby equation as given in Equation (2.19), is now replaced with K_{mix}. This new conductivity defines the mixture of the polymer, char and gas. The conductivity for this mixture of species can be determined by either Rule of Mixtures; Series Rule of Mixtures defined as

$$K_{mix} = \left(\frac{\widehat{\phi_p}}{K_p} + \frac{\widehat{\phi_g}}{K_g} + \frac{\widehat{\phi_c}}{K_c} \right)^{-1} \tag{6.11}$$

or the Parallel Rule of Mixtures,

$$K_{mix} = \widehat{\phi_p} K_p + \widehat{\phi_g} K_g + \widehat{\phi_c} K_c \tag{6.12}$$

As a result, there are two new methods which are defined as Eshelby-Parallel Method for when the Parallel Rule of Mixtures is used and the Eshelby-Series Method for when the Series Rule of Mixtures is used. The Rule of Mixtures equations, given above, consider a new volume fraction. This is because this method only considers the volume fraction, of the polymer, char and gas which are present within a unit cell, i.e. volume not occupied by fibres. This new volume fraction is defined as $\widehat{\phi_i}$ for each species i. The new volume fraction is defined for the solid species as

$$\widehat{\phi_i} = \frac{\frac{m_i}{\rho_i}}{V_p(t_0)} \tag{6.13}$$

Where the initial volume of polymer is given by $V_p(t_0)$. Equation (6.13) only defines the volume fraction for the char and polymer. However, it is not possible to use the above method to determine the volume fraction of gas, as the gas is considered compressible. Therefore, the volume of gas is again determined by considering the remaining volume which is not occupied by any of the solid species. This is defined by

$$\widehat{\phi_g} = 1 - \widehat{\phi_{ch}} + \widehat{\phi_p} \tag{6.14}$$

These proposed modifications to the Eshelby Methods and the original Rule of Mixtures are considered in Figure 6.12. The comparison here is conducted for when there is no char produced due to the pyrolysis and hence the polymer is degrading into just gas. The results shown in Figure 6.12 show that the bulk conductivity for K_2 as the polymer volume fraction decreases.

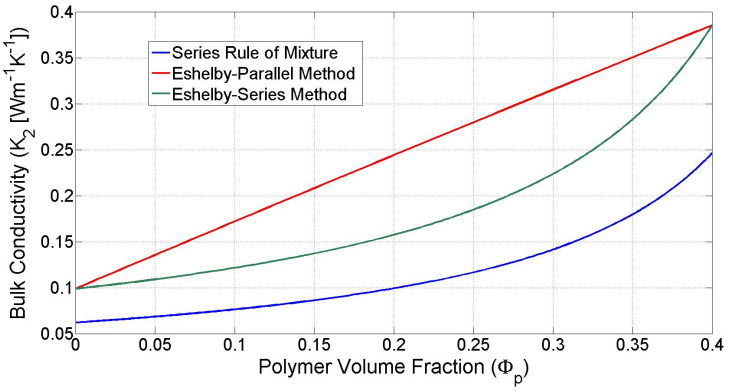

FIGURE 6.12: Comparison between the modified Eshelby Methods and the Series Rule of Mixtures as the volume fraction of polymer is decreased

Figure 6.12 shows that both modified Eshelby Methods predict a higher thermal conductivity than the Series Rule of Mixtures, as expected. The two modified Eshelbly Methods predict the same conductivity when ϕ_p is 0 and ϕ_p is 0.4. This is because, at these limits, the Series and the Parallel Rule of Mixtures give the same bulk conductivity for K_{mix}. In between these values, the two Eshelby values vary due to the variation in the Rule of Mixtures. The effect of this variation on the numerical predictions is

considered in the later chapters.

6.4.5 Summary of Homogeneous Methods

When considering a homogenisation approach for modelling a piece of CFC, it is important to predict the bulk material properties. A series of analytical and numerical methods have been considered to predict the bulk conductivity along local direction 2. From the analytical methods, it appears that the Series Rule of Mixtures is the least accurate whereas the Eshelby Method appears more realistic. However, the major limitation with both these models is that they assume that the fibres are uniformly distributed. It has been shown that within a CFC this is not typically the case. Given a non-uniform fibre distribution, these analytical methods becomes less accurate. A numerical model has been built which can predict the bulk conductivity of a composite material given a non-uniform fibre distribution. Using these models, it has been possible to predict that the bulk conductivity within CFC is influenced by percolation. Although it has been shown that these effects do not completely dominate the bulk conductivity. It has been shown that when considering σ_2 and σ_3, it is important to consider the percolation effects. This implies that the highly conductive carbon fibres dominate the conductivity, with the polymer matrix and the reaction products having minimal affect.

For the thermal conductivity, it has been shown that, as the fibre and the polymer have more comparable thermal conductivities, percolation effects have less of an impact on the bulk thermal conductivity. Therefore, the reaction products might play an important role in defining the bulk conductivity and so need to be considered. Given the Eshelby Method has proven more realistic than the Series Rule of Mixtures, it would be better to use this within our thermo-chemical degradation models. Before the Eshelby Method could be used, the equation has been modified to allow the inclusion of the reaction products. A comparison of the Series Rule of Mixtures, and this new Eshelby Method will be considered later when the numerical model is experimentally verified.

6.5 Summary

This chapter has considered a framework designed to represent a carbon fibre composite material as a homogenised material. A series of different methods for predicting the bulk thermal and electrical conductivity have been considered. From this study, it is evident that these different conductivities require different methods for predicting their bulk conductivity. The above discussions have shown that to predict the bulk electrical conductivity accurately, the percolation method needs to be considered. To predict accurately the bulk thermal conductivity, this study has proposed a modified Eshelby Method. With this framework in place, the next step is to develop the thermo-chemical degradation model.

Chapter 7

Thermo-Chemical Degradation Model

With the numerical framework for modelling CFCs outlined in the previous chapter, the next step is to develop a bespoke numerical model which can investigate the damage caused by a lightning strike. With the review of previous thermo-chemical degradation models in mind, (Section 2.3), this chapter gives an overview of the required physical processes, followed by an explanation of the implementation required to model these physical processes. After this, the implementation of the model is then validated by considering its convergence against known solutions.

7.1 Modelling Overview

To model the damage caused by a lightning strike, firstly the energy input into a piece of CFC due to the lightning strike needs to be defined. As discussed in Section 2.2.4, a lightning strike has two energy inputs, volumetric Joule heat (discussed on Section 2.2.4.1) and a heat flux from the plasma arc (discussed in Section 2.2.4.2). The heat input from both of these processes is a function of the electrical current density within the material due to the current injection. The two heat sources then create a temperature profile within the material as a result of the thermal conduction.

The temperature profile then leads to the thermo-chemical degradation and phase change of the carbon fibres, as shown in Chapter 5 and discussed in Section 2.3. The polymer pyrolysis produces a combination of gas and char. The transport of the produced gas needs to be considered, as it is believed that the resultant internal gas pressure causes cracking and delamination within the decomposing material. The cracking and delamination has been witnessed in Chapter 5. It has also been recognised that there are mechanical processes which can damage a piece of CFC due to a lightning strike [9], but

these mechanical processes are believed to have minimal impact on the overall damage. This has been discussed, with regards to the experimental results in Section 5.2.3. A flow chart which summaries all these physical processes is given in Figure 7.1.

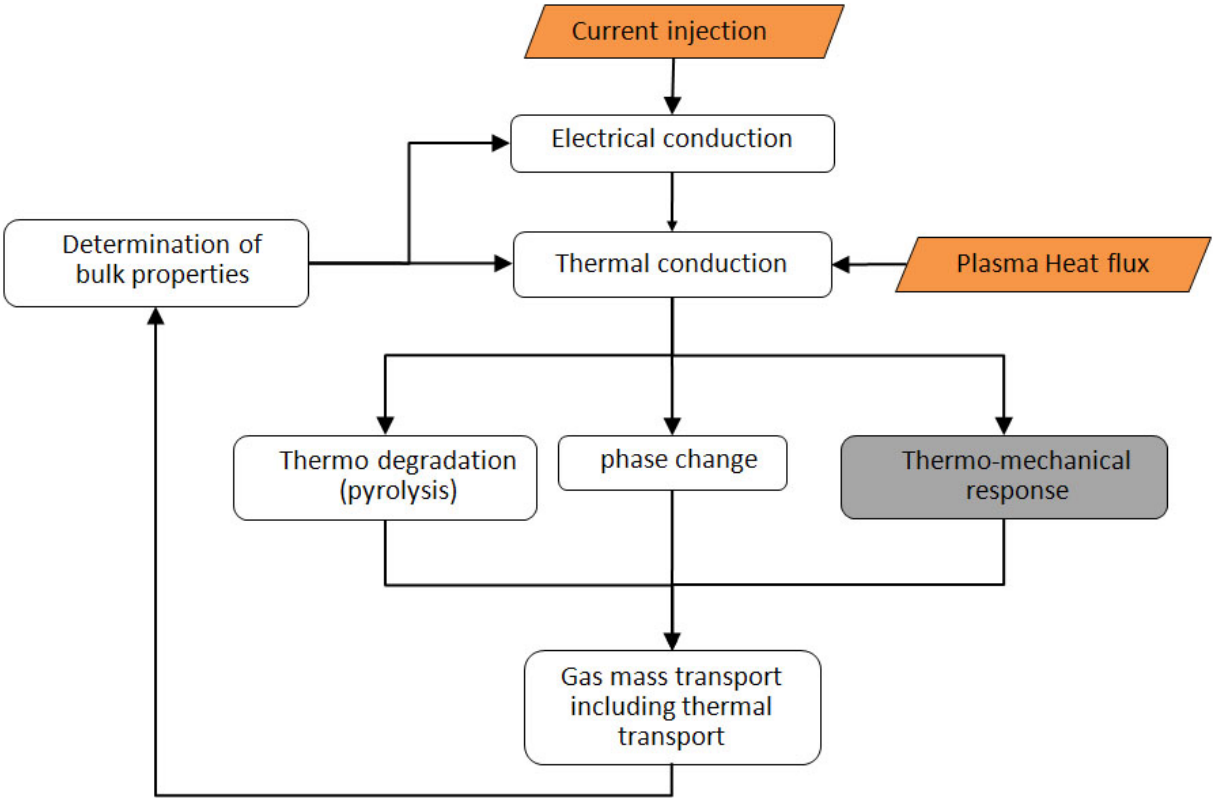

FIGURE 7.1: Overview of the different physical processes required to model the thermo-chemical degradation, along with how they are linked together

Based on the discussion presented above and by considering the experimentally observed damage from the lighting strike current impulse tests given in Section 5.2.3, the following refinements to the physical processes can be made. Firstly, because the mechanical processes are believed to have minimal impact on the damage, these physical processes can be ignored. Secondly, as experimentally observed in Section 5.2, it can be assumed that the fibre phase change has minimal impact on the results, and can therefore also be ignored. Despite these assumptions, the main limitation for modelling the damage caused by a lightning strike relates to the question of 'how can a wandering arc be modelled?'. The importance of the arc wandering has been discussed in Section 5.2.3. At present, whilst there are models to describe the energy input from an arc [37, 136, 27], there are no mathematical relationships which describe how an arc wanders and how it distributes its energy into a piece of CFC. As a result, the model considered here only investigates the thermo-chemical degradation due to laser ablation, thus avoiding this problem. It is possible to model the resultant damage from a laser beam more accurately than that of a lightning strike, since the heat input from a laser beam is very well defined. The model described here, is therefore, designed to replicate the

laser ablation experiment conducted in Section 5.1. The results from this study remain representative of the damage caused by a lightning strike, as the physical processes which result from a laser ablation are comparable to those from a lighting strike, as discussed in Section 5.2.3. To conclude, this model, therefore, still gives indicative conclusions as to the role of the physical processes to the damage caused to CFC due to a lightning strike.

7.2 Governing Physical Equations

The models governing physical processes which have been highlighted in Figure 7.1 are now considered in detail. Based on the discussion in the previous section, there is no attempt in the following work to include the corresponding physical processes for the electrical or the mechanical processes.

7.2.1 Thermal Transport

The thermal transport model solves for the temperature profile (T) within the material by considering

$$\frac{d\left(\rho C_V T\right)}{dt} = \nabla\left(\kappa \nabla T\right) + \frac{Q_d}{V}\frac{dm_p}{dt} - \nabla\left[v\left(\rho_g C_{V\,g} T + P\right)\right] \tag{7.1}$$

The material properties are given by the bulk specific heat capacity at constant volume (C_V), bulk density (ρ) and the bulk thermal conductivity (κ). The bulk heat capacity is considered for a constant volume because the gas filtration is dependent on pressure, and so it is not appropriate to consider the heat capacity at a constant pressure. This is contrary to the assumptions of previous studies (Section 2.6.4). These material properties are defined as bulk material properties due to the homogenisation approach. The methods for calculating these bulk material properties have been given in Chapter 6.

The physical meaning of the terms given in Equation (7.1) are now considered. The left hand side (LHS) term in Equation (7.1), considers the change in internal energy, in a fixed volume, as a function of time. The first term on the right hand side (RHS) considers the thermal conduction throughout the material. The second term on the RHS side considers the change in enthalpy (Q_d) due to the polymer pyrolysis. The final term on the RHS considers the variation in internal energy due to the resultant gas transport. The change in internal energy is given by the gas convection due to the gas filtration velocity, v_g, and the work done by the change in internal gas pressure (P). The resultant energy transport due to the mass transport was outlined by J. Anderson [137]. An assumption, inherent within the final term on the RHS, is that the equation assumes that all species within each unit cell are in thermal equilibrium. This removes the need to define a thermal transport equation separately for each species.

The thermal transport is coupled to the chemical reaction by the bulk thermal conductivity, which is a function of the species and the change in enthalpy. The species volume fraction is determined by the mass of the species in a given cell, as defined in the previous chapter by Equation (6.1). The mass of each species is controlled by the chemical reaction, which is dependent on temperature (T). Furthermore, after a chemical reaction, the internal energy of the system is changed due to Q_d.

7.2.2 Chemical Degradation and Gas Transport

To model the chemical degradation, each species requires its own equation. There is however, no need to consider an equation for the carbon fibre, as it is assumed that carbon fibres do not undergo a chemical reaction because they are considered to be solid and immobile. The governing equation for the polymer degradation is

$$\frac{dm_p}{dt} = -R \tag{7.2}$$

As is evident from Equation (7.2), the mass of the polymer (m_p) decreases due to the polymer pyrolysis. The pyrolysis reaction rate (R) is given by the Arrhenius equation,

$$R = Am_p \left(\frac{m_p(t) - m_p(t_\infty)}{m_p(t_0)} \right)^n \exp\left(-\frac{E_a}{\Re T} \right) \tag{7.3}$$

Where n, A, E_a and $\Re$ are the reaction order, the pre-exponential factor, the activation energy and the molar gas constant, respectively. The initial and final mass of the polymer are given by $m_p(t_\infty)$ and $m_p(t_0)$ respectively. The reaction products (char and gas) are incorporated by considering the conservation of mass, i.e. the rate at which the polymer is decomposing, is equal to the rate at which the char and gas is produced. The fraction of polymer mass which decomposes into gas is given by ζ_g. From the conservation of mass, it is evident that the mass fraction of char which is produced is defined by $1 - \zeta_g$. The governing equation for the mass of gas is given as

$$\frac{dm_g}{dt} = \zeta_g R + \nabla \left(v_g \, m_g \right) \tag{7.4}$$

The first term on the RHS considers the rate at which the mass of gas is produced. The second term on the RHS considers the mass of gas transport through the decomposing material. The governing equation for the mass of char is given by

$$\frac{dm_{ch}}{dt} = (1 - \zeta_g)R \tag{7.5}$$

This equation is similar to that for the gas (Equation (7.4)), only as the char is considered to be an immobile solid, there is no mass transport term included. The gas filtration

velocity (v_g) is given by Darcy's law such that

$$v_g = -\frac{\gamma \nabla P}{\mu \Phi_g} \tag{7.6}$$

Where γ and μ are the permeability and the gas viscosity respectively. The permeability represents the ability of a porous medium to allow a fluid to pass through and is, therefore, a function of the decomposing material. For this study, the permeability is given by Equation (2.30), as discussed in Section 2.6.3.1. The second term in the denominator represents the porosity of the material. The porosity is the fraction of empty spaces (voids) within a material through which the gas can filtrate. Since it is initially assumed that there are no voids within the CFC and that there are no mechanical forces (de-lamination etc.) considered by this model, it can be shown that the only free space through which a gas can filtrate is the space occupied by the gas. Hence, the porosity can be equated to the volume fraction of gas.

The final term to defined in Equation (7.6) is the gas pressure (P), which is calculated by assuming the ideal gas Law, i.e.

$$P = \frac{m_g \Re T}{M V_g} \tag{7.7}$$

Where M is the molar gas constant for the specified gas and V_g is the volume occupied by the gas within each cell. The volume occupied by the gas is determined by Equation (6.3).

7.2.3 Boundary and Initial Conditions

Based on the governing equations outlined above, the following boundary conditions and initial values need to be defined. Starting with the thermal transport, the initial temperature is assumed to be constant uniform temperature given by $T(t_0)$. To consider the heat flux from the laser beam, the corresponding thermal boundary conditions are modelled by a circular 2D Gaussian function, with the function being defined over the x-z plane:

$$Q_{flux}(x,z) = \frac{P_L}{A_{\mathrm{G}}} \exp\left[-\left(\frac{(x-x_0)^2}{2\Lambda^2} + \frac{(z-z_0)^2}{2\Lambda^2}\right)\right] \tag{7.8}$$

Where the beam radius is given as Λ and the Gaussian peak is defined around x_0 and z_0. The peak heat flux from the laser beam is defined by the power output from the laser (P_L), divided by the area under the Gaussian curve A_{G}. Additionally, all the boundaries are also considered to exhibit thermal convection and thermal radiation. The thermal convection is mathematically expressed by

$$q = h\left[T - T_{amb}\right] \tag{7.9}$$

Where h and q are the heat transfer coefficient and the heat flux density from the surface. The temperature on the surface is given by T and a constant ambient temperature is defined by T_{amb}. The thermal radiation is defined by assuming a black body radiation and so is defined by

$$q = \sigma_b \epsilon_{cfc} \left[T^4 - T_{amb}^4 \right] \tag{7.10}$$

here σ_b and ϵ_{cfc} are the Stefan Boltzmann constant and the emissivity of the CFC. The final set of initial conditions to consider are the initial mass of each species within a cell. The initial polymer ($m_p(t_0)$) and carbon fibre ($m_f(t_0)$) mass within a cell is given by the initial fibre volume fraction $\phi_f(t_0)$ and the density of each species. Hence, the initial fibre mass is defined as

$$m_f(t_0) = \phi_f(t_0) \rho_f V_{cell} \tag{7.11}$$

and the initial polymer mass is given by

$$m_p(t_0) = \left[1 - \phi_f(t_0) \right] \rho_p V_{cell} \tag{7.12}$$

These equations impose the not unreasonable assumption, that initially there is no char or gas within the CFC. Given that the gas transport is driven by the pressure gradient (shown in Equation (7.6)), the pressure at all boundaries is considered to be constant at 1 Atm. Therefore, the gas can escape through any boundary which has a favourable pressure differential.

7.3 Implementation of Numerical Model

Having considered the numerical equations required to represent the physical processes, the next step is to implement these physical processes into a numerical model. The choice of implementation is not totally obvious. Before considering the implementation of the equations, the model discretisation is considered.

7.3.1 Model Geometry

An illustration of the generic geometry used for all the forthcoming studies is shown in Figure 7.2. The model is cuboid with Cartesian spatial dimensions of L_x, L_y and L_z along the global axis directions x, y and z. A cylindrical coordinate system was also considered, as this would improve the efficiency of the model by reducing the number of mesh elements. However, it is not possible to represent the anisotropy of the CFC material properties using this coordinate base and so a three dimensional Cartesian coordinate system was chosen.

The geometry outlined in Figure 7.2 is discretised using a non-uniform mesh. A non-uniform mesh has been chosen, as it can dramatically improve the efficiency of the

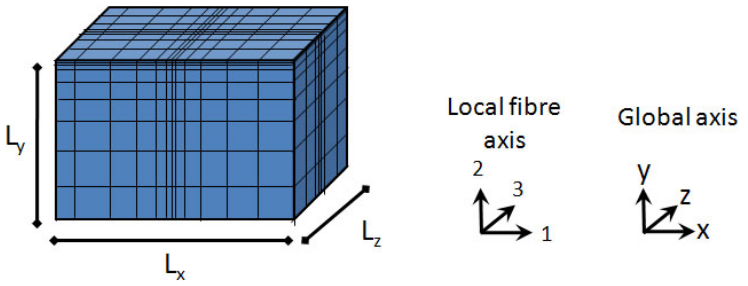

FIGURE 7.2: Generic geometry considered by this bespoke numerical model. The local fibre axis is defined with the fibre direction parallel to the x direction

solution by reducing the number of grid points. The design of the non-uniform mesh requires knowledge of the gradients of the dependent variables, as the accuracy of a solution is dependent on the size of mesh in relation to the gradient of the dependent variables. A steep gradient requires a fine mesh to obtain an accurate solution. By defining that the peak heat flux occurs in the centre of the top surface ($x - z$ plane in Figure 7.2), it is evident that the largest gradients will surround this region. This leads to the design of the non-uniform mesh shown in Figure 7.2. A more detailed illustration of the non-uniform mesh generated for use within this model is shown in Figure 7.3. This mesh represents a 1D line down through the centre (along y direction) of the geometry shown in Figure 7.2.

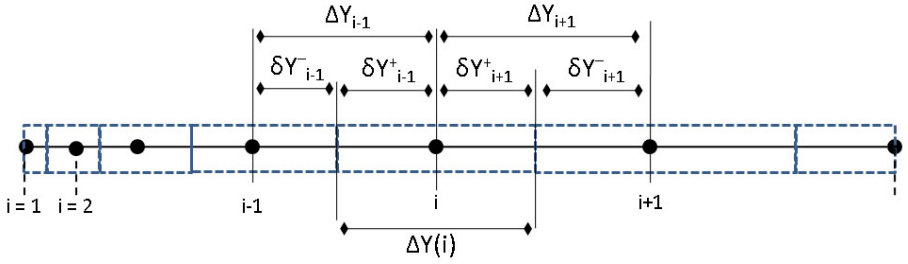

FIGURE 7.3: Illustration of the non-uniform mesh used within the numerical model

The element size depicted in Figure 7.3 is defined by the following arithmetic series,

$$\Delta Y(i) = \Delta Y(i-1) + d = \Delta Y(1) + d_y(i-1) \tag{7.13}$$

Where d_y is the element growth factor in the y direction and $\Delta Y(i)$ is element size for grid point 'i'. For the purpose of this study, the growth factor is equal to the initial element size i.e. $\Delta Y(1) = d_y$ and hence the mesh size in the y direction is defined by $\Delta Y(1)$. Notice that the first element in Figure 7.3 is given by half its original size, with the element node being placed at the boundary. The mesh is generated for the x and z direction using the same arithmetic series presented in Equation (7.13). However, $\Delta Y(1)$ is replaced by either $\Delta X(1)$ or $\Delta Z(1)$. Furthermore, the element growth rate for each of these principle directions can be independently controlled by $\Delta X(1)$ and $\Delta Z(1)$, respectively. By assuming the peak heat flux is in the centre of the top surface, the

initial mesh elements, $\Delta X(1)$ and $\Delta Z(1)$ are positioned in the centre of the x-z plane. The size of these mesh elements can then calculated symmetrically outwards from this point. With the element size in each dimension defined, the volume of each cell can be calculated, which is given by V_{cell}.

7.3.2 Fractional Step Method

Due to the large number of physical processes and the highly coupled nature of the equations, a fully coupled model would be unnecessarily complex and prove very slow to solve. These complications are overcome by applying a fractional step method, which replaces the direct fully coupled model by a linked chain of models [138]. Following from the above discussions in this chapter, the physical processes can logically be split into a series of sub models, as shown in Figure 7.4. Each of these sub models is then solved in turn from time t_τ to $t_\tau + \triangle t$. This time duration is referred to as the size of the global time step ($\triangle t$). This sequence is repeated a predefined number of time steps until the total simulation time is reached. Within each separate model the global time step ($\triangle t$) is split up and solved over a series of smaller sub time steps (δt_s). The size of the sub time step (δt_s) is defined by the number of division (n_s) into which the global time step ($\triangle t$) is divided into. It is, therefore, possible to define a different sub time step size for each of the models, with subscript 's' referring to the different models i.e. subscript 's' becomes R indicating the size of the sub time step taken by the chemical reaction model δt_R. Two further subscripts are defined as T and m, which refer to the thermal conduction and the mass transport models, respectively.

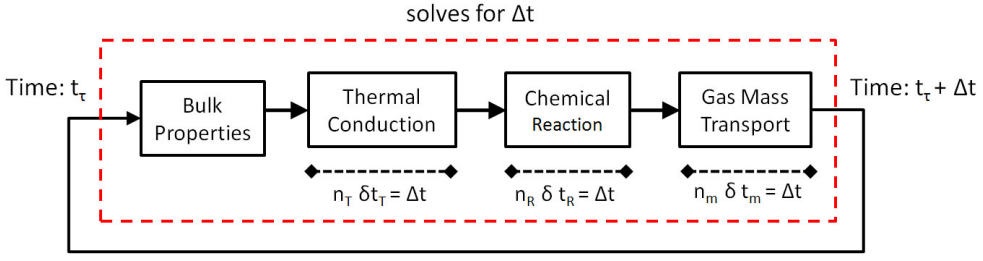

FIGURE 7.4: Diagram of the different models and the order in which they are solved in using the fractional step method

Following on from the discussion in Section 2.4.3.1, the convergence of the numerical solution is a function of the global time step size ($\triangle t$), the number of divisions each model is solved for (n_s) and the mesh growth rates. After having next considered the implementation of the physical equations, the discussion then considers the convergence of the implemented equations with reference to these parameters.

7.3.3 Implemented Equations

The methods for implementing the equations outlined above are now considered. The model is implemented in the same order presented (from left to right) in Figure 7.4. Therefore, the thermal conduction model is implemented and validated first. This is initially implemented in 1D before expanding the subroutine into 3D. Once the thermal conduction model has been implemented, the chemical degradation model and its coupling with the thermal conduction model, is then validated in 1D. The final subroutine, to implement is the gas transport model. This is done in two parts, firstly only the mass transport is implemented before the energy transport due to the gas mass transport is implemented within the same subroutine. All these equations have been implemented within Matlab.

7.3.3.1 Bulk Material Properties

The first section of the fractional step method outlined in Figure 7.4 requires the bulk material properties to be calculated. These bulk material properties are then passed into the relevant models when required. Before the bulk material properties are determined, first the volume fraction of each species is calculated using Equation (6.1). Then, using these volume fractions the bulk conductivities are calculated using the selected methods outlined in Section 6.4.5.

7.3.3.2 Thermal Conduction Model

The thermal transport given in Equation (7.14), is a decoupled form of the full equation given above in Equation (7.1). This allows for the thermal conduction to be solved separately from the other physical components. The resultant thermal conduction equation is given by

$$\int_{V_{cell}} \int_{t_T} \frac{\partial \left(\rho C_V T\right)}{\partial t} dt_T \, dV_{cell} = \int_{V_{cell}} \int_{t_T} \left[\nabla \left(\kappa \nabla T\right) + Q_J\right] \, dt_T \, dV_{cell} \tag{7.14}$$

The implementation of this thermal conduction equation assumes the bulk thermal conductivity is constant with temperature.

To reduce the required solution time, the thermal conduction model is solved by splitting up Equation (7.14) and solving for each of the principle directions (x, y and z) in turn separately [64]. The implicit finite difference equation for the one dimensional thermal conduction along the y direction is mathematically expressed as

$$\frac{\Delta Y(i)}{\delta t_T} \rho C_v T^1(i) = \kappa'_{+1} \frac{T^1(i+1) - T^1(i)}{\Delta Y(i+1)} - \kappa'_{-1} \frac{T^1(i) - T^1(i-1)}{\Delta Y(i-1)} + \frac{\Delta Y(i)}{\delta t_T} T^0(i) \rho C_v \tag{7.15}$$

Where the terms given a superscript '1', refer to their values for the current time step $(t_\tau + \delta t_T)$, and the terms denoted by a superscript '0' refer to their value at the previous time step (t_τ). The thermal conductivities in Equation (7.15), are given by κ_{+1} and κ_{-1}, where these conductivities refer to a weighted bulk thermal conductivity. The bulk conductivity is weighted to take into a variable thermal conductivity throughout the material. The weighted bulk conductivity is given by

$$\kappa'_{+i} = \left(\frac{1 - f_{+i}}{\kappa(i)} + \frac{f_{+i}}{\kappa(i+1)} \right)^{-1} \tag{7.16}$$

and

$$\kappa'_{-i} = \left(\frac{1 - f_{-i}}{\kappa(i)} + \frac{f_{-i}}{\kappa(i-1)} \right)^{-1} \tag{7.17}$$

The weighting terms, f_{+i} and f_{-i}, are given by the ratio of the element lengths as defined in Figure 7.4, by

$$f_{+i} = \frac{\delta^- Y_{+i}}{\delta^- Y_{+i} + \delta^+ Y_{+i}} \tag{7.18}$$

$$f_{-i} = \frac{\delta^- Y_{-i}}{\delta^- Y_{-i} + \delta^- Y_{-i}} \tag{7.19}$$

From these equations, a tri-diagonal matrix of the heat fluxes between elements is created. This matrix is then solved using a direct Gaussian elimination method. The temperature profile along x and z direction is then solved separately using the same method as outlined above.

7.3.3.3 Chemical Reaction

The resultant thermal profile is then passed into the chemical reaction model. The chemical reaction model considers only the chemical reaction and its resultant effect on the internal energy of the system. The polymer decomposition is described by Equations (7.2) and (7.3). These equations have been expanded so they can be solved analytically at each mesh element. The polymer degradation is considered for two cases: for when $n = 1$

$$m_p^1(i) = \exp \left[\ln \left(m_p^0(i) \right) \right) - \delta t_R A \exp^{\frac{E_a}{\Re T(i)}} \tag{7.20}$$

and for when $n \neq 1$

$$m_p^1(i) = m_p^0(i) \sqrt[1-n]{C^{1-n}(i) - (1-n)\, \delta t_R A \exp^{-\frac{E_a}{\Re T(i)}}} \tag{7.21}$$

Assuming the final mass of polymer, $m_p(t_\infty)$, in Equation (7.3) is zero, the fraction of polymer mass which remains at any given time ($C(i)$) can be expressed by

$$C(i) = \frac{m_p^1(i)}{m_p^0(i)} \tag{7.22}$$

From Equations (7.4) and (7.5), the resultant increase in the mass of gas and char without any transport terms can be expressed as

$$m_g^1(i) = \zeta_g \left[m_p^0(i) - m_p^1(i)\right] + m_g^0(i) \tag{7.23}$$

$$m_{ch}^1(i) = (1 - \zeta_g) \left[m_p^0(i) - m_p^1(i)\right] + m_g^0(i)) \tag{7.24}$$

As a result of the chemical reaction, the internal energy is reconsidered. This is achieved by considering the relevant terms in the thermal transport equation (Equation (7.1)), which results in the following thermal equation

$$\int_{V_{cell}} \int_{t_R} \frac{\partial \left(\rho C_V T\right)}{\partial t} \, dt_R \, dV_{cell} = \int_{V_{cell}} \int_{t_R} \frac{Q_d}{V} \frac{\partial m_p}{\partial t} \, dV_{cell} \, dt_R \tag{7.25}$$

The analytical form of this equation is then given as

$$T^1 = \frac{T^0 C_v^0 + \dfrac{\left[m_p(t^0) - m_p(t^1)\right] Q_a}{(m_g + m_f + m_p + m_{ch})}}{C_v^1} \tag{7.26}$$

Here, C_v^0 and C_v^1 are respectively the bulk heat capacity at constant volume before and after the chemical reaction has been considered for this time step.

7.3.3.4 Gas Mass Transport with Resultant Thermal Transport

The new species and temperature profiles are then passed to the gas transport model. Only one transport equation for gas is required as the other species (carbon fibre, polymer and char) are considered to be solid and immobile. The gas transport is implemented by considering the transport along only the y direction. This assumption is made given that the gas will try and escape through the decomposing material towards the atmosphere along the most direct route, which in this case is along the y direction towards the heated surface. The gas mass transport is, therefore,

$$\frac{\partial m_g}{\partial t} = -\frac{\partial m_g v_g}{\partial y} \tag{7.27}$$

which is written in the following form for use within the numerical model

$$m_g^1(i) = \frac{m_g^0(i) - \dfrac{v_g(i+1)\, m_g^1(i+1)\, \delta t_m}{\Delta Y(i+1)}}{1 - \dfrac{v_g(i)\delta t_m}{\Delta Y(i)}} \tag{7.28}$$

Due to the gas mass transport, the internal energy of the system needs to be reconsidered. This is achieved by considering the final term of the thermal transport equation (Equation (7.1)). The resultant thermal equation due to the gas mass transport is given in the integral form as

$$\int_{V_{cell}} \int_{t_m} \frac{\partial \left(\rho C_V T\right)}{\partial t}\, dV_{cell}\, dt_m = \int_{V_{cell}} \int_{t_m} -\frac{\partial}{\partial\, y} \left[v_g \left(\rho_g C_{V\ g} T + P\right)\right]\, dV_{cell}\, dt_m \tag{7.29}$$

The finite element form of this equation is

$$T^1(i) = \frac{\Delta Y(i)\, T^0(i)\, H^0(i) - \delta t_m\, v_g^1(i+1)\, T^1(i+1)\, m_g^1(i+1)\, \left(C_{v_g} + \dfrac{\Re}{M_g}\right)}{\Delta Y(i)\, H^1(i) - \delta t_m\, v_g^1(i)\, m_g^1(i)\, \left(C_{v_g} + \dfrac{\Re}{M_g}\right)} \tag{7.30}$$

Where

$$H^0(i) = m_g^0(i) C_{v_g} + m_p^0(i) C_{v_p} + m_f^0(i) C_{v_f} + m_{ch}^0(i) C_{v_{ch}} \tag{7.31}$$

and

$$H^1(i) = m_g^1(i) C_{v_g} + m_p^1(i) C_{v_p} + m_f^1(i) C_{v_f} + m_{ch}^1(i) C_{v_{ch}} \tag{7.32}$$

Both of the transport equations given in Equation (7.30) and (7.28), are solved using an explicit backward difference Euler scheme [64].

7.3.4 Discussion

The physical processes required to represent the thermo-chemical degradation of a composite material due to a thermal heat flux have been considered above. Due to the highly coupled nature of the problem, the model has been implemented using a fractional step method. The modelling sections and the order in which they are solved, has been outlined above. With the finite element equations defined, the next step is to validate the implementation of the model. The discussion presented here only considers the validation of the implementation, and there is no attempt to verify the physical assumptions or to investigate the numerical predictions.

7.4 Thermo-chemical Degradation Model Validation

The implementation of the bespoke numerical model is validated as each modelling section in turn, is built from the bottom up. This validation is conducted by considering the convergence of the model for a 'worst case scenario'. Where possible, this convergence is determined against a known solution, because if the bespoke numerical model converges towards a known solution, then the implementation of the model has been validated. The convergence is considered for a 'worst case scenario' as it is known that the accuracy of the dependent variables is related to the mesh and time step sizes. Hence, from this study, it is also possible to determine the required mesh size and time steps which are needed for the numerical model to obtain accurate solutions. The 'worst case scenario' considered for this study is the heat flux from the lightning strike plasma arc for component C as defined by F. Lago [27]. The heat flux density from component C is greater than for the laser ablation, so the choice of this heat flux will not diminish from the accuracy of the laser ablation results. The convergence of this model is investigated with relation to $\Delta X(1)$, $\Delta Y(1)$, $\Delta Z(1)$ and the size of the time steps $\triangle t$, δt_T, δt_R and δt_m. The validation and conduction is conducted is as follows: First, the thermal conduction model is implemented and verified. With a thermal conduction model validated the next step is to couple this with the chemical reaction model. Once the implementation of the thermal conduction and the chemical reaction is completed and validated the validation of the gas transport model is considered.

7.4.1 Thermal Conduction Model

The thermal conduction model is initially validated against a 1D case study before validating it against a 3D study. A 1D study is considered first, given that the implementation of the 3D model is based on a separation of the principle directions.

7.4.1.1 Thermal Conduction - One Dimensional

For the purpose of the 1D study, the bulk conductivity is given by local axis direction 3. Direction 3 is chosen, as this is the direction of the lowest thermal conductivity and, hence in turn, the steepest thermal gradient. A diagram of the geometry used for the 1D case is shown in Figure 7.5. The heat flux on the left hand boundary is given by the peak plasma heat flux from the continuous current lightning strike profile as defined by [27] to be $4 \times 10^8 Wm^{-2}$. The material properties used are given in Appendix A. The solution is obtained for a time of 1 ms.

The convergence of the thermal conduction model is considered against two independent sources. Firstly, against an analytical thermal conduction solution given by Carslaw and Jeager in [139] and secondly against the commercially available finite element analysis

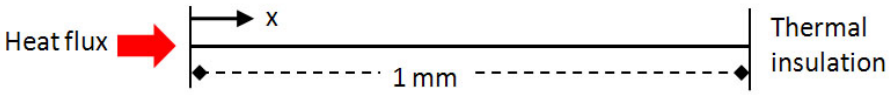

FIGURE 7.5: Schematic diagram of the 1D model

package, COMSOL [84]. The analytical solution is included since the predicted temperature obtained is always correct for this specific case given the assumptions considered. The validation of the COMSOL model is considered, because in future studies, where analytical solutions are not available, the bespoke numerical model will be validated against replica COMSOL models. The convergence of the bespoke numerical model is determined by calculating the maximum temperature difference between two temperature solutions. The maximum temperature difference is defined by

$$\epsilon = \max|T(y) - T^*(y)| \tag{7.33}$$

where $T(y)$ represents the temperature from either the bespoke numerical model or the COMSOL model and $T^*(y)$ is the temperature from the analytical solution. As well as the maximum temperature difference, the spatial coordinate of the maximum temperature difference is also obtained, this is given by y^*. From these pieces of information, the fractional difference (F_d) between the two results at this maximum temperature difference is obtained by considering

$$F_d \ = \ \epsilon / T^*(y^*) \tag{7.34}$$

The implementation of the COMSOL model and the analytical method are now considered in detail.

7.4.1.2 COMSOL Model - 1D

The numerical model implemented within COMSOL is a replica of the bespoke numerical model shown in Figure 7.5. The COMSOL model is solved using a uniform mesh with the temperature between grid points defined by a linear interpolation function. The solution of the finite element equations is obtained by using a direct solver called UMFPACK [134]. The convergence of the COMSOL model is determined by varying the number of uniformly distributed mesh elements. Within COMSOL, it is only possible to define a maximum allowed time step size and so as it is not possible to force the solver to take a predefined time step size. Therefore, the convergence of the COMSOL model can only be considered as a function of mesh size. The global time step size was chosen to be 0.1 μs.

7.4.1.3 Analytical Method

The analytical solution considered to determine the temperature profile from a uniform heat flux, was proposed by Carslaw and Jaeger [139]. The analytical solutions states that the temperature ($T(y,t)$) at a given distance from the heat source (y) after a given time (t) is determined by

$$T(x,t) = \frac{2q_0}{k}\sqrt{\alpha t}\ \ \text{ierfc}\left(\frac{y}{2\sqrt{\alpha t}}\right) \tag{7.35}$$

where 'ierfc' is the integral error function defined as

$$\text{ierfc}(u) = \int_{\infty}^{u} \text{erfc}(u)du = \frac{2}{\sqrt{\pi}}e^{-u^2} - u[1 - \text{erf}(u)] \tag{7.36}$$

$$\text{erf}(u) = \frac{2}{\sqrt{\pi}}\int_{0}^{u} e^{-u^2}du \tag{7.37}$$

Where u is a dummy variable. The analytical solution considers the thermal diffusivity (α_T), which is given as

$$\alpha_T = \frac{\kappa}{\rho C_V} \tag{7.38}$$

Where κ, ρ and C_V are the same bulk material properties used in the bespoke numerical model.

7.4.1.4 1D - Validation

The convergence of the 1D thermal conduction model is first considered for the COMSOL with respect to the number of mesh elements. This is shown in Figure 7.6.

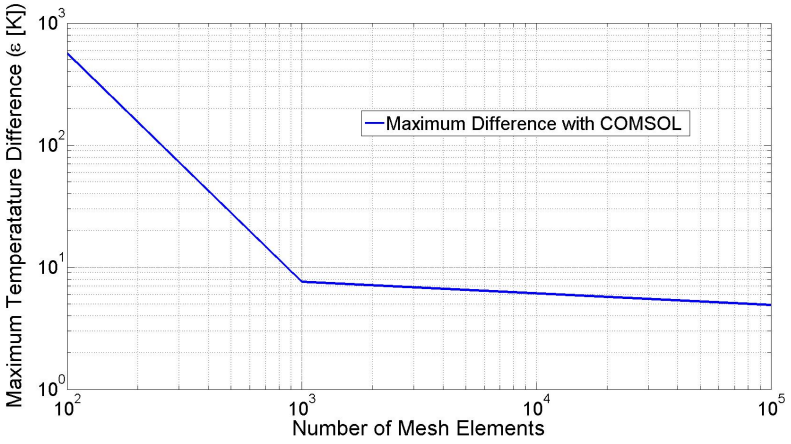

FIGURE 7.6: Maximum temperature difference within the COMSOL model when compared against the analytical model as a function of total number of mesh elements. These results are for $\triangle t = 2\,\mu s$

In Figure 7.7, the convergence of the bespoke numerical model is considered with respect to the number of mesh elements.

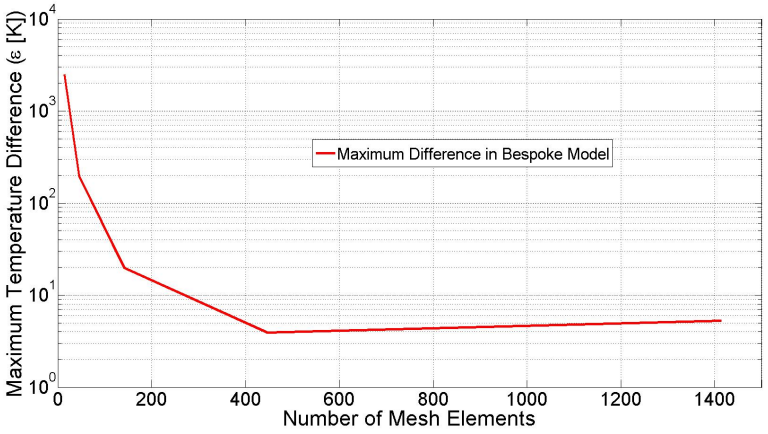

FIGURE 7.7: Maximum temperature difference within the bespoke numerical model when compared against the analytical model as a function of the number of mesh elements. These results are for $\triangle t = 2\,\mu s$

It is evident from Figure 7.6, that the COMSOL model displays a quadratic convergence (i.e. quadratic decrease in maximum temperature difference), as the number of mesh elements is increased. However, due to the non-uniform mesh used within the bespoke numerical model, Figure 7.7 shows a linear convergence as the number of elements is increased. This increase in number of mesh elements corresponds to a decrease in mesh growth rate. Figures 7.6 and 7.7 both show that after the initial convergence, a plateau region forms due to the maximum difference being dominated by either a rounding error or due to the finite time step size. Therefore, any further increase in the number of mesh elements (i.e. decrease in mesh growth factor) has minimal or no effect on decreasing the maximum temperature difference. This plateau region occurs for a greater number of mesh elements within the COMSOL model compared with that of the bespoke model. As the solution time of these numerical methods is proportional to the number of mesh elements, the bespoke numerical model has a shorter solution time than the COMSOL model with a uniform mesh. For the bespoke numerical model, the minimum temperature difference of 5.2 K equates to a percentage difference of approximately 0.02%, which occurs for a mesh growth factor $\Delta Y(1)$ of 10 nm.

Next, the convergence due to the size of the global time step is considered in the same manner. The global time step is considered rather than δt_T, because as there is only one physical model currently included, δt_T and $\triangle t$ (defined in Figure 7.4) are the same. The convergence of the bespoke numerical model is shown in Figure 7.8.

From Figure 7.8, it is evident that as the global time step is decreased, the maximum temperature difference between the bespoke numerical model and the analytical model decreases, i.e. the solution converges. When the time step is greater than 2 μs, there is a linear convergence with respect to the size of the global time step. This behaviour

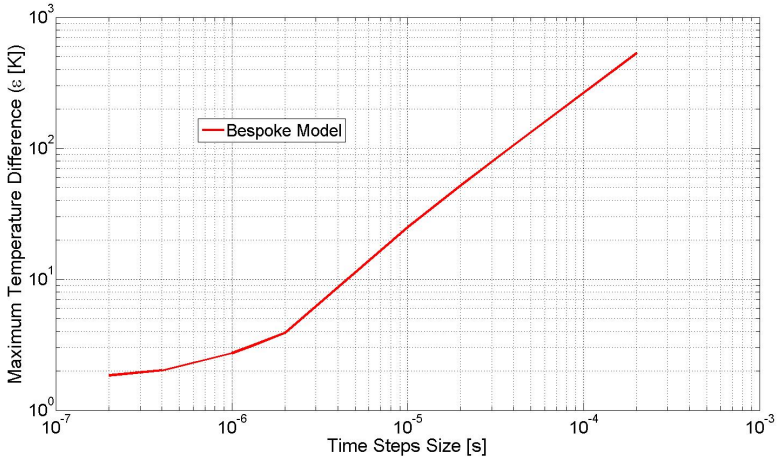

FIGURE 7.8: Convergence of the thermal profile with respect to the size of the global time step for $\Delta Y(1) = 10\ nm$

is expected, due to the fully implicit implementation. When the size of the global time step decreases below 2 μs, the rate of convergence decreases and a constant maximum difference forms. This is caused by the maximum difference being dominated by either rounding errors or the mesh size. Taking the maximum temperature difference of 1.8 K, which occurs at 0.2 μs, there is a fractional difference of 0.04%.

From the above studies, the implementation of the 1D thermal conduction model has been validated, as the temperature profile obtained from the bespoke numerical model is accurate to within 1%, given a mesh growth factor ($\Delta Y(1)$) is at least 2 μm and a global time step is no greater than 1 μs.

7.4.2 Thermal Conduction in 3D

Having shown that the 1D thermal conduction model has been implemented correctly, it is now possible to validate the implementation of the 3D thermal conduction model. It has not been possible to find an analytical solution which defines the temperature profile for such a model. This is due to the anisotropy of the CFC. Therefore, the validation for this model is conducted by investigating the convergence of the numerical solutions with respect to COMSOL. For this study, a heat flux is defined on the top surface by a 2D Gaussian function, as defined in Equation (7.8). This is designed to replicate a plasma or a laser beam heat flux. The arc radius Λ is taken to be 1 mm and the peak heat flux is the same as that considered for the 1D study above. The remaining boundaries are considered to be thermally insulating. The model is solved for a solution time of 1 ms. An illustration of the geometry used is given in Figure 7.9.

The bulk material properties for this model are defined by the Rule of Mixtures, in all directions, as given in Chapter 6. This provides the lowest thermal conductivities and

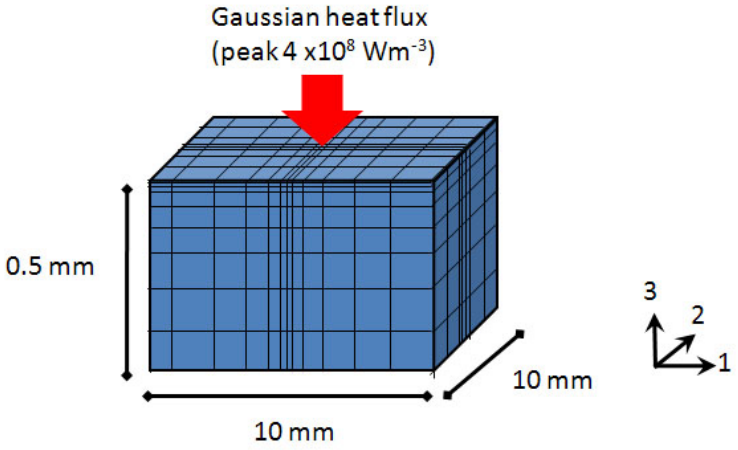

FIGURE 7.9: Diagram of the geometry used in the validation of the 3D thermal conduction model

so creates a large thermal gradient. This satisfies the 'worst possible case' philosophy of this validation study. The material properties used within this model are given in Appendix A.

7.4.2.1 COMSOL Model - 3D

The COMSOL model developed, is an exact replica of the 3D thermal conduction model outlined above. This COMSOL model now has a non-uniform mesh, designed around a similar concept as the non-uniform mesh shown in Figure 7.9. The mesh parameters used within this model were chosen by checking the convergence of the COMSOL model as the mesh size was decreased. The temperature profile between mesh elements was defined by a linear interpolation functions. The finite element equations were then solved using a direct solver called UMFPACK [134].

7.4.2.2 3D Thermal Conduction - Convergence

The convergence of the 3D thermal conduction model is again considered with reference to the maximum temperature difference, defined by Equation (7.34). This is initially considered by varying the mesh growth rate in the y direction ($\Delta Y(1)$) before considering the remaining mesh growth factors independently. From Figure 7.10, it is evident that as $\Delta Y(1)$ decreases, the maximum temperature difference decreases, and so the solution converges. When the mesh growth factor ($\Delta Y(1)$) is less than 0.2 μm the maximum temperature difference remains relatively constant and so decreasing $\Delta Y(1)$ further has minimal effect on reducing the maximum temperature difference. From these results, when $\Delta Y(1)$ is equal to 0.1 μm then the fractional difference is 0.27%.

The convergence due to variations in $\Delta X(1)$ and $\Delta Z(1)$ are now considered, with these

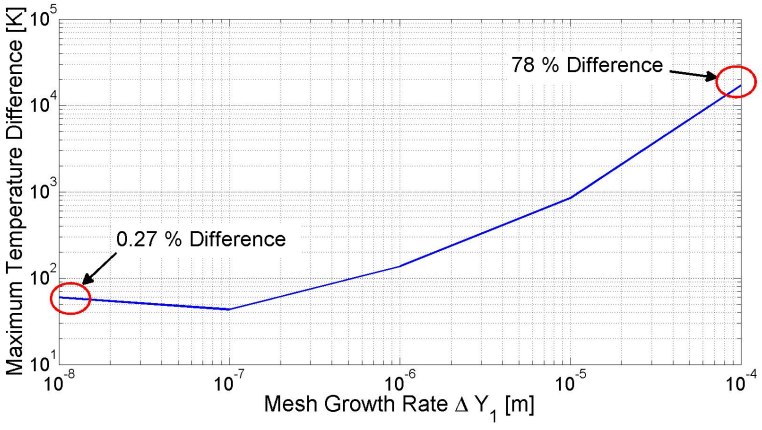

FIGURE 7.10: Maximum temperature difference as a function of the mesh growth rate in the y direction. For this study $\triangle t = 20\,\mu s$

results shown in Figures 7.11 and 7.12, respectively.

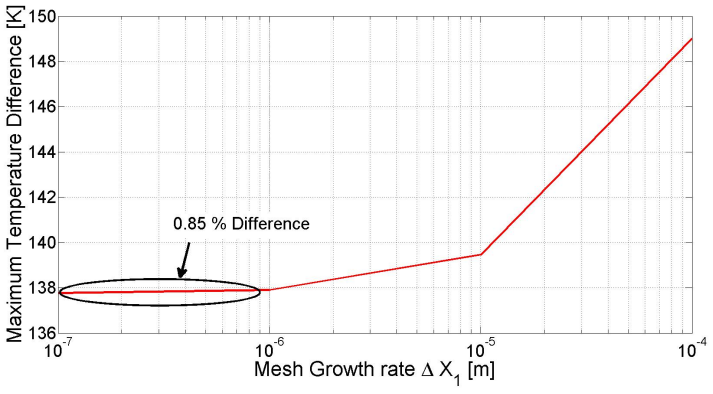

FIGURE 7.11: Maximum temperature difference as $\Delta X(1)$ is varied. These results used the following parameters: $\Delta Y(1) = 1\,\mu m$, $\Delta Z(1) = 0.1\,\mu m$ and $\triangle t = 20\,\mu s$

The results in Figures 7.11 and 7.12 show that the numerical solutions convergence (i.e. decrease in maximum temperature difference) as $\Delta X(1)$ or $\Delta Z(1)$ decrease. The convergence due to all the mesh growth rates show a similar trend, although it is evident that the convergence is most affected by $\Delta Y(1)$ rather than either $\Delta X(1)$ or $\Delta Z(1)$. Using the global step ($\triangle t$) of 20 μs with $\Delta X(1)$ equal to 1 μm, $\Delta Z(1)$ equal to 1 μm and $\Delta Y(1)$ equal to 0.1 μm, the fractional difference of the model is 0.85%. The final model parameter to consider is the size of the global time step. The results for varying the global time step are shown below in Figure 7.13.

The results presented in Figure 7.13, show that as the size of the global time step decreases, there is a linear decrease in maximum temperature difference. When the global time step is $10\,\mu s$, the predicted temperature has a maximum fractional difference of 0.11%. Whilst a smaller global time step would further reduce the fractional difference, it would also dramatically increase the solution time for a negligible increase in accuracy.

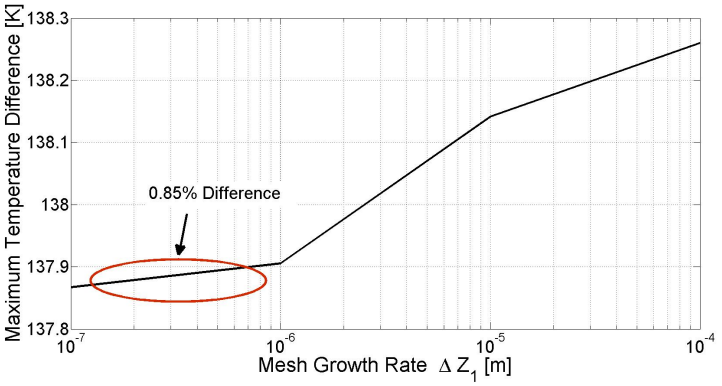

FIGURE 7.12: Maximum temperature difference as $\Delta Z(1)$ is varied. These results used the following parameters: $\Delta Y(1) = 1\,\mu m$, $\Delta X(1) = 0.1\,\mu m$ and $\triangle t = 20\,\mu s$

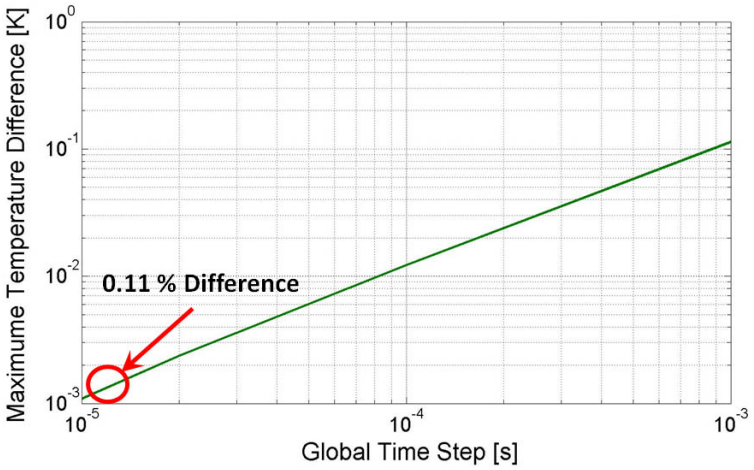

FIGURE 7.13: Maximum temperature difference as a function of global time step used. For this model $\Delta X(1) = 1\ \mu m$, $\Delta Z(1) = 1\ \mu m$ and $\Delta Y(1) = 0.1\ \mu m$

7.4.2.3 Thermal Conduction Discussion

The above discussion has shown that the bespoke numerical model can predict the temperature profile to within an accuracy of 0.11%. This validates the implementation of the 3D thermal conduction model.

7.4.3 Thermo-chemical Reaction Model

Having validated the implementation of the thermal conduction model, the next aspect to validate is the implementation of the chemical reaction model. To achieve this, the thermal conduction model and the chemical reaction model are implemented together using the fractional step, as outlined in Figure 7.4. However, as only the thermal conduction and the chemical reaction model are considered here, the fractional step has been modified and now appears as shown in Figure 7.14.

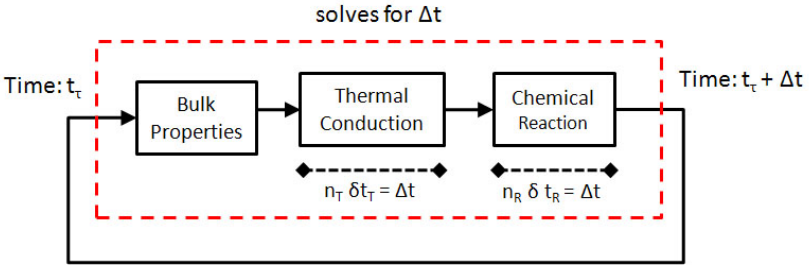

FIGURE 7.14: Fractional step for the implementation of thermal conduction and chemical reaction considered in this validation

This validation is again conducted by considering the convergence of the numerical predictions using the same geometry, material properties and boundary conditions as those used for the 1D thermal conduction validation, shown in Figure 7.5. The model considers a simulation time of 1 ms. The reaction kinetics required by the Arrhenius equation (Equation (7.3)) are taken from the experimental results in Chapter 4. One exception to this is that initially the convergence considers the reaction order (n) to be 1. A separate validation study has also been conducted for when the reaction order (n) is equal to 1.3, although for the reasons presented in Section 7.4.3.2, this study is not presented here.

The convergence of the bespoke model is determined by comparing the numerical predictions against a replica model made in COMSOL. However, COMSOL is unable to fully implement correctly the change in energy due to a chemical reaction. This is because the COMSOL implementation does not consider the change in heat capacity as the polymer degrades. Therefore, this validation considers the case where $Q_d = 0\ Jkg^{-1}$. This partly breaks the coupling between the thermal conduction model and the chemical reaction model. Hence, the validation here is solely validating the implementation of the Arrhenius equation.

7.4.3.1 Convergence of the Thermo-chemical Model

The convergence of the thermo-chemical degradation model is investigated by considering the size of the time steps ($\triangle t$, δt_T and δt_R) and the mesh growth rate, $\Delta Y(1)$. The size of the global time step is taken from the conclusions of the 1D thermal conduction model i.e. $\triangle t$ equals 1 μs. The number of thermal conduction subs steps (n_T) is 10, which results in a thermal conduction sub step size (δt_T) of 0.1μs. By defining ten thermal conduction sub steps, allows for some conduction to occur within the thermal conduction model. This leaves only the chemical reaction sub time step size, δt_R, and the mesh growth rate, $\Delta Y(1)$, as the parameters which this validation study needs to consider. The convergence of the bespoke model is defined with respect to the difference in the amount of polymer mass which has degraded (Δm_p) between the bespoke model

and the COMSOL model. The difference in polymer mass degraded is given by

$$\Delta m_p = \left[\Sigma m_p(t_0) - \Sigma m_p(t)\right] - \left[\Sigma m_p^*(t_0) - \Sigma m_p^*(t)\right] \tag{7.39}$$

where $m_p(t)$ is the mass of the polymer at time (t) and $m_p(t_0)$ is the initial mass of the polymer, obtained from the bespoke numerical model. The mass of the polymer determined from COMSOL is given by $m_p^*(t)$. A fractional difference in the amount of polymer degraded is then calculated with respect to the amount of polymer mass degraded within the COMSOL model. The fractional difference in the amount of degraded polymer mass is shown as a function of mesh growth rate in Figure 7.15 and as a function of reaction time step in Figure 7.16.

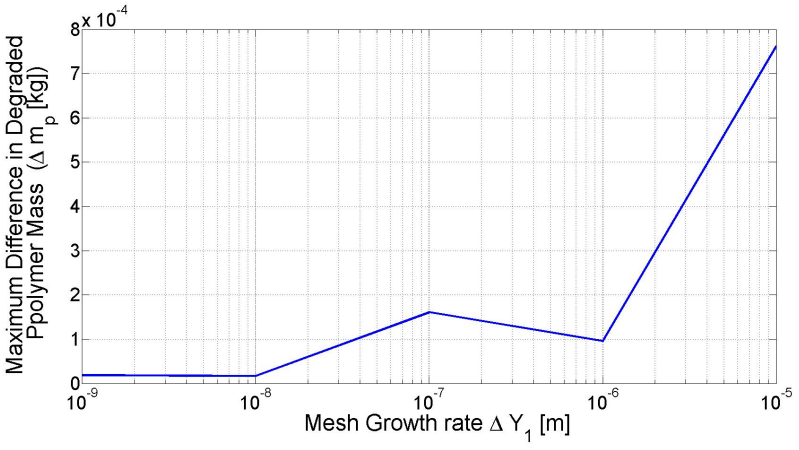

FIGURE 7.15: Accuracy for the chemical reaction model as the mesh size is varied

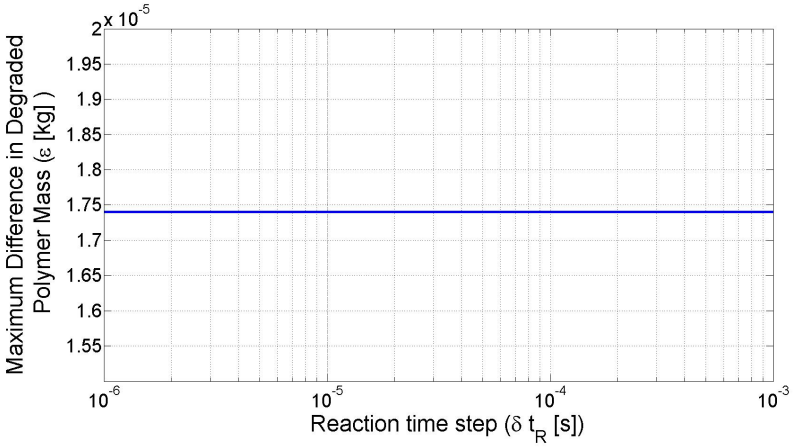

FIGURE 7.16: Accuracy for the chemical reaction model as the reaction time step size is varied

The decrease in the difference in degraded polymer mass as the mesh growth rate decreases (Figure 7.15) implies that the bespoke numerical does indeed converge to a consistent solution for a mesh growth rate of $\Delta Y(1) = 1\,\mu m$. However, Figure 7.16 shows that there is no variation in the amount of degraded polymer as δt_R is varied. This is because the change in energy due to a reaction (Q_D) has not been considered in

this model.

It is shown in Figure 7.17 that the mesh growth rate affects the accuracy of the model by the ability of the grid points to map accurately the reaction front. The reaction front is defined by the spatial region where the peak reaction rate is occurring. Furthermore, it is evident from Figure 7.17 that the numerical model predicts a steep reaction front and hence a small mesh growth rate is required to portray this step reaction front accurately
.

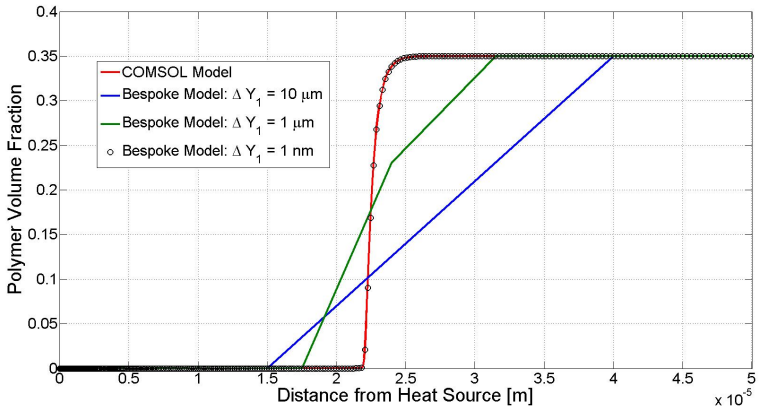

FIGURE 7.17: Ability of the thermo-chemical degradation model to accurately map the reaction front as a function of mesh growth rate

Given that the reaction front moves through the material over time and that due to the non-uniform mesh, the mesh elements get larger the further through the material one goes, it is important to investigate how the mesh growth rate affects the accuracy of the chemical reaction model as the reaction front moves through the material. The fractional difference in the amount of polymer which has been degraded as a function of time is shown in Figure 7.18. This has been shown for two different mesh growth rates. Given the maximum damage depth from the experimental laser ablation study and the separate current impulse components are less than 2.5 mm, the model will consider the accuracy at this damage depth.

The results in Figure 7.18 show that as the reaction front moves through the material, there are random fluctuations within the fractional difference of degraded polymer. This is due to the limitation of the mesh locations to accurately map the reaction front, and so at certain times, the grid points can more accurately map the reaction front than at other times. Regardless of these fluctuations, for the damage depth considered above, these mesh growth rates show no increase in fractional difference in the amount of polymer which has degraded as the reaction front moves through the material. Furthermore, the maximum percentage difference in the amount of degraded polymer for when $\Delta Y(1)$ is equal to 0.1 μm, and is never greater than 0.5%.

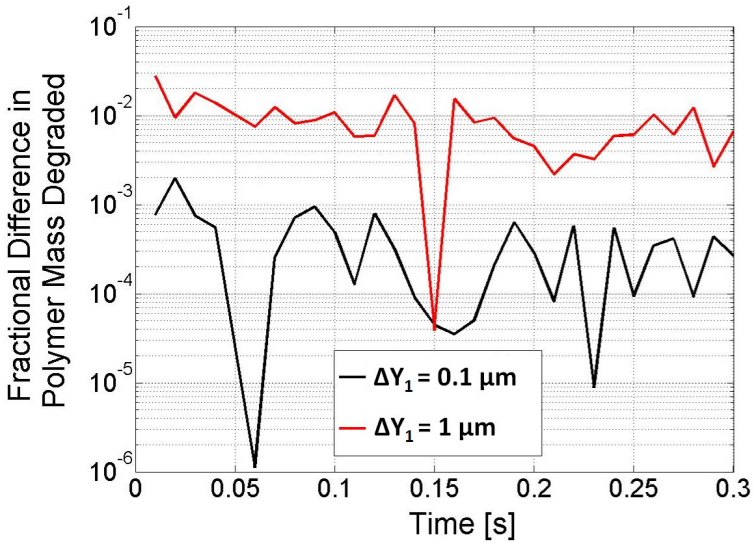

FIGURE 7.18: Fractional difference in mass loss varied as the reaction front moves through the material towards a depth of 2.5 mm

7.4.3.2 Thermo-chemical Reaction Model - Discussion

The thermo-chemical reaction model has been implemented and the convergence of the numerical solution has been investigated, with reference to a replica model made in COMSOL. From this study, it has been shown that given appropriate time steps and mesh growth factors, the implementation of this model is valid. The choice to validate the 1D model rather than a 3D model has no bearing on the relevance of the validation. This is because the accuracy relates to the ability to determine the reaction front due to the thermal profile and is not affected by the amount of mass that is contained within a cell.

The two assumptions made regarding the validation study above are now addressed. Firstly, the above study considered the reaction order, n, equal to 1 when it has been experimentally shown in Chapter 4 to actually be equal to 1.3. A similar study to that presented above has been conducted for n equal to 1.3. This study showed the convergence of the numerical model is independent of the reaction order, and consequently the results for different reaction orders are not presented. Secondly, within this validation study, it has not been possible to validate fully the entire thermo-chemical reaction model due to the omission of the change in energy due to the thermo-chemical reaction. Instead, a study was conducted (not shown here) to investigate the convergence of this model with the change in enthalpy taken from the TGA study in Section 4.2.2.1. This study showed that the convergence of the model was obtained when n_R is 50, which equates to δt_R of $0.2\mu s$ for a global time step ($\triangle t$) of 10 μs. Whilst this does not unequivocally validate this implementation, it does indicate the implementation is correct. The numerical studies in the next chapter further validate the implementation of this model.

7.4.4 Gas Transport

With the implementation of the thermo-chemical reaction model validated, the next step is to incorporate this with the gas transport model. This is done in two parts; firstly, the gas mass transport is implemented alone, before secondly, the thermal gas transport is incorporated into the same model. These physical processes are initially implemented separately despite both physical processes being incorporated within the same modelling section, as discussed in section 7.3.3.4.

Despite significant effort, it was impossible to find any analytical solutions for either the gas mass transport or the thermal gas transport which could conform to this study. It is also not possible to compare the solutions from the bespoke numerical model against a replica model made in COMSOL. This is because the strong coupling between the mass transport and the chemical reaction cause large instabilities to develop within the COMSOL model, causing the numerical solution to diverge. As a result, the validation of these models purely considers the convergence of the numerical solution. Whilst a converged solution does not guarantee a valid implementation, it does indicate whether the model is behaving as expected.

7.4.5 Gas Mass Transport

As the gas mass transport model only considers the gas filtration in the y direction (as outlined in Section 7.3.3.4), the convergence can, therefore, be conducted using the same 1D geometry that has been used to validate the 1D thermal conduction model, discussed in Section 7.5. The bulk material properties are determined using the Series Rule of Mixtures with the material properties defined by appendix C. For this study, the heat flux is changed, and instead of considering the peak plasma heat flux, the peak heat flux from the laser ablation study is considered i.e. $4 \times 10^6\, Wm^{-2}$. The addition of the gas transport model requires a constant pressure to be defined at all external boundaries. For this study, all boundaries are held at a constant pressure of 1 Atm. As this model is an expansion of the previous models, with a lower heat flux, the same model parameters as determined previously can be used. The parameters used are $\Delta Y(1)$ equal to 1 μm, n_T equal to 10 and n_R equal to 50. This number of sub steps correspond to δt_T of 0.1 μs and δt_R equal to 0.02 μs, given that the same global time step as above is used. The mesh growth rate is not investigated here, because assuming the reaction front has been accurately mapped, the internal gas pressure responsible for the gas transport, is independent of mesh size. This means that there are two remaining variables which can be considered, the global time step size ($\triangle t$) and the gas transport sub step size (δt_m).

7.4.5.1 Gas Mass Transport - Convergence

Before investigating the convergence, it is appropriate to consider what effect these two parameters ($\triangle t$ and δt_m) will have on the numerical predictions. Starting with the size of the global time step, it is evident that the size of the global time step will influence how much new gas is produced between the start of each new gas transport step. This newly produced gas, initially causes a large pressure increase and hence subsequently an initially large gas filtration velocity. It is obvious that this initially large filtration velocity will reduce over time, resulting in a more steady state gas flow. If this reduction in gas filtration velocity is rapid, a small gas transport sub step is required to accurately resolve this variation in filtration velocity. Hence, if the transport sub step is too large, the gas is moved too far, or even removed (escaped) from the system completely. By reconsidering the global time step size, it is evident that with a smaller global time step, less gas is produced by the chemical model, lowering the initial high filtration velocity, which means a larger sub transport step can be considered. Therefore, the convergence of the model is a function of both of these two parameters. The size of the global time step and the size of gas transport sub step have been considered separately. However, it became evident that by fixing the global time step size and increasing the number of gas transport sub steps (n_m), the simulation time increased dramatically. Therefore, the study here considers a fixed number of gas transport steps of 6000, and instead the size of the global time step is varied.

Figure 7.19 shows that as the size of the global time step is decreased the amount of gas (shown by mass) within the decomposing material increases.

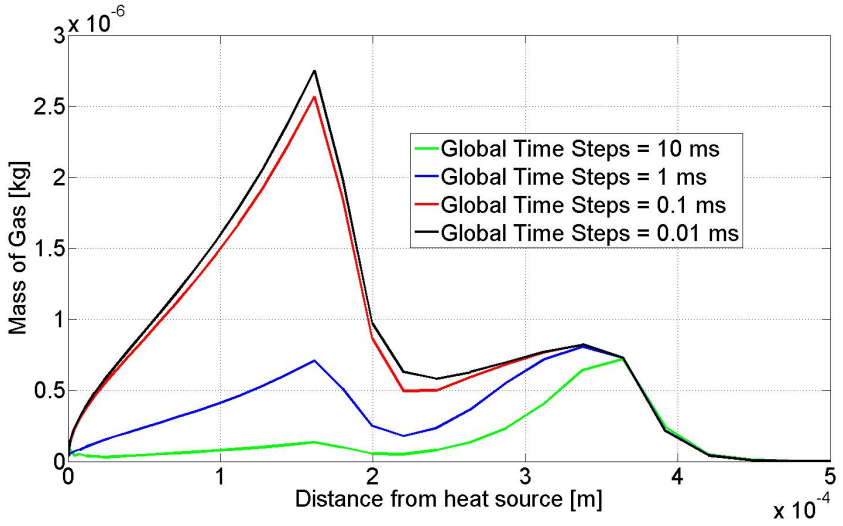

FIGURE 7.19: Mass of gas as a function of distance from the heated surface as the time step is varied

This result is further shown by the increase in internal gas pressure as the global time step is reduced, as shown in Figure 7.20. Both these results can be explained by considering that when the global time step (Δt) is greater than 1 ms, too much gas is removed

from the system, and so the internal gas pressure falls below the boundary condition pressure of 1 Atm, which is obviously erroneous. However, as the size of the global time step is decreased, the internal gas pressure and mass profile do converge to a sensible solution, as this erroneous pressure profile disappears. These results are expected, based on the discussion presented above, as when the global time step is reduced, there is a lower increase in gas pressure for the start of a mass transport step, and hence the gas transport sub step can more accurately map the filtration velocity as a function of time. Therefore, in summary, given a global time step of 0.01 ms a converged solution is produced.

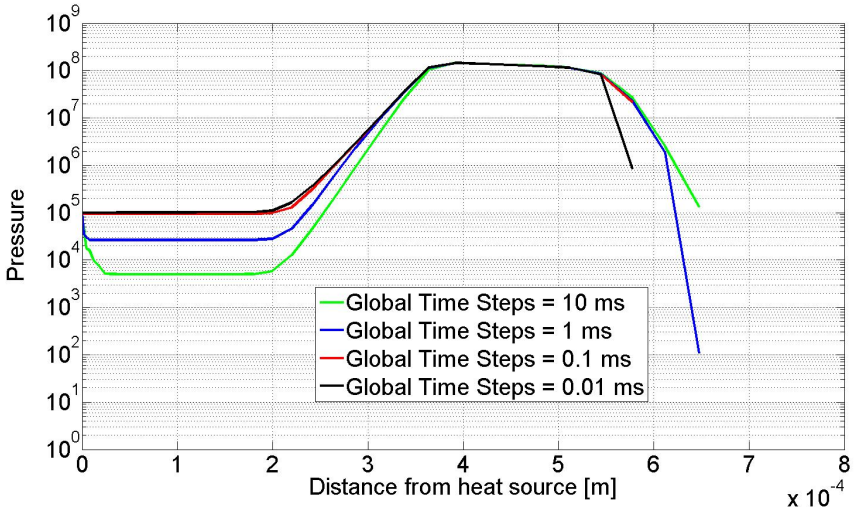

FIGURE 7.20: Pressure as a function of distance from the heated surface as the time step is varied

7.4.6 Gas Thermal Transport - Convergence

The thermal transport due to the gas mass transport is now incorporated into the same model as above. The thermal transport convergence is investigated by considering the temperature profile as a function of global time step size. These results are shown in Figure 7.21.

Figure 7.21, shows that as the global time step is increased, there is an increase in temperature. This increase in temperature is due to the internal gas pressure falling below 1 Atm, as shown in Figure 7.20 for the corresponding time steps. This occurs because if the pressure falls below 1 Atm within the material, there must be an increase in pressure back to the constant boundary pressure of 1 Atm. The increase in pressure causes a large amount of work to be done on the system, and hence there is a temperature rise. As the global time step is reduced, this temperature increase, decreases, as the gas pressure remains above 1 Atm. By considering Figure 7.21, it is clear that the numerical solutions convergence to a consistent temperature when the time step is 0.01 ms.

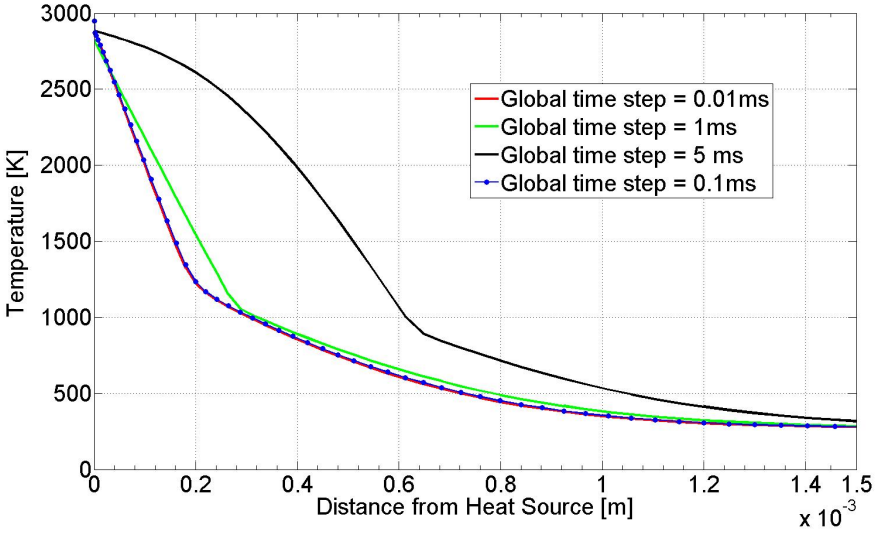

FIGURE 7.21: Convergence of the temperature profile as the global time step is varied for the thermal gas transport

7.4.6.1 Gas Transport - Discussion

The validation of the gas transport model has been investigated above with respect to the convergence of the numerical solutions. The results presented above have shown that given a sufficiently small time step, both the gas mass transport and the gas thermal transport models converge to a consistent solution. Whilst this does not completely validate the implementation of this model, it does indicate that the implementation was correctly implemented.

7.5 Summary

Based on the physical processes outlined in Chapter 7, a bespoke numerical thermo-chemical degradation model has been developed to predict the thermal damage caused to a piece of CFC due to a heat flux. The implemented numerical model has then been verified, as the model has been built from the bottom up. It is evident that using the model parameters highlighted above, a converged solution with an accuracy better than 5 % occurs when the global time step size ($\triangle t$) is equal to 0.1 ms and the sub time step parameters are defined by Table 7.1.

	Maximum Time Step Size
Thermal Conduction (t_T)	1 μs
Chemical Reaction (t_R)	0.2 μs
Mass transport (t_M)	1.67 ns

TABLE 7.1: Time step sizes required to obtain a converged solution

The required mesh growth rate parameters to obtain a converged solution are $\Delta X(1)$

equal to 10 μm, $\Delta Y(1)$ equal to 1 μm and $\Delta Z(1)$ equal to 10 μm.

An accuracy of 5% is sufficient for the model to make realistic predictions. Whilst a further reduction in overall error is possible, the increased solution time required is very considerable. In addition, when the errors introduced by the modelling assumptions and the experimental studies are considered, a further increase in model accuracy will not increase the overall accuracy of the numerical predictions.

Chapter 8

Verification of Physical Assumptions

Having outlined the physical processes required for the bespoke numerical model and then validated the implementation of these processes in the last chapter, the next step is to verify the physical assumptions made within the model. The verification here is conducted in two parts. Firstly, the homogenisation assumption used to represent numerically a piece of CFC is verified through an experimental study. Secondly, the bespoke thermo-chemical degradation predictions are compared against the laser ablation experiment conducted in Chapter 5. From this comparison, the question as to whether the gas transport has a significant impact on the resultant damage has been assessed.

8.1 Verification of the Homogeneous Approach

This verification is conducted by initially considering the current flow predicted by a numerical quasi-static DC conduction model before comparing these results against an experimental study.

8.1.1 Geometry and Material Properties

For this model, the CFC material is assumed to have σ_1 equal to $7 \times 10^3\ Sm^{-1}$ with σ_2 and σ_3 equal to $1\ Sm^{-1}$. These electrical conductivities have been taken from the discussion of the experimental study given in Section 4.1.5. The geometry used here comprises two square unidirectional layers of CFC laminates, stacked on top of each other, with the local axis direction 1 (fibre direction) rotated through 90° between the top and bottom layer. Two circular electrodes are placed above and below the centre of the CFC stack. An illustration of the geometry used is shown in Figure 8.1.

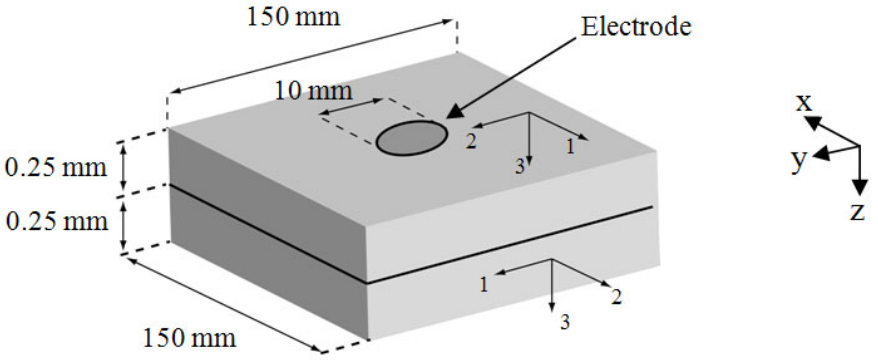

FIGURE 8.1: Schematic diagram of the CFC stack model

8.1.1.1 Governing Equations and Boundary Conditions

The solution of the steady state current flow problem in terms of the electric current density J and the electric field E are given by

$$\nabla \cdot J = 0, E = -\nabla\phi, J = \sigma E \tag{8.1}$$

which in turn together with Ohms law results in formulation equation for the electric potential(ϕ):

$$\nabla \cdot (\sigma \nabla \phi) = 0 \tag{8.2}$$

The application of the Dirichlet's principle to Equation (8.1) and Equation (8.2) is equivalent to seeking the minimum of the generated Joule heat (Q_J) i.e.

$$Q_J \rightarrow min\left(\iiint_{volume} J \cdot E dV\right) \tag{8.3}$$

The external boundary conditions are provided by electrical insulation on all surfaces, except where the electrodes are placed. The potential for the top electrode is assumed to be $\phi_{top} = 4.5V$ and the bottom electrode is grounded. The geometry in Figure 8.1 is meshed with cubic elements, which are uniformly spaced on the top surface before being swept through the thickness of the model. It was found that smooth equipotential surfaces could be obtained by linear shape functions. Due to the complex shape of the equipotential surfaces, the application of quadratic or higher order shape functions results in an erroneous fluctuations within the equipotential surfaces causing a drop in the model accuracy.

8.1.2 Numerical Predictions

The predicted current density in the z direction, is shown in Figure 8.2. The current density is plotted for a slice through the middle of the CFC panel, at the interface between the two plies. The bottom left corner of the image shows that the majority of

the current is travelling straight down through the centre of the CFC (negative number is defined as being downwards). This is exactly what one would expect for a standard isotropic material. The strong anisotropy of the CFC panel, however, creates an additional current flow. This can been seen by the positive current density in the top right corner, which implies that current in this region is travelling back up into the top layer. This is counter intuitive from what is expected.

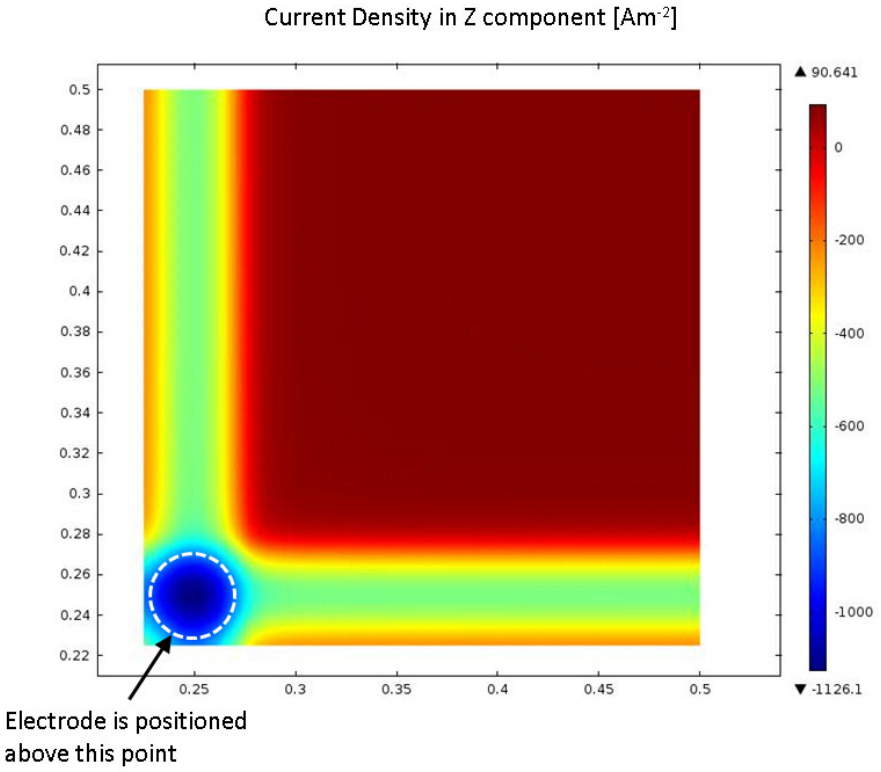

FIGURE 8.2: Current density in the z direction at the interface between the two layers. A negative current density implies that the current is travelling down towards the ground electrode. Notice the positive (upward flowing current) current density in the top right corner

The complex upwards current flow accounts for roughly 8 % of the total current flow. Therefore, whilst it is evident that the majority of the current does flow in the expected direction, there is a considerable proportion of complex current flow, which warrants further investigation. To investigate this further, the equipotential surfaces shown in Figure 8.3 were considered. The equipotential surfaces within $\pm 1\%$ of the mid potential, $0.5\phi_{top}$, have a twist, as the potential effectively flips over. This appears very unusual, as normally the potential is expected to follow a gradual and uniform change throughout the entire volume resulting in the mid equipotential surface being flat. However, the current flow paths inside the CFC panel do explain this twist in the potential, as the current should take the path of least resistance.

The diagram in Figure 8.4a illustrates the simplified current flow pattern, while Figure 8.4b shows the model predictions for the real pattern. Taking the current starting point

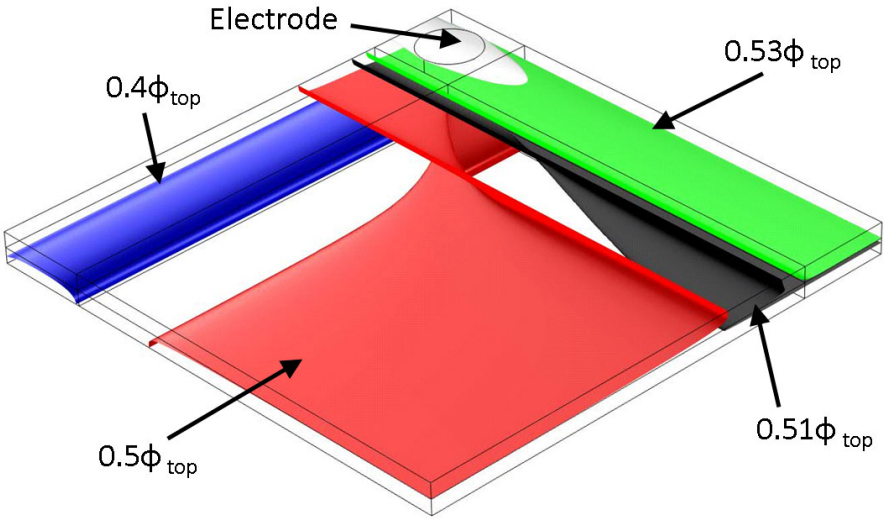

FIGURE 8.3: Image of the equipotential surfaces inside the panel. Note the twisting of the $0.5\phi_{top}$ equipotential surface and a small potential drop in the twisting region

to be the top electrode, some of the current initially flows along the local axis direction 1 in the top layer. As it travels along the top layer, it begins also to penetrate through the thickness of the panel towards the bottom layer. In the bottom layer, the direction with high σ_1 is rotated by 90° in the plane, and so the current prefers to flow in this direction as it reaches the bottom layer. After having been distributed over a large surface area, the current starts to flow back up into to the top layer, towards the furthest corner from the electrode. When it re-enters the top layer, it again travels along the top layer's highly conductive direction and, at some point, begins to penetrate back down through the panel into the bottom layer. When in the bottom layer, the current now flows along the highly conductive direction to reach the bottom ground electrode. In summary, the flow path is akin to travelling around all four sides of the square panel due to the resistance distribution within this CFC panel. The interesting observation is that the current travels a much longer distance than expected and also passes through the low conductivity directions 3 times.

The rationale behind these somewhat unusual current flow may be better explained by the minimum energy formulation given by the action integral shown in Equation (8.3), rather than from Equation (8.2) and Equation (8.1), as the current density J is minimised throughout the sample by following the high conductivity directions. Such a distribution reduces the current density without experiencing significant resistance. The only issue with this explanation is connecting the current flow in the top and the bottom layers. This is resolved by the twisting of the potential, which does not contribute to a significant increase in Joule heat, as the twisting potential occurs over a small potential range and hence the electric field (E) is kept at a minimum value.

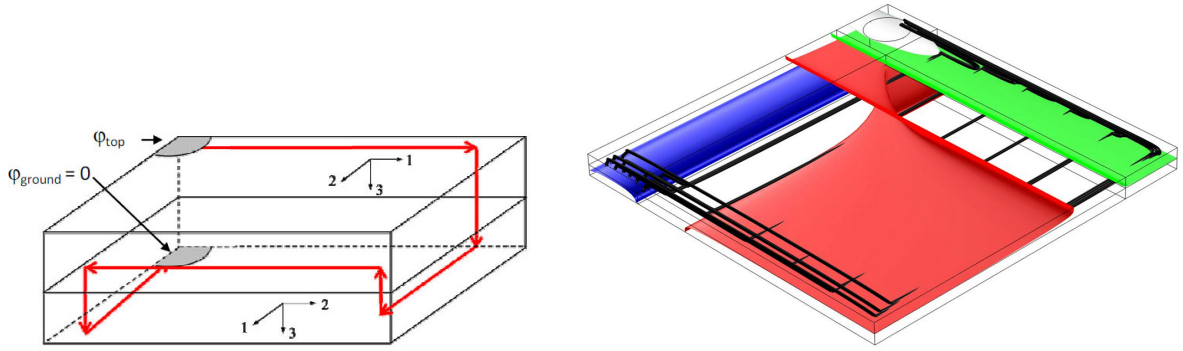

(a) (b)

FIGURE 8.4: a) Schematic diagram of the upward travelling current flow pattern b) Numerical current flows lines with equipotential surfaces

8.1.3 Experimental Verification

The numerical predictions were verified against the experiment by measuring the electrical potential down the edge of the sample using a needle connected to a digital voltmeter. The potential difference was then compared against the corresponding predictions from the numerical model.

8.1.4 Experimental Method

An experiment was designed to validate the numerical model, discussed above, and is shown in Figure 8.5. A two-layer CFC panel with the same geometry as that of the numerical model was obtained for this experiment. The two circular electrodes, made from aluminium were attached to the sample using silver paste. This paste also acted to improve the electrical contact between the CFC and the electrodes. The needle was connected to a digital voltmeter and then placed touching the side of the CFC at $(x, z) = (0, 0)$. The needle was then moved down the edge of the sample from z equal to $0\,mm$ to z equal to $5\,mm$, with the potential difference recorded as the needle is moved. Once the needle reaches $5\,mm$, i.e. the bottom of the CFC, the needle is moved along the x axis to a new location and the measurements are repeated as before.

8.1.5 Experimental Results

The experimental results are shown in Figure 8.6. In the top laminate, the potential difference remains constant, which is consistent with predictions shown in Figure 8.3. In each vertical slice between $0\,mm$ and $25\,mm$, the potential difference begins to significantly decrease in the bottom laminate. As measurements are taken further along the edge of the sample, i.e. x greater than $45mm$, the behaviour of the potential changes. At

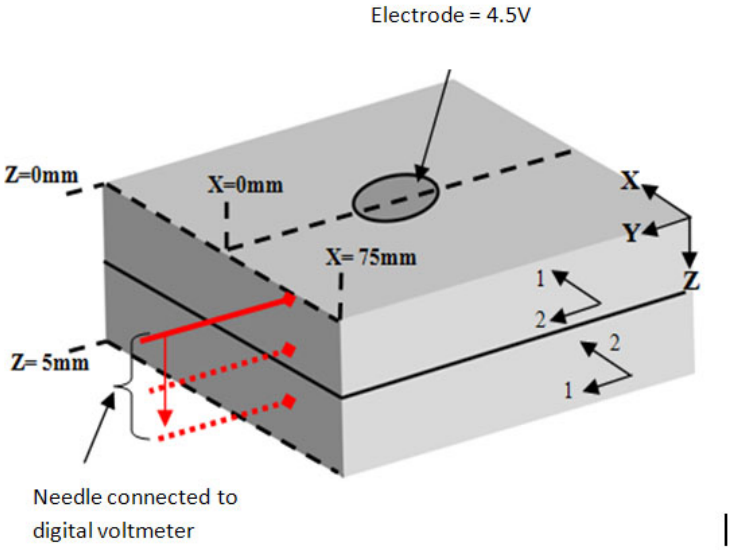

FIGURE 8.5: Schematic diagram of the experimental setup. The needle which was connected to a digital voltmeter and used for taking measurements is shown in red.

this point, the potential in the bottom laminate stops decreasing and begins to increase, as shown in Figure 8.7.

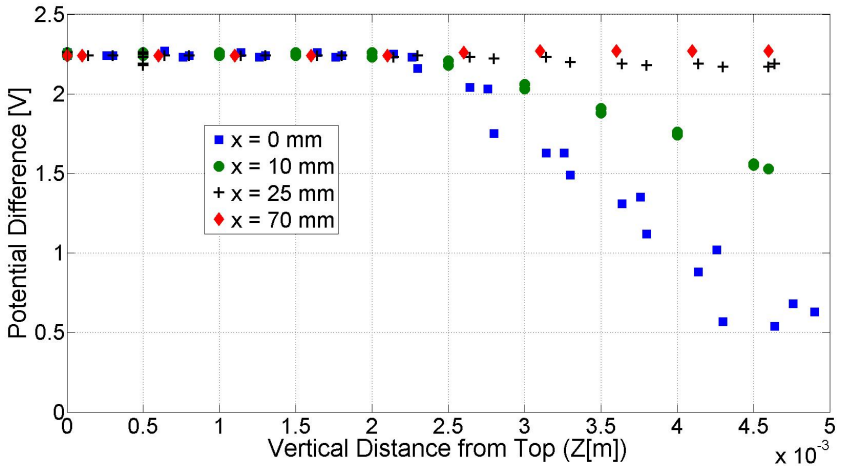

FIGURE 8.6: Experimental results of the potential difference down the edge of the panel (z) for different locations along the edge at $x = 0\,mm$, $x = 10\,mm$, $x = 25\,mm$ and $x = 70\,mm$

8.1.6 Comparison of Numerical Predictions with Experimental Results

A series of graphs showing a comparison between the predicted voltage profile and the experimental results are shown in Figures 8.8, 8.9 and 8.10.

From Figure 8.8, it is evident that the experimental measured voltage profile at x equal to $0\,mm$, is very similar to the numerical predictions. However, the same cannot be

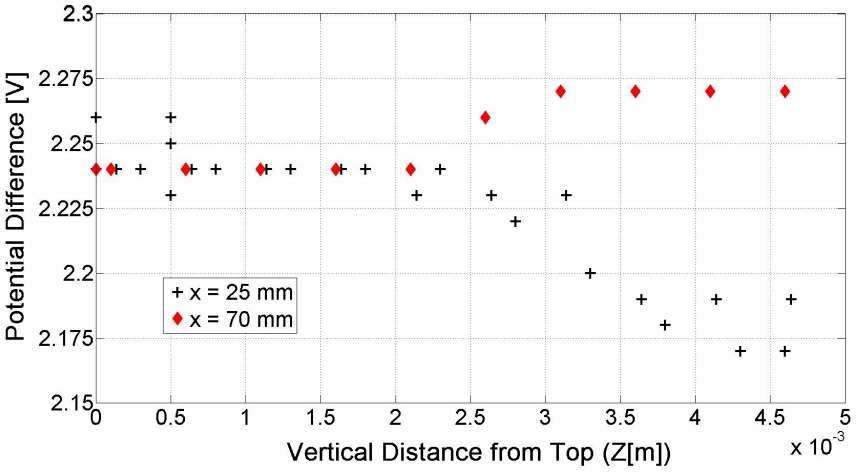

FIGURE 8.7: A zoomed in view of the experimental results for $x = 25\,mm$ and $x = 70\,mm$

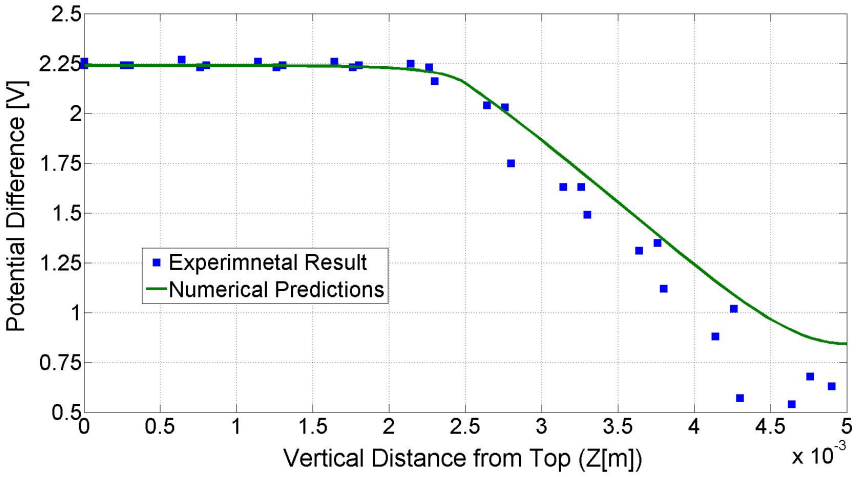

FIGURE 8.8: Comparison between the experimental results and the numerical predictions at $x = 0\,mm$. For this model $\sigma_1 = 7 \times 10^3\ Sm^{-1}$ and $\sigma_2 = \sigma_3 = 1\ Sm^{-1}$

said when comparing the results at x equal to $25\,mm$, as shown in Figure 8.9. At this distance, it appears that the numerical model is predicting a twisted equipotential profile, whilst the twisting in the experimental results occurs at greater values of x. The voltage profile shapes observed for x equal to $70\,mm$ in Figure 8.10 are very similar, although the magnitude of the voltage plateau which occurs when z is greater than $3mm$ is far greater within the numerical model than for the experimental results.

Due to the differences observed between the numerical predictions and the experimental results, a parametric study has been conducted to investigate the sensitivity of the numerical predictions to the electrical conductivities $(\sigma_1, \sigma_2, \sigma_3)$. At this stage, no attempt is made to solve the inverse problem, i.e. to determine the materials conductivities from the potential measurements. The discussion starts by considering the sensitivity to σ_1. The comparisons presented in Figures 8.11, 8.12 and 8.13, show that the numerical predictions are not sensitive to variations in σ_1.

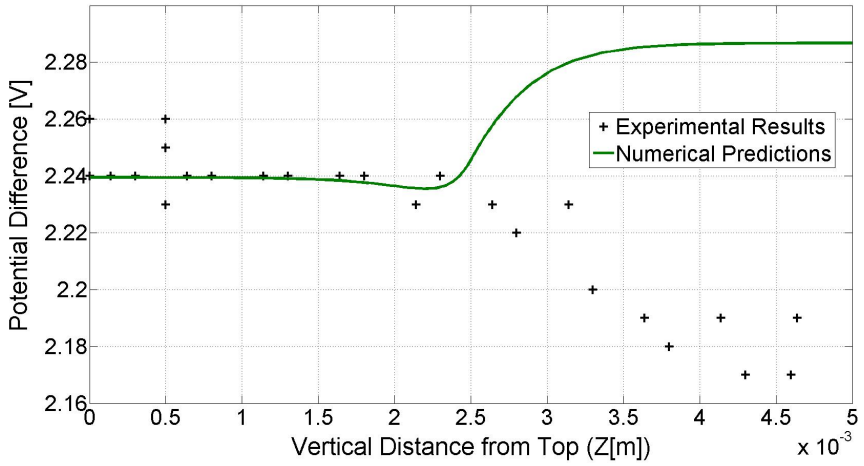

FIGURE 8.9: Comparison between the experimental results and the numerical predictions at $x = 25\ mm$. For this model $\sigma_1 = 7 \times 10^3\ Sm^{-1}$ and $\sigma_2 = \sigma_3 = 1\ Sm^{-1}$

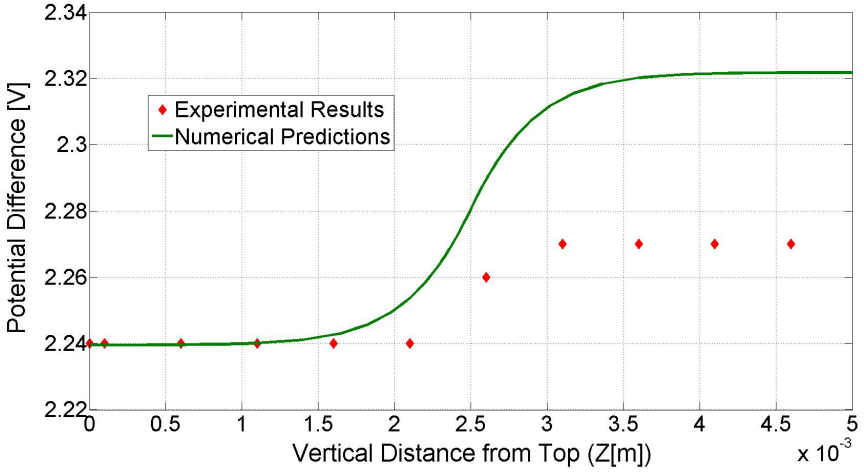

FIGURE 8.10: Comparison between the experimental results and the numerical predictions at $x = 70\ mm$. For this model $\sigma_1 = 7 \times 10^3\ Sm^{-1}$ and $\sigma_2 = \sigma_3 = 1Sm^{-1}$

Next the sensitivity with respect to σ_2 and σ_3 is considered. The results in Figure 8.14, show that, as σ_2 is independently increased, the position at which the twisted potential occurs is moved to greater distance along x direction. Whereas Figure 8.15 shows that a decrease in σ_3 causes the twisting potential to move further along the x axis.

From these results it is evident that the location at which the twisting potential occurs is sensitive to both σ_2 and σ_3. It is further evident that the location of the twisting potential is related in some way to the fraction of $\dfrac{\sigma_2}{\sigma_3}$.

8.1.6.1 Discussion on the Experimental Comparison

It can be seen that the experimental results portray the same potential difference trends as those predicted by the numerical model. This implies that the numerical model

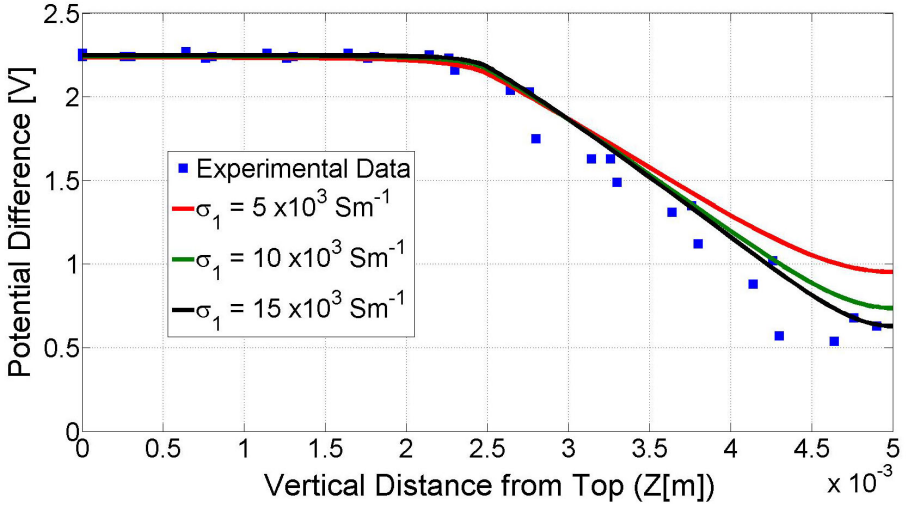

FIGURE 8.11: Comparison between the experimental results and the numerical predictions as σ_1 is varied at $x = 0mm$. The remaining conductivities are $\sigma_2 = \sigma_3 = 1\ Sm^{-1}$

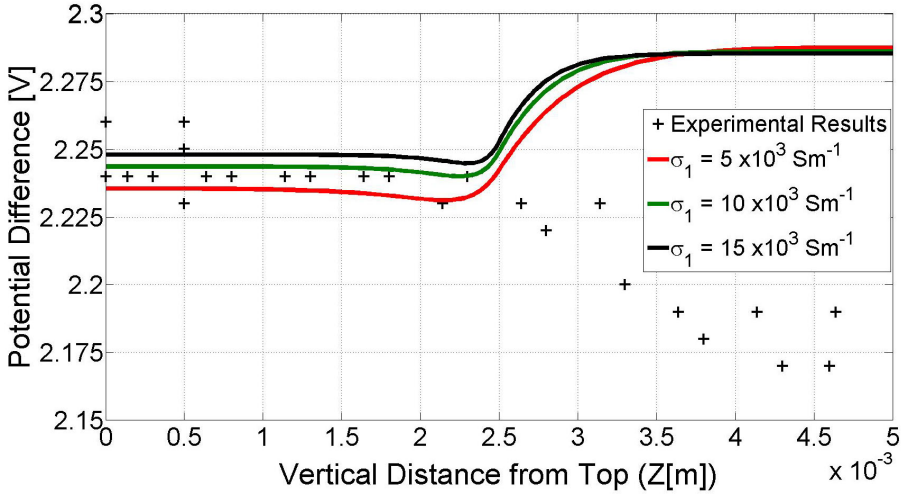

FIGURE 8.12: Comparison between the experimental results and the numerical predictions as σ_1 is varied for $x = 25mm$. The remaining conductivities are $\sigma_2 = \sigma_3 = 1\ Sm^{-1}$

supports the real physical nature of the predicted phenomena as the twisting potential and the upward current flow patterns occur in the experiment. More broadly, this study has verified the approach of numerically representing a piece of CFC as a homogeneous block. The sensitivity study implies that to achieve a more accurate agreement between the numerical predictions and the experimental results, σ_3 should be smaller than σ_2. This can be explained as there is expected to be a thin epoxy region between the plies, which reduces σ_3.

8.1.7 Twisting Potential in Typical CFC lay-up

Having numerically identified a phenomenon in highly anisotropic materials with a simple two ply CFC. The next question is what happens with a more typical quasi-isotropic

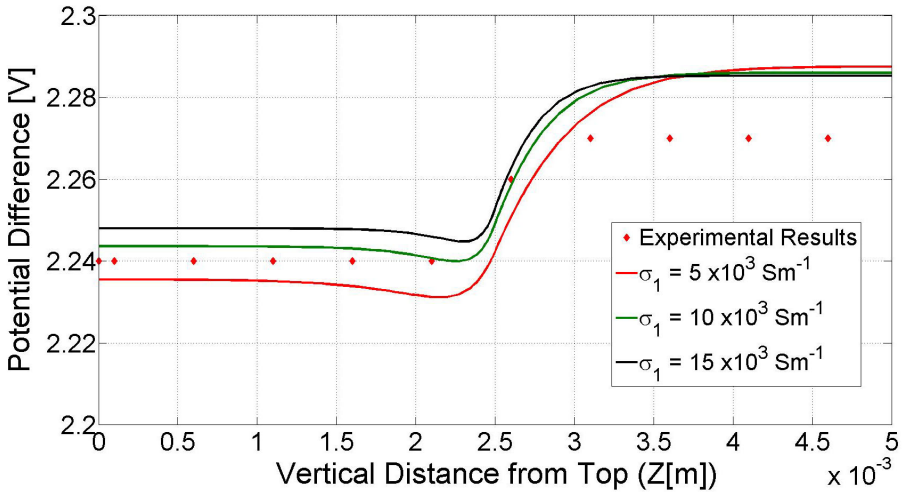

FIGURE 8.13: Comparison between the experimental results and the numerical predictions as σ_1 is varied at $x = 70mm$. The remaining conductivities are $\sigma_2 = \sigma_3 = 1Sm^{-1}$

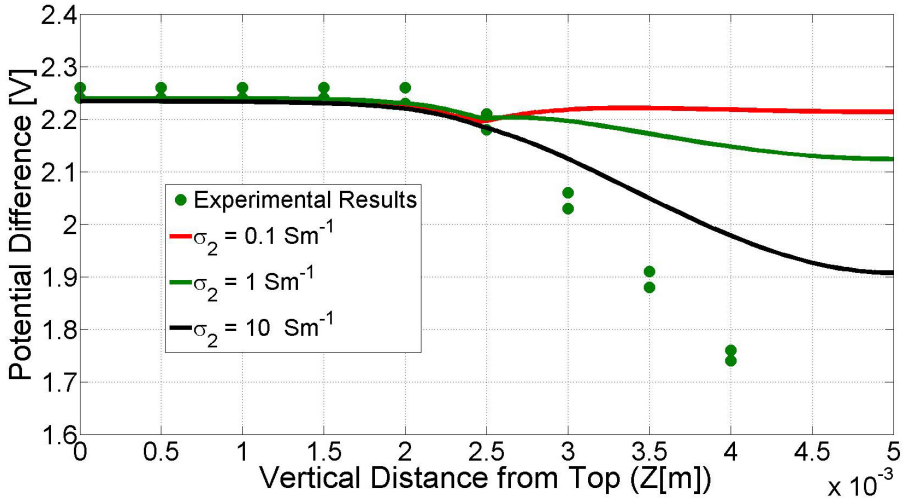

FIGURE 8.14: Comparison between the experimental results and the numerical predictions as σ_2 is varied at $x = 10mm$. The remaining conductivities are $\sigma_1 = 7 \times 10^3\ Sm^{-1}$ and $\sigma_3 = 1\ Sm^{-1}$

CFC panel. Whilst considering a quasi-isotropic panel, the location of the electrical grounding is also varied to investigate what affect this has on the twisting equipotential surfaces.

8.1.7.1 Numerical Model

For this study, the same numerical model as that considered for the previous study is used. However, the design of the CFC is changed to consider a typical 22 ply CFC, with each ply again being considered as a homogeneous anisotropic block. The geometry of the numerical model is shown below in Figure 8.16, and the orientation of the fibres in each ply is defined in Appendix A. The dimensions used in the geometry, correspond to

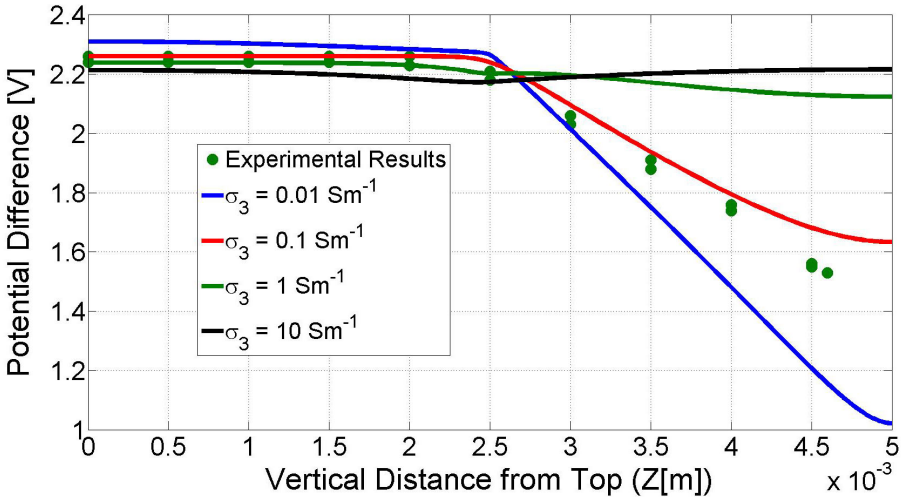

FIGURE 8.15: Comparison between the experimental results and the numerical predictions as σ_3 is varied at $x = 10mm$. The remaining conductivities are $\sigma_1 = 7 \times 10^3\ Sm^{-1}$ and $\sigma_2 = 1\ Sm^{-1}$

the area which surrounds the damaged region from current impulse D, as discussed in Section 5.3. The electrical conductivities used here are the same as those experimentally obtained previously i.e. σ_1 is $7 \times 10^3\ Sm^{-1}$ with σ_2 and σ_3 equal to $1\ Sm^{-1}$.

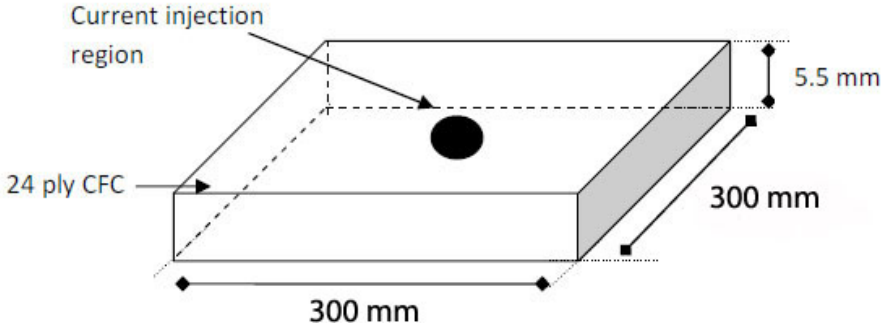

FIGURE 8.16: Schematic diagram of the geometry used in the numerical model

The electrical input for this model comes from an inward current density positioned in the centre of the top surface, as shown in Figure 8.16. This is given by the 2D Gaussian function, as defined in Equation (7.8), where the arc radius (Λ) is given as 5.3 mm. For this study, the peak current density refers to the current from component C, which is defined by ED-84 to be 500 A [11]. The grounding locations shown in Figure 8.17 were considered. The area of the grounding plates on the top and bottom surfaces are defined by the experimental current impulse tests outlined in Section 3.4.2.3.

Three further compound grounding combinations were also considered. These are (1) a combination of all three grounding locations (top + bottom + side), (2) a combination of the top and bottom grounding surfaces and (3) a combination of the grounding on the top and sides. The combination of top and bottom grounding locations is of principle importance, since this model represents the grounding locations used in the

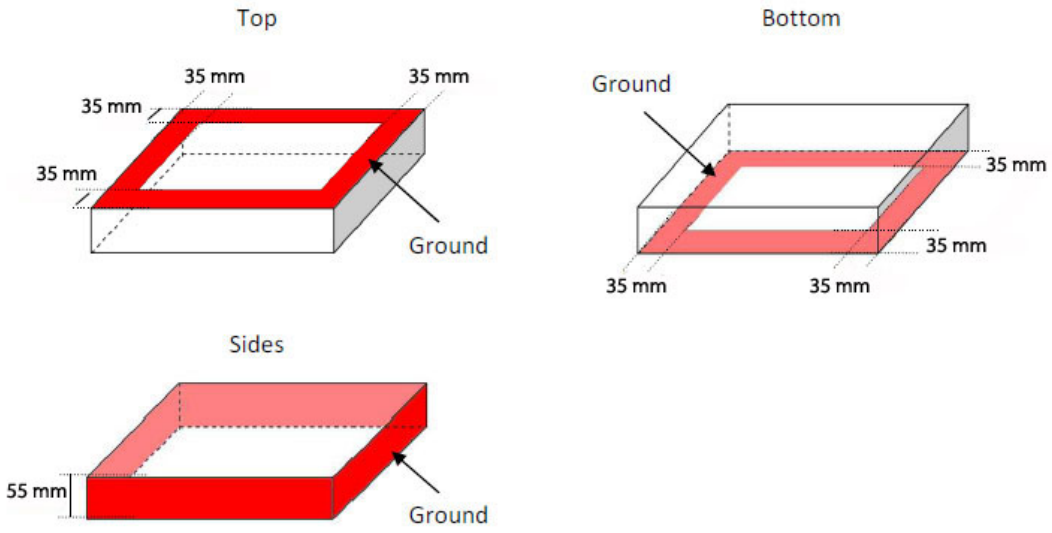

FIGURE 8.17: Diagrams showing the different grounding locations which were considered

experimental current impulse tests, outlined in Section 3.4.2.3. All remaining boundaries are considered to be insulated.

8.1.7.2 Results

The equipotential surfaces for each of the six different grounding locations are shown in Figures 8.18, 8.19 and 8.20. It is noticeable from these figures that the twisting equipotential surfaces are only observed when the samples are grounded on the bottom surface only. Furthermore, it is interesting to note that this twisting equipotential is only apparent within the top two plies. This corroborates the explanation as to why the twisting only occurs near the surface since, below the top few plies, the current density is minimised throughout the domain (i.e. fully spread out) and hence there is no further energy saving to be made by a twisting equipotential surface and hence the twisting is limited to the top few plies.

When the grounding is either on the top or the sides, Figure 8.19 shows that there are no twisting equipotential surfaces. This is explained when the sides are grounded, as the highly conductive direction along the fibres leads straight to the ground, and therefore, no complex equipotential surfaces are observed. A similar effect occurs when only the top surface is grounded. As for this case, the current flows along the fibres to reach the sides, from where it then flows back up towards the top surface. This, therefore, explains the equipotential ring marked on Figure 8.19 of $2.5\,V$.

The numerical predictions for when all the surfaces (top, bottom and side) are grounded is shown in Figure 8.20a. From these equipotential surfaces, it is evident that the side

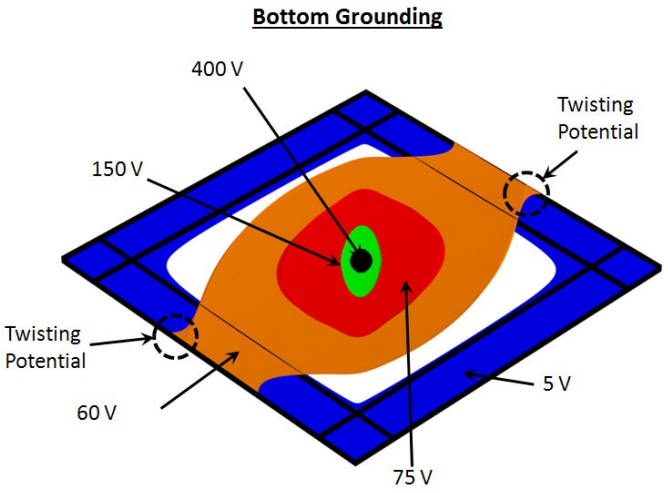

FIGURE 8.18: Equipotential surfaces for a quasi-isotropic CFC when the ground is only on the bottom face. Note the twisting equipotential surface at 60 V

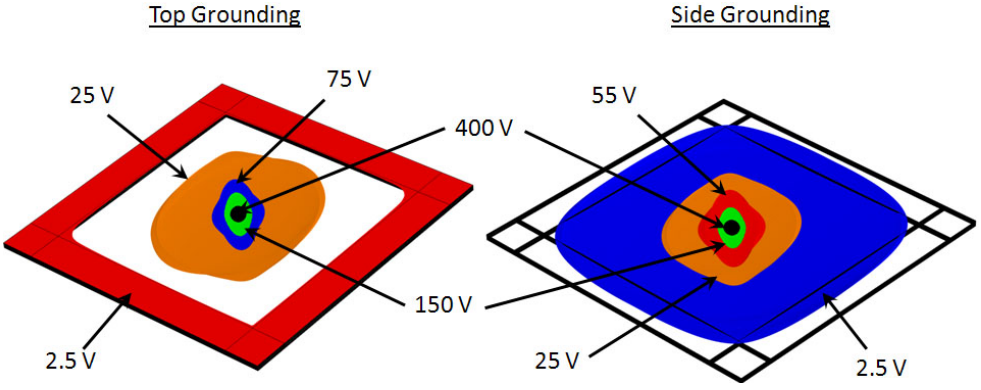

FIGURE 8.19: Equipotential surfaces for a quasi-isotropic CFC when the ground is on the top surface (left) and on the sides (right)

grounding dominates the resultant equipotential surfaces that are witnessed. This is not a surprise given that the highly conductive direction along the fibres will dominate the path to ground. For the same reasons, similar results are also noticed when the top and sides are grounded (not shown here). The equipotential surfaces, when the top and bottom surfaces are grounded, are given in Figure 8.20b and show a very similar result to when solely the top is grounded (Figure 8.19a). This result implies that the majority of the current stays within the top few plies and so the bottom grounding is effectively ignored.

As the location of the electrical grounding determines the current flow pattern, it is important to investigate how this affects the amount of Joule heat which is released into the CFC. The importance of this heating mechanism has already been highlighted in Section 2.2.4.3. The amount of Joule heat released for each grounding location is calculated using the numerical solutions from the models above and Equation (2.2). The total Joule heat released for each different set of grounding locations are shown in

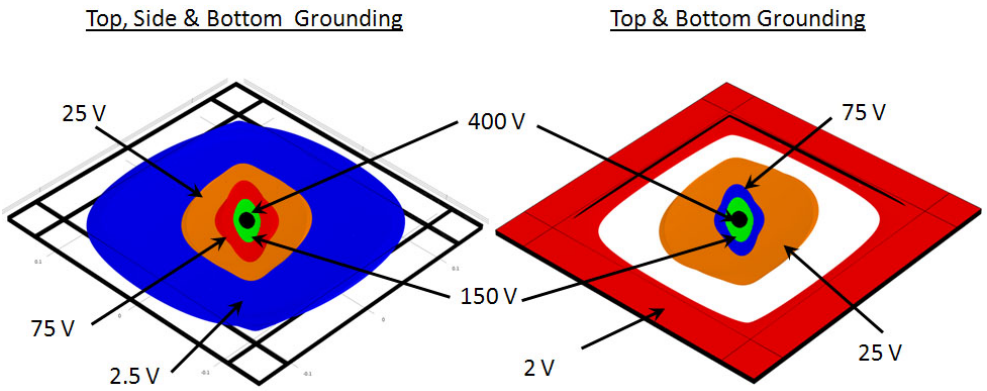

FIGURE 8.20: Equipotential surfaces for a quasi-isotropic CFC when the above grounding locations are combined

Table 8.1.

Grounding location	Total Joule Heat [kW]
Top	519
Bottom	557
Sides	509
Top, Bottom & Side	508
Top & Side	514
Top & Bottom	508

TABLE 8.1: Total energy from the Joule heat which is deposited into the system due each grounding location

It is evident that by excluding the results for when only the bottom is grounded, the total energy input is very similar across the different grounding locations. When the sample is grounded at the bottom only, there is a noticeable increase in the amount of Joule heat which is released into the CFC. Therefore, from the point of view of the energy input, this implies that as long as only the bottom is not grounded, the location of the grounding should cause minimal variation on the damage witnessed to the CFC. It is also evident that a similar amount of Joule heat is released, when only the top is grounded and the top and bottom surfaces are grounded. This further implies that there is negligible current travelling towards the bottom electrode, as stated above.

8.1.8 Summary of Homogeneous Methods

The above discussions have considered how an electrical current flows inside a highly anisotropic material. The numerical results showed complex current flow patterns, with twisting equipotential surfaces, occurring approximately within $\pm 1\%$ of the mid potential. Such potential profiles result in an upward current flow in the corners of the anisotropic material. The upward current flow paths can be explained by the restive distribution within the CFC panel. In other words, the Joule heat is minimised by reducing the current density component in the direction of low conductivity rather than just

taking the shortest path between the electrodes. This may appear counter intuitive, as the current travels back and forth through the thickness of the panel three times rather than just once.

A bespoke experiment was conducted to verify these numerical predictions. The experimental results confirm the upward current flow which has been observed in the numerical model. However, the experimental results cannot be explained with the electrical conductivity values obtained from the previous chapter within the numerical model. The reason for this is unknown, although it could be explained by the different fibre layup affecting the through thickness conductivity. Another possible reason for this could be that the panel does show slight signs of warping. This warping is believed to be an unavoidable consequence of the chosen fibre layup and could certainly affect the bulk conductivity within the CFC. To follow on from this, a sensitivity study has been conducted to determine how sensitive the numerical predictions are to the electrical conductivity. Results show that the location of the twisting potential is sensitive to σ_2 and σ_3, with σ_1 having no significant impact.

The numerical model was then expanded to represent a typical quasi-isotropic CFC panel. Whilst conducting this investigation, the location of the grounding was varied, to investigate if this had an effect on the numerical predictions. It was noticed that, only when the ground is at the bottom of the sample, was there a twisting equipotential surface. Using these numerical solutions, the total energy deposited into the CFC due to the Joule heat as a result of the different grounding locations has been investigated. This study showed that when the grounding is on the bottom, there is a substantial increase in the amount of Joule heat released. For the remaining grounding locations, the total energy deposited into the system due to Joule heat is comparable. This demonstrates that as long as the grounding is not solely on the bottom of a panel, the damage caused by the Joule heating should be independent of grounding location.

8.2 Thermo-Chemical Degradation Model

The numerical predictions from the thermo-chemical degradation model outlined in Chapter 7 are now considered in relation to the laser ablation experiment conducted in Chapter 5. The numerical predictions are initially considered for a 1D case, as the results from such a case are simpler to interrogate than the results from a 3D model. Due to the symmetry entailed, the 1D model implemented here, effectively considers an infinitely large flat plate being uniformly heated on the top surface. It is, therefore, not possible to compare the numerical predictions from the 1D model against the experimental results. However, as the heat flux density is reduced (i.e. not increased), it is still possible to investigate qualitatively the numerical predictions from the 1D model to understand what is physically occurring to the CFC sample during the laser abla-

tion. After considering the physical meaning behind the numerical predictions for the 1D case, the model is then expanded into 3D to allow a direct comparison between the experimental results and the numerical predictions.

8.2.1 1D Thermal Degradation Model

The 1D laser ablation model is designed to replicate a 1D line down through the centre of the CFC, which requires that the bulk material properties are defined along local axis direction 3. An illustration of the geometry is shown below in Figure 8.21.

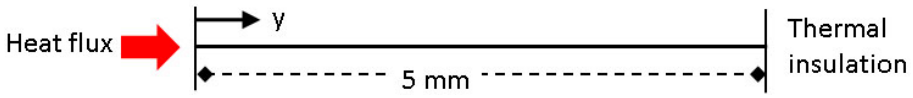

FIGURE 8.21: Geometry and boundary conditions used for the 1D laser ablation model

As this model represents the local axis direction 3, the bulk thermal conductivity (κ_3) for this study is given by the Series Rule of Mixtures (defined by Equation (2.12)). The choice of method for determining the bulk conductivity in direction 3 is not important as the numerical predictions are only being considered quantitatively. The material properties used in this model are shown in Appendix C. The heat flux for this model is given by the peak power density of the 6 Watt laser beam. This is calculated by dividing the power of the laser beam (6 Watts) by the area under the laser beams Gaussian function as considered in Equation (7.8). The reaction kinetics used for this study are taken from the TGA results, given in Table 4.5. As with the validation study conducted in the previous chapter, these initial studies will consider the reaction order (n) to be one. For this 1D study, is it also assumed that the polymer degrades solely into gas with no char being produced. The impact of both assumptions is considered in a later section of this chapter. To ensure the numerical predictions relate to a converged solution, unless otherwise stated, the mesh and time step parameters from the validation study, given in Table 7.1, are used to obtain a numerical solution.

8.2.1.1 1D results

The numerical predictions are first investigated by considering the temperature profile shown in Figure 8.22. These results show that moving away from the heat source (at y equal zero), deeper into the material, the temperature decreases. The most noticeable aspect of this temperature decrease, is that there is a definite change in thermal gradient around $1250\,K$.

By considering the effective polymer density ($m_p^\dagger$) shown in Figure 8.23, it is evident that the change in thermal gradient occurs at same location as the decrease in effective polymer density. This location is called the reaction front, as it portrays the location

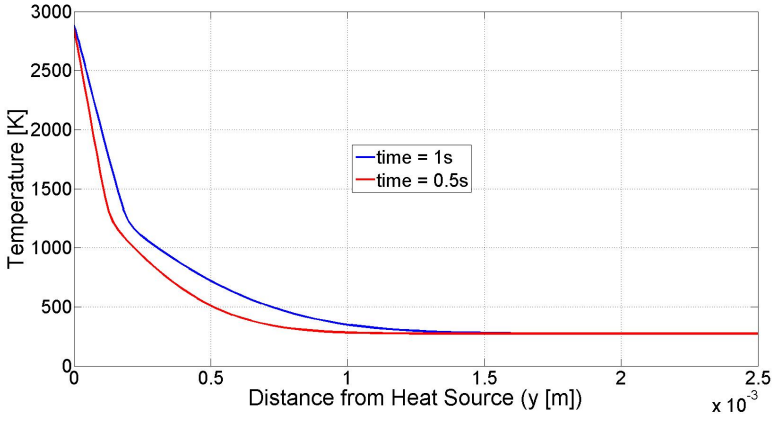

FIGURE 8.22: Laser ablation temperature profile with the 1D model

of the peak reaction rate. It is evident from Figure 8.23 that the polymer degradation occurs rapidly over a small spatial region. This sudden polymer degradation leads to a rapid change in the bulk material properties due to the variation in polymer volume fraction, which in turn causes the sudden change in the thermal gradient seen in Figure 8.22.

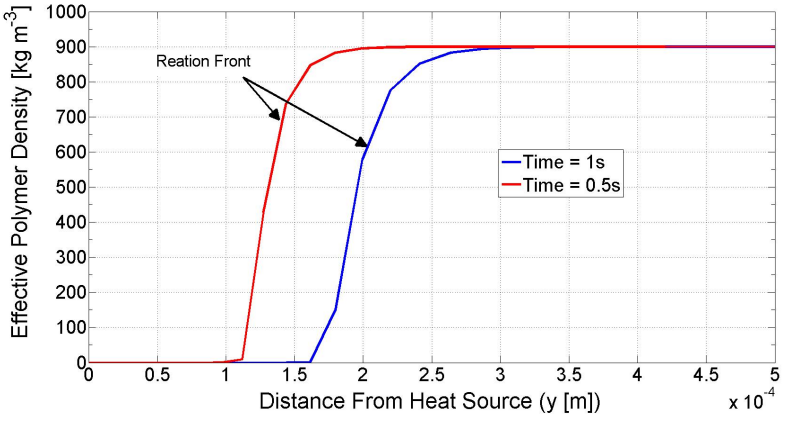

FIGURE 8.23: Predicted affective polymer density for two times, within the material

The effective polymer density is considered in Figure 8.23 rather than the polymer mass, because due to the non-uniform mesh it is not appropriate to compare the polymer mass within different cells. The effective polymer density ($m_p^\dagger$) is defined by

$$m_p^\dagger = \frac{m_p}{V_{cell}} \tag{8.4}$$

This approach is also used to define an effective gas density ($m_g^\dagger$), which is considered later.

The reaction products of the polymer degradation are now considered. Starting with the gas volume fraction shown in Figure 8.24, it is evident that this profile mirrors

the polymer density profile, given in Figure 8.23. This is expected as the degraded polymer leaves empty space for the produced gas to occupy, as defined by Equation (6.3). However, Figure 8.25 shows that the effective gas density ($m_g^\dagger$) does not have the same profile as that of the gas volume fraction (Figure 8.24). This is because the produced gas is allowed to filtrate through the decomposing material and escape. If there was no gas filtration, then the gas density profile would mirror that of the gas volume fraction, with the total mass of gas being equal to the total mass of degraded polymer, due to the conservation of mass. By comparing the effective gas and polymer density, it is evident that the majority of the gas produced has escaped from the decomposing CFC.

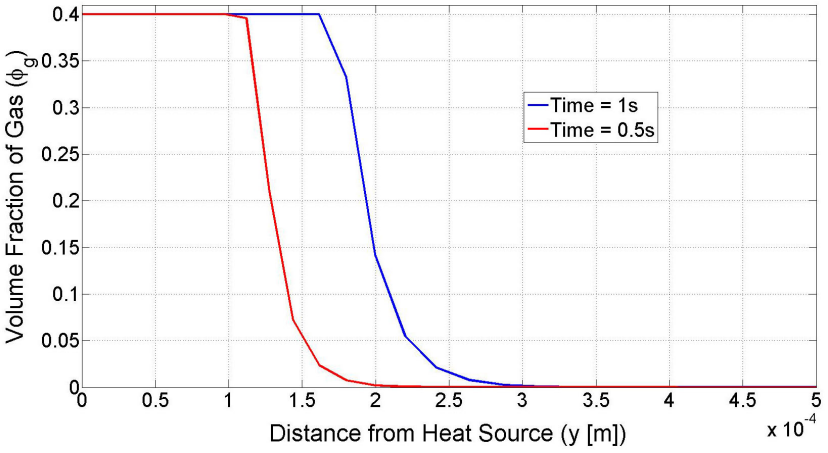

FIGURE 8.24: Gas volume fraction

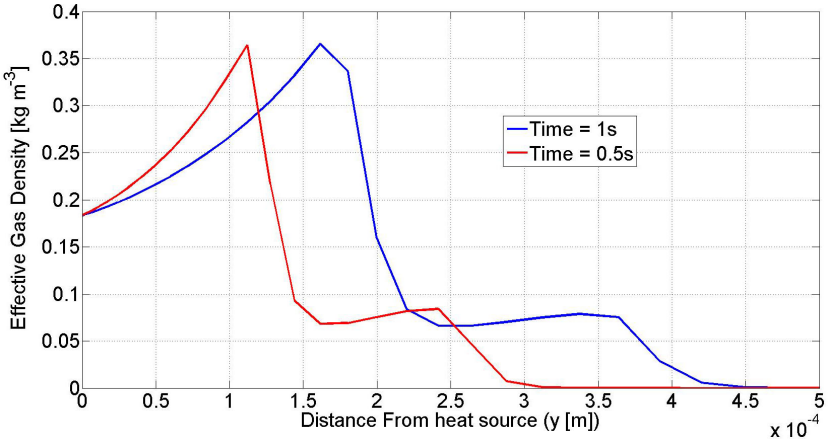

FIGURE 8.25: Effective gas density

The effective gas density profile predicted for one second is now investigated in more detail. Starting at y equals zeros, the effective gas density shows an initial increase until the reaction front at approximately $0.16mm$, where the effective gas density peaks. After this peak, there is a sudden decrease in gas density followed by a roughly constant gas density between $0.25\,mm$ and $0.36\,mm$. The decrease in gas density between $0.17\,mm$ and $0.21\,mm$ matches the decrease in gas volume fraction shown in Figure 8.24. After

the constant gas density plateau, the effective gas density decreases towards zero. To understand what causes this profile, the gas filtration through the decomposing material is considered.

The gas filtration velocity given by Darcy's law (Equation (2.28)) is dependent on the gradient of the internal gas pressure (P), permeability of the decomposing material (γ) and gas volume fraction (porosity). With the gas volume fraction having already been considered above, the remaining two terms are now considered.

The gas pressure profile, shown in Figure 8.26, can be broken down into three distinct regions, with each region being explained with reference to the ideal gas law, given in Equation (7.7).

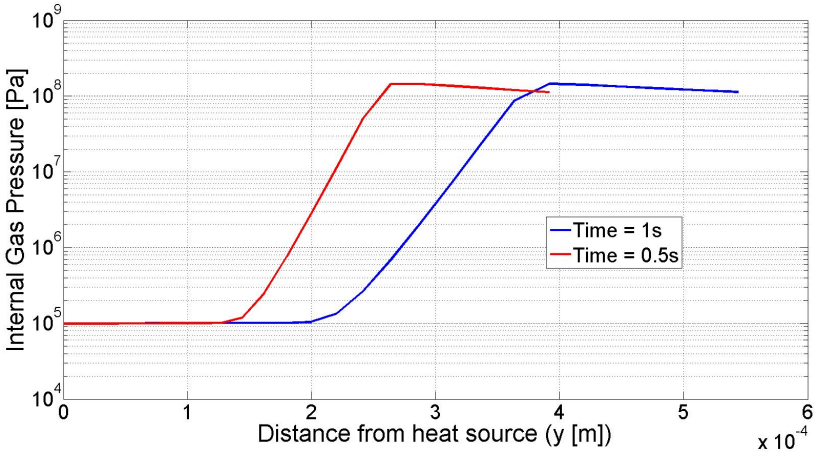

FIGURE 8.26: Internal gas pressure

By considering the pressure after 1 s and moving along the x axis from the origin (i.e. increasing distance from the heat source), the initial region shows what appears to be a constant pressure. There is in fact a slight increase in pressure between the heat source boundary (i.e. y equals zeros) and y equals $0.2\,mm$ (not visible due to the log scale used in the graph). The slight increase in pressure is caused by the increasing effective gas density overcoming the decrease in temperature. After this initial region, there is a large increase in gas pressure of several orders of magnitude. The increase is caused by the gas volume fraction tending towards zero and dominating the pressure predicted by the ideal gas law. There comes a point, however, where the effective gas density becomes so small that the pressure stops increasing and hence reaches a peak. Since the volume fraction of gas can be defined with reference to the reaction front, it is observed that the peak pressure occurs ahead of the reaction front. The peak internal gas pressure is approximately $2 \times 10^8\ Pa$, which is 3 orders of magnitude greater than atmospheric pressure. It appears that the peak pressure appears roughly constant with time as the reaction front moves through the material.

The permeability of the decomposing material as a function of gas volume fraction is

shown in Figure 8.27. This figure shows that when the gas volume fraction (Φ_g) is less than 0.05, there is a rapid decrease in permeability. This rapid decrease indicates that when the gas volume fraction is below 0.05, the friction due to the large surface area compared to the small volume of gas dominates the gas filtration through the decomposing material.

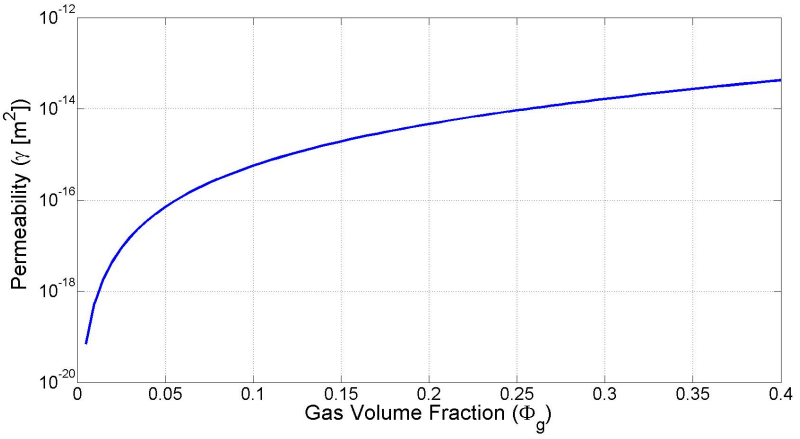

FIGURE 8.27: Permeability of the decomposing material as a function of gas volume fraction

The internal gas pressure and the permeability, by themselves, do not directly explain what causes the plateau region in the effective gas density to form. To explain this, the gas filtration velocity through the decomposing material at the beginning and end of a given time step are considered. The effective gas density and the filtration velocity for the beginning and end of a time step at t equals one second are shown in Figures 8.28 and 8.29, respectively. The negative gas filtration velocity presented in Figure 8.29, indicates that the gas moves towards the heat source at y equals $0\,m$, as expected. From an initial inspection of Darcy's law (Equation (7.6)), the large pressure increase, shown in Figure 8.26, should produce a large filtration velocity in the same region. However, Figure 8.29, shows this is not the case. This is because the small gas volume fraction which causes the large pressure increase, also causes the permeability term to heavily restrict the gas filtration velocity. By comparing the gas filtration velocity at the start of the gas transport step, there is a noticeable peak in filtration velocity at approximately $0.19mm$. This is due to the newly produced gas which has been produced by the chemical reaction model, since the previous gas transport step. By the end of this gas transport step, this peak velocity has diminished as this newly produced gas has dissipated and the so the gas velocity forms a smooth profile.

From the numerical predictions presented in Figures 8.28 and 8.28, it is possible to explain why this plateau region in the effective gas density profile forms. By initially recognising that the plateau region is ahead of the reaction front, there is minimal gas produced here and hence, there is a small gas volume fraction. Therefore, due to the surface tension (introduced by the permeability) the gas filtration velocity is highly

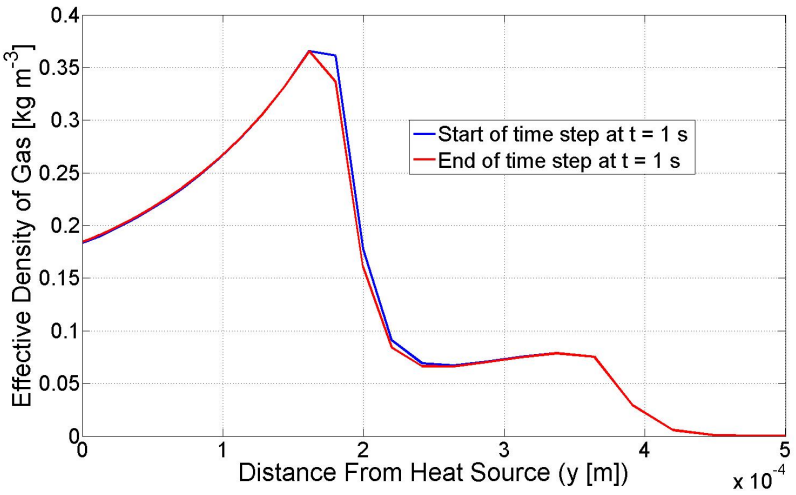

FIGURE 8.28: Affective gas density and the gas filtration velocity at the start and end of the gas transport step

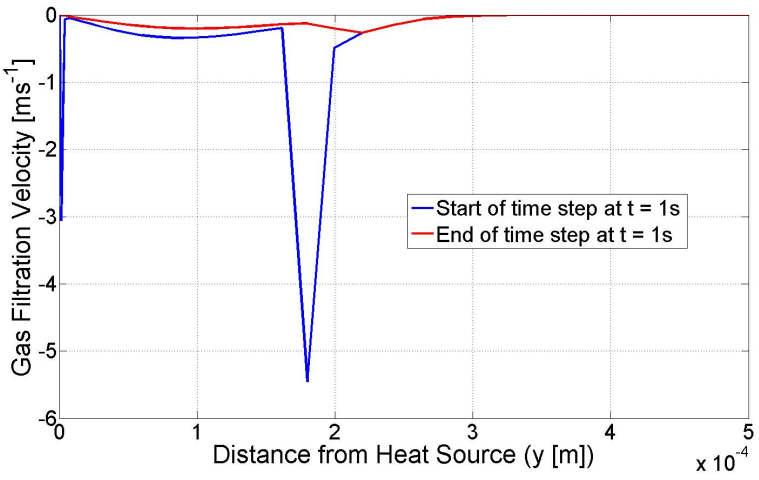

FIGURE 8.29: Affective gas density and the gas filtration velocity at the start and end of the gas transport step

restricted (discussed above). But as the amount of gas increases, i.e. the closer one gets to the reaction front, the permeability stops dominating which allows the gas to filtrate through the material. The gas filtration velocity soon begins to decrease behind the reaction front, since the gas filtration velocity is no longer dominated by the internal gas pressure, as there is a roughly constant pressure behind the reaction front. This leads to the plateau region forming, as the produced gas is only moved a small distance from just in front of the reaction to just behind the reaction front, when the volume fraction is high enough. This movement in gas can be seen by considering the slight decrease in gas density shown in Figure 8.28.

As has been stated in Section 7.6, the application of Darcy's law to determine the gas filtration velocity assumes that the gas velocity is perfectly laminar with no turbulence.

This assumption can be validated by considering the Reynolds number. The Reynolds number is the ratio between the viscous forces and the laminar forces and is calculated using

$$Re = \frac{\rho_g \, v_g \, L}{\mu} \tag{8.5}$$

Where L and μ are the characteristic length and the dynamic viscosity of the gas. It is known that for Darcy's law to be valid the, Reynolds number needs to be less than 10. The gas viscosity is a material property of the gas and is given in Appendix C. The characteristic length defines the size of the domain through which the gas is travelling. Assuming the gas occupies a region where there is no polymer, the characteristic length is the distance between neighbouring fibres. Due to the random nature of the fibre locations, there is no fixed value for this dimension. It is, therefore, assumed that the fibre gap is no greater than half the radius of a fibre i.e. L equal to 4 μm. This is probably an over estimate given the cross sectional image of a CFC given in Figure 2.21. However, by over estimating L, the Reynolds number will only ever be an overestimate and hence if the Reynolds number satisfies the condition to use Darcy's law (i.e Re less than 10) with the assumed value of L, then the Reynolds numbers should satisfy the application of Darcy's law within a decomposing CFC. To determine Reynolds number for this scenario, the gas filtration velocity at the start of time step given in Figure 8.29 is used. This is shown below in Figure 8.30.

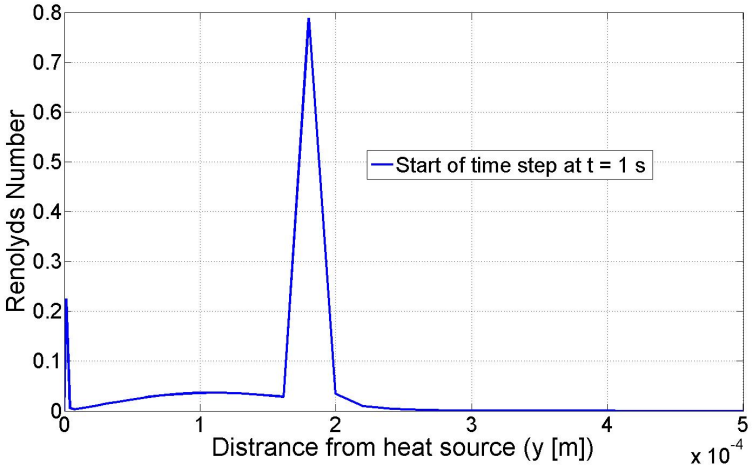

FIGURE 8.30: Reynolds number for the start of the mass transport step at 1 s

The gas filtration velocity used to calculate the Reynolds number is taken at the start of the transport time step, since the gas filtration velocity at the start of the time step is greater than at the end of the time step. It is important to consider the greatest filtration velocity, as Equation (8.5) demonstrates that Re increases with velocity and hence if Re is less than 10 with the largest velocity then the application of Darcy's law will be valid for all lower velocities. The Reynolds numbers, calculated using the gas filtration velocity in Figure 8.29 are shown in Figure 8.30. This figure shows that the

maximum Reynolds number is less than 10, and hence the application of Darcy's law is a valid assumption.

8.2.1.2 Effect of Thermal Gas Transport

Whilst all the numerical predictions up to this point have considered a model which includes the gas transport (including the gas convection), the obvious question is what effect does the gas transport have on the internal energy of our system and hence the predicted damage? This question arose due to discussions in Section 2.6.4, where the study by Florio et al. [58], stated that the inclusion of the gas transport model on decomposing composites has a considerable effect on the predicted damage. However, in this discussion, doubt was cast on the physical processes used in their model. To investigate what effect the gas transport has on the predicted damage, the same 1D model used above is considered again, only for this study the model is re-solved, with and without the transport model being included. The numerical predictions from these models are compared by considering the difference in the mass of degraded polymer (Π), which is defined by

$$\Pi = \mid (\Sigma m_p(t_0) - \Sigma m_p(t)) - \left(\Sigma m_p(t_0) - \Sigma m_p^*(t)\right) \mid \tag{8.6}$$

Here, $\Sigma m_p(t_0)$ and $\Sigma m_p(t)$ are the summation of the total polymer mass at the initialisation of the model and later at time t. The superscript '*' refers to the model which included the gas transport. The difference of the degraded polymer, shown in Figure 8.31, will highlight any differences in temperature profile which would have affected the chemical reaction.

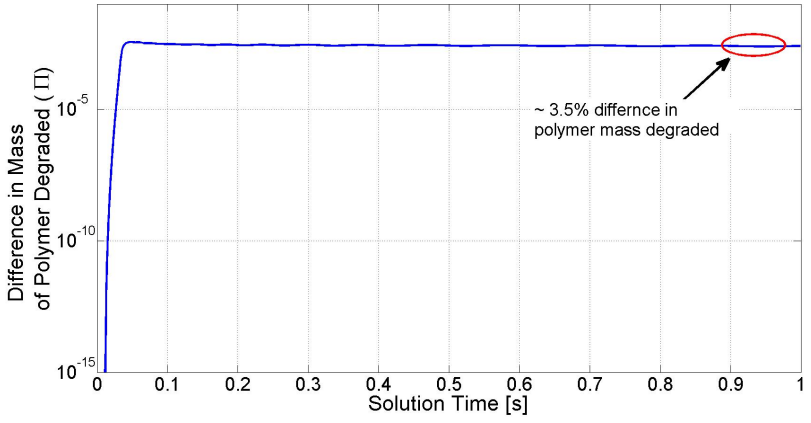

FIGURE 8.31: Difference in the amount of polymer mass which degraded when the gas transport and been included and omitted

From Figure 8.31, it is evident that for solution times above 0.1 s, there is a roughly constant difference in the amount of polymer which has degraded. The percentage difference in the amount of polymer degraded at 1s is roughly 3.5%. This slight difference

can also be seen in temperature profiles predicted by these two models, as shown in Figure 8.32.

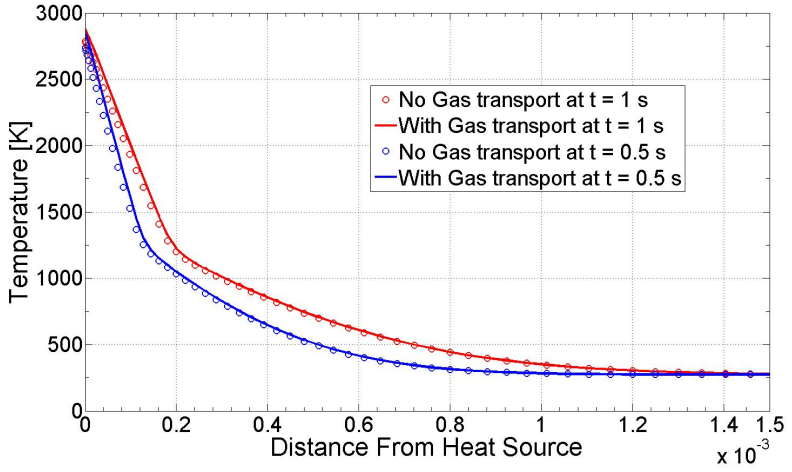

FIGURE 8.32: Temperature profiles at different times when the model includes and does not include the gas transport

With reference to Figure 8.32, there is minimal variation in the temperature profiles due to the inclusion of the gas transport model.

8.2.1.3 Future Use of the Gas Transport Model

From the results presented above, if the mechanical damage (de-lamination or cracking) due to the large internal gas pressure is ignored, then it has been shown that the inclusion of the gas transport model has only a slight impact on the predicted thermo-chemical degradation. Therefore, as the inclusion of gas transport makes the model very slow to solve, the obvious question which arises is, 'is it necessary to include the gas transport model in the thermo-chemical degradation model?'. Despite there being no physical reason to include the gas transport model, since it does not have a significant impact on the numerical results, its partial inclusion is justified as the aim of this study is to investigate the peak internal gas pressure in order to help explain the internal cracks or de-laminations witnessed in the experimental studies conducted in Chapter 5. To investigate this, the gas mass transport subroutine used to calculate the pressure needs to remain with the model.

Therefore, the mass transport subroutine is included without the gas thermal transport. With the thermal gas transport subroutine omitted, the global time step size of the model can be reconsidered to improve the efficiency of the solution. It is clear that the global time step can be increased by recalling that the convergence of the mass gas profile has no effect on either the magnitude or the location of the peak internal gas pressure (shown in Figure 7.20). However, it was noticed, that the non-converged mass transport solutions

created an erroneous temperature increase due to the internal gas pressure failing below 1 Atm. Although, with the omission of the thermal gas transport subroutine, the mass transport has no coupling with the remainder of the physical model, and so the non-converged gas solution has no impact on the overall numerical predictions. Therefore, if only the gas mass transport model is included, larger time steps are sufficient to capture the converged gas behaviour near the reaction front, including the peak pressure, whilst retaining a converged solution for the remaining dependent parameters.

8.2.1.4 Discussion

The 1D thermal degradation model has been considered with respect to the laser ablation experiment conducted in Section 5. The physical meaning behind the 1D predictions have been investigated. The numerical predictions indicate that, for the 1D case, the peak internal gas pressure is large enough to cause de-laminations and cracking, which could explain the experimental results presented in Chapter 5, although a further 3D study is required to confirm this prediction.

As well as the gas pressure, the above discussion has also validated the assumption to use Darcy's law, by considering the Reynolds number. It has also been shown that the thermal gas transport has minimal effect on the numerical predictions. Therefore, in future models, the thermal gas transport model is removed leaving just the gas mass transport.

Despite these conclusions, the numerical predictions presented above cannot be compared with the experimental laser ablation results. The next section of this chapter considers expanding this model into 3D.

8.2.2 3D Thermal Degradation Model

The predictions from the 3D degradation model are compared against the experimental laser ablation results presented section 5.1.

8.2.3 3D Geometry and Boundary Conditions

Rather than modelling the entire piece of CFC as shown in Figure 5.1, the geometry used by the numerical model only considers the region directly around the point of laser ablation, as shown in Figure 8.33. However, it is important that the dimensions of the geometry considered within the numerical model are similar to those of the sample used in the experiment. This is important because the distance between the heat source and the boundaries can affect the numerical solutions. This effect can be shown by initially considering the case when the boundaries are at an infinite distance away from the heat

source. In such a case, the boundaries will have a uniform constant temperature with the ambient as no heat from the heat source will reach these boundaries. However, if the boundaries are close to the heat flux, then they will not be at constant ambient temperature and hence the heat transport away from these boundaries by thermal convection and radiation needs to be considered. The heat transport away from the material due to convection and radiation is typically less efficient than conduction through the material, and so there is a temperature build up within the model due to the closeness of the boundaries. Therefore, to compare the numerical predictions with the experimental results, the location of the boundaries from the heat source in the experiment need to be the same as those used within the numerical model. The boundary of principle importance is that which is perpendicular to the fibre direction. This boundary is important as given the high conductivity along the fibres, there is a high probability that this boundary will not be at a constant ambient temperature. In the numerical model, the location of this boundary is defined by the length of the model along the x direction which is given by L_x. Unfortunately, the sample dimensions shown in Figure 5.1 cannot be directly used by the numerical model for L_x, since the experimental sample had the fibre axis in the top ply at 45 deg to the x axis. To resolve this issue L_x is given as the length of the fibres in the sample at this 45 degree angle. This equates to L_x being 10 mm. The remaining sample dimensions are straightforward to determine. The thickness of the geometry (L_y) is taken to be the same as that of the real CFC sample i.e. 5 mm. The sample dimensions in the z direction (L_z) are given to be that of L_x. An illustration of the geometry used in the numerical model is shown in Figure 8.33.

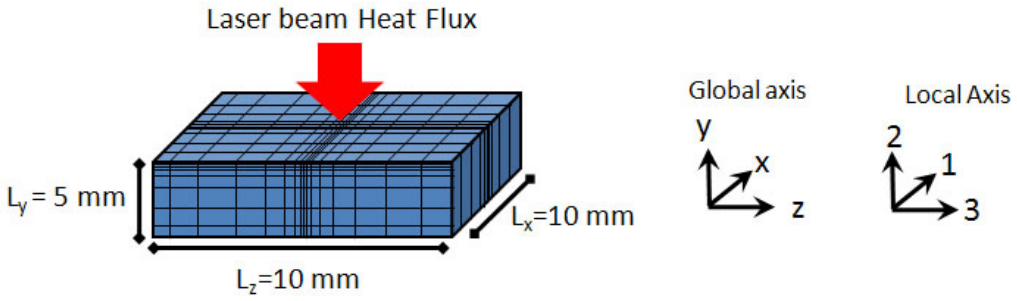

FIGURE 8.33: Damage dimensions from laser ablation

This numerical model considers the piece of CFC to be unidirectional, with the fibre axis orientated along the x axis. This is a reasonable assumption to make as given the damage depth is limited to the first few plies and that the through thickness conductivity is the same regardless of the ply orientation. Therefore, the change in fibre orientation in subsequent plies should have minimal impact on the numerical results.

The laser beam heat flux is defined by Equation (7.8), where the peak heat flux is positioned in the centre of the top surface as shown in Figure 8.33. The remaining boundary conditions are defined as thermal convective with thermal radiation, as defined by Equations (7.9) and (7.10), respectively . The mesh growth rates are defined by the

convergence study in the previous chapter, i.e. $\Delta Y(1)$ equal to $1\,\mu m$ with $\Delta X(1)$ and $\Delta Z(1)$ equal to $10\,\mu m$. To optimise the solution time, the time step sizes used have been recomputed for the 3D laser beam heat flux following the same procedures outlined in Section 7.4. From this study, the global time step ($\triangle t$) was taken to be $100\,ms$ with t_T equal to $10ms$, t_R equal to $2\,ms$ and finally t_m equal to $16.6\,\mu s$. The material properties used in this model are given in Appendix C and the bulk thermal conductivities are calculated using the Rule of Mixtures. The reaction kinetics used in this study are taken from the experimental results presented in Table 4.5, with one modification, namely, the reaction order (n) which is assumed to be 1. The effect of this assumption is considered later.

8.2.3.1 3D Model Results - Polymer Degradation

The predictions from the numerical model are discussed by considering the three damage dimensions outlined in Section 5.1. The discussion starts by considering the predicted damage along the major and minor axis of the polymer degradation. The numerical predictions and the experimental results for these parameters are shown in Figure 8.34 and Figure 8.35. The numerical damage dimensions are obtained by interrogating the numerical predictions to determine the length of the region where the polymer volume fraction has fallen below 5% of its original volume fraction i.e. $\Phi_p = 0.05\Phi_p(t_0)$. These results are given by the coloured circles in Figures 8.34 and 8.35 and are referred to as 'Raw Numerical Predictions'. The choice of polymer volume fraction used to determine the damage dimensions is not critical given the steep reaction front seen in Figure 8.23. The numerical predictions in Figure 8.34 and Figure 8.35 show a step like profile. This step pattern is solely due to the discretization of the geometry by the mesh. Numerical studies have shown that decreasing the mesh growth rate, reduces the step profile creating a smoother trend. This smooth trend follows the leading edge of the step profile for a coarser mesh. Therefore, rather than solving the numerical model with a smaller mesh growth rate than is required to obtained a converged solution, the leading edge from each step for this mesh are joined up to form a more realistic damage profile. This smooth trend line is shown by the solid line in Figure 8.34, where it is referred to as the 'Fitted Numerical Predictions'.

The numerical predictions for the major and minor axes both show an increasing trend as a function of time. The major axis shows a larger damage length than the minor axis due to the higher conductivity along the major axis direction (x axis). By comparing the fitted numerical predictions with the experimental results for the major axis, it is evident that the numerical predictions overestimate the experimentally observed damage. Despite this, it is encouraging that after the initial rapid increase, the rate at which the predicted major length increases is roughly comparable to rate at which the experimental major length increases. The comparison between the experimentally observed

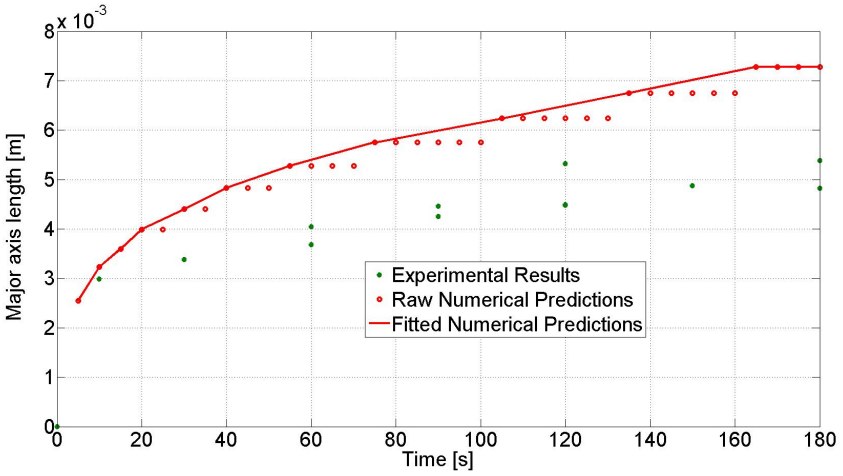

FIGURE 8.34: Comparison between the thermo-chemical degradation predictions against experimental laser ablation results for the major axis

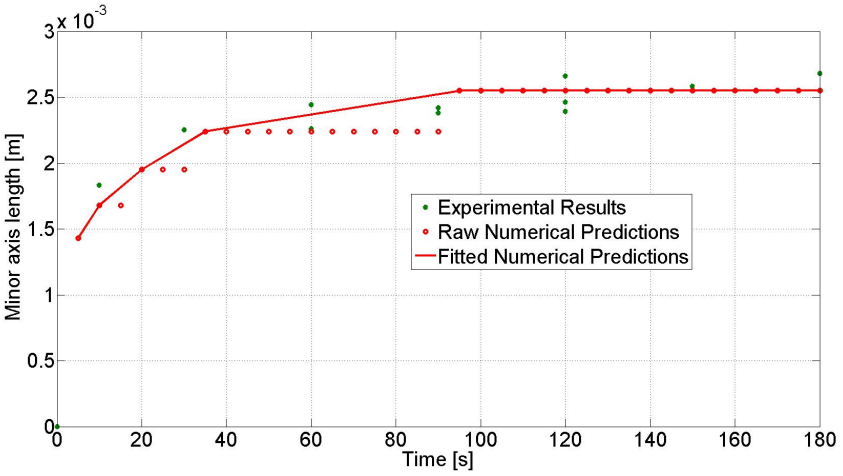

FIGURE 8.35: Comparison between the thermo-chemical degradation predictions against experimental laser ablation results for the minor axis

minor length gives very good agreement with the numerical predictions throughout the entire ablation time.

The final damage parameter to compare with the numerical predictions is the maximum damage depth, and this is shown in Figure 8.36. The leading step edges are again fitted with a smooth trend line, as discussed above.

Comparing the numerical predictions with the experimental results (Figure 8.36) shows that the numerical predictions underestimate the experimentally observed damage depth. It is again apparent that after the initial rapid increase in damage depth, the numerical predictions and the experimental results show a comparable rate of damage depth increase. The possible reasons for this are discussed later in Section 8.2.4.

Having compared the damage dimensions, the predicted internal gas pressure is considered. Figure 8.37 shows the internal gas pressure for a cross section along the minor

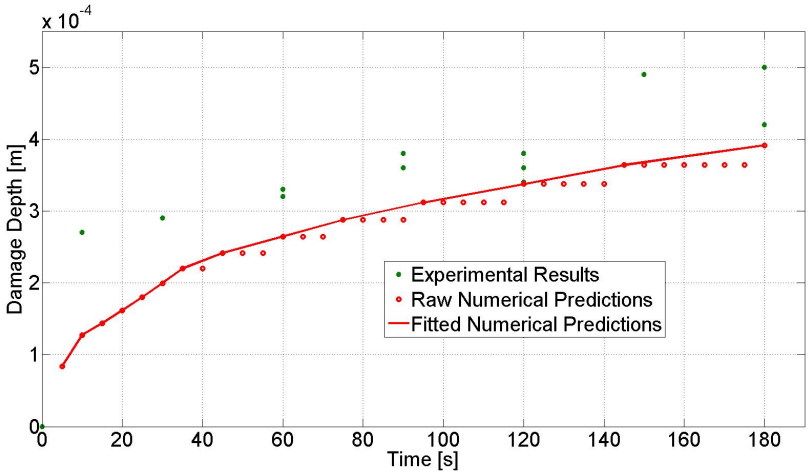

FIGURE 8.36: Comparison between the thermo-chemical degradation predictions against experimental laser ablation results for the maximum damage depth

axis after 180s. Starting from the heat flux surface at the top of the image, the pressure increases radially outwards from the peak heat flux. As explained previously, the sudden increase in pressure occurs just ahead of the reaction front meaning the shape of the reaction front can be inferred from Figure 8.37. The reaction front shows the same topology as that seen by the X-ray tomography image in Figure 5.3. The discontinuity from peak pressure to zero internal gas pressure is due to the gas density in the model being so small that it is recorded as zero, and hence the internal pressure is undefined at these locations.

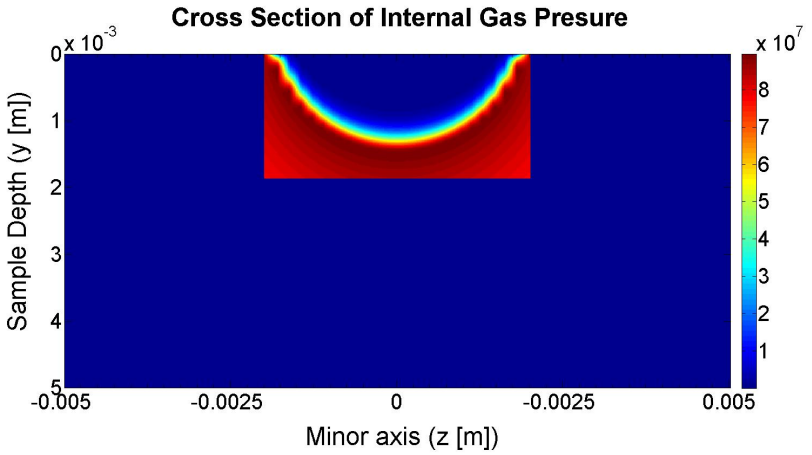

FIGURE 8.37: The internal gas pressure shown by a cross section normal to the fibres (i.e. minor axis plane) for $t = 180\,s$

To get a better understanding of the internal gas pressure, the gas pressure down through the centre of the material as a function of time is plotted in Figure 8.38. The internal gas pressure profile present here shows the same trends as that already discussed for the 1D case in Figure 8.26.

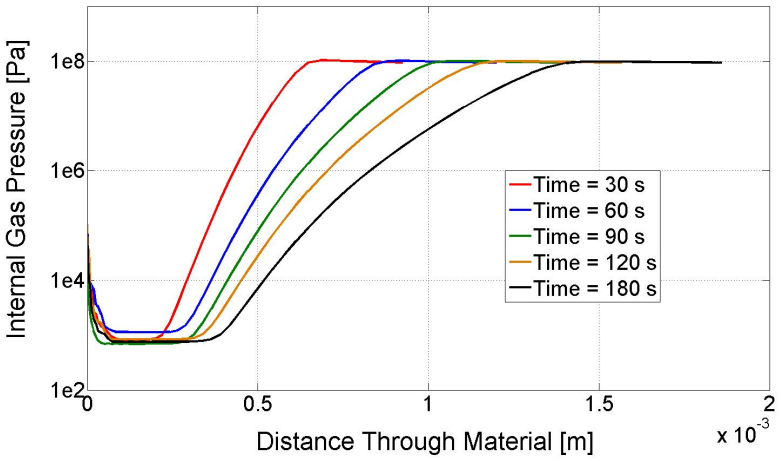

FIGURE 8.38: Internal gas pressure along a 1D line down through the centre of the CFC as a function of time

The peak internal gas pressure is again roughly constant with time, with a pressure of 1×10^8 Pa. The magnitude of this gas pressure is certainly large enough to cause cracks and de-laminations within the decomposing CFC. The peak pressure is, however, likely to be an overestimate, as with such a large pressure the fibre will be lifted up, which will increase the available volume and hence reduce the pressure. The peak pressure calculated here is very similar to that of the peak pressure obtained by the 1D model above. This reaffirms the choice to investigate the 1D predictions first, as the physical reasoning for the numerical predictions explained by the 1D model are the same as those occurring in the 3D model.

8.2.3.2 Fibre Damage Comparison

The experimental laser ablation results showed that the carbon fibres immediately surrounding the peak laser beam heat flux have been degraded and removed (shown in Figure 5.2). Whilst this numerical model has not considered the degradation of the carbon fibres, it is possible to determine to what extent the fibre might have undergone a phase change, by considering the predicted temperature. This can be done, as it is known that carbon fibre vaporise at 3000 K [23], and therefore if the model predicts a temperature above this, then it can be said that the fibres have been vaporised. To determine the extent to which the numerical model predicts fibre vaporisation, the temperature profile on the top surface at the end of the simulation is shown in Figure 8.39.

It is clear from the temperature profile in Figure 8.39, the model does not predict any fibres vaporisation, since the peak temperature on the top surface predicted by the numerical model is 1347 K (i.e. less than the 3000 K required to vaporise the carbon fibre [23]). As fibre removal was observed by the X-ray tomography, shown in Figure 5.2,

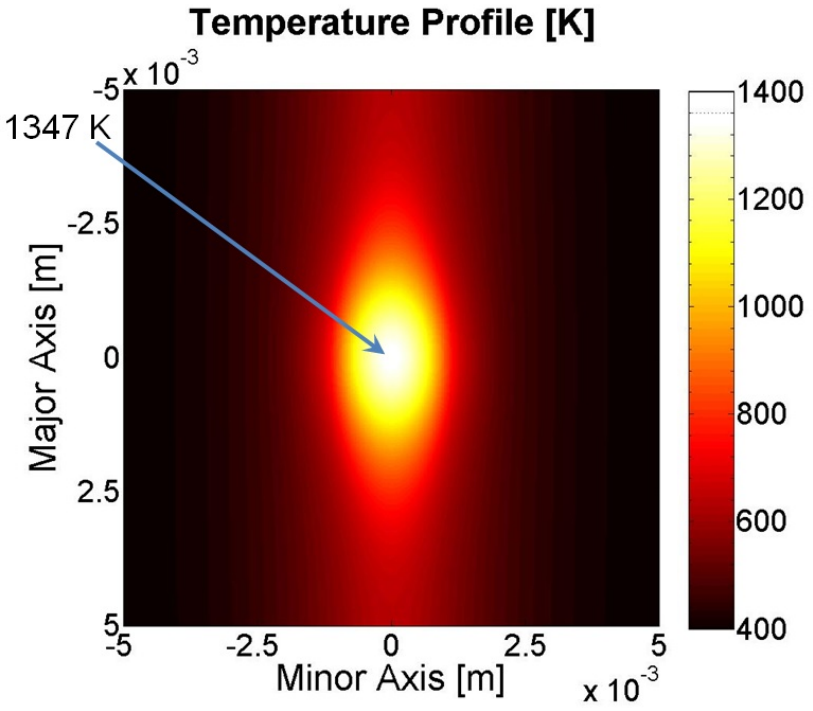

FIGURE 8.39: Temperature profile for the top surface after $t = 180\,s$

the numerical predictions indicate that either the carbon fibres are removed by burning in air, or the temperature on the top boundary is under predicted by the numerical model.

8.2.4 Discussion

The bespoke thermo-chemical degradation model has been used to investigate the laser ablation experiment conducted in Section 5.1. The predictions from the numerical model have been compared against the spatial extent of the damage witnessed by the experimental study in Section 5.1.1. The predicted damage for the major axis is an over estimate from what has been experimentally observed whilst the maximum damage depth predicted by the numerical model underestimates what has been experimentally observed. The minor axis gives a very good agreement, which can be explained by the laser beam radius having a dominate effect on the minor axis rather than the bulk conductivity. The under and over estimate of the major damage dimension and the damage depth, could be explained by the following reasons. Firstly, the Rule of Mixtures used to determining the bulk conductivity and the material parameters may not be accurate, as discussed in Section 6.4.2. Secondly, the numerical model did not consider carbon fibre removal. However, the experimental results have shown that fibre removal does occur. The inclusion of fibre removal would increase the damage depth as the heat flux would effectively be radiated into deeper depths of the material due to the fibre removal. This would also reduce the major axis as the heat flux from the laser can propagate along

the exposed edges of the damage fibres, which are at greater depths within fibre damage region, which would reduce the temperature profile along the fibre direction. Despite all this, the numerical model does not predict any fibre removal due to vaporisation and so it is most likely that a different physical processes, which has not been modelled, caused the fibre degradation. One such process could be the oxidation of the fibres within the high temperature of the laser beam. This process is highlighted in Section 2.6.2.1, but was not included within this numerical model, as it was considered that due to the fast heating of a lightning strike its impact on the numerical results would be negligible. However, due to the slower heating rate of the laser ablation, the carbon fibres could have been damaged in this way.

8.3 Parametric Study of Dominant Factors

Based on the discussion from the initial comparison between the numerical predictions and the experimental results, a sensitivity of the numerical predictions to certain parameters are considered. This includes a discussion on the different methods for determining the bulk conductivity, as highlighted in Section 6.4.4 and a selection of material properties. For these studies, the model is considered to be the same as above, only now the entire gas transport model has been omitted to further improve the efficiency of the numerical model. The discussion starts by considering the different methods for determining the bulk conductivity κ_2 and κ_3 before considering the sensitivity of the material properties.

8.3.1 Sensitivity to Bulk Conductivity Methods

The initial study presented above used the Series Rule of Mixtures for determining κ_2 and κ_3. This method was considered first, as it has been widely used in previous similar studies [59, 58]. However, it has been shown in Chapter 7 that there are more accurate methods for determining the bulk thermal conductivity in directions 2 and 3. Therefore, the numerical predictions are now considered, if instead of the Series Rule of Mixtures, the modified Eshelby Method is used. In Section 6.4.4, a modification to the Eshelby Method has been designed to determine κ_2 and κ_3. This modification resulted in two new Eshelby Methods, defined as the Eshelby-Series Method and the Eshelby-Parallel Method. The predicted major and minor axis damage for both the Series Rule of Mixtures and the two modified Eshelby Methods are presented in Figures 8.40 and 8.41.

From Figures 8.40 and 8.41, it is evident that both modified Eshelby Methods predict a reduced major and minor damage when compared against the Series Rule of Mixtures. This is expected as the modified Eshelby Methods predict an increased κ_2 and κ_3, which

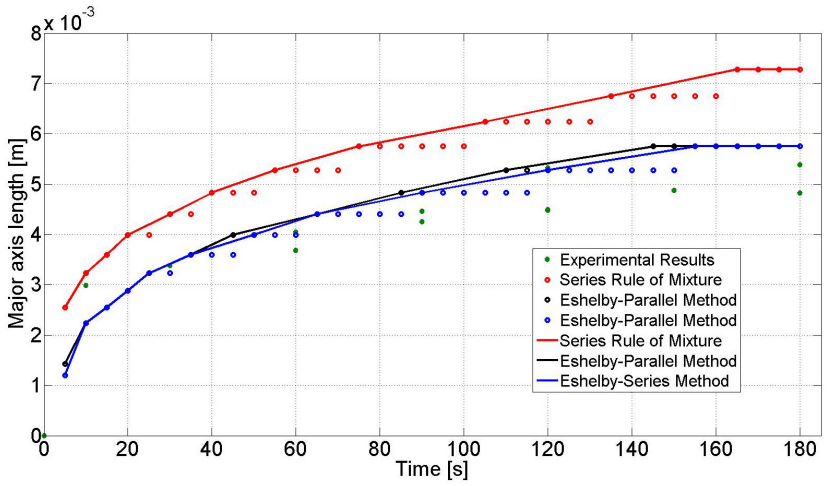

FIGURE 8.40: Comparison between the predicted major axis damage due to different methods for predicting κ_2 and κ_3

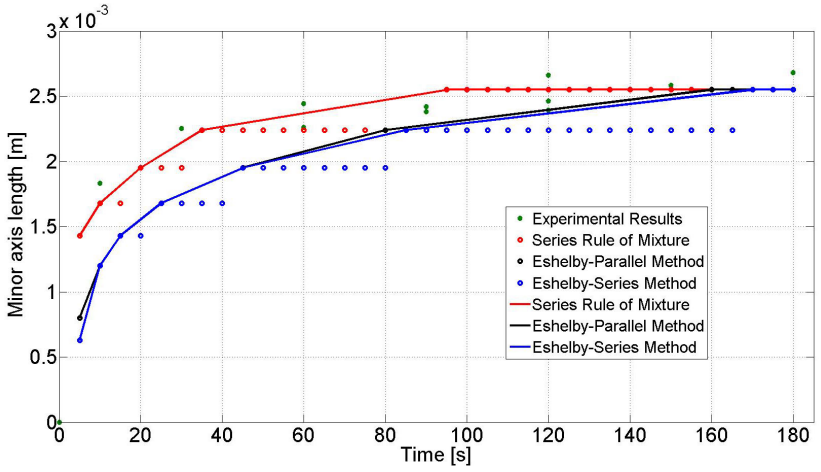

FIGURE 8.41: Comparison between the predicted minor axis damage due to different methods for predicting $\kappa 2$ and κ_3

reduces the temperature build up as the heat can more easily conduct away, and hence less damage is caused. Despite the modified Eshelby Methods having no impact on κ_1, the major axis is decreased, because when κ_2 and κ_3 are increased, more heat can travel along those directions, instead of along the fibres. This reduces the temperature profile along the fibre direction, and hence reduces the major axis damage length. Notice that there is minimal difference in the predicted damage between the two modified Eshelby Methods. This is because, as shown in Figure 6.12, both of these modified Eshelby Methods calculate the conductivity at Φ_p equal to $\Phi_p(t_0)$ and Φ_p equal to 0, to be the same. And due to the very steep reaction front, the bulk conductivity will typically be calculated for one of these two states and, so evidently, there is minimal difference in predicted damage depth. The same comparison is now considered for the damage depth, as shown in Figure 8.42.

With reference to Figure 8.42, notice that there is only a slight decrease in predicted

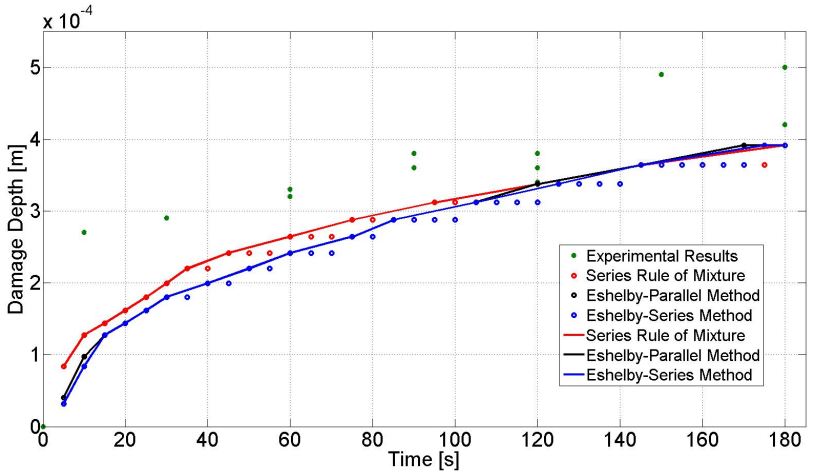

FIGURE 8.42: Predicted damage depth is affect by of changing the method by which the bulk thermal conductivity is calculated for κ_2 and κ_3

damage depth between the Series Rule of Mixtures and the modified Eshelby Methods. This predicted decrease in damage is expected given the discussion present above for the major and minor axes.

8.3.1.1 Discussion on Modified Eshelby Method

From the results above, it is evident that the proposed Eshelby Method reduces the predicted damage along each dimension. This is expected as the modified Eshelby Methods calculate a higher bulk conductivity for κ_2 and κ_3 than the Series Rule of Mixtures. It has been shown that the changes in κ_2 and κ_3 have the greatest impact on the predicted major axis damage, with the damage depth being the least affected.

8.3.2 Sensitivity to Material Properties

The sensitivity of the numerical model predictions to the material properties used within the model have been investigated. The material properties which have been considered are split into two groups; these are the reaction parameters and the thermal properties. The reaction parameters considered are the Activation energy (E_a), the Pre-exponential factor (A), the reaction order (n), the change in enthalpy (Q_d) and the mass fraction of char produces due to the pyrolysis (ζ_g). The thermal parameters which are considered are the thermal conductivity of the polymer κ_p and the fibre κ_f, and the initial fibre volume fraction $\Phi_p(t_0)$. For this sensitivity study, the bulk thermal conductivity κ_2 and κ_3 are calculated using the Series Rule of Mixtures. The mesh growth rates and time step are the same as defined in Section 8.2.2. To avoid the location of boundaries affecting the numerical predictions, (as outlined in Section 8.2.3) the size of the geometry is increased to allow each of the boundaries to have a roughly constant ambient temperature. The

new model has the following dimensions L_x equal to 0.1 m, L_y equal to 5 mm and L_z equal to 10 mm, where these dimensions are defined by Figure 8.33.

The sensitivity of the damage dimensions (e.g. major, minor and depth) are defined by the ratio of which each damage dimensions is varied with respect to a specific modelling parameter. An example of this for the major axis of damage and the damage depth, for the two different values of κ_f, is shown in Figures 8.43 and 8.44. The ratio of the major damage dimensions is determined by dividing the predicted major axis damage for when κ_f is 25 $Wm^{-1}K^{-1}$ by the predicted major axis damage when κ_f is 5 $Wm^{-1}K^{-1}$, at a solution time of 180 s. This is repeated for the minor axis and damage depth as well. The choice of time is not overall important, given that after the initial reaction, for time above 100s, the increase in damage dimensions are roughly parallel over time.

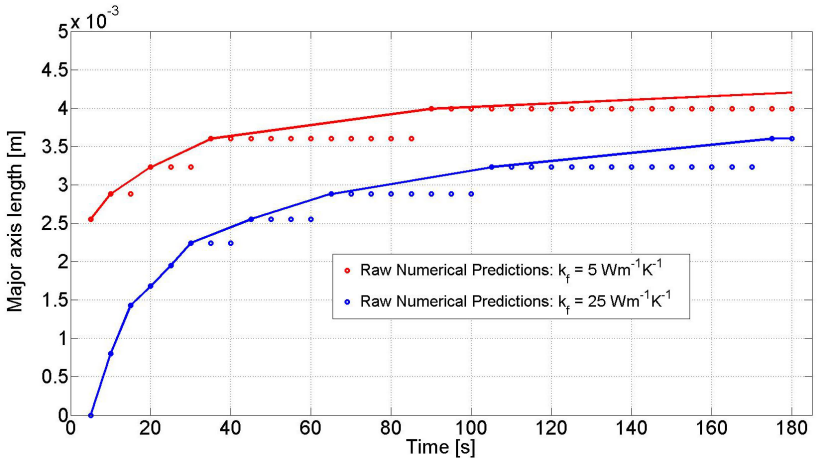

FIGURE 8.43: Variation in predicted major axis as the conductivity of the fibre (κ_f) is varied

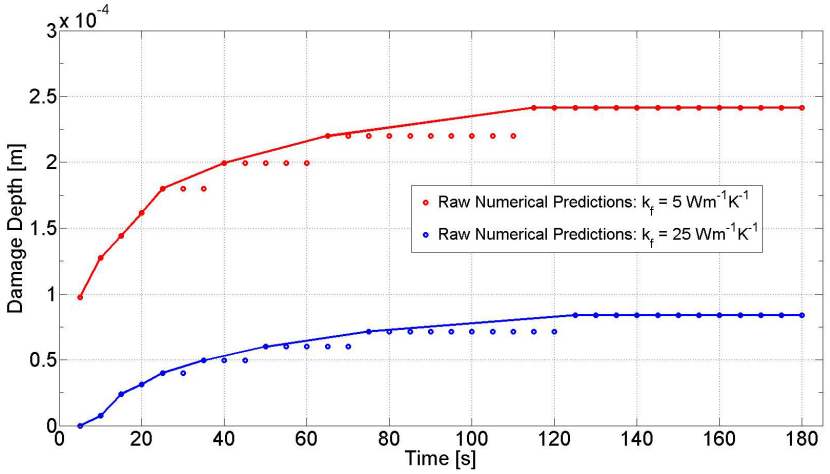

FIGURE 8.44: Variation in predicted damage depth as the conductivity of the fibre (κ_f) is varied

By comparing the predictions in Figure 8.44 with the predicted damage depth given in Figure 8.36 for the true sample geometry, there is a noticeable reduction in predicted

damage dimensions due to the increased geometry dimensions. This reduction highlights the importance of the correct dimensions used by the numerical model.

The ratio difference, as defined above, for each of the material parameters is summarised in Table 8.2.

Parameter	Range	Major Ratio	Minor Ratio	Depth Ratio
E_a	124.7 to 207.5$kJ\text{mol}^{-1}$	2.6	1.71	3.8
A	1×10^9 to 1×10^{15} s	2.3	2.0	3.25
n	1.3 to 1	1.07	1.07	1.08
Q_d	1×10^6 to -1×10^6 Jkg^{-1}	1	1	1
k_p	0.01 to 0.1 WmK^{-1}	1.69	1.5	2.7
k_f	5 to 25 WmK^{-1}	1.17	1.6	2.9
ζ	0 to 0.4	1	1	1.3
$\Phi_p(t_0)$	0.2 to 0.4	1.78	1.87	2.17

TABLE 8.2: Sensitivity of the different parameters to the predicted damage

From Table 8.2, the activation energy (E_a) and the pre-exponential factor (A) have the greatest impact on the numerical predictions. The next most sensitive parameters are the thermal conductivity parameters i.e the thermal conductivity of polymer (κ_p) and fibre (κ_f) and the initial volume fraction of the polymer $\Phi_p(t_0)$. For all these parameters, the greatest sensitivity occurs to the damage depth rather than the major or minor axis, as this is the direction towards which the heat flux is directed. The change in enthalpy (Q_d) due to the pyrolysis has an almost negligible impact on the predicted damage. Given that there is only a small mass of polymer degraded, there is only a small reduction in energy due to the mass change. The amount of char produced only affects the damage depth slightly, but given that κ_{ch} is approximately the same as κ_p, this is as expected. The variation of initial polymer volume fraction does seem to have a significant impact on the bulk predicted damage.

It has been assumed during the previous investigations within this study that reaction order (n) can be taken as one, rather than the experimentally determined value 1.3. The results presented in Table 8.2 have demonstrated that the reaction order has minimal effect on the spatial extent of the predicted damage. This is because the variation in reaction order only has a slight impact on the polymer degradation rate at small volume fractions. Therefore, the assumption of a reaction order equal to one does not affect the conclusions from the results present previously.

8.3.3 Discussion

From the above discussion, the main dominant terms which affect the sensitivity of this numerical model to predict the damage from a laser ablation are: T_a, A, k_p, k_f and $\Phi_p(t_0)$. This justifies the effort to undertake the experimental work detailed in Chapter 4 to determine the reaction kinetics for this specific type of CFC.

8.4 Summary

This chapter details the validation of the homogeneous approach to represent a piece of CFC. This was achieved by investigating the electrical conduction through a piece of CFC. The initial numerical predictions showed complex equipotential surfaces, which have subsequently been experimentally validated. This in turn validates the homogeneous assumptions used within this model to represent numerically a piece of CFC.

The second half of this chapter considered using the bespoke thermo-chemical degradation model to investigate the laser ablation damage caused to a piece of CFC. This was achieved by first investigating the numerical predictions from the 1D model. From this study, two interesting conclusions have been drawn; first, it is has been shown that gas transport appears to have minimal effect on the predicted damage, and secondly the produced gas within the material is large enough to cause the cracking and delaminations witnessed by the experimental study.

The thermal degradation model was then expanded into 3D to allow for the predicted spatial extent of the damage to be compared against the experimental results. The polymer degradation predicted by the numerical model showed reasonable agreement with the experimental results. However, whilst the numerical model did not directly consider the carbon fibre degradation, it has been shown that the numerical model does not predict any fibre vaporisation. This is contrary to what has been observed from the experimental laser ablation study. The lack of fibre damage is believed to be as a result of not including the required physics for the fibre degradation i.e. the fibre degraded by another physical process rather than vaporisation. The sensitivity of the numerical predictions to a selection of material properties has then been conducted. From this study, it is evident that the numerical predictions are sensitive to the reaction kinetics, E_a and A, and the properties used to define the bulk thermal conductivity.

Chapter 9

Conclusion

This thesis has investigated the damage caused to carbon fibre composite (CFC) materials due to a lightning strike. This is done through a series of experimental studies, before a complete thermo-chemical degradation model has been developed to investigate the underling physical processes, which lead to the observed damage. Before each of these studies is conducted, a comprehensive review of the state of the art knowledge has been completed. From this review, key assumptions and results made by previous studies have been highlighted, which have been further investigated and validated.

9.1 Research Contribution

The work presented in this thesis forms a significant contribution to the understanding of the physical processes which cause the damage to CFCs due to a lightning strike. This is done initially through a comprehensive review of the different numerical and experimental studies, which have investigated the lightning strike damage and also more generally the thermo-chemical degradation of composite materials due to a variety of different heat sources. Discussions presented in this thesis have indicated that these previous numerical models are limited by their implementation and the assumptions inherent within. Therefore, efforts have been made within this thesis to remove or improve these assumptions, which are discussed below.

Previous studies have shown that the principle heating mechanism within CFCs due to a lightning strike results from the Joule heat caused by the injection of current. These studies have generally assumed that CFCs can be regarded as a perfect resistor and hence all the injected current directly leads to Joule heating. Since the injected current is an impulse consisting of a series of frequencies, this thesis has included an experimental study to determine the validity of this assumption. The results from this experimental study have shown that a quasi-isotropic CFC can be treated as a pure resistor up to a

frequency of 10 kHz. By considering the frequencies present within the lightning strike current impulse (given in Section 2.2.3.2), it is evident that the majority the injected current will principally lead to Joule heat.

With the electrical properties of CFCs understood, the thesis has then considered the typical damage caused to a piece of CFC due to a lightning strike. There are no published studies which have previously investigated how the damage varies due to the different lightning strike current impulse components i.e. A,B,C or C^* and D. This is because previous published studies have focused on either the initial return stroke (A or D) and/or the continuous component (C or C^*). The experimental study in this thesis has concluded that whilst the surface damage dimensions from each lightning strike component is different, the damage from all the components resembles polymer degradation with fracturing and/or degradation of the carbon fibres leading to lifting up of fibres. Furthermore, these experimental results have shown that there is no linear increase in damage depth or area as the impulse current components are combined. These experimental results have also indicated that the size of any lightning strike damage is strongly dependent on arc wandering.

Within the current state of the art knowledge, there is no method for describing or predicting how an arc will wander on the surface of a panel. Since the experimental lightning strike study has shown that this phenomenon plays an important physical role in distributing the energy input (heat) into CFCs and consequently the damage caused, an analogous damage method is required which can be used to investigate numerically the physical processes which lead to the observed damage. This study has experimentally established that the damage caused by laser ablation shows similar physical processes to that which is responsible for the damage caused by lightning strikes, albeit without any additional electrical phenomena. This conclusion has been drawn by investigating the laser ablated CFC samples using X-ray tomography. This technique has produced images which indicate the ablated samples have undergone polymer and fibre degradation with evidence of de-lamination and cracking occurring between plies. Therefore, given the same observed damage, the physical processes behind lightning strike damage is numerically investigated through a proxy with laser ablation.

Before the bespoke thermo-chemical degradation model can be implemented, the numerical framework required to represent numerically a piece of CFC is considered. A comprehensive review of previous studies and modelling techniques used to represent numerically composite materials was conducted. From these studies, it is evident that the most appropriate approach, for this type of study, is to represent numerical CFCs through a homogenisation approach. The homogenisation approach requires the bulk material properties to be either experimentally measured or numerically predicted. This study has investigated the relevance and accuracy of a series of analytical methods for predicting the bulk thermal and electrical conductivity for CFCs. From these studies, it is apparent that due to the very large difference between the electrical conductivity of

the fibre and the polymer, the fibre to fibre contacts dominate the bulk electrical conductivity. Hence, to predict the electrical conductivity, it is important to consider the percolation effects. As a result, this study has defined the empirical parameters required by the percolation power law to predict bulk electrical conductivity of CFC. However, as the thermal conductivity of the CFC components are more comparable, the Eshelby Method has proven the most accurate at predicting the bulk thermal conductivity. This method, however, is limited to only considering a composite material comprised of two species i.e. fibre and polymer. Whilst this is true for an undamaged piece of CFC, during the thermo-chemical degradation, CFCs are comprised of more than two species with the addition of gas and char. Therefore, a significant outcome from this study is the proposed modification to the Eshebly Method, which permits its application to composite materials with more than two constituent components.

With the CFC numerical framework in place, a thermo-chemical degradation model has been developed. This study is the first time that a complete physical process framework designed to investigate the thermo-chemical degradation due to a lightning strike has been proposed. This requires inclusion of the gas transport which results from the decomposing polymer. However, given the current limitation of the state of the art knowledge regarding arc wandering, the implementation of the model is simplified by decoupling the electrical processes to allow model validation, using experimentally obtained laser ablation damage. With the equations required to represent the thermo-chemical degradation of CFC in place, their implementation to form a bespoke thermo-chemical degradation model is investigated. Due to the complex and coupled nature of the physical processes, the implementation is not trivial and hence this study proposes a fractional step method to obtain a numerical solution. The implementation of the fractional step method has been validated by considering the convergence of the numerical predictions against where possible analytical or replicate models made in commercial FEA packages.

Using this numerical model, this thesis has investigated the key assumptions inherent within the implementation of the physical processes. The first assumption considered is that of numerically representing CFCs through the homogenisation approach. This is investigated by initially considering the electrical conduction model using the homogeneous anisotropic approach. The initial results from this model showed initially unexpected current flow patterns. A further important contribution from this study is that an experimental study has subsequently validated these numerical predictions. This result, in turn, has validated the homogenisation approach used to numerically represent CFCs.

This thesis has finally investigated the physical processes used to represent the thermo-chemical damage due to laser ablation. This investigation has focussed on gas transport through the decomposing material. This model adds to the current state of the art knowledge by demonstrating that the inclusion of this gas transport has minimal effect on the predicted thermo-chemical damage. Although with the inclusion of the gas

transport within the model, the numerical predictions do indicate the internal gas pressure is certainly large enough to explain the cracking and de-laminations which have been observed from both lightning strike and laser ablation experiments. The bespoke thermo-chemical degradation model is then validated by comparing the numerical predictions with the spatial extent of the measured damage from the experimental laser ablation study. The numerical predictions have shown reasonable agreement with the observed experimental laser ablation damage, which demonstrates the validity of the implemented physical processes.

With the extensions to the numerical model proposed in the following section, the model can be used to improve the understanding of lightning strike damage to CFCs. With such an understanding and using the bespoke numerical model as a simulation tool, the long term benefit of this thesis is to investigate and optimise the CFC lightning protection methods. This thesis, therefore, makes a step towards improving and optimising the lighting strike protection to CFC aircraft by the development of a numerical model.

9.2 Recommendations for Future Work

Despite the contribution made by this thesis, a number of further research avenues have been identified which merit further work:

Whilst the numerical predictions for the laser ablation damage have given good agreement with the experimentally measured damage (Section 8.2.3.1), the model considers the thermal properties to be constant with temperature. It has been shown in previous studies that the thermal and electrical conductivity are actually temperature dependent and so a future study should investigate what impact these effects will have on the numerical predictions. Before the proposed numerical model can be expanded to consider the non-linearity of temperature dependent material properties, a series of experimental studies need to be conducted to determine the temperature dependence of the CFC material considered within this study.

Whilst the initial aim of this model was to investigate the damage caused due to a lightning strike, with the time limitations and the apparent dominance of the arc wandering, it has not been possible to investigate directly the lightning strike damage. However, an analogue for lightning strike damage, which is easier to model has been realised through laser ablation. Despite this, further work should be conducted to develop the thermo-chemical degradation model to incorporate the lightning strike arc attachment and subsequent arc wandering. With this development, it should be possible to use the proposed thermo-chemical degradation model to draw comparisons between the experimentally damage CFC panels and the numerical predictions.

Finally, this thesis has only considered the damage caused to CFC panels without light-

ning strike protection. In reality, the CFC panels used within aircraft structures include a layer of lightning strike protection to minimise the lightning strike damage. There are a variety of protection methods including applying expanded metal foil over the top surface of the CFC or painting a metallic layer on the top surface. With the model expanded to investigate the lightning strike damage to unprotected panels, this model can be further expanded to investigate these protections methods in detail, and consider what if any optimisation can be made to these protection methods.

Appendix A

Quasi-isotropic Fibre Orientation

Quasi-isotropic CFC material is formed by the layering up of multiple unidirectional CFC plies. As well as local axis group a global axis group is defined as outlined in section 2.1.3. The global axis is used to define the rotation of the fibres within each ply. For the purpose of this study, the following CFC orientation as shown in Table 2 is considered [140].

Ply Number	Orientation (^{o})
1	45
2	135
3	0
4	0
5	90
6	0
7	135
8	0
9	45
10	45
11	0
12	0
13	45
14	45
15	0
16	135
17	0
18	90
19	0
20	0
21	135
22	45

TABLE A.1: Orientation of carbon fibres in each ply of CFC, The orientation is given in degrees, where the zero degree is defined along the direction where the global axis x is parallel to the local axis direction 1 [140]

Appendix B

Potential Divider Results

Below is a selection of raw results, taken from the oscilloscope during the potential divider experiment conducted in Section 4.1.3.2.

B.1 Quasi-isotropic CFC Panel

Shown below are results for the quasi-isotropic panel at the following frequencies; B.1a) 1 Hz, B.1b) 500 Hz and B.2a) 1 kHz, B.2b) 10 kHz.

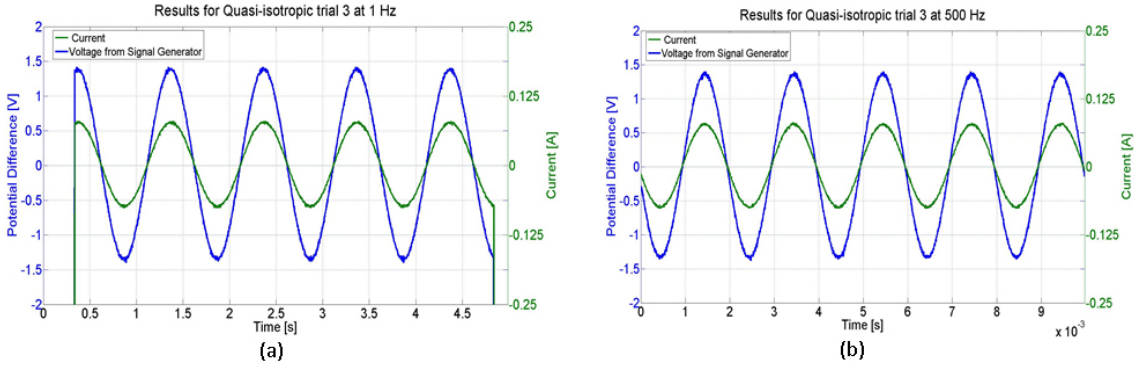

FIGURE B.1: The results show the potential difference across the signal generator (red) and current at the known resistor (green) for a) 1 Hz and b)500 Hz. These results are for the quasi-isotropic panel of CFC

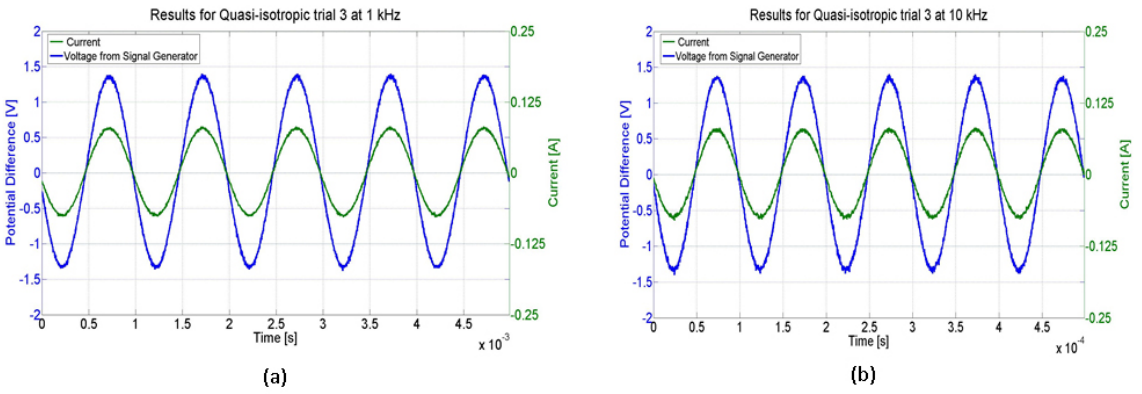

FIGURE B.2: The results show the potential difference across the signal generator (red) and current at the known resistor (green) for a) 1 kHz and b)10 kHz. These results are for the quasi-isotropic panel of CFC

B.2 Unidirectional CFC Panel

Shown below are results for the unidirectional panel at the following frequencies; B.3a) 1 Hz, B.3b) 500 Hz and B.4a) 1 kHz, B.4b) 10 kHz.

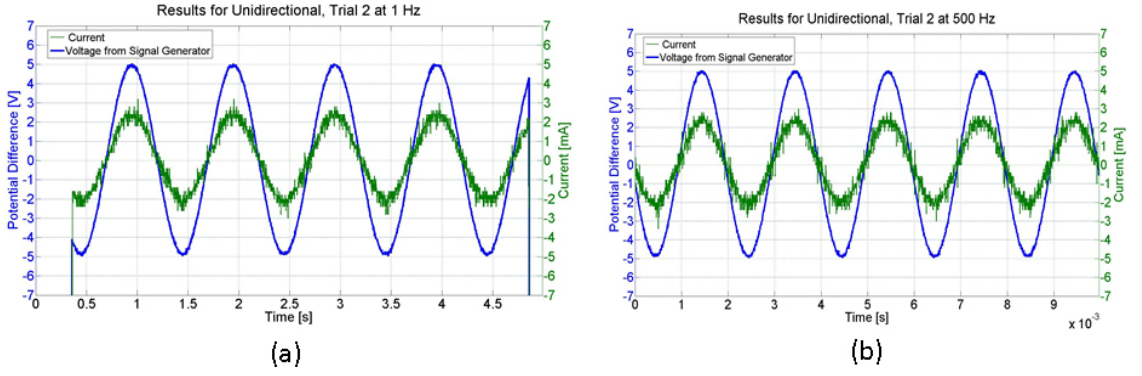

FIGURE B.3: The results show the potential difference across the signal generator (red) and current at the known resistor (green) for a) 1 Hz and b)500 Hz. These results are for the unidirectional panel of CFC

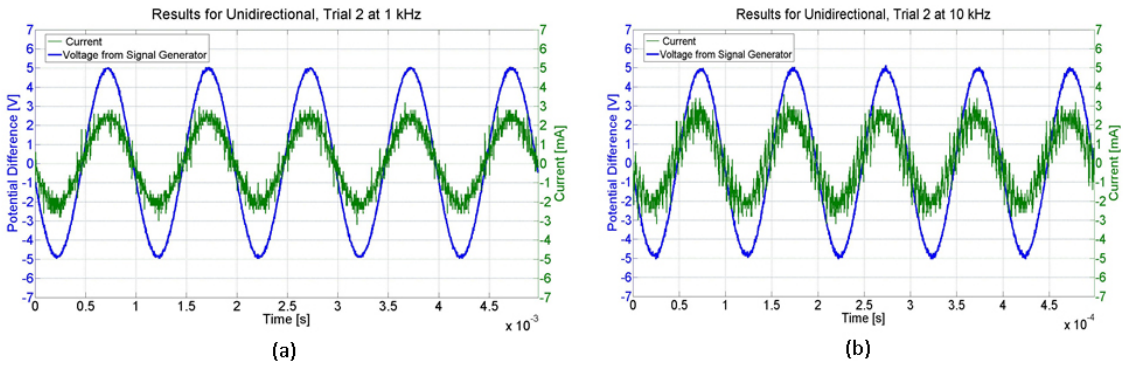

FIGURE B.4: The results show the potential difference across the signal generator (red) and current at the known resistor (green) for a) 1 kHz and b)10 kHz. These results are for the unidirectional panel of CFC

Appendix C

Material Properties

Material Property	**Symbol**	**Value**	**Unit**)
Epoxy (polymer) thermal conductivity	κ_p	0.1	WmK^{-1}
Epoxy (polymer) Density	ρ_p	900	kgm^{-3}
Epoxy (polymer) heat capacity	$C_{v\,p}$	2500	$Jkg^{-1}K^{-1}$
Epoxy (polymer) electrical conductivity	σ_p	1×10^{-6}	Sm^{-1}
Carbon fibre thermal conductivity	κ_p	9.37	WmK^{-1}
Carbon fibre Density	ρ_p	794	kgm^{-3}
Carbon fibre heat capacity	$C_{v\,f}$	1760	$Jkg^{-1}K^{-1}$
Carbon fibre electrical conductivity	σ_p	62×10^3	Sm^{-1}
Gas thermal conductivity (CO_2)	κ_p	0.025	WmK^{-1}
Gas Density (CO_2)	ρ_p	1.997	kgm^{-3}
Gas heat capacity (CO_2)	C_{vg}	1012	$Jkg^{-1}K^{-1}$
Gas electrical conductivity (CO_2)	σ_p	n/a	Sm^{-1}
Char thermal conductivity	κ_p	0.2	WmK^{-1}
Char Density	ρ_p	1300	kgm^{-3}
Char heat capacity	$C_{v\,ch}$	1589	$Jkg^{-1}K^{-1}$
Char electrical conductivity	σ_p	n/a	Sm^{-1}
Gas Viscosity	η	1×10^{-5}	$kgs^{-1}m^{-1}$
Molar mass of gas	M	0.044	$kg\text{mol}^{-1}$
Gas constant	$\Re$	8.31	$JK^{-1}\text{mol}^{-1}$
Aluminium Density	ρ_{Al}	2800	kgm^{-3}
Aluminium Specific Heat Capacity	C_{Al}	897	$Jkg^{-1}K^{-1}$
Aluminium Electrical Conductivity	σ_{Al}	35	Sm^{-1}

TABLE C.1: Material properties used within the numerical model

Appendix D

List of Publications and Awards

D.1 Awards

The two following awards have been presented to author of this thesis during his PhD studies

Best Paper Award at EPNC 2010 presented by The International Journal for Computation and Mathematics in Electrical and Electronic Engineering (COMPEL) EMERALD

'Diploma for Young Scientists' for a high-quality presentation of a paper at the International Conference on Lightning Protection 2010 and notable contributions to the field of lightning research and lightning protection.

D.2 Conference Papers

The following papers have been presented at International conference. Papers are listed in chronological order

Chippendale, R. D., Zhang, C., Golosnoy, I. O., Lewin, P. L. and Sykulski, J. K. (2010) 'Transport properties and current flow patterns in homogeneous strongly anisotropic materials'. XXI Symposium on Electromagnetic Phenomena in Nonlinear Circuits (EPNC 2010), Dortmund and Essen, Germany, 29 June - 02 July 2010. PTETiS Publishers, Poznan, Poland, 45-46.

Chippendale, R. D., Golosnoy, I. O., Lewin, P. L., Murugan, G. S. and Lambert, J. (2010) 'Model of Structural Damage to Carbon Fibre Composites due to Thermo-Electric Effects of Lightning Strikes.' International Conference on Lightning Strike Protection, Cagliari, Italy, 13 - 17 September 2010.

Chippendale, R. D. and Golosnoy, I. O. (2011) Percolation Effects In Electrical Conductivity Of Carbon Fibre Composites' CEM 2011, Wroclaw, Poland, 11 - 14 April 2011. The Institution of Engineering and Technology, 186-187.

Chippendale, R. D., Golosnoy, I. O. and Lewin, P. L. (2011) 'Effects of different components of a lightning strike waveform on the heating of different material: Aluminium Alloys vs. Carbon Fibre. At International conference on lightning and static electricity, Oxford, UK, 6 - 8 September 2011. CD-ROM.

Chippendale, R. D., Golosnoy, I. O. and Lewin, P. L. (2011) 'Numerical modelling of the damage caused by a lightning strike to carbon fibre composites' International Conference on Lightning and Static Electricity, Oxford, UK, 6 - 8 September 2011. CD-ROM. 2010

D.3 Peer Reviewed Journal Papers

The following papers have been published in peer reviewed academic journals

Chippendale, R. D., Golosnoy, I. O., Lewin, P. L. and Sykulski, J. K. (2011) 'Transport properties and current flow patterns in homogeneous strongly anisotropic materials'. COMPEL: The International Journal for Computation and Mathematics in Electrical and Electronic Engineering, 30, (3), 1047-1055.

D.4 Journal Papers under Preparation

The following paper is currently being prepared for publication

Chippendale, R. D., Golosnoy, I. O., Lewin, P. L. 'Numerical Model of the Laser Ablation damage caused to Carbon Fibre Composite Materials, including the Decomposing Gas Transport' (Working Title), aim to be published in Journal Of Physics D-Applied Physics.

References

[1] *Milestones of flight - 1903 Wright Flyer.* Symithsonian National Air and Space Museum, http://airandspace.si.edu/exhibitions/gal100/wright1903.html.

[2] D. H. Middleton. *Composite Materials In Aircraft Structures.* Longman Scientific and Technical, 1990.

[3] J. Bold. Airbus composite training. Keynote at VPD Conference, 2007.

[4] M. C. Y. Niu. *Composite Airframe Structures.* Hong Kong Conmilit Press limited, 2002.

[5] A. Baker, A. Dutton, and D. Kelly. *Composite Materials For Aircraft Structures.* American Institute of Aeronautics and Astronautics, 2004.

[6] J. Hawk. The boeing 787 dreamliner; more than an airplane. 2005.

[7] D. Chung. *Carbon Fiber Composites.* Butterworth-Heinemann, 1994.

[8] V. A. Rakov and M. A. Uman. Lightning - physics and effects. *Cambridge University Press*, 2003.

[9] F.A. Fisher and J.A. Plumer. *Lightning Protection of Aircraft.* Lightning Technologies (NASA), 1977.

[10] R. H. Golde. *Lightning vol. 2.* Academic Press Inc, 1977.

[11] EUROCAE. *Aircraft Lightning Environment and Related Test Waveforms Standard (ED-84)*, 1997.

[12] F. Uhlig. *Contribution a l'etude des effets directs du foudroiement sur les materiaux structuraux constituant un aeronef (contribution to the study of the lightning direct effects on the aircraft structural materials).* PhD thesis, Universite de Paris, 1998.

[13] P. Feraboli and M. Miller. Damage resistance and tolerance of carbon/epoxy composite coupons subjected to simulated lightning strike. *Composites Part A: Applied Science and Manufacturing*, 40:954 – 967, 2009.

[14] D. Hull. *An Introduction to Composite Materials*. Cambridge Solid State Science Series, 1996.

[15] T. Edwards. Composite materials revolutionise aerospace engineering. *Ingenia*, 36:24–28, 2008.

[16] J. W. Klett, V. J. Ervin, and D. D. Edie. Finite-element modeling of heat transfer in carbon/carbon composites. *Composites Science and Technology*, 59:593 – 607, 1999.

[17] P. Morgan. *Carbon Fibers and Their Composites*. CRC Press, 2005.

[18] D. Rosato. Boeing versus airbus competing metal to composite focus. 2007.

[19] Toray. Data sheet - t700s, 2007. http://www.toraycfa.com/pdfs/T700SDataSheet.pdf.

[20] Toray. Functional and composite properties. 2005. http://www.torayca.com/en/techref/index.html.

[21] G. Savage. *Carbon-Carbon Composites*. Chapam and Hall(Springer), 1993.

[22] D. Hull and T. W. Clyne. *An Introduction to Composite Materials*. Cambridge University Press, 1996.

[23] C.F. Cheng, Y.C. Tsui, and T.W. Clyne. Application of a three dimensional heat flow model to treat laser drilling of carbon fibre composites. *Acta Materialia*, 46:4273–4285, 1998.

[24] T. Calvert. *Guide to composite materials - Reinforcements Catalogue*. SP Systems (now known as Gurit), 2000.

[25] C. Pradere, J.C. Basale, J.M Goyheneche, R. Pallier, and S. Dilhaire. Thermal properties of carbon fibres at very high temperatures. *Carbon*, 47:737–743, 2009.

[26] L. Scruggs and W. Gajda. Low frequency condcutivity of unidirectional graphite/epoxy compsoite samples. *Electromagnetic compatibility symposium record*, 19:396–402, 1977.

[27] F. Lago, J. J. Gonzalez, P. Freton, F. Uhlig, N. Lucius, and G. P. Piau. A numerical modelling of an electric arc and its interaction with the anode: part iii. application to the interaction of a lightning strike and an aircraft in flight. *Journal Of Physics D-Applied Physics*, 39:2294 2310, 2006.

[28] V. Zdenka, Z. Rimska, and J. Spacek. Ac conductivity of carbon fibre-polymer matrix composites at the percolation threshold. *Polymer Composites*, 23:95–103, 2002.

[29] I.O. Ayish and A.M. Zihlif. Electrical properties of conductive network in carbon fibre/polymer composites. *Journal of reinforced plastics and composites*, 29:3237–3243, 2010.

[30] H. C. Kim and S. K. See. Electrical properties of unidirectional carbon-epoxy composites in wide frequency band. *Journal of Physics D: Applied Physics*, 23:916–921, 1990.

[31] W. Thonggruang, P. Bunnaul, P. Smithmaitrie, and K. Chetpattananondh. Electrical and mechanical properties of ternary composites from natural rubber and conductive fillers. *Journal of science and Technology*, 30:361–366, 2008.

[32] M. A. Uman. *The Lightning Discharge*, volume 39 of *International Geophysics Series*. Academic Press, 1987.

[33] V. Cooray. Lightning protection. *Iet power and energy series*, 58, 2010.

[34] EUROCAE. *Aircraft Lightning Test Method(ED-105)*, 2005.

[35] EUROCAE. *Aircraft Lightning Zoning Standard(ED-91)*, 2006.

[36] A. Gleizes, J. J. Gonzalez, and P. Freton. Thermal plasma modelling. *Journal of Physics D: Applied Physics*, 38:153–183, 2005.

[37] I. A. Metwally, F. Heidler, and W. Zischank. Measurement of the rear-face temperature of metals struck by lightning long-duration currents. *European transactions on electrical power*, 14:201–222, 2004.

[38] P. Zhu, J. J. Lowke, R. Morrow, and J. Haidar. Prediction of anode temperatures of free burning arcs. *Journal of Physics D: Applied Physics*, 28:1369–1375, 1995.

[39] N. A. Sanders and E. Pfender. Measurement of anode falls and anode heat transfer in atmospheric pressure high intensity arcs. *Journal of Applied Physics*, 55, 1984.

[40] M. Shiraishi and M. Ata. Work function of carbon nanotubes. *Carbon*, 39, 2001.

[41] F. Lago, J. J. Gonzalez, P. Freton, and A. Gleizes. A numerical modelling of an electric arc and its interaction with the anode: Part i. the two-dimensional model. *Journal Of Physics D-Applied Physics*, 37:883–897, 2004.

[42] J. J. Gonzalez, F. Lago, P. Freton, M. Masqure, and X. Franceries. Numerical modelling of an electric arc and its interaction with the anode: part ii. the three-dimensional model?influence of external forces on the arc column. *Journal Of Physics D-Applied Physics*, 38:306–318, 2005.

[43] R. Mc Brayer and G. L. Weinstock. Lightning attachment characteristics for metal/composite materials. *IEE Electromagnetic compatibility synposium record*, 19th:223–227, 1977.

[44] B. Lepetit, C. Escure, S. Guinard, I. Revel, G. Peres, and Y. Duval. Thermomechanical effects induced by lightning on carbon fiber composite materials. *International Conference on Lightning and Static Electricity*, 2011.

[45] G. W. Reid. Investigations into the damage for various types of unprotected carbon fibre composites with a variety of lightning arc attachments. *International Aerospace and Ground Conference on Lightning and Static Electricity*, pages 11–15, 1991.

[46] B. Clarke and G. W. Reid. Further investigations into the damage of various types of unprotected carbon fibre composites with a variety of lightning arc attachments. *International Aerospace and Ground Conference on Lightning and Static Electricity*, 1994.

[47] B. Pridham. Effects of lightning strike damage on the strength and stiffness of carbon fibre composite aricraft skins. *International Conference on Lightning and Static Electricity*, 2003.

[48] N. Jennings and C. J. Hardwick. A computational approach to predicting the extent of the arc root damage in cfc panels. *15th International Aerospace and Ground Conference on Lightning and Static Electricity*, pages 41.1 – 41.8, 1992.

[49] T. Ogasawara, Y. Hirano, and A. Yoshimura. Coupled thermal-electrical analysis for carbon/epoxy composites exposed to simulated lightning current. *Composites - Part A: Applied Science and Manufacturing*, 41:973–981, 2010.

[50] A. P. Mouritz, S. Feih, E. Kandare, Z. Mathys, A. G. Gibson, P. E. D. Jardin, S. W. Case, and B. Y. Lattimer. Review of fire structural modelling of polymer composites. *Composites Part A: Applied Science and Manufacturing*, 40:1800 – 1814, 2009.

[51] A. P. Mouritz and A. G. Gibson. Fire properties of polymer composite materials. *Solid mechanics and its applications*, 143, 2006.

[52] J. E. J. Staggs. Heat and mass transport in developing chars. *Polymer Degradation and Stability*, 82:297 – 307, 2003.

[53] R. M. Sullivan and N. J. Salamon. A finite element method for the thermochemical decomposition of polymeric materials - i theory. *International Journal of engineering science*, 30:431–441, 1992.

[54] J. Trelles and B. Y. Lattimer. Modelling thermal degradation of composite materials. *Fire and Materials*, 31:147–171, 2007.

[55] H. L. McManus and C. C. Chamis. Stress and damage in polymer matrix composite materials due to material degradation at high temperatures. *NASA: Technical Memorandum (4682)*, 1995.

[56] R. Negarestani, M. Sunder, M. A. Sheikh, P. Mativenga, L. Li, Z. L. Li, P. L. Chu, C. C. Khin, and H. Y. Zheng. Numerical simulation of laser machining of carbon fibre reinforced composites. *Journal of Engineering Manufacture*, 224:1017–1026, 2009.

[57] C.T. Pan and H. Hocheng. Evaluation of anisotropic thermal conductivity for undirectional frp in laser machining. *Composites - Part A: Applied Science and Manufacturing*, 32:1657–1667, 2001.

[58] J. Florio, J. B. Henderson, F. L. Test, and R. Hariharan. A study of the effects of the assumption of local thermal equilibrium on the overall thermally induced response of a decomposing glass filled polymer composite. *International Journal of Heat and Mass Transfer*, 34:135 – 147, 1991.

[59] J. B. Henderson and T. E. Wiecek. A mathematical model to predict the thermal response of decomposing, expanding polymer composites. *Journal of Composite Materials*, 21, 1987.

[60] Y. Wu and N. Katsube. A thermomechanical model for chemically decomposing composites–i. theory. *International Journal of Engineering Science*, 35:113 – 128, 1997.

[61] H. L. N. McManus and G. S. Springer. High temperature thermomechanical behaviour of carbon-phenolic and carbon-carbon composites, ii. results. *Journal of Composite Materials*, 26:230–255, 1992.

[62] R. M. Sullivan and N. J. Salamon. A finite element method for the thermochemical decomposition of polymeric materials–ii. carbon phenolic composites. *International Journal of Engineering Science*, 30:939 – 951, 1992.

[63] J. E. J. Staggs. A simplified mathematical model for the pyrolysis of polymers with inert additives. *Fire Safety Journal*, 32:221–240, 1999.

[64] S. Patankar. *Numerical Heat Transfer and Fluid Flow.* Taylor and Francis, 1980.

[65] D. A. Anderson, J. C. Tannehill, and R. H. Pletcher. *Computational fluid mechanics and heat transfer.* McGraw-hill, 1984.

[66] F. Stig and S. Hallstrom. A modelling framework for composites contain 3d reinforcement. *Composite Structures*, 94:2895–2901, 2012.

[67] T. Sujidkul and Z. Xia. Coupled thermal-mechanical modelling of carbon fibres reinforced polymer composite for damage detection. *Composite Part B*, 43:1631–1636, 2012.

[68] P. C. Powell and A. J. Ingen Housz. *Engineering with Polymers.* CRC Press, 1998.

[69] A. J. Whittaker and R. Taylor. Thermal transport properties of carbon carbon fibre composites - iii. mathmatical modelling. *Proceedings of the Royal Society London A*, pages 199–211, 1990.

[70] B. W. James, G. H. Wostenholm, G. S. Keen, and S. D. McIvor. Prediction and measurement of the thermal conductivity of composite materials. *Journal of Physics D: Applied Physics*, 20:261–268, 1987.

[71] M. W. Pilling, M. A. Black, and B. Yates. The thermal conductivity of carbon fibre reinforced composites. *Journal of Materials Science*, 14:1326–1338, 1979.

[72] R. Rolfes and U. Hammerschmidt. Transverse thermal conductivity of cfrp laminates: A numerical and experimental validation of approximation formulae. *Composites Science and Technology*, 54:54–54, 1995.

[73] P. S. J. Korab, S. Kavecky, P. Sebo, and G. Korb. Thermal conductivity of unidirectional copper matrix carbon fibre composites. *Composites Part A: Applied Science and Manufacturing*, 33:557–581, 2002.

[74] G. Springer and S. Tsai. Thermal conductivities of unidirectional materials. *Journal of Composite Materials*, 1:166–173, 1967.

[75] G. A. Khare, N. Chandra, and S. Jean-Franois. An eshelby tensor based model for optimization of thermal conductivity and coefficient of thermal expansion of the composites.

[76] R . C. Profelhof, J. L. Throne, and R. R. Ruetsch. Method for predicting the thermal conductivity of composite systems: A review. *Polymer Engineering and Science*, 16:615–625, 1976.

[77] S. G. Weber X. Xu. Carbon fiber/epoxy composite ring?disk electrode: Fabrication, characterization and application to electrochemical detection in capillary high performance liquid chromatography. *Journal of Electroanalytical Chemistry*, 630:75–80, 2009.

[78] Y.P. Mamunyaa, V.V. Davydenko, and P. Pissisb. Electrical and thermal conductivity of polymer filled with metal powders. *European Polymer Journal*, 38:1887–1897, 2002.

[79] M. Taya and N. Ueda. Prediction of the in-plane electrical conductivity of a misoriented short fiber composite: Fiber percolation model versus effective medium theory. *Journal of Engineering Materials Technology*, 109:252–256, 1987.

[80] G. E. Pike and C. H. Seager. Percolation and conductivity: A computer study i*. *Physical Review B*, 10, 1974.

[81] M. M. Tomadakis and S. V. Sotirchos. Transport properties of random arrays of freely overlapping cyclinders with various orientation distributions. *Journal of Chemical Physics*, 98:616–626, 1993.

[82] M. Webber and M. Kamal. Estimation of the volume resistivity of electrical conductive composites. *Polymer Composites*, 18:711–724, 1997.

[83] D. Kumlutas, I. H. Tavman, and M. T. Coban. Thermal conductivity of particle filled polyethylene composite materials. *Composite science and technology*, 63, 2003.

[84] Comsol. 1998-2013. http://www.comsol.com/.

[85] J. T. Clarke and B. R. fox. Rate of heat vaporization of graphite above 3000k. *The Journal of chemical physics*, 51:3231–3240, 1969.

[86] W.s.o Rodden, S.S. Kudesia, D.P. Hand, and J.D.C Jones. A compreshensive study of the long pulse nd:yag laser drilling of a multi-layer carbon fibre composite. *Optics Communictaions*, 210:319–328, 2002.

[87] V. I. Zinchenko, V. V. Nesmelov, and V. D. Goldin. Prediction of thermal degradation of thermoprotective materials on the basis of their composition and properties of components. *Combustion, Explosion, and Shock Waves*, 41:57–63, 2005.

[88] J. M. Davies, Y. C. Wang, and P. M. H. wong. Polymer composites in fire. *Composites Part A: Applied Science and Manufacturing*, 37:1131–1141, 2006.

[89] J. E. J. Staggs. Modelling thermal degradation of polymers using single-step first-order kinetics. *Fire Safety Journal*, 32:17–34, 1999.

[90] K. A. Trick, T. E. Saliba, and S. S. Sandhu. A kinetic model of the pyrolysis of phenolic resin in a carbon/phenolic composite. *Carbon*, 35:393 – 401, 1997.

[91] E. Farkas, Z. G. Meszena, A. Toldy, S. Matk, B. B. Marosfoi, and G. Marosi. Modelling of transport processes in a developing char. *Polymer Degradation and Stability*, 93, 2008.

[92] P. P. Guilloit Ka. M. Ng M. J. MacDonald, C. Chu. A generalized blake-kozeny equation for multisized spherical particles. *AIChE Journal*, 37:1583–1588, 1991.

[93] J.A. Teixeirac M. Motac A. Yelshinc R.P. Diasa, C.S. Fernandesb. Permeability analysis in bisized porous media: Wall effect between particles of different size. *Journal of Hydrology*, 349:470–474, 2008.

[94] A. Bejan D. A. Nield. *Convection in Porous Media*. Springer, 2002.

[95] Hexcel. *HexPly M21*, March 2010.

[96] Solartron Analytical. *Dielectric Interface: 1296 - Operating Manual*. Solartron Group Ltd, 1999.

[97] K. A. Bakshi, A. V. Bakshi, and U. A. Bakshi. *Electrical Measurements*. Technical Publications Pune, 2009.

[98] Ece lab - the schering bridge, 2006. http://ecelab.com/schering-bridge.htm.

[99] Haefely. *Tettex Instruments: 2914 Test Cell for Solid Insulates*, 2000.

[100] S. Wang, D. D. L. Chung, and J. H. Chung. Impact damage of carbon fibre polymer matrix composites studied by electrical resistance measurements. *Composites, Part A: Applied science and manufacturing*, 36:1707–1715, 2005.

[101] M. Kupke, K. Schlte, and R. Schuler. Non destructive testing of frp by d.c and a.c electrical methods. *Composite Science and Technology*, 61:387–347, 2001.

[102] RS Components. *Silver loaded Electrcially Conductive Paint 5gm (stock number: 186-3593)*.

[103] M. E. Brown. *Introduction to Thermal Analysis: Techniques and Applications*. Kluwer Academic Publishers, 2001.

[104] D. M. Price, D J. Hourston, and F. Dumont. *Encyclopedia of Analytical Chemistry: Thermogravimetry of Polymers*. John Wiley and Sons Ltd, 2000.

[105] S. Sauerbrunn and P. Gill. *Decomposition kinetics using TGA*. TA Instruments: Thermal Analysis and Rheology, 2002.

[106] J. H. Flynn and L. A. Wall. A quick, direct method for the determination of the activation energy from the thermogravimetric data. *Polymer Letters*, 4:323–328, 1966.

[107] H. E. Kissinger. Reaction kinetics in differential thermal analysis. *Analytical Chemistry*, 29:1702–1706, 1957.

[108] ASTM. Standard test method decomposition kinetics by thermogravimetry (astm-1641-99). 1999.

[109] H. Wang, J. Yang, S. Long, X. Wang, Z. Yang, and G. Li. Studies on the thermal degradation of poly (phenylene sulfide sulfone). *Polymer Degradation and Stability*, 83:229 – 235, 2004.

[110] A. Gu and G. Liang. Thermal stability and kinetics analysis of rubber modified epoxy resin by high resolution thermogravimetric analysis. *Journal of Applied Polymer Science*, 89:3594–3600, 2003.

[111] K. A. Trick and T. E. Saliba. Mechanisms of the pyrolysis of phenolic resin in a carbon/phenolic composite. *Carbon*, 33:1509 – 1515, 1995.

[112] Y. Wu and N. Katsube. A constitutive model for thermomechanical response of decomposing composites under high heating rates. *Mechanics of Materials*, 22:189 – 201, 1996.

[113] J. E. J. Staggs. A simple model of polymer pyrolysis including transport of volatiles. *Fire Safety Journal*, 34:69 – 80, 2000.

[114] S. Montserrat, K. Malek, and P. Colomer. Thermal degradation kinetics of epoxy-anhydride resins: I influenced of silica filler. *Thermochimica Acta*, 313:83–95, 1998.

[115] C. Schick. Differential scanning calorimetry (dsc) of semicrystalline polymers. *Anal Bioanal Chem*, 395:1589–1611, 2009.

[116] P.S. Gill, S. R. Sauerbrunn, and M. Reading. Modulated differential scanning calorimetry. *Journal of thermal analysis*, 40:931–939, 1993.

[117] J. Anesin. Melting curves and heat of fusion of indium. *Metrologia*, 21:7–9, 1985.

[118] A. Wolynski, T. Herrmann, P. Mucha, H. Haloui, and J. Huillier. Laser ablation of cfrp using a picosecond laser pulses at different wavelengths from uv to ir. *Physics Procedia*, 12:292–301, 2011.

[119] D. Herzog, P. Jaeschke, O. Meier, and H. Haferkamp. Investigation on the thermal effect caused by laser cutting with respect to static strength of cfrp. *International Journal of Machine Tools and Manurfacture*, 48:1464–1473, 2008.

[120] M. DellErbaa, L.M. Galantuccib, and S. Migliettaa. An experimental study on laser drilling and cutting of composite materials for the aerospace industry using excimer and co2 sources. *Composites Manufacturing*, 3:1419, 1992.

[121] Coherent Inc. *VERDI V2,V5 and V6 - Diode-Pumped Laser Technology*, 2003.

[122] Y. Hirano, S. Katsumata, Y. Iwahori, and A. Todoroki. Artificial lightning testing on graphite/epoxy composite laminate. *Composites, Part A: Applied science and manufacturing*, 41:1461–1470, 2010.

[123] P. Feraboli and M. Kawakami. Damage of carbon/epoxy composite plates subjected to mechanical impact and simulated lightning. *Jounral of Aircraft*, 47:999–1012, 2010.

[124] G. W. Reid. Mechanical damage to aircraft structures from lightning strikes. *Proceedings of the Institution of Mechanical Engineers, Part G: Journal of Aerospace Engineering*, 207:1–14, 1993.

[125] ASTM. *Standard Guide for Computed Tomography (CT) Imaging (ASTM1441-00)*, 2000.

[126] NDT Resource Centre. *Introduction to Ultrasonic Testing*. www.ndt-d.org/EducationResources/CommunityCollege/Ultrasonics/cc_ut_index.htm.

[127] T. Hasiotis, E. Badogiannis, and N. G. Tsoivalis. Application of ultrasonic c scan technology for tracing defects in laminated composite materials. *Journal of Mechanical Engineering*, 57:192–203, 2009.

[128] NCC UK. *NCC - Available Equipment*. http://nccuk.com/equipment.

[129] J. Scott and C. V. Zyl. *Introduction to EMC*. Newness, 1971.

[130] D. Thomas. *Engineering Electromagnetics*. Pergamon Press Inc, 1972.

[131] NPL Kaye and laby. Tables of physical and chemical constants 3.11.1 properties of polymers, 2005. http://www.kayelaby.npl.co.uk/chemistry/3_11/3_11_1.html.

[132] W. S. O. Rodden, S. S. Kudesia, D. P. Hand, and J. D. C. Jones. A comprehensive study of the long pulse nd:yag laser drilling of multi-layer carbon fibre composites. *Optics Communications*, 210:319 – 328, 2002.

[133] B. Harris. *Engineering Composite Materials*. Insitute of Materials, London, 1999.

[134] T. A. Davis. Algorithm 832: Umfpack, an unsymmetric-pattern multifrontal method. *CM Transactions on Mathematical Software*, 30:196–199, 2004.

[135] J Sandler, M. S. P. Shaffer, T. Prasse, W. Bauhofer, K. Schulte, and A. H. Windle. Development of a dispersion process for carbon nanotubes in an epoxy matrix and the resulting electrical properties. *Polymer*, 40:59675971, 1999.

[136] P. F. Little, A. W. Hanson, and J.A. Dobbing. Arcs of metal sheets in simulated lightning dischargesio. *IEEE International Symposium on EMC*, pages 375–380, 1985.

[137] J. D. Anderson. *Fundamentals of Aerodynamics*. McGraw-Hill Science/Engineering/Math, 2001.

[138] N. N. Yanenko. *The method of fractional steps: The solution of problems of mathematical physics in several variables*. Springer, 1971.

[139] H. S. Carslaw and J.C. Jaeger. *Conduction of Heat in Solids*. Oxford University Press, 1959.

[140] Airbus. Technical drawing - cfc flat panel. 2008.